SAGITTARIUS B2 NORTH

BIRTH OF A SUPER-STELLAR CLUSTER?

Inagural-Dissertation
zur
Erlangung des Doktorgrades
der Mathematisch-Naturwissenschaftlichen Fakultät
der Universität zu Köln
vorgelegt von

Andreas Stefan Schwörer
aus Freiburg im Breisgau

Köln, 13. Juli 2020

Berichterstatter: Prof. Dr. Peter Schilke
Prof. Dr. Stefanie Walch-Gassner

Tag der mündlichen Prüfung: 09. September 2020

Meinen Eltern

Für Eine Wunderschöne Kindheit

Und jedem Anfang wohnt ein Zauber inne,
Der uns beschützt und der uns hilft, zu leben.

Stufen – Hermann Hesse

Abstract

Sagittarius B2 (North) is a chemically rich, high-mass star-forming region located within the giant molecular cloud complex Sgr B2 in the central molecular zone (CMZ) of our Galaxy. The CMZ provides an extreme environment in terms of pressure, turbulent Mach number, and gas temperature, which are much higher than those found in star-forming regions distributed throughout the Galactic disk, but comparable to the physical conditions found in starburst galaxies. Thus, Sgr B2 is a good target to study star formation under extreme conditions in our local environment.

In this thesis I use an unbiased, spectral line-survey that covers the frequency range from 211 to 275 GHz and obtained with ALMA (angular resolution of $0\farcs4$, or 3300 au) to study the small-scale structure of the dense gas in Sgr B2(N). Complementary observations with ALMA cover a smaller frequency range at 1 mm, but achieve an angular resolution of $0\farcs05$ ($\sim$400 au). In order to derive the kinematic properties of the gas in a chemically line-rich source like Sgr B2(N), I developed a python-based tool that stacks all the detected line transitions of any molecular species. This allows me to increase the signal-to-noise ratio of our observations and average out line blending effects, which are common in line-rich regions.

The dust continuum emission at 242 GHz of Sgr B2(N) reveals the presence of filamentary structure on scales of 0.1 pc. These filaments are also visible in the emission maps of the molecular species CH_3OCHO, CH_3OCH_3, CH_3OH and H_2CS. In total, eight filaments are found that converge to the central hub (with a mass of 2000 $M_\odot$, assuming a temperature of 250 K) and extending for about 0.1 pc (up to 0.5 pc). The spatial structure, together with the presence of the massive central region, suggest that these filaments may be associated with accretion processes, transporting material from the outer regions to the central dense hub. I derive velocity gradients along the filaments of about 20–100 km s^{-1} pc^{-1}, which are 10–100 times larger than those typically found on larger scales ($\sim$1 pc) in other star-forming regions. The mass accretion rates of individual filaments are $\lessapprox 0.05$ $M_\odot$ yr^{-1}, which result in a total accretion rate of 0.16 $M_\odot$ yr^{-1}. Some filaments harbor dense cores that are likely forming stars and stellar clusters. I determine an empirical relation between the

luminosity and stellar mass of the clusters. The stellar content of these dense cores is on the order of 50% of the total mass. The timescales required for the dense cores to collapse and form stars, exhausting their gas content, are compared with the timescale of their accretion process onto the central hub. This suggests that the cores may merge in the center when already forming stellar clusters but still containing a significant amount of gas, resulting in a 'damp' merger. Besides, I detect in emission of SiO and CO an outflow originating from the central core with roughly 230 $M_\odot$ The average abundance ratio of SiO to H_2 is $10^{-8.7\pm0.4}$ and increases with velocity. The mass loss rate of the outflow is with 0.047 $M_\odot$ one third of the mass accretion rate. Moreover, I find in the northern satellite core a compact object with RRL-maser emission and partially thick thermal emission, proposing the presence of a photo-evaporating disk with a RRL-maser as observed in MWC349.

I conclude that the high density and mass of the central region, combined with the presence of converging filaments with high mass, high accretion rates and embedded dense cores already forming stars, suggest that Sgr B2(N) may have the potential to evolve into a super stellar cluster.

Zusammenfassung

Sagittarius B2 (Nord) ist eine chemisch reiche und massive Sternentstehungsregion, die sich innerhalb des riesigen Molekülwolkenkomplexes Sgr B2 in der zentralen molekularen Zone (engl. central molecular zone, CMZ) unserer Galaxie befindet. In der CMZ liegen Druck, Mach-Zahl und Gastemperatur allesamt viel höher als in anderen Sternentstehungsregionen innerhalb der galaktischen Scheibe. Allerdings sind diese extremen Bedingungen durchaus vergleichbar mit denen in weit entfernten Starburst-Galaxien. Sgr B2 ist aufgrund seiner Nähe folglich gut geeignet, um den Vorgang der Sternentstehung in extremen Umgebungen zu untersuchen.

In dieser Arbeit verwende ich ein 'spectral line-survey', welches den Frequenzbereich von 211 bis 275 GHz abdeckt und mit ALMA aufgezeichnet wurde (Winkelauflösung von $0\farcs4$, oder 3300 au), um kleinste Strukturen des dichten Gases in Sgr B2(N) zu untersuchen. Zusätzlich nutze ich ALMA Beobachtungen mit einer Winkelauflösung von $0\farcs05$ ($\sim$400 au). Um die kinematischen Eigenschaften des Gases in chemisch reichen Regionen wie Sgr B2(N) ermitteln zu können, habe ich ein Python-basiertes Tool entwickelt, das alle detektierten Übergänge einer Molekülart zusammenfasst und mittelt. Dies verbessert das Signal-Rausch-Verhältnis unserer Beobachtungen wesentlich, da Überlagerungen von Übergangslinien verschiedener Moleküle, ein häufiges Phänomen solcher Gebiete, weniger gewichtet werden.

Die Staubkontinuumsemission von Sgr B2(N) bei 242 GHz zeigt Filamentstrukturen in der Größenordnung von von ca. 0,1 pc. Diese Filamente sind auch in den Emissionskarten der Moleküle CH_3OCHO, CH_3OCH_3, CH_3OH und H_2CS sichtbar. Insgesamt wurden acht Filamente entdeckt, die in Richtung des zentralen Hubs (mit einer Masse von 2000 $M_\odot$, unter der Annahme einer Temperatur von 250 K) konvergieren und sich über etwa 0,1 pc (bis zu 0,5 pc) erstrecken. Die räumliche Anordnung so wie die hohe Masse im Zentrum legen nahe, dass diese Filamente Material von den äußeren Regionen nach innen transportieren. Die Geschwindigkeitsgradienten entlang der Filamente betragen ca. 20–100 km s^{-1} pc^{-1} und sind damit 10-100 mal höher als in anderen Sternentstehungsregionen (in Maßstäben von $\sim$1 pc). Die Massenakkretionsraten einzelner Filamente betragen $\lessapprox$ 0,05 $M_\odot$ yr^{-1} und summieren sich zu

einer Gesamtakkretionsrate von 0,16 $M_\odot$ yr^{-1}. Einige Filamente beherbergen dichte Kerne, die wahrscheinlich Sterne und Sternhaufen bilden. Ich ermittle eine empirische Beziehung zwischen der Leuchtkraft von Clustern und ihrer stellaren Masse. Der Sterngehalt dieser dichten Kerne liegt in der Größenordnung von 50% ihrer Gesamtmasse. Die benötigte Zeit der dichten Kerne, um unter ihrem eigenen Gewicht zu kollabieren und Sterne zu bilden, ist vergleichbar mit der Zeit, die sie benötigen, um das Zentrum zu erreichen. Vermutlich transportieren folglich die Kerne noch eine große Menge an Gas und Staub in den zentralen Hub, während in ihnen allerdings schon Sternhaufen entstanden sind ('damp merger'). Des Weiteren zeigen die Emissionskarten von SiO und CO einen Ausfluss (engl. outflow) ausgehend vom zentralen Hub mit einer Masse von 230 $M_\odot$. Das Häufigkeitsverhältnis von SiO zu H_2 wurde auf ungefähr $10^{-8,7\pm0,4}$ bestimmt und nimmt bei zunehmender Gasgechwindigkeit zu. Die Masseverlustrate beträgt 0,047 $M_\odot$, was ungefähr ein Drittel der Massenakkretionsrate entspricht. Darüber hinaus finde ich im nördlichen Kern Rekombinationslinien Maser Emission und thermische Emission, die eventuell von einer photo-verdampfenden Akkretionsscheibe verursacht werden (ähnlich wie in MWC349).

Zusammengefasst: Die hohe Dichte und Masse der Zentralregion, die konvergierenden Filamente mit hohen Akkretionsraten und die enthaltenen dichten Kerne, die bereits Sterne bilden, legen nahe, dass Sgr B2(N) das Potenzial haben könnte, sich zu einem super-stellaren Cluster zu entwickeln.

Contents

List of Figures

List of Tables

List of abbreviations

ALMA	Atacama Large Millimeter Array
CASA	Common Astronomy Software Applications
CDMS	Cologne Database for Molecular Spectroscopy
FWHM	full width at half maximum
GC	globular cluster
GMC	giant molecular clouds
IMF	Initial Mass Function
ISM	interstellar medium
JPL	Jet Propulsion Laboratory
H I	neutral hydrogen
H II	ionized hydrogen
HCH II region	hypercompact H II region
HMC	hot molecular core
LSM	line stacking method
RRL	radio recombination line
SED	spectral energy distribution
Sgr B2	Sagittarius B2
Sgr B2(M)	Sagittarius B2 Main
Sgr B2(N)	Sagittarius B2 North
YSO	young stellar object
UCH II region	ultracompact H II region
VLA	Very Large Array
VLT	Very Large Telescope
YMC	young massive cluster
YSO	young stellar object
XCLASS	eXtended CASA Line Analysis Software Suite

Part I

Introduction

1 The star forming process

Without doubt, our Sun is the most prominent star. And when night falls, we can admire on a cloudless sky with naked eyes three to six-thousand other stars. Modern telescopes scanned the sheer endless starry firmament and recorded even several billions more. But all these stars have not endless time to live. When their time has come, they will pass away, and from the remaining matter new stars will rise like a Phoenix; The cosmic cycle of life.

But how does a new star form? The nurseries of stars within the interstellar medium (ISM) are molecular clouds (see section 1.2), which are composed by dense and cold gas and dust. First indications of their existence were already obtained in the 18th and 19th century. Wilhelm Herschel is quoted as saying "Hier ist wahrhaftig ein Loch im Himmel" (Houghton 1942), while he was observing a starless, dark region in the constellation of Scorpion. From today's perspective this area was a star forming region, wrapped in dense gas, which is obscured in visible light. However, this gas shines brightly in the millimetre and submillimetre part of the electromagnetic spectrum and that is why I used for my research the ALMA telescope (see section 3.2). In the following sections, I will describe the environment as well as the mechanism of star formation.

1.1 The Interstellar Medium

The ISM is a imprecise expression for anything between stars: Atoms, molecules, dust grains, the interstellar radiation field, cosmic rays and magnetic fields. With 70% of the interstellar gas mass, hydrogen is the most abundant element; about 60% is in the form of atomic hydrogen (H I), 20% of it is in the molecular form (H_2) and 20% is ionized

hydrogen (H II). The second most abundant molecule is helium, which contributes with roughly 28% to the total gas mass. Consistently, heavier elements do only account with 2%. The physical conditions (e.g., density and temperature) of the medium is found to be very diverse and thus, the ISM is often designated as a multi-phase medium. As explained in a review by Klessen & Glover (2016), these phases are classified in

- ▷ Warm Neutral Medium (WNM): Warm and diffuse atomic gas with kinetic temperatures in the range 5000–8000 K and densities of 0.01–0.1 cm^{-3} (Field 1969).
- ▷ Cold Neutral Medium (CNM): Cold and dense atomic gas with T ∼100 K and densities of ∼30 cm^{-3} (Field 1969).
- ▷ Hot Ionized Medium (HIM): Very hot, low-density gas which has been heated by stellar winds and blast waves from novae and supernovae. The temperature is about 10^6 K and the density is roughly 10^{-2} cm^{-3}. This medium is believed to fill about half of the volume of the galactic disk (McKee & Ostriker 1977).
- ▷ Warm Ionized Medium (WIM): Hot and diffuse gas outside the localized H II regions, which are photoionized by UV photons from OB stars. The WIM is a fundamental gas phase constituent of the Milky Way which accounts for 90% or more of the total ionized gas in the ISM. The temperature ranges from about 6000 to 10000 K and has a low density of only 0.1 cm^{-3}.
- ▷ Molecular Gas: The coldest and densest phase of the ISM with temperatures of 10–20 K and densities above 10^2 cm^{-3}. It is the kind of gas of which molecular clouds are made.

Besides of gas, also small dust grains are part of the ISM. They only account with roughly 1% to the total mass. However, their function is very important in the process of star formation, since they are very important for cooling. Dust grains absorb (and scatter) photons in the UV and optical ranges of the electromagnetic spectrum and reemit photons with longer wavelength (far-infrared and also mm/submm), which can escape out of the dense environment. The grain material is mainly carbonaceous (Mathis et al. 1977) or silicates (Draine & Lee 1984).

1.2 Molecular clouds

It is dark in molecular clouds, since most of the star light is excluded by dust extinction ($A_\nu \gtrsim 5$ mag). These clouds are made mainly of molecular gas, predominantly of molecular hydrogen. Almost all the available carbon is in CO. It is freezing cold with temperatures around 10–20 K. Thus, dust grains in molecular clouds become coated with thin icy mantles, which plays an important role for the formation of many molecular species. The chemistry in molecular clouds is driven by cosmic rays rather than starlight and, furthermore, the relatively high densities of 10^2 cm^{-3} enable the formation of complex molecules (Williams & Viti 2014). The colossus among these clouds are the so-called giant molcular clouds (GMCs), which are mainly distributed around the mid-plane of galaxies. They have characteristic masses of 10^4–10^6 $M_\odot$ and typical sizes on the order of 50 pc across (e.g., Blitz 1993). One example is the famous star-forming complex Orion A with $\sim 10^4$ $M_\odot$ (see Fig. 1.1). The target of my research, Sagittarius B2, has even the enormous mass of 10^7 $M_\odot$ (see section 3.1). Overall, the structure of GMCs to be clumpy with local regions of significant larger density. There are clumps with (A_ν ~10 mag), densities of 10^3 cm^{-3}, diameters of a couple of parsecs, temperatures of roughly 10 K and masses of ~30 $M_\odot$. Zooming in on smaller scales substructures with even higher densities are found; Dense cores with densities of 10^4 cm^{-3}, A_ν >10 mag, masses of ~10 $M_\odot$, temperatures of ~10 K and sizes of 0.1 pc. An excess of temperature, induced by photons from forming stars, can cause a large set of chemical reaction, resulting in the formation of many complex molecules. These cores are named as hot molecular cores (HMCs) and have a size of 0.05–0.1 pc, an extinction coefficient A_ν from more than 50–1000 mag, temperatures between 100–300 K, densities of 10^7–

Figure 1.1: Hershel image of the Orion A giant molecular cloud. The image is a composite of the wavelengths of 70 microns (blue), 160 microns (green) and 250 microns (red) and spans about 1.3 x 2.4 degrees. Credit: ESA/Herschel/Ph. André, D. Polychroni, A. Roy, V. Könyves, N. Schneider for the Gould Belt survey Key Programme. https://sci.esa.int/s/A6ezkQ8/

10^9 m^{-3} and masses of 10–3000 $M_\odot$. All values are taken from Carroll & Ostlie (2014) and summarized in Table 1.1.

Table 1.1: Properties of molecular clouds, clumps, dense cores and hot molecular cores.

	molecular clouds	clumps	dense cores	hot molecular cores
size [pc]	2–50	0.1–2	<0.1	0.05–0.1
extinction A_ν [mag]	∼5	10	>10	50–1000
density [cm^{-3}]	10^2–10^3	10^3	10^4	10^7–10^9
mass [$M_\odot$]	10^2–10^6	30	10	10–3000
temperature [K]	10–20	10	10–70	100–300

Note. Values as reported in Carroll & Ostlie (2014).

1.3 Filamentary structures

The Herschel Space Observatory revealed over the last decades the omnipresence of interstellar filaments at many different scales. And a growing number of observations show evidence that they play a fundamental role in the star formation process. It has been found in local low-mass star forming regions at scales of a few pc that filaments are hatcheries of prestellar cores (e.g. Taurus B211/B213 , see Fig. 1.2, Palmeirim et al. 2013; Marsh et al. 2016; André et al. 2010; Molinari et al. 2010). Similarly, molecular clouds forming

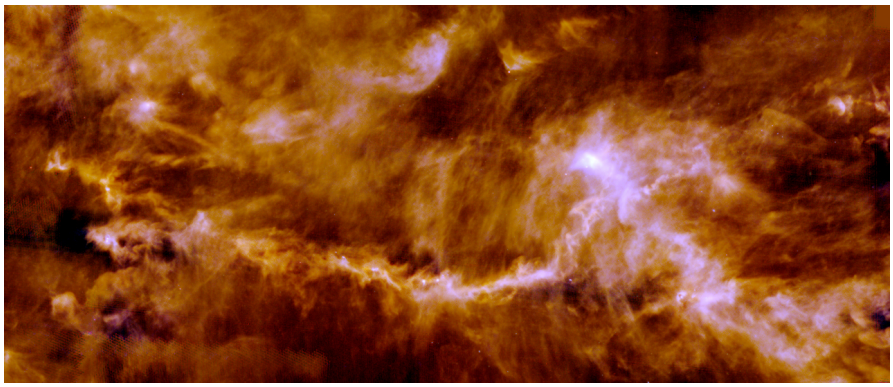

Figure 1.2: Three-color image of the B211/B213 filament in the Taurus Molecular Cloud combines Herschel bands at 160 μm (blue), 250 μm (green) and 500 μm (red). The image spans about 2x5 degrees. The observations revealed an intricate pattern of filaments dotted with a few compact, bright cores: the seeds of future stars. Credit: ESA/Herschel/PACS, SPIRE/Gould Belt survey Key Programme/Palmeirim et al. 2013. `https://sci.esa.int/s/8YYqz18`

high-mass stars (O and B spectral type stars) are found to be pervaded by large and complex filamentary networks, when observed at large scales of a few pc (see e.g. Orion: Suri et al. 2019; Hacar et al. 2018; MonR2: Treviño-Morales et al. 2019). In these cases, stellar clusters are found to form in dense hubs with densities $>10^6$ cm^{-3}. Denser high-mass star forming regions like W33A ($\sim 10^7$–10^8 cm^{-3}), when observed with high enough angular resolution, show filamentary structures at scales of a few 1000 au and converging toward the most massive objects forming in the clusters (Maud et al. 2017; Izquierdo et al. 2018). The widespread presence of these filaments indicate that they may persist for a large fraction of the lifetime of a molecular cloud and may transport mass to the central regions.

The origin of filamentary cloud structure is unclear, but different scenarios have been proposed: Individual filaments can arise from compression of initially uniform gas by converging turbulent flows (Klessen & Glover 2016). In more magnetically dominated models, self-gravity pulls gas to the mid-plane after turbulence dissipates, and ambipolar diffusion allows gravitational instabilities to create filamentary structures (Nakamura & Li 2008). Whereas Pudritz & Kevlahan (2013) proposed that filaments may form at the intersection of colliding flows.

1.4 Low-mass star formation

From all that has been said: Stars form in molecular clouds and molecular clouds are pervaded by filaments, which have local regions of significant larger density, dubbed clumps (Fig. 1.3, stage 1). These clumps can fragment in an hierarchical manner to condensations of bound and dense cores. Due to turbulent motion (e.g., originated by super nova explosions or cloud-cloud collisions) and local instabilities the cores start to collapse in a free-fall scenario (Fig. 1.3, stage 2). The collapse occurs initially iso-thermal, since the produced energy can be radiated away through the thin envelope. The cores now condense into rotating spheres of gas that serve as stellar embryos, known as 'proto-stars' (Fig. 1.3, stage 3). The density of these objects is much higher, and therefore the radiation can not longer escape, and the heating has started. Material from the envelope is still accreted onto the stellar embryo and due to the rotation a circumstellar (keplerian) accretion-disk

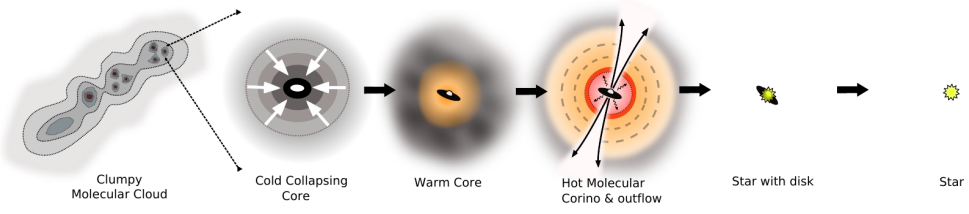

Figure 1.3: The process of low-mass star formation. Credit: Original cartoon by Cormac Purcell, modified by Adam Ginsburg.

has formed. When the density and temperature are high enough, deuterium fusion begins, and the pressure of the resultant radiation decelerate (but does not stop) the collapse. In order to remove the excess angular momentum of the infalling material, bipolar outflows (Fig. 1.3, stage 4) occur. Slowly, the mass of the protostar becomes larger than the mass of the infalling envelope and it reaches a temperature of a few hundred Kelvins. When the surrounding gas and dust envelope disperses and accretion process stops, the star is considered a pre-main-sequence star. As soon as the star ignites and hydrogen burning sets in, the primary energy source is not longer gravitational contraction but nuclear fusion. The star is now dubbed as main-sequence star on the Hertzsprung–Russell diagram.

In the previous paragraph, the formation of low-mass stars has been explained only in a nutshell. For a more detailed description, including explanations on the Jeans mass (stability criteria of molecular clouds/the critical mass where gravitation and gas pressure are in equilibrium) or the Hayashi track (luminosity–temperature relationship of infant stars), see for instance the introduction to star formation from Ward-Thompson & Whitworth (2011).

1.5 High-mass star formation

While low-mass stars, due to their large number, constitute most of the total stellar mass in our galaxy, high-mass stars (M>8 $M_\odot$) dominate the energy input into the interstellar medium, through supersonic winds and strong ultraviolet radiation, and enrich the ISM with heavy elements (Schilke 2015, Tan et al. 2014). Also, they play a major role in shaping morphology of their host galaxies and can trigger or terminate star formation. The theory of low-mass star formation is well-supported by observational evidences and as described above stars form by gravitational collapse of rotating dense cores within molecular clouds. However, for massive stars the mechanism of star formation is not well understood. Their formation process will differ from low-mass stars in significant ways: while the Kelvin-Helmholtz timescale of low-mass stars is significantly longer than the time required to assemble them, for any reasonable accretion rate it is shorter for high-mass stars (Schilke 2015). The Kelvin-Helmholtz timescale is the period in which nuclear reactions have not yet been triggered, and the protostar compensates its energy losses by gravitational contraction. The time for this phase is given by

$$t_{\mathrm{KH}} = \frac{\mathrm{GM}^2}{\mathrm{RL}}, \tag{1.1}$$

with G as gravitational constant, M the protostellar mass, R the protostellar radius, and L the Luminosity. This time scale can differ for a 1 $M_\odot$ star to a 15 $M_\odot$ star with up to three orders of magnitude as shown by Iben (1965). The time required to assemble them can be estimated with the free-fall time, which can be calculated by

$$t_{\mathrm{ff}} \approx \left(\frac{3\pi}{32\mathrm{G}\rho}\right)^{1/2}, \tag{1.2}$$

where ρ is the density. Comparing both time scales will show for high-mass stars (M$\gtrsim$8 $M_\odot$) under any reasonable density distribution that $t_{\rm KH} \ll t_{\rm ff}$. Consequently, the star begins nuclear fusion while it is still accreting more gas. The arising problem comes from the radiative pressure of the newly formed star, which should be powerful enough to push against the infalling material and stop the accretion process, resulting in an non-longer growing proto-star. However, stars above M>8 $M_\odot$ have been observed and thus, a new theory for high-mass star formation or an adapted theory for stars of all masses is needed. Over the last decades, two possible concepts crystallized out, the monolithic collapse (e.g., Tan & McKee 2002) and competitive accretion (e.g., Bonnell et al. 1998).

The monolithic collapse is a scale up version of low-mass star formation. The key idea is that the radiative pressure can escape through the cavities, which are milled by outflows or jets in the envelope. Thus, accretion through the circumstellar disk onto the protostar can proceed unhindered. However, very high accretion rates 10^{-4}–10^{-3} $M_\odot$ are required.

An alternative approach has been presented by Bonnell et al. (1998). They considered star formation in a cluster. All stellar embryos are created with equal mass, and then gather mass through Bondi-Hoyle accretion. Their accretion rate therefore is determined by their location in the cluster potential and stars have to compete for their resources; thus, this scenario follows the principle the rich gets richer. Under these assumptions, the most massive stars found in clusters must be located at the cluster center.

Despite the difficulties in the theoretical understanding of the formation of high-mass stars, observational evidences enable to sketch a picture of the evolutionary sequence for the formation of high-mass stars (see Fig. 1.4). The main difference to the low-mass star formation is that high-mass stars are able to produce high energy UV photons, which ionize the surrounding material (H II regions). This can affect the neighboring dense cores and may lead to the termination of star formation. H II regions and hot molecular cores are observational evidences of ongoing high-mass star formation.

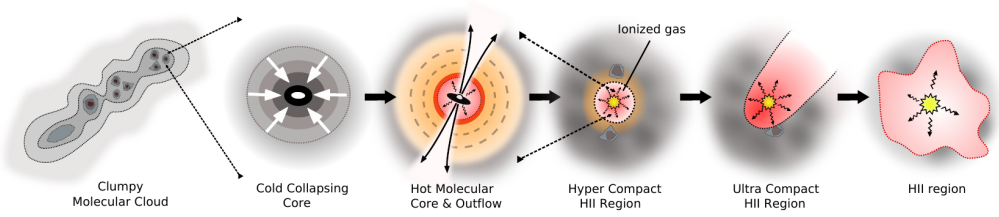

Figure 1.4: The process of high-mass star formation. In contrary to low mass stars (see Fig. 1.3), high-mass stars can produce high energy UV photons, which are ionizing the surrounding material and can terminate star formation in neighboring cores. Credit: Original cartoon by Cormac Purcell, modified by Adam Ginsburg.

2

Young Massive Cluster

In chapter 1 I described how individual stars form. However, stars usually do not form in isolation, they form in clustered environments (Lada & Lada 2003). In particular, this applies to high-mass stars (de Wit et al. 2005). Traditionally, astronomers have drawn a clear distinction between the relatively young and less massive open clusters (associated with the Galactic disk) and the old and more massive globular clusters (GCs) that reside mostly in the bulge and halo (as reviewed by Portegies Zwart et al. 2010). The latter are extremely dense clusters of old stars with low metallicity, which are, with ten billion years, among the oldest in the universe, and are unusually rich in stellar exotica. Open cluster are, as their name suggests, leaky and their members can drift away, while globular cluster stay gravitationaly bound for a long period of their lifetime. The Milky Way contains over 150 old globular clusters (e.g., Fig. 2.1), which have ages of 5–13 Gyr and masses of roughly 10^4–10^6 $M_\odot$ (Longmore et al. 2014). Open clusters have only masses of ∼500 $M_\odot$ and their

Figure 2.1: The globular star cluster Messier 55 in the constellation of Sagittarius harbors stars, which are with ten billion years among the oldest in the Universe. Credit: ESO/J. Emerson/VISTA. https://www.eso.org/public/images/eso1220a/

number is estimated at 23,000–37,000 currently in the Galaxy. Also our Sun is considered as a former member of an open cluster, which as time got by dissolved.

2.1 Properties of young massive clusters

What I described in the previous section is only half the story. There is a third kind of clusters, young massive clusters (YMCs). These kind of clusters are relatively young (<100 Myr), comparable to those of many Milky Way open clusters, but their masses (>10^4 $M_\odot$) and projected lifetimes coincide with those of the old GCs (Portegies Zwart et al. 2010). One prominent example is the YMC R136, which is located in the Large Magellanic Cloud in the Tarantula Nebula, 30 Doradus (e.g., Fig. 2.2), with estimated 10^5 stars. But also our Milky Way Galaxy harbors a handful of these clusters such as Arches, Quintuplet or Westerlund I. The latter is currently known to be the most massive one in our local environment (Clark et al. 2005). The properties of many of these are catalogued in Portegies Zwart et al. (2010) and clearly summarized in the review of Longmore et al. (2014): "YMCs typically have radii of ∼1 pc and core stellar densities ≥10^3 $M_\odot$ pc^{-3}. They are generally spherical, centrally-concentrated and often mass segregated (i.e. more massive stars are preferentially found towards the center of the cluster). The initial cluster mass distribution is not trivial to measure, but over many orders of magnitude in mass appears to be reasonably well approximated by a power law, $dN/dM \propto M^{-2}$, across all environments. YMCs are found predominantly in starburst galaxies and mergers – a couple of thousand are known to exist in the Antennae and NGC 3256, for example. These YMCs are typically more massive than those found in the Local Group and Milky Way. In the local universe (i.e. not starbursts/mergers), YMCs are typically found in the disks of galaxies." But YMC did not only form in the past, their formation process can also be observed today. For instance, recent observations of Leroy et al. (2018) revealed ∼14 bright, compact sources in NGC 253 starburst galaxy, which all seem to form new young massive clusters.

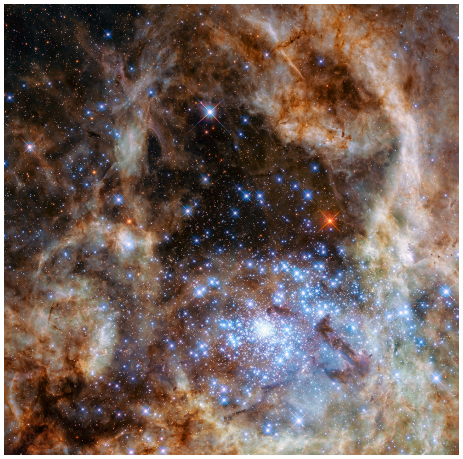

Figure 2.2: The central region of the Tarantula Nebula in the Large Magellanic Cloud with the YMC R136. This cluster contains hundreds of young, blue stars, among them the most massive stars detected in the universe so far. Credit: NASA, ESA, and P. Crowther (University of Sheffield). https://hubblesite.org/image/3716/gallery/

Due to the similarity of GCs and YMCs, YMCs are often considered as their younger cousins or progenitors (e.g., Longmore et al. 2014,Walker et al. 2016). If true, they could provide a better understanding of extreme cluster formation or even help to gain some insight in the star formation at the early Universe. However, their formation process is still poorly understood, in particular, the mechanism of mass accumulation. In the following section I will present the two most prominent proposed scenarios, the 'in-situ' and the 'conveyor belt' formation.

2.2 In situ and hierarchical cluster formation

As mentioned in the previous section, the formation process of YMCs is not well understood, also since only a poor sample of YMC progenitors in different evolutionary stages have been observed: G0.253+0.016 (a.k.a. 'the Brick', e.g., Longmore et al. 2012, Rathborne et al. 2014) and the clouds 'd', 'e' and 'f' (e.g., Immer et al. 2012, Walker et al. 2015, Walker et al. 2016) within the CMZ. However, Longmore et al. (2014) gives a few simplified considerations on the possible initial conditions, which can help to find observable evidences. The first consideration focused on the initial gas reservoir. In order to form a cluster with $M_* \geq 10^4$ $M_\odot$ (following the definition in section 2.1) a huge mass reservoir is needed. These two parameter are related by the star formation efficiency ϵ in the form $M_{gas}^{init} = M_* \ / \ \epsilon$. The second aspect to be considered is the size of the cluster. For this, we can distinguish two different cases: first, the final stellar cluster radius R_* is much smaller than the size of the initial mass reservoir (R_{gas}^{init}), and second, both radius are similar. These considerations can be expanded leading to the two mainly-accepted scenarios:

The 'in-situ' formation ('wet merger'):
In this scenario, the required amount of gas mass is gathered into the same volume of the final stellar cluster before star formation sets in (R_{gas}^{init}=R_*). The difficulty arises from the fact that this requires extreme densities. Such densities would result in a exceptionally short free-fall time for the dense gas. Consequently, gathering the final mass has also to be short or the star formation inside the final cluster volume is delayed or suppressed due to an unknown reason. On the basis that the accumulation time is very short and star formation is almost instantaneous once the gas is accumulated, only clumps with mass M_{gas} and radius R_* with ongoing star formation should be observed. In case of the delayed star formation, significant numbers of clouds with mass close to M_{gas} and radius R_* but with no active star formation should be observed.

The 'conveyor belt' formation ('dry merger'):
In this scenario, the mass reservoir extends farther away than the final stellar cluster size ($R_{gas}^{init} > R_*$). Thus, stars can form in regions with much lower densities. In order for the proto-cluster to reach the required final stellar densities, the gas and forming stars must converge into a bound stellar system. Possible ways are transport of sub-cluster via filaments or a gravitational collapse of a single cloud. Therefore, clouds with M_{gas} and radius R_* with no hints of ongoing star formation should never be observed. In many works the described scenario is also dubbed as hierarchical cluster formation (Fujii 2015).

The first scenario, the 'in-situ' formation, is often labeled as 'wet merger' since mainly gas is transported towards the center, while the second scenario, the 'conveyor belt' formation, is named as 'dry merger', since an important fraction of the collected gas is already converted to stars while approaching the cluster center. Both scenarios are visualized in Fig. 2.3. Sagittarius B2 North, my source of interest, fulfills the initial conditions with a mass of roughly 10^4 $M_\odot$ and with access to a total mass reservoir of 10^7 $M_\odot$ (see section 3.1). In numerical simulations, Fujii (2015) found for YMCs a local star forming efficiency larger than 50%, Pfalzner & Kaczmarek (2013) report values of 60–70%. On the basis of these numbers Sagittarius B2 North has the potential to form a YMC and thus, provides the unique opportunity to study the formation process and early stages of a of YMC in our local environment. In part III, I analyze the mechanism of mass accumulation and in chapter 8, I discuss my results with regard to both proposed scenarios. An other open issue in the process of YMC formation is the impact of feedback. Whether or not the expulsion of residual gas by feedback affects the boundedness of stellar structure depends on the division between gas exhaustion and gas expulsion. In order to explore the gas expulsion, I study in section 7.3 the outflow in Sagittarius B2 North.

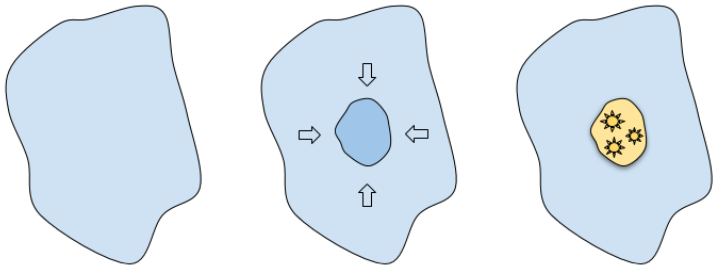

(a) In-situ formation ('wet merger')

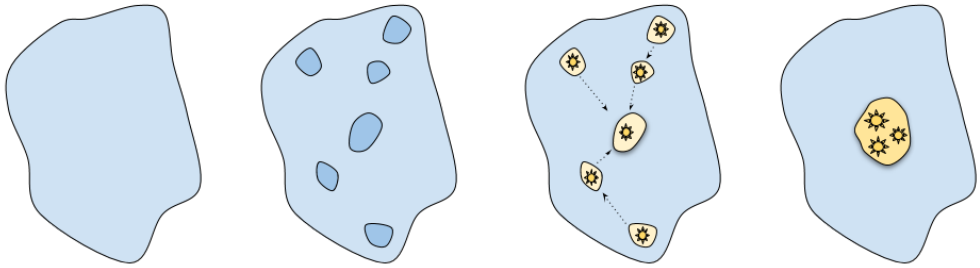

(b) conveyor belt formation ('dry merger')

Figure 2.3: (1) In the 'in-situ' scenario, the required amount of gas mass is gathered into the same volume of the final stellar cluster before star formation sets in. Extreme densities required, which results in a short free-fall time for the dense gas. This implies that gathering the final mass has also to be short or star formation is delayed ('wet merger').
(2) In the 'conveyor belt' scenario, the mass reservoir extends farther away than the final stellar cluster size. Thus, stars can form in regions with much lower densities and be transported towards the center of the cluster ('dry merger').

3
Sagittarius B2

3.1 The star-forming complex Sagittarius B2

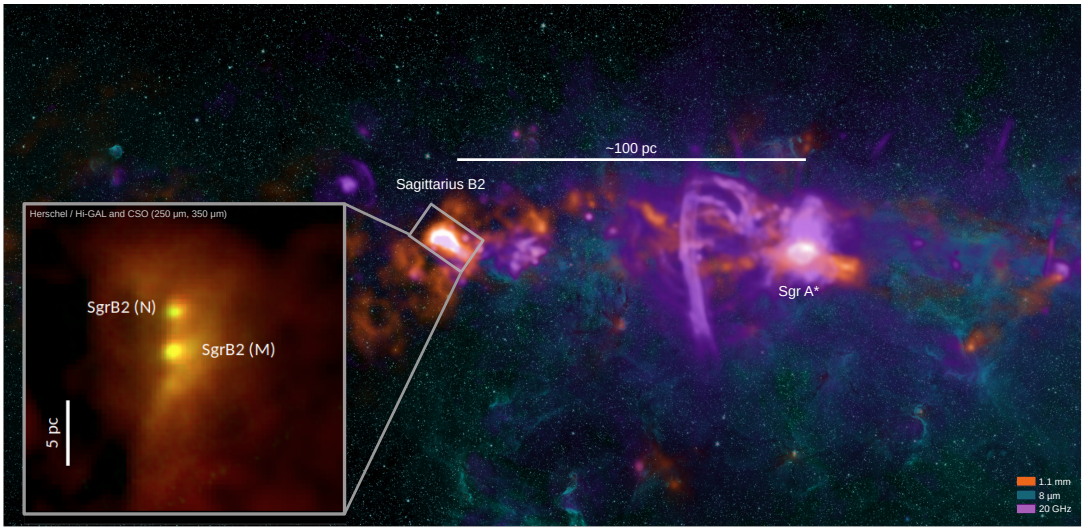

Figure 3.1: Central Molecular Zone of the Milky-way Galaxy. The star-forming complex Sagittarius B2 appears bright in emission at 1.1 mm (orange), which traces cold dust. Within the cloud there are two main spots of star formation. Sgr B2(M) and Sgr B2(N). Latter, is the target of my analysis. Emission at 8 μm (petrol) shows hot dust/polycyclic aromatic hydrocarbon (PAH), while the emission observed at 20 GHz (purple) is tracing hot ionized gas. Credit: CMZ image, A. Ginsburg, NRAO.

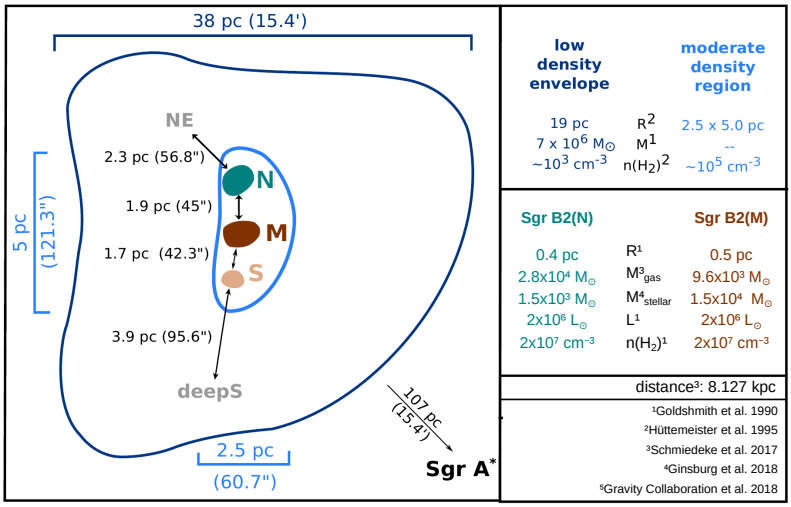

Figure 3.2: Sketch of the Sgr B2 region, based on Hüttemeister et al. (1995), adapted from Schmiedeke (PhD. thesis, 2017) and finally updated.

The star-forming complex Sagittarius B2 (hereafter Sgr B2) is the most massive cloud in our Galaxy with a mass of 10^7 $M_\odot$ and H_2 densities of 10^3–10^5 cm^{-3} (Schmiedeke et al. 2016, Hüttemeister et al. 1995, Goldsmith et al. 1990), located at a distance[1] of 8.127 ± 0.031 kpc (Gravity Collaboration et al. 2018) in the vicinity of the Galactic center SgrA* (at a projected distance of 107 pc) within the Central Molecular Zone (CMZ, see Fig- 3.1). The CMZ provides an extreme environment in terms of pressure, turbulent Mach number, and gas temperature (∼60 to >100 K), which are much higher than those found in star-forming regions distributed throughout the Galactic disk (Ginsburg et al. 2016, Morris & Serabyn 1996), but comparable to the physical conditions found in starburst galaxies. Therefore, the CMZ and Sgr B2 are perfect targets to study star formation under extreme conditions in our local environment. Based on its density structure, it has been proposed that Sgr B2 is composed of three different parts (Hüttemeister et al. (1995), visualized in Fig. 3.2): A low-density envelope with n_{H_2} ∼10^3 cm^{-3} , a moderate-density region with n_{H_2} ∼10^5 cm^{-3} extending around local hot molecular cores, which are the most compact and densest regions with n_{H_2} ∼10^7 cm^{-3} .

The complex Sgr B2 harbors two main sites of star formation, the hot molecular cores Sgr B2 Main (M) and North (N), with masses of 10^4–10^5 $M_\odot$. Moreover, active high-mass star formation (numerous ultracompact H II regions, see, e.g., Schmiedeke et al. 2016; Gaume et al. 1995; Mehringer et al. 1993), X-ray sources associated with H II regions, X-ray sources with no radio or IR counterparts (Takagi et al. 2002), dense cores (Sánchez-Monge et al. 2017), embedded protostars, and molecular masers (Goicoechea et al. 2004) have been observed. Over all, Sgr B2 could be the progenitor of one or multiple YMCs.

[1]For consistency with previous findings in the literature, for our calculations I used the distance 8.34 ± 0.16 kpc (Reid et al. 2014)

Figure 3.3: The ALMA telescope on the Chajnantor plains nearly 5000 m above sea level. Credit: NRAO/AUI/NSF.

3.2 ALMA observations

For my analysis I made use of observations with the Atacama Large Millimetre/submillimetre Array (ALMA). This telescope has been build to study light from some of the coldest objects in the Universe. This light has wavelengths of around a millimeter, between infrared light and radio waves. The nurseries of stars, molecular clouds, are cold and dense objects that are obscured in visible light (see section 1.2), but they shine brightly in the millimetre and submillimetre part of the electromagnetic spectrum. Thus, this state-of-the-art telescope is the perfect instrument to study the formation process of the most massive stars in our Universe.

ALMA is an astronomical interferometer, composed of 66 high-precision antennas. These antennas can work together as a 'single' telescope to provide higher resolution images of astronomical objects. Whereas by single dish telescopes the spatial resolution is proportional to λ/D, where λ is the wavelength of the incoming radiation and D the diameter of the dish, the resolution of interferometer depends on the maximum separation of the individual antennas (called baseline). Since large single-dish telescopes are difficult to manufacture, expensive and above a certain size also impractical in handling, interferometer are a good alternative to achieve an high angular resolution. That is the positive side of the balance sheet of interferometers, however, for achieving this high angular resolution, you also have to accept the loss of emission due to the gaps between the antennas. Because of these gaps, an interferometer filters out the large scale extended emission. In order to counteract this issue, the *uv–plane* (the Fourier transform of the sky-plane) should be sampled with as many baselines as possible. Also combining single-dish and interferometer data can help to recover extended emission. For more details about 'Interferometry and Synthesis in Radio Astronomy' I refer to the same named book by Thompson et al.

(2017). The 66 high-precision antennas of ALMA are divided into fifty antennas with a size of 12 meters in the 12-m array, closely spaced twelve antennas with a size of 7 meters (known as the Atacama Compact Array, ACA), and four 12 meter antennas (known as the Total Power array for single-dish observations). The most compact configurations of the 12-m array with a baseline of 160 m, can reach a resolution of 1.″5 at 230 GHz. In the most extended configuration of the 12-m array, a baseline of 16 km, ALMA can even achieve an angular resolution of 0.″018 at 230 GHz.

Data-set I

The observed data are part of the project "Physical and chemical structure of massive proto-clusters" (ALMA#2013.1.00332.S) lead by the PI P. Schilke. In June 2014 and June 2015, Sgr B2 was observed with ALMA during its Cycle 2. 34–36 antennas were used in an extended configuration with baselines in the range from 30 to 650 m, which provided an angular resolution of 0.″3–0.″7 (corresponding to ∼3300 au). The observations are sensitive to angular scales of only <5″, and thus larger scale extended emission is filtered out. The chosen spectral scan mode surveyed the whole ALMA band 6 (211 to 275 GHz, see Fig. 3.7) with 10 different spectral tunings, providing a spectral resolution of 0.5–0.7 km s^{-1}. Sgr B2(N), with phase center at α(J2000)=$17^h47^m19^s.887$, δ(J2000)=−28°22′15.″76, was observed in track-sharing mode together with Sgr B2(M). The calibration and imaging processes[2] were carried out with CASA[3] version 4.4.0. All the images were restored with a common Gaussian beam of 0.″4. Further details of the observations, calibration, and imaging are provided in Sánchez-Monge et al. (2017).

The observations resulted already in a first publication (see Sánchez-Monge et al. 2017), where mainly the continuum emission towards Sgr B2(M) and Sgr B2(N) has been studied. However, the line-survey contains also (thousands of) spectral lines of diverse molecular species, which will be evaluated in this thesis (see part III). Hereafter, I will briefly present the result achieved so far and describe the morphology of Sgr B2(N) (see also Fig. 3.4):

Most of the mass in Sgr B2(N) is concentrated in the central HMC, later named as dense hub. Besides of the massive central core, Sgr B2(N) harbors in a distance of ∼4.″5 (or 0.18 pc) a second bright core in the north (later named 'satellite' core). The new ALMA observations revealed in total 20 sources (cores) in the field of view. A comparison with previous SMA 345 GHz and VLA 40 GHz observations exposed that the brightest sources are dominated by (partially optically thick) dust, and an important degree of contamination from ionized gas free-free emission in weaker sources. The chemical richness observed

[2]The calibration and imaging processes has been conducted by A. Sànchez-Monge, I. Physikalisches Institut, Universität zu Köln, Zülpicher Strasse 77, 50937, Köln, Germany.

[3]The Common Astronomy Software Applications (CASA, McMullin et al. 2007). Downloaded at `http://casa.nrao.edu`

in many of them suggest a cluster of small hot molecular cores. These cores are further explored in section 7.2.3. Besides of the continuum sources, also filamentary-like structures are found to converge towards the center. The morphology, together with the massive hub suggests that these filaments are transporting material towards the center. In order to analyze their kinematic structure, I study the spectral lines of different molecular species in section 7.2.1.

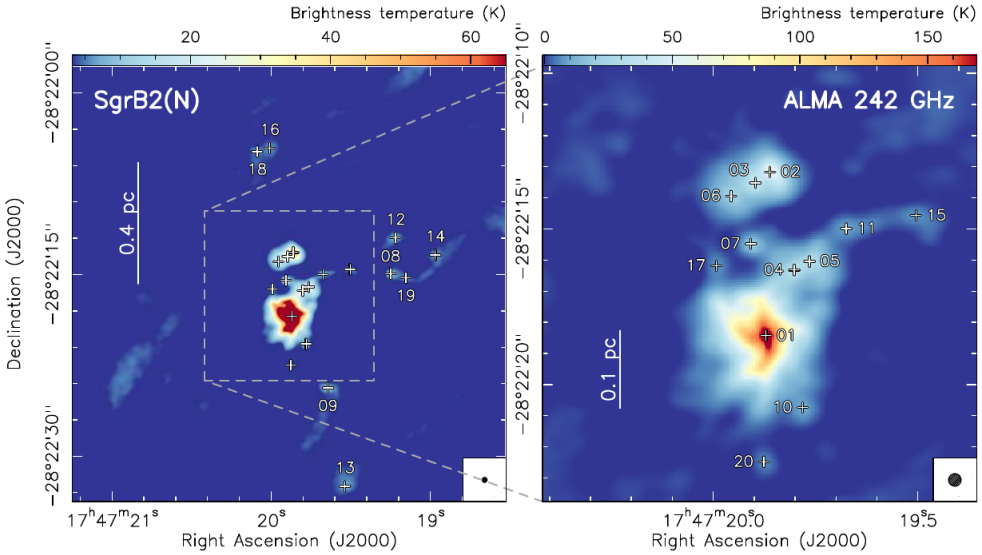

Figure 3.4: ALMA 242 GHz continuum emission towards Sgr B2(N). The right panel shows a close-up view of the central 0.56 pc. The identified 20 continuum sources are indicated with crosses. The label numbers are sorted by mass, starting with 01 as most massive object. Credit: Sánchez-Monge et al. (2017).

Data-set II

This data-set is part of the project "(How) do very massive stars form in our Galaxy?" (ALMA#2016.1.00550.S) lead by the PI A. Ginsburg. In the year 2017, Sgr B2 was observed with ALMA using the 12 m Array with 40 antennas in an extended configuration, which provided an angular resolution of ∼0.″05 (corresponding to ∼400 au). This is roughly a factor ten higher compared to the spatial resolution in data-set I. The observations are sensitive to angular scales of only <0.″5. The spectral resolution is 1.34 km s^{-1}, slightly coarser compared to data-set I. Sgr B2(M), with phase center at α(J2000)=17^{h}47^{m}20^s.1300, δ(J2000)=−28°23′06.″100, was observed in track-sharing mode together with Sgr B2(N). The four spectral windows are centered at the frequencies 217.90 GHz, 219.86 GHz, 231.87 GHz and 233.744 GHz, each with a bandwidth of 1875 MHz. The calibration and imaging processes[4] were carried out with CASA. All the images were restored with a individual Gaussian beam per velocity channel in the range of 0.″05–0.″07. Besides the observations in the ALMA band 6, the same project also observed Sgr B2(N) and Sgr B2(M) at 3 mm with an angular resolution of ∼0.″08 and a spectral resolution of 2.944–3.425 km s^{-1}. The filaments identified in data-set I are resolved higher and a network of sub-filaments and fibers has been revealed. I got access to these data towards the end of my PhD. and thus, they are mainly used to proof my findings. However, in chapter 7.3.4 they are used to study the ionized gas in Sgr B2(N).

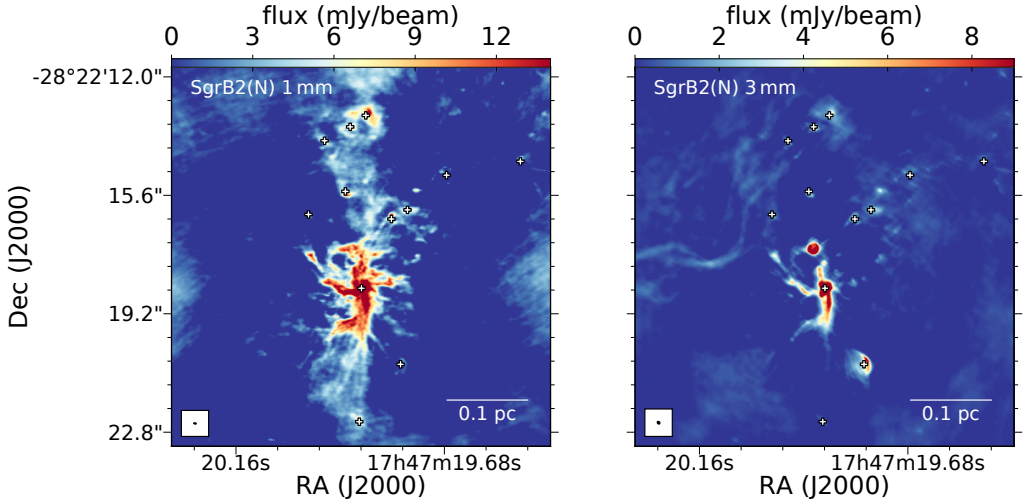

Figure 3.5: ALMA continuum emission at 1 and 3 mm towards Sgr B2(N). The identified 20 cores (Sánchez-Monge et al. 2017) are indicated with crosses. The emission at 1 mm is more sensitive to dust emission whereas the emission at 3 mm more to the ionized gas.

[4]The calibration and imaging processes has been conducted by A. Ginsburg, Department of Astronomy, University of Florida, P.O. Box 112055, Gainesville, FL, USA.

Comparison of data-sets

In recent years, the quality of observations improved a lot. In order to demonstrate the advances, different observations towards Sgr B2(N) are presented in Fig. 3.6. The first image has been taken with the SMA (Submillimeter Array, located in Hawaii, 4080 m above sea level) by Qin et al. (2011) and is mainly resolving two cores. The ALMA observations of data-set I have a similar spatial resolution of 0.″4, but a better uv-coverage, and reveal filamentary structures. The latest data-set II resolves the filaments in a network of sub-filaments and fibers.

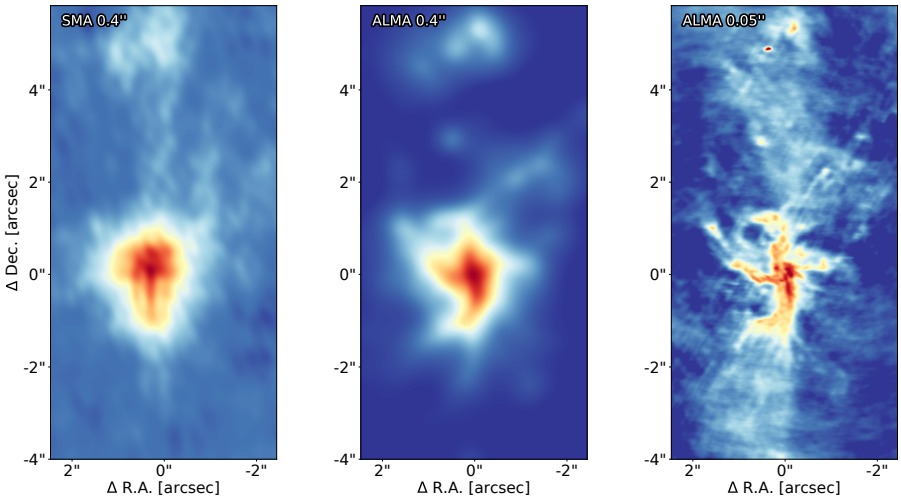

Figure 3.6: Comparison of different observations towards Sgr B2(N). *Left panel:* Observations with the SMA telescope (Qin et al. 2011) resolve two cores. *Middle panel:* Observations with ALMA (data-set I) with a similar spatial resolution but better uv-coverage resolve filamentary structures. *Right panel:* Observations with ALMA providing a resolution of 0.″05 data-set II resolve a network of sub-fialments and fibers. The images are centered at the position of the central core with coordinates α(J2000)=$17^h47^m19^s.87$, δ(J2000)=$-28°22'18''.43$.

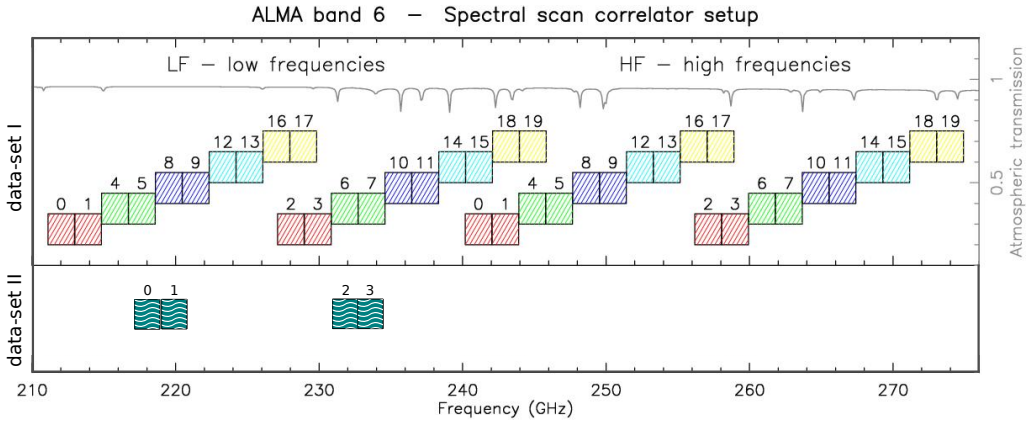

Figure 3.7: Sketch of the setup of the ALMA correlator during the spectral scan observations in the ALMA band 6. The observations of data-set I were divided in two frequency ranges: low frequencies from 211 to 246 GHz, and high frequencies from 240 to 275 GHz. Each frequency tuning is depicted with a different color, while the different boxes refer to the four spectral windows per tuning. The number of the spectral windows, as given in the ALMA observations, are given on top of each box. The gray line shows the transmission of the atmosphere at the ALMA site with a precipitable water vapor of 0.7 mm. The bottom panel indicates the four spectral windows observed in data-set II. This figure has been adapted from Sánchez-Monge et al. (2017).

4

About this work

4.1 Motivation

A gigantic molecular cloud is located in the immediate vicinity (projected distance ∼100 pc) to the center of our Home Galaxy: Sagittarius B2. Its neighborhood, the Central Molecular Zone (CMZ), provides an extreme environment in terms of pressure, turbulent Mach number, and gas temperature (∼60 to >100 K), which are much higher than those found in star-forming regions distributed throughout the Galactic disk (Ginsburg et al. 2016, Morris & Serabyn 1996), but comparable to the physical conditions found in starburst galaxies. Besides, this cloud is with $\sim 10^7$ $M_\odot$ the most massive one in our Milky-way. Thus, Sgr B2 is the perfect target to study star formation under extreme conditions in our local environment and to probe if the known physical relations in the formation process of stars stay valid even in such an outstanding case.

One main site of star formation within the molecular cloud complex is Sgr B2 North, my source of interest, which has a mass of $\sim 10^4$ $M_\odot$ and densities of 10^5–10^7 $M_\odot$ pc^{-3} (Sánchez-Monge et al. 2017, Schmiedeke et al. 2016). These high densities, the large mass reservoir of the envelope, and high star formation activity in a number of dense cores suggest that Sgr B2(N) may gather enough mass to form a super-stellar cluster or young massive cluster (YMCs are described in chapter 2) such as Arches or Quintuplet.

So far only little is known about the initial conditions of YMCs and their formation process. In particular, the mechanism of mass accumulation raises numerous questions. However, different formation scenarios have been proposed ('in-situ' and 'hierarchical'/'conveyor belt' cluster formation) and thus, Sgr B2 constitute a good candidate to review their assumptions and predictions observationally. Although this cloud is located

close to our our Sun (∼8.1 kpc) compared to starburst galaxies, it is necessary to achieve high angular resolutions to study in detail the dense molecular gas. The spatial resolution of our sub-millimeter observations (data-set II) with the state-of the art telescope ALMA is with 0.″05 close to the currently highest achievable resolution[1] of 0.″018 at 230 GHz. Furthermore, the rich chemistry in the molecular cloud-complex Sgr B2 introduces many difficulties. For instance, most of the molecular lines are not well isolated, but suffer from line blending of other species. Thus, the characterization of the moving gas is not a simple business. Our line survey (data-set I) offers the possibility to study many transitions of the same molecular species simultaneously, which makes it possible to overcome the line-blending issue. For this purpose I developed the line-stacking method, presented in chapter 5.

Finally, YMCs are often considered as younger cousins or progenitors of Globular Clusters. GCs are extremely dense clusters of old stars, which are with ten billion years, among the oldest in our Universe. If the relationship between YMCs and GCs is true, YMCs, and therefore also Sgr B2(N), could help to gain some insight in the star formation at the early Universe. Even though, it may be difficult to draw a head-to-head comparison.

4.2 Outline

This thesis is organized as following:
In **Part I**, I present the basic concepts of star and cluster formation and their arising problems. Also my source of interest, Sagittarius B2, is introduced as well as the observations I made use of.

In **Part II**, I describe new methods, which I developed for the analysis of the complex data-sets. The first method (line-stacking, chapter 5) helps to explore kinematic structures of chemically rich regions like Sgr B2, where it is not offhandedly possible to identify well isolated transitions, which are conventionally used to determine velocities in a simple way. The second method resulted in the relation between stellar cluster luminosity and stellar cluster mass.

Part III includes the analysis of the observations and the discussion of my results. In the analysis section, I explore the kinematic structure (section 7.2.1) along the identified filaments towards Sgr B2(N) and determine the accretion rates (section 7.2.2). Both are are 10–100 times larger than usually found in other star-forming regions. In section 7.2.3 the stellar mass of the dense cores and their free-fall times are estimated. I find that although clusters have enough time to form within the cores, they will not exhaust all their gas before approaching the center. In section 7.3, I investigate feedback processes

[1] Only a global network of radio telescopes can achieve a higher angular resolution (e.g., the Event Horizon Telescope with 60 microarcseconds).

as outflows and H II regions. The main outflow contains roughly 230 $M_\odot$ and thus ranks high compared to other sources. Finally, I detect a new radio recombination line maser object within the northern (satellite) core of Sgr B2(N).

The conclusion given in **Part IV** summarizes my results and put them in the context of high-mass cluster formation. In the following outlook I singled out a few interesting aspects, which could be explored further, and present some preliminary results.

At the end of each section I add a grey rectangular box with the main take-home messages.

Part II

Methods

5

The Line Stacking Method

Gas in molecular clouds is constantly moving. But how can we observe with which velocity it flows? The effect which is used by the Astronomers to derive velocity information, can be experienced in everyday life. An ambulance with switched on siren is approaching, passing and drives away. We can hear that the sound pitch changes from lower to higher. This effect is known as the Doppler effect and it describes the change of an observed frequency in relation to a moving source. The observed frequency is approximately given by

$$f_{\mathrm{obs}} = \left(1 + \frac{\Delta v}{c}\right) f_{\mathrm{rest}}, \tag{5.1}$$

where f_{obs} is the observed frequency, f_{rest} the rest frequency of the emitting source, Δv the relative velocity between the source and the observer, and c the constant speed of sound (or for us Astronomers, the constant speed of light, respectively). In other words, the observed frequency of molecular transitions is decreasing or increasing, if the emitting source (i.e. molecular gas) is moving away or towards us (illustrated in Fig. 5.1). It is important to note that with this method we observe the motions in the gas (i.e., its velocity) along the line of sight. Hence, gas that is moving perpendicular to the line of sight will be erroneously seen as stationary. Consequently, we always have to take projection effects into account.

In practice, we can observe molecular lines (i.e transitions of molecules) to determine how much the observed frequency f_{obs} differs from the from the rest frequency f_{rest} listed in catalogs such as CDMS and JPL databases[1] and derive from the frequency difference

[1] Cologne Database for Molecular Spectroscopy (CDMS, Müller et al. 2005, Thorwirth et al. 2000) and Jet Propulsion Laboratory (JPL, Pickett et al. 1998)

(Δf = f_{obs}-f_{rest}), the relative velocity Δv to us, observers. An example with synthetic data is shown in Fig. 5.2. However, for lines which are blended by transitions of other molecular species, wrong assignments of frequencies and consequently velocities are a common problem. In chemically-rich regions like Sgr B2, it is not offhandedly possible to identify well isolated transitions (e.g. Fig. 5.3), which are usable to determine velocities in a simple way. The analysis of line-rich sources, often with thousands of lines, has many pitfalls due to an unknown number of spectral line components (produced by distinct layers of gas moving at different velocities) and contamination of multiple molecular species. Moreover, large velocity gradients across the observed region as well as different chemical compositions throughout the source are obstructive. In spite of these adversities, I convert the difficulty of the presence of innumerable lines within a blind survey into an advantage. For this, I have developed an automatized (python based) tool to stack all transitions of a certain species to increase the signal-to-noise ratio and to average out line blending effects. The process of stacking is commonly used in Astronomy to increase the signal-to-noise ratio of for example, weak radio galaxies, recombination lines and even faint molecular line transitions (see e.g., Beuther et al. 2016, Lindroos et al. 2015, Loomis et al. 2018). In my specific case, stacked data also simplifies the structure and shape of the spectral lines, thus making it possible to analyze the velocity and kinematic properties.

The line stacking method has to be performed in velocity space and not in frequency space, since Δf (the difference between the observed and the rest frequency) varies for different transitions of the same molecular species. Δv describes a physical property of the object and stays therefore constant for all transitions along the entire frequency band (see Fig. 5.2 and Eq.5.1). In the following sections, I will describe the exact procedure of stacking and perform several tests with synthetic data.

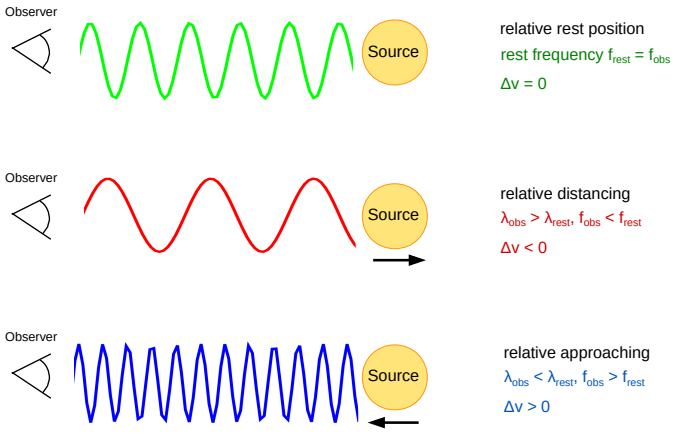

Figure 5.1: Simplified illustration of the Doppler effect. Source is moving away, results in 'stretched' wavelengths and smaller frequencies. For relative approaching vice versa.

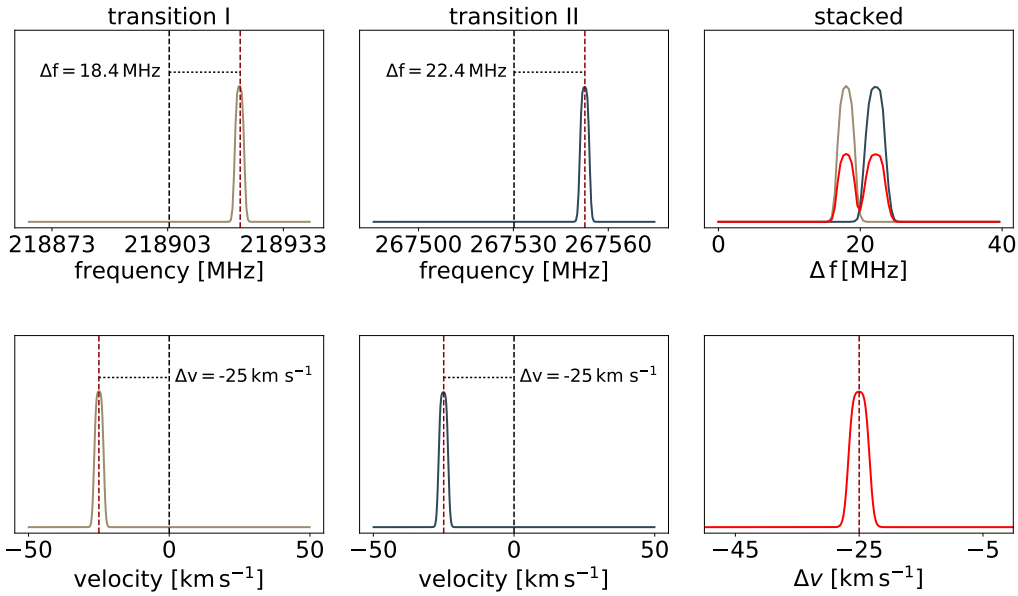

Figure 5.2: Line stacking performed for two transitions of the molecular species OCS both in frequency and velocity space. The synthetic spectrum has been produced with XCLASS[2], assuming a velocity of 25 km s^{-1}. Both transitions are converted from frequency (*top panels*) to velocity (*bottom panels*) by using the Doppler equation (Eq. 5.1). The dashed vertical lines indicate the rest frequencies of the transitions as listed in catalogs like CDMS. The velocity at 0 km s^{-1} corresponds to these rest frequencies. The spectrum in the *top right panel* shows two peaks, while in the *bottom right panel* the transitions appear at the same velocity difference.

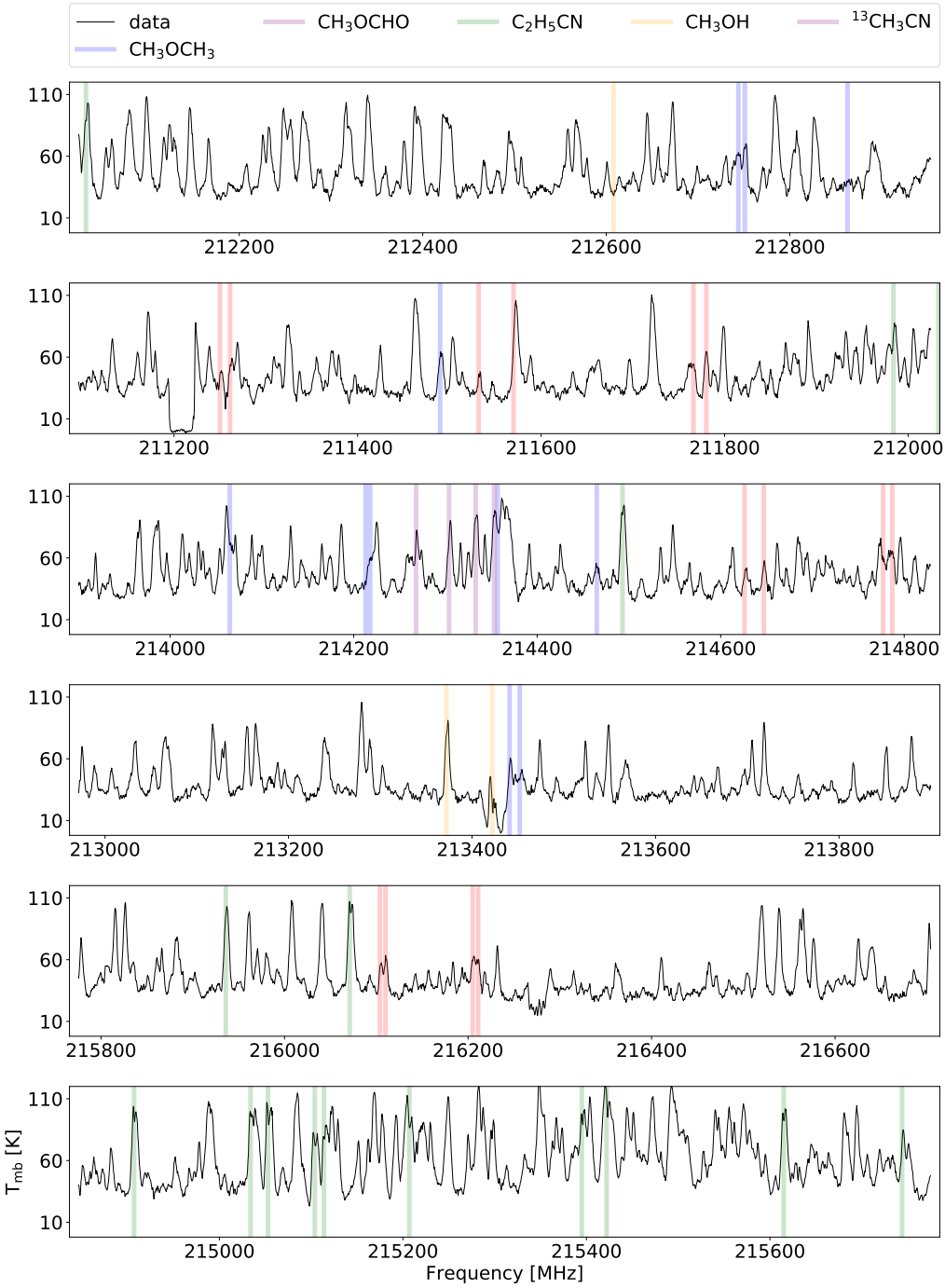

Figure 5.3: An exemplary cutout (only ∼5% of the covered frequency range) of a spectrum within Sgr B2(N) at the position with coordinates α(J2000)=$17^h47^m19^s.897$, δ(J2000)=$-28°22'13''.59$. A few transitions of molecular species, which I used in my analysis, are marked.

5.1 Modus operandi

The method is carried out in three main steps, illustrated in Fig. 5.4. First (step A in the figure), I correct our observed data by the source LSR velocity, corresponding to about 64 km s^{-1} for Sgr B2(N). This step is not necessary, but this correction simplifies the process of line identification. Subsequently, I produce a synthetic spectrum with XCLASS[2] for any molecular species assuming similar conditions (i.e., temperatures, column densities) as the one that represent the region (Möller et al. in prep). An accurate fit of the observed data to derive the best temperature, column densities and velocities is helpful but not mandatory. Reasonable assumptions are enough to determine at which frequency transitions are detected in the observations, since the synthetic spectrum is used for the identification of bright transitions. For example, for the case of CH_3OCHO (Methyl Formate), I have identified 250 bright lines above a 10 σ threshold in the frequency range 211 to 275 GHz. This selection prevents us from including transitions that are included in the catalog entries of the CDMS and JPL catalogues, but are too weak and most likely non detected, in our source of interest. Moreover, the exclusion of the weak transitions, reduces the addition of components highly dominated by noise or by the presence of (bright) transitions from other species.

Second (step B in Fig. 5.4), I cut out all the identified transitions and produce subspectra centered at them. These spectra are transformed from frequency to velocity by applying the Doppler equation. The velocity at 0 km/s (see Fig. 5.4) corresponds to the rest frequency listed in the database, since I have corrected the data by the source LSR velocity. The spectra are uniformly resampled and rebinned, using the python packages `signal` and `numpy`, to ensure that the channels in the velocity frame have the same width.

Last (step C in Fig. 5.4), all spectra are averaged using the arithmetic mean. In the final stacked spectra, the signal-to-noise ratio has increased, while at the same time line blendings are averaged out. This simplifies the analysis of the kinematic properties like velocity, linewidth, lineshape or number of components.

The stacking process can be applied to a sub-sample of transitions, selected e.g., by excitation energy level ($E_{\rm upper}$) or Einstein A coefficient, parameters that are included in the molecular line databases CDMS and JPL.

To ensure that the results of this method are reliable, some tests with pure synthetic data are presented in the following section.

[2]The software XCLASS (eXtended CASA Line Analysis Software Suite) is a tool for identifying and fitting spectral lines: Möller et al. (2017), which make uses of the Cologne Database for Molecular Spectroscopy (CDMS) and Jet Propulsion Laboratory (JPL) catalogs, via the Virtual Atomic and Molecular Data Centre (VAMDC, Endres et al. 2016).

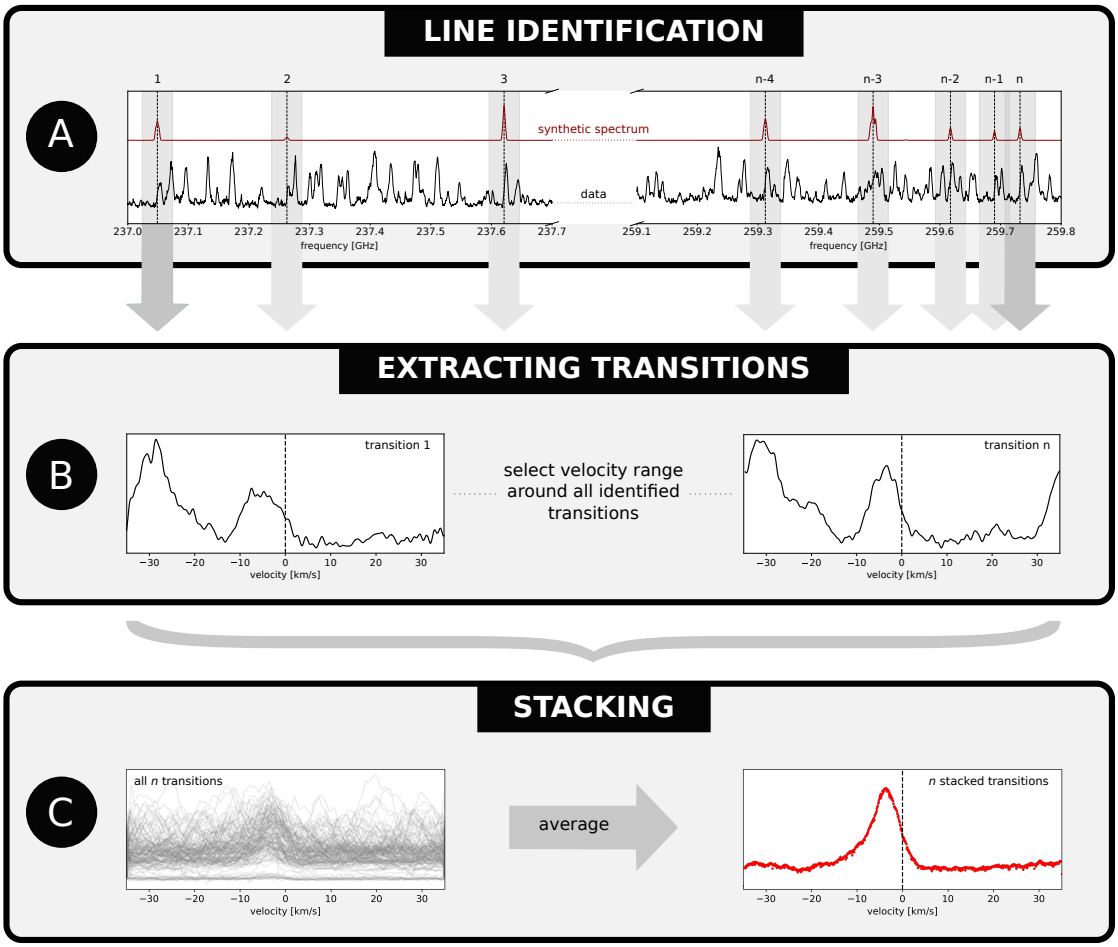

Figure 5.4: Line stacking process for molecular lines in a spectral survey. **Step A**: Correct observed spectrum, shown in black in the top, by the source LSR velocity (corresponding to 64 km s^{-1} for Sgr B2(N)). Create a synthetic spectrum (shown in red, and using XCLASS) for the considered molecular species. This will be used for the identification of detectable transitions (highlighted with a gray shadow area). **Step B:** Extract a portion of the spectrum centered at each transition, and transform the frequency axis into velocity using the Doppler equation. Each cutout spectra is uniformly resampled and rebined. **Step C:** Sum up all the cutout spectra and divide by the number of transitions. Normalization has been waived to prevent that noise and lines from other molecular species are not scaled up. Line blendings are statistically averaged out and the true line shape and the velocity can be determined.

5.2 Quality assurance with synthetic data

For the following reliability check of the line stacking method, I generated a synthetic spectrum of the molecular species C_2H_3CN (Acrylonitrile) in the frequency range of 211–275 GHz with XCLASS. Acrylonitrile is a good candidate since it has, in this frequency range, approximately 165 clear detectable transitions, which provides a good statistic. The synthetic spectrum of C_2H_3CN is produced including two different velocity components ($comp_I$/$comp_{II}$) with velocities of 0 and -5 km s^{-1}, linewidths of 5 and 2 km s^{-1}, same column densities of 3×10^{17} cm^{-2}, and temperatures of 75 and 300 K. The velocity resolution is 0.45 km s^{-1} (in the following analysis defined as 1 σ level).
The results are shown in Fig. 5.5. In panel *A*, I have stacked all 165 transitions included in the synthetic spectrum. The stacked spectrum (shown in red) has a clear two-velocity component profile. I fit Gaussians to the stacked spectra and recover the velocities of the stacked lines with an high accuracy (deviation of 0.03/0.11 km s^{-1} with respect to the original values, i.e. below 1 σ). The linewidths are also only slightly larger (0.12/0.23 km s^{-1}, below 1 σ) compared to the original values. In a second run, I performed line stacking with a sub-sample of transitions selected by excitation energy levels $E_{\rm low}$ smaller than 70 K (see Fig. 5.5, panel B). In this scenario, $comp_I$ dominates the resulting stacked-spectrum, whereas stacking of transitions between energies of 300–400 K (panel *D*) renders $comp_{II}$, consistent with the fact that $comp_{II}$ was created with a higher temperature (300 K) compared to comp I (75 K). Hence, stacking transitions restricted to certain energy ranges can give an indication of the present excitation conditions of individual components. For testing the robustness of the line stacking method, I include white noise at a level of $\sim$4 K to each sub-spectrum (panel *E*). However, the result stays almost unaffected (0.02/0.12 and 0.13/0.17 km s^{-1}, below 1 σ offset for the velocity and linewidth of the two components). In the next stage, I tightened the thumbscrews and included to each sub-spectrum 10 Gaussians with randomly selected amplitudes from 0 to 120 K and FWHMs from 1 to 6 km s^{-1}(panel *F*), simulating transitions of other molecular species. The obtained velocity and linewidth of the component with lower amplitude ($comp_I$) is more affected but still within reasonable deviations of marginal $\sim$0.3 km s^{-1}(below 1 σ). This increase in the linewidth is likely produced by the presence of the neighboring Gaussians, which act like noise and result in the broadening effect. Therefore, line-stacking of chemically rich regions will result in slightly broader lines. I note that the included Gaussians also result in generating an artificial continuum. In the next run, I combined the synthetic spectrum with the observed data of Sgr B2(N). I note that the molecule C_2H_3CN is not detected in our data and therefore the only transitions that should be found are those included in the synthetic spectrum. After performing line stacking, I recover the velocities of the two components with a similar accuracy like in the previous step. Thus, the results, which I will obtain by line stacking, in the analysis part of my thesis, are reliable.

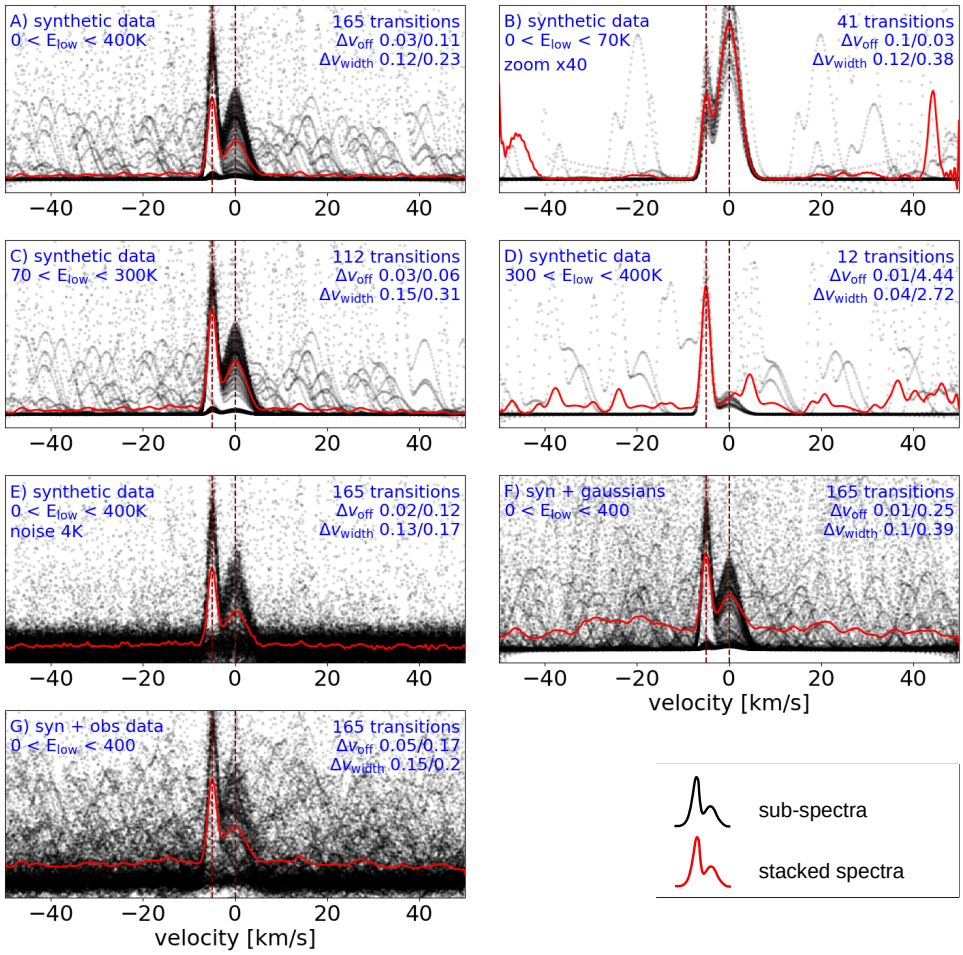

Figure 5.5: Stacked transitions of the molecular species C_2H_3CN in the frequency range of 211–275 GHz . The accuracy of the outcome by the line stacking method has been tested for *A)* stacking all 165 transitions, *B)* only 41 transition with excitation energy levels below 70 K, *C)* 112 transitions with excitation energy levels between 70 an 300 K, *D)* 12 transitions with excitation energy levels between 300 and 400 K, *E)* all 165 transitions including to each sub-spectrum white noise at a level of ∼4 K, *F)* all 165 transitions including to each sub-spectrum Gaussians, which are simulating blending lines, and *G)* 165 transitions, which are embedded in observed line-rich spectra.

I found out that the accuracy of the line stacking method depends strongly on the provided statistics (number of stacked transitions). In particular, if the stacked transitions are strongly affected by line blendings. The number of required transitions in order to get a reliable result is not fixed since the present conditions (e.g. line blendings and relative intensity of the stacked lines) are crucial. However, in an additional stress test I try to quantify this finding. In my setup, I use the same synthetic spectrum of C_2H_3CN with two

components like above and stack different numbers of transitions, between 2 and 101. To each sub-spectrum I add noise of 4 K as well as Gaussians (simulating blending lines) with random amplitudes between 4 K and 97 K, which corresponds to an intensity 1.2 times higher than the maximum amplitude in the synthetic spectrum (later labeled as 'relative line intensity' $I_{blending}/I_{peak}$). I have to note that the amplitudes of the added Gaussians are randomly but also uniformly distributed. However, in observations, the intensity distribution of blending lines seems to follow a power law function with an exponent of -1 (see Fig. A.3). Therefore, the result of my simulations must be understood as an extreme case and an upper limit.

The total number of added Gaussians can be varied and is in the first run fixed to 20, which corresponds to 50 lines per GHz. This line density has been found in previous studies for Sgr B2(N) (Sánchez-Monge et al. (2017), e.g. in Fig. A.3). The resulting velocities and linewidths are again determined by fitting Gaussians. As initial guess for the fitting routine, the velocities of the two main peaks in the stacked spectra have been selected. I perform 150 iterations for each bunch of transitions. The results are listed in Table 5.1. The parameter v_{off} indicates the velocity obtained using the line stacking method. The listed values are the mean of all 150 iterations per bunch of stacked transitions. The parameter $|\ \Delta v_{off}\ |$ indicates the absolute difference between the expected value (0 km s^{-1}/$-$5 km s^{-1}) and the value obtained using the line stacking method. The given errors are the standard deviations of the obtained velocities of all iterations. The results are visualized in Fig. 5.6 and 5.7. For comp$_{II}$, the precision of v_{off} drops below 1 σ for 23 transitions (3 σ for 20 transitions) and the velocity converges to the input value. Since comp$_I$ has a lower intensity (amplitude) than comp$_{II}$ the obtained velocity converges at a higher number of stacked transitions. The variation of the obtained velocity drops below 1 σ for 86 transitions (3 σ for 68 transitions). The accuracy of the measured linewidths are comparable to them found for the parameter velocity. The results are presented in Appendix A. In the analysis part of my thesis, I will stack 246 transitions of the molecular species CH_3OCHO, 142 transitions of CH_3OCH_3, 85 transitions of CH_3OH and 68 transitions of $^{13}CH_3OH$. Since the uniform distribution of amplitudes of the blending lines represent an extreme scenario, the line stacking method will provide reliable results even for $^{13}CH_3OH$, which has only 68 transitions within the observed frequency range.

In order to get a better understanding of the parameter 'line density', which describes the line richness of spectra, I repeat the procedure of the previous paragraph for different line densities and explore its parameter space. The results for comp$_{II}$ are presented in Fig. 5.8. I found a linear relation between the accuracy of the line stacking method and the line density. For comp$_I$ I found the same linear behavior but with decreased slope (see Fig. 5.9). Thus, the relative intensity between blending line and stacked lines seems to have a strong impact on the outcome of the line stacking method. To explore this behavior further, I vary the parameter 'relative line intensity' (the intensity ratio between blending line and intensity peak of the synthetic spectrum). The result for two different

line densities can bee seen in Fig. 5.10. I found an exponential behavior with a growth factor R_{50} of 0.008 for a line density of 50 lines per GHz and a growth factor R_{25} of 0.014 for a line density of 25 lines per GHz.

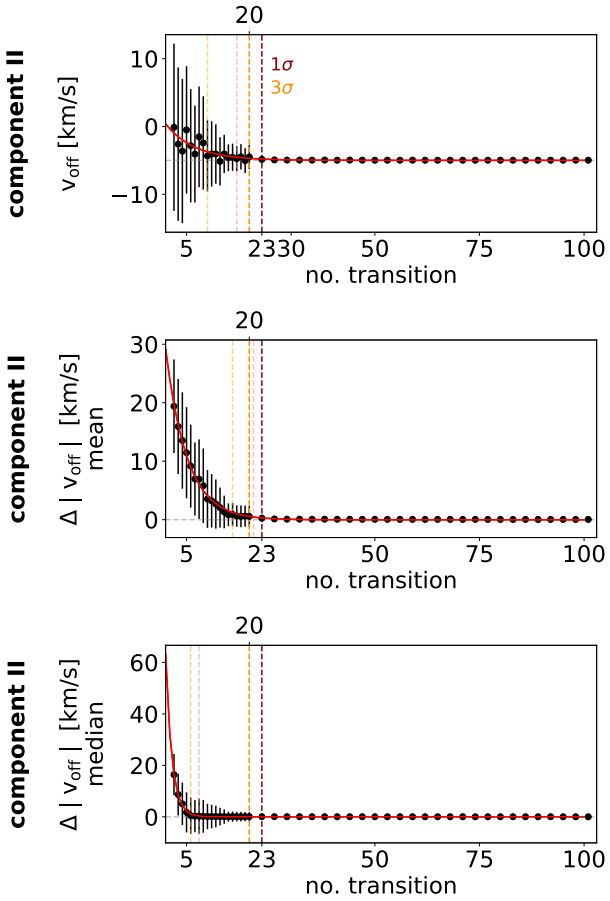

Figure 5.6: Visualization of Table 5.1. The velocity obtained using the line stacking method converges to the input velocity of -5 km s^{-1}. The red and orange dashed lines indicate, where the standard deviation (error) of the measured velocity drops below 1 or 3 σ. The transparent lines show where the obtained velocity deviates less than 1 and 3 σ.

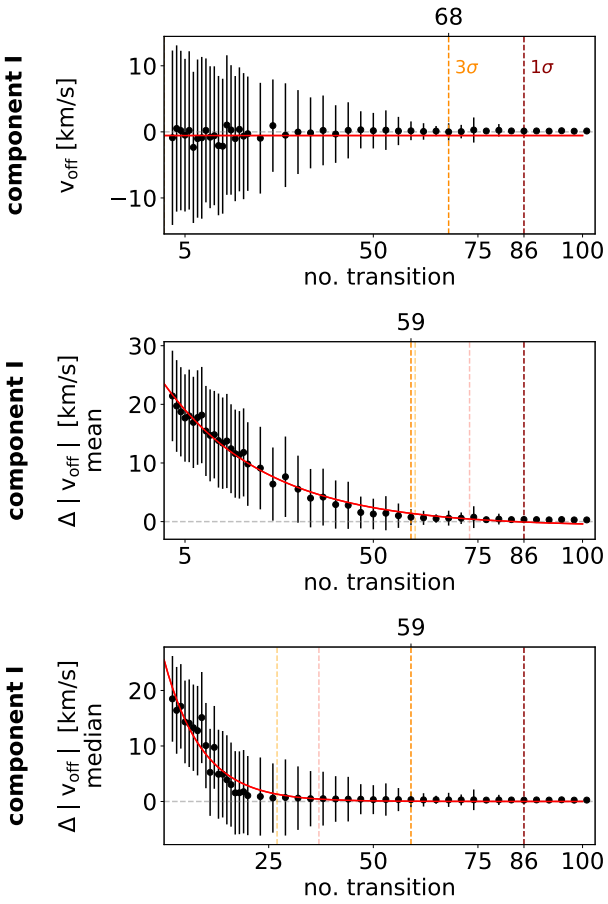

Figure 5.7: Same like Fig. 5.6 for component I.

Table 5.1: Obtained velocities for different number of stacked transitions.

no. trans[a]	lines per GHz[(d)]	component I			component II		
		v_{off}[b] [km s^{-1}] 0 km s^{-1}	$\mid \Delta v_{off} \mid$[c] [km s^{-1}] mean	$\mid \Delta v_{off} \mid$[c] [km s^{-1}] median	v_{off}[b] [km s^{-1}] -5 km s^{-1}	$\mid \Delta v_{off} \mid$[c] [km s^{-1}] mean	$\mid \Delta v_{off} \mid$[c] [km s^{-1}] median
2	50	-0.89±13.2	21.43±7.72	18.49±7.72	-0.12±12.34	19.4±8.01	16.4±8.01
3	50	0.51±12.58	19.72±7.82	16.42±7.82	-2.6±11.31	15.93±8.13	8.65±8.13
4	50	0.2±12.07	18.73±7.61	17.14±7.61	-3.64±10.64	13.54±8.24	5.07±8.24
5	50	-0.5±11.55	17.67±7.45	14.33±7.45	-0.51±9.4	11.45±7.79	1.73±7.79
6	50	0.22±11.98	18.03±7.89	14.1±7.89	-2.84±8.37	9.16±7.09	0.47±7.09
7	50	-2.35±11.44	16.92±7.78	13.29±7.78	-4.07±7.14	6.95±6.25	0.27±6.25
8	50	-1.02±11.97	17.75±8.06	12.76±8.06	-1.53±7.43	6.93±6.8	0.23±6.8
9	50	-0.9±12.24	18.17±8.21	15.12±8.21	-2.43±6.88	5.8±6.37	0.2±6.37
10	50	0.22±10.89	15.46±7.68	10.07±7.68	-4.34±5.24	3.54±4.94	0.14±4.94
11	50	-0.81±10.74	14.71±7.84	5.25±7.84	-4.05±4.82	3.23±4.57	0.13±4.57
12	50	-0.59±10.51	14.83±7.46	9.75±7.46	-4.06±4.38	2.68±4.2	0.12±4.2
13	50	-2.08±10.54	13.82±8.02	4.91±8.02	-5.15±3.57	2.07±3.42	0.11±3.42
14	50	-2.17±10.21	13.38±7.79	4.91±7.79	-4.06±2.83	1.32±2.79	0.1±2.79
15	50	1.03±10.56	13.75±8.03	3.9±8.03	-4.62±1.98	0.83±1.95	0.09±1.95
16	50	0.29±9.8	12.43±7.58	3.04±7.58	-4.54±2.01	0.89±1.97	0.1±1.97
17	50	-1.02±9.47	11.59±7.51	1.56±7.51	-4.75±1.84	0.62±1.82	0.09±1.82
18	50	0.38±9.38	11.39±7.46	1.57±7.46	-4.48±1.87	0.57±1.86	0.08±1.86
19	50	-0.65±9.54	11.8±7.51	1.76±7.51	-5.04±1.83	0.61±1.8	0.08±1.8
20	50	-0.28±8.65	9.82±7.13	1.06±7.13	-4.5±1.8	0.57±1.79	0.08±1.79
23	50	-0.96±8.38	9.13±7.04	0.89±7.04	-4.86±0.6	0.25±0.59	0.07±0.59
26	50	0.94±6.99	6.4±6.24	0.62±6.24	-4.93±0.23	0.13±0.23	0.07±0.23
29	50	-0.5±7.85	7.65±6.86	0.72±6.86	-4.96±0.15	0.09±0.14	0.06±0.14
32	50	-0.03±6.35	5.53±5.72	0.6±5.72	-4.96±0.15	0.09±0.14	0.06±0.14
35	50	-0.15±5.37	4.0±4.98	0.5±4.98	-4.97±0.05	0.07±0.04	0.05±0.04
38	50	0.22±5.28	4.18±4.85	0.51±4.85	-4.96±0.1	0.08±0.09	0.06±0.09
41	50	-0.33±4.36	2.91±4.11	0.45±4.11	-4.98±0.04	0.07±0.03	0.05±0.03
44	50	0.23±4.25	2.78±4.02	0.42±4.02	-4.96±0.13	0.07±0.13	0.05±0.13
47	50	0.31±2.81	1.56±2.71	0.41±2.71	-4.97±0.04	0.06±0.03	0.05±0.03
50	50	0.18±2.69	1.3±2.61	0.33±2.61	-4.98±0.03	0.06±0.02	0.05±0.02
53	50	0.26±2.99	1.43±2.91	0.35±2.91	-4.98±0.03	0.05±0.02	0.04±0.02
56	50	0.13±2.14	1.01±2.08	0.34±2.08	-4.98±0.03	0.05±0.02	0.04±0.02
59	50	0.16±1.42	0.75±1.37	0.32±1.37	-4.97±0.03	0.05±0.02	0.05±0.02
62	50	0.06±1.25	0.64±1.2	0.29±1.2	-4.98±0.03	0.05±0.02	0.04±0.02
65	50	0.12±0.77	0.52±0.72	0.31±0.72	-4.98±0.03	0.05±0.02	0.04±0.02
68	50	-0.0±1.3	0.59±1.27	0.29±1.27	-4.98±0.03	0.05±0.02	0.04±0.02
71	50	0.04±1.02	0.58±0.98	0.28±0.98	-4.98±0.03	0.04±0.02	0.04±0.02
74	50	0.28±1.9	0.76±1.86	0.3±1.86	-4.98±0.03	0.05±0.02	0.04±0.02
77	50	0.13±0.21	0.33±0.15	0.25±0.15	-4.98±0.03	0.04±0.02	0.04±0.02
80	50	0.24±0.94	0.43±0.92	0.28±0.92	-4.98±0.03	0.04±0.02	0.04±0.02
83	50	0.14±0.21	0.34±0.14	0.27±0.14	-4.98±0.03	0.04±0.02	0.04±0.02
86	50	0.12±0.39	0.36±0.35	0.24±0.35	-4.98±0.02	0.04±0.01	0.04±0.01
89	50	0.14±0.21	0.34±0.14	0.28±0.14	-4.98±0.02	0.04±0.02	0.04±0.02
92	50	0.11±0.19	0.3±0.13	0.25±0.13	-4.98±0.02	0.04±0.01	0.04±0.01
95	50	0.17±0.21	0.35±0.14	0.3±0.14	-4.98±0.02	0.04±0.02	0.04±0.02
98	50	0.1±0.19	0.29±0.13	0.24±0.13	-4.97±0.02	0.04±0.02	0.04±0.02
101	50	0.13±0.17	0.29±0.1	0.25±0.1	-4.98±0.02	0.04±0.01	0.03±0.01

Notes. [(a)] Number of stacked transitions. [(b)] v_{off} indicates the velocity obtained using the line stacking method. The listed values are the mean of all 150 iterations per bunch of stacked transitions. The error is the related standard deviation of all iterations per bunch of stacked transitions. [(c)] $\mid \Delta v_{off} \mid$ indicates the absolute difference between the expected value (0 km s^{-1}/−5 km s^{-1}) and the line stacking method obtained value. The listed values are the mean/median of all 150 iterations per bunch of stacked transitions. [(d)] To the synthetic spectrum of each transitions Gaussians with random amplitudes and linewidths at random velocities have been added (see sec. xx). 50 lines per GHz, corresponds to 20 Gaussians in the selected velocity range.

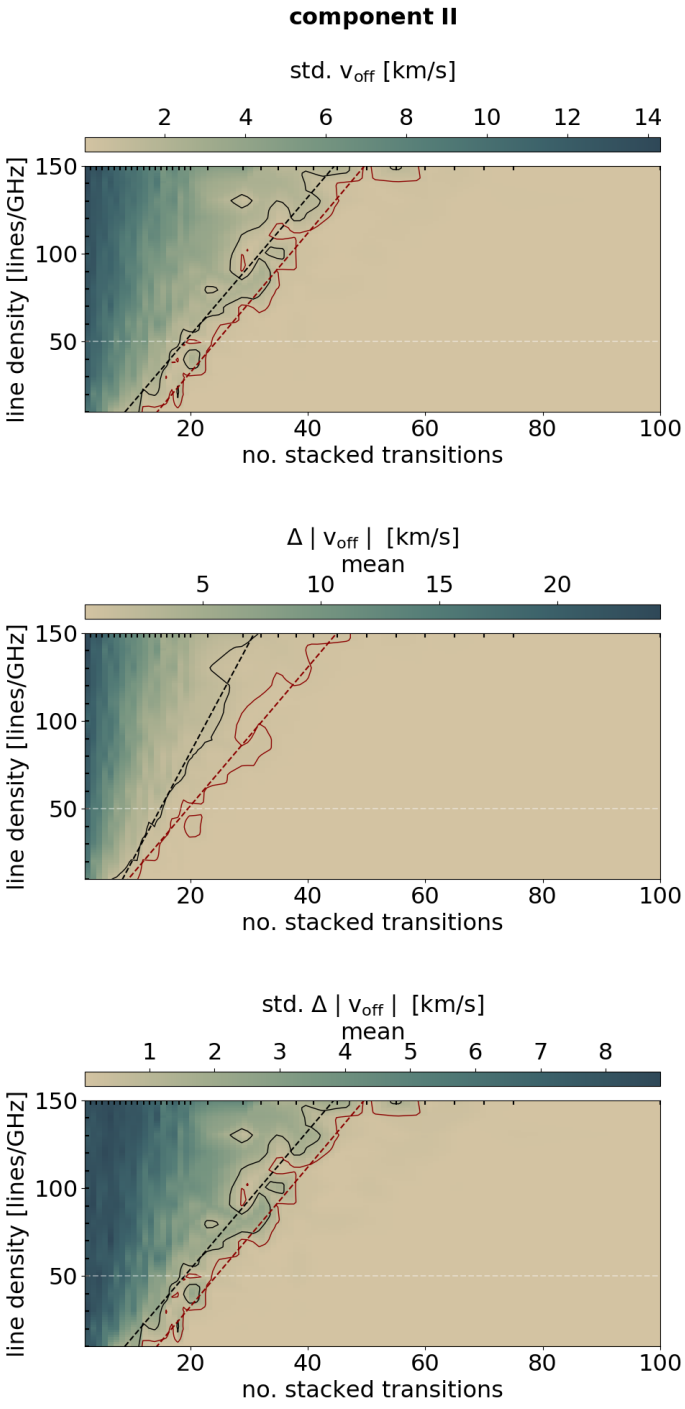

Figure 5.8: Impact of the line density on the accuracy of the line stacking method for different number of stacked transitions. The red and black contours indicate where the deviation of the line stacking method is less than 1 or 3 σ. The red and black dashed lines fit the contours and show a linear trend. The white dashed line indicates the cut-out shown in Fig. 5.6.

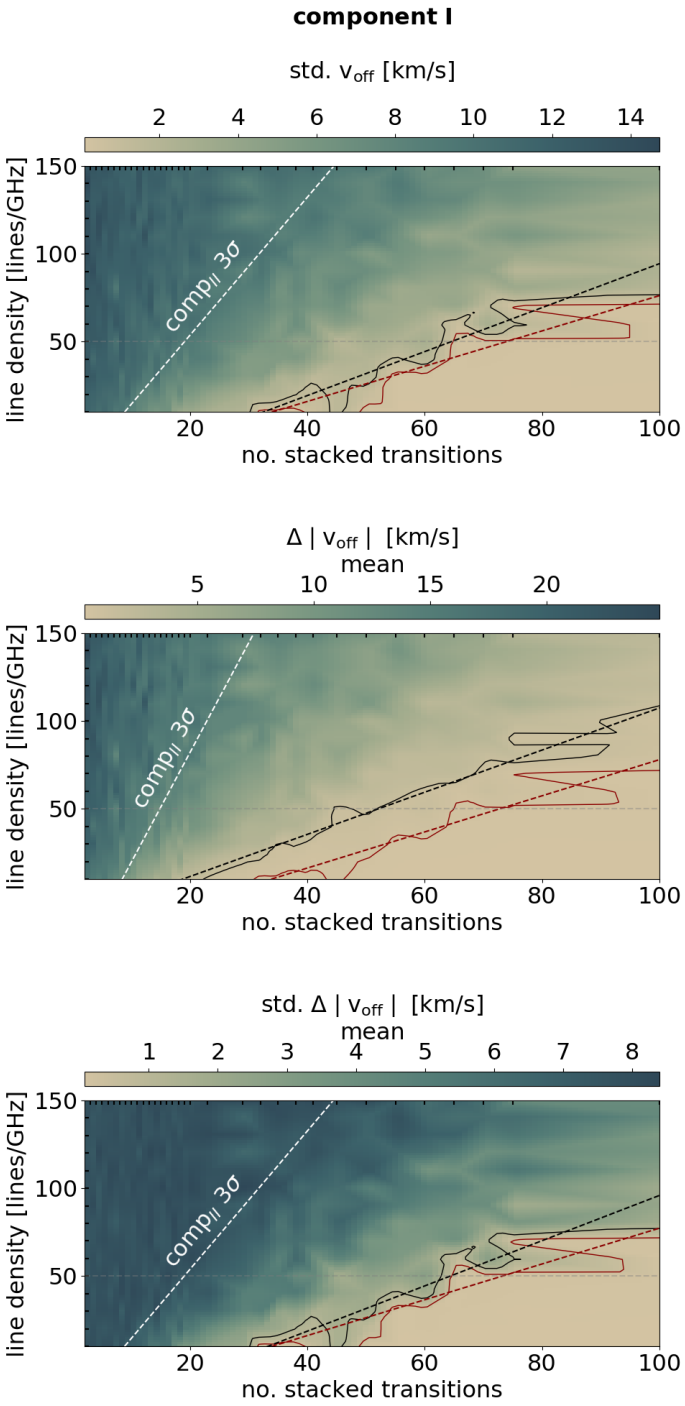

Figure 5.9: Same like Fig. 5.8 for component I.

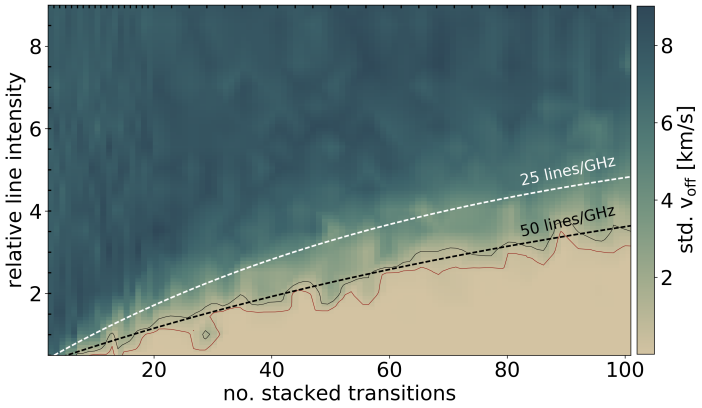

Figure 5.10: Impact of the (relative) line intensities on the accuracy of the line stacking method for different number of stacked transitions. The line density of blending lines is fixed to 50 lines per GHz. The accuracy is visualized with the red and black contours, which indicated the 1 and 3 σ deviation to the input parameter. The relation seems to be exponential with a growing rate of R_{50}=0.008. The white dashed line indicates the exponential behavior (R_{25}=0.014) for a line density of 25 lines per GHz.

Line stacking with synthetic data

- ▷ by providing a good statistic, the line stacking method can unveil the velocity information (i.e. linewidth, velocity and number of velocity components) with an high accuracy.
- ▷ noise and transitions of other molecular species result in an artificial continuum, which is not affecting the velocity information.
- ▷ stacking transitions restricted to certain energy ranges can be used for studying the excitation conditions of the individual components.

6

Cluster Luminosity and stellar mass relation

Star-forming regions contain many complex structures. Among them, dense cores seem to be omnipresent (see section 1.2). These objects are an accumulation of molecular gas of relatively high density of typically 10^4 to 10^6 cm^{-3}, sizes below 0.1 pc and are suggested to be the very early stage of star formation. In Sgr B2, these objects are found to have much higher densities of 10^7 to 10^9 cm^{-3}, one to two orders of magnitude larger than the stellar densities of super star clusters (Sánchez-Monge et al. 2017). Their high temperatures of 50–200 K (determined by fitting the spectral lines of different molecular species with the software XCLASS, Möller et al. in prep) suggest the presence of already formed stars inside the cores. The stellar content can be derived from the luminosity of the dense cores, considering them as spherical black bodies, and will be performed later in the analysis part of my thesis (see section 7.2.3). The relation between stellar luminosity and stellar mass, can be found in literature. In this chapter, I will derive the relation between stellar cluster luminosity and stellar cluster mass using simple numerical simulations. First, I will demonstrated that the assumption of a black body is reasonable.

6.1 Black body assumption

I derive the stellar luminosity of the dense cores assuming that they are spherical black bodies and use the Stefan-Boltzmann law. However, these dense cores are not perfect black bodies, and the dust opacity has to be taken into account. The modified black body or Planck function is

$$B_{\nu,\mathrm{mod}}(T) = B_\nu(T)\,(1 - e^{-\tau_\nu}), \tag{6.1}$$

where $B_\nu(T)$ is the Planck function at temperature T and τ_ν is the optical depth at frequency ν, which is proportional to the density along the line of sight, given by

$$\tau_\nu = \int_{\text{line of sight}} \kappa_\nu \, \rho \, dl, \tag{6.2}$$

with κ_ν being the absorption coefficient (opacity) per unit of total mass density and ρ the density.

I modeled the modified Planck function for different hydrogen column densities $N_{\mathrm{H_2}}$ between 10^{20}–10^{25} cm^{-2} and a temperature of 100 K (see Fig. 6.1, left panel). The absorption coefficients are taken from Ossenkopf & Henning (1994) according to dust grains with thin ice mantles and gas densities of 10^6 cm^{-3}. Their trend with frequency is shown in Fig. 6.2. I assumed a dust-to-gas mass ratio of 100.

The total brightness of an emitting source can be obtained by integrating over the (modified) Planck function

$$B(T) = \int_0^\infty B_\nu(T) \, d\nu. \tag{6.3}$$

For a perfect black body, this results in

$$B(T) = \sigma T^4, \quad \sigma = 5.67 \times 10^{-5} \text{erg cm}^{-2}\text{s}^{-1}\text{K}^{-4}, \tag{6.4}$$

where σ is the Stefan-Boltzmann constant. The luminosity calculated from a numerical integration over the Planck function and multiplied by a spherical surface of a given radius matches the luminosity calculated with the Stefan-Boltzmann law. For a more detailed derivation see Wilson et al. (2009).

In Fig. 6.1 (right panel), the ratio between the brightness of a perfect black body and a modified black body as function of the column density is presented. For hydrogen densities above roughly $5{\times}10^{23}$ cm^{-2}, the total brightness obtained for a modified Planck function is in agreement with the brightness of a perfect black body, with deviations of less than 6%. At the observed high column densities, the emission is optically thick already at lower frequencies compared to lower column densities (see deviations from the Planck function in Fig. 6.1), and the variation in the total integrated brightness is not significant.

In Sgr B2(N) column densities about 10^{24} cm^{-2} are obtained (Sánchez-Monge et al. 2017). Hence, the assumption of a black body is reasonable and the luminosity, which is proportional to the total brightness, can be calculated with the Stefan-Boltzmann law (see Eq. 7.5) given by

$$L = 4\pi r^2 \sigma T^4. \tag{6.5}$$

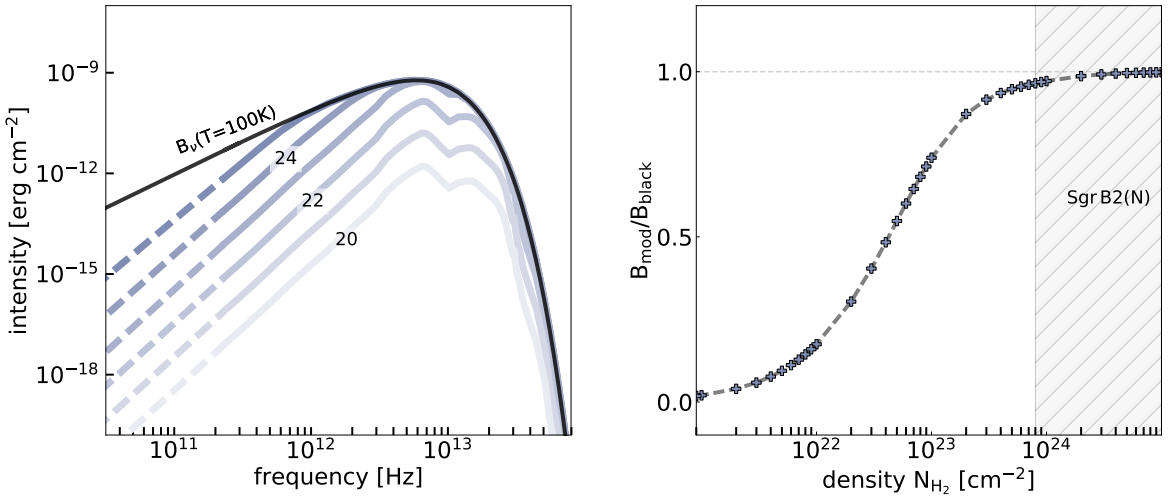

Figure 6.1: *Top panel:* Modified Planck function for different column densities from 10^{20} to 10^{25} cm^{-2} at a temperature of 100 K. The solid gray curves are calculated based on the opacities of Ossenkopf & Henning (1994), while the dashed lines are obtained from the extrapolation of the two lowest frequency values in Ossenkopf & Henning (1994). The Planck function or perfect black body at a temperature of 100 K is shown with a black solid and thick line. *Bottom panel:* Ratio between the total brightness of the modified Planck function and a perfect black body. The grey crosses marked the ratio for specific column densities, while the dashed lines show the trend. The hatched area indicates the range of column densities found in the dense cores of Sgr B2(N).

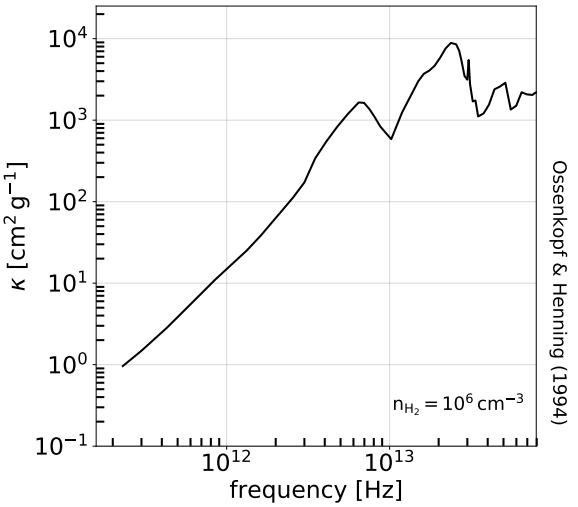

Figure 6.2: Absorption coefficients κ according to dust grains with thin ice mantles and gas densities of 10^6 cm^{-3}.

Black body assumption

▷ assuming that the dense cores in Sgr B2 are emitting as spherical black bodies is reasonable. Thus, the luminosity of the dense cores can be calculated with the Stefan-Boltzmann law.

6.2 Stellar luminosity and mass relation for clusters

We can now calculate the total luminosity of the dense cores, or rather their harbored star clusters, but how do the individual stars contribute to the total luminosity? How many members are in the wrapped star clusters and what do we know about their masses? For a better understanding, I simulated 10^5 clusters with a random amount of stars. The number of stars varies between 1 and $5{\times}10^4$, with masses from 0.1 and 100 $M_\odot$. The mass distribution of stars for each cluster follows the Initial Mass Function (IMF, Kroupa 2001, shown in Fig. 6.4), which is an empirical relation describing the initial distribution of masses for a population of stars

$$\xi(M) \propto \begin{cases} M^{-1.3} & \text{if } 0.1\ M_\odot < M \leq 0.5\ M_\odot \\ M^{-2.3} & \text{if } M > 0.5\ M_\odot \end{cases} \tag{6.6}$$

where ξ is the number of stars of a certain mass. The stellar luminosity (L) for a given star of mass M follows the relation (see Eker et al. 2018)

$$\log\left(\frac{L}{L_\odot}\right) = a \cdot \log\left(\frac{M}{M_\odot}\right) - b, \tag{6.7}$$

where the constants a and b vary depending on the stellar mass. For the range of masses considered, I use (based on Eker et al. 2018):

$$\begin{aligned}
0.1 < \mathrm{M}/M_\odot \leq 0.45 \quad & \log L = 2.028 \times \log \mathrm{M} - 0.976 \\
0.45 < \mathrm{M}/M_\odot \leq 0.72 \quad & \log L = 4.572 \times \log \mathrm{M} - 0.102 \\
0.72 < \mathrm{M}/M_\odot \leq 1.05 \quad & \log L = 5.743 \times \log \mathrm{M} - 0.007 \\
1.05 < \mathrm{M}/M_\odot \leq 2.40 \quad & \log L = 4.329 \times \log \mathrm{M} + 0.010 \\
2.40 < \mathrm{M}/M_\odot \leq 7.0 \quad & \log L = 3.967 \times \log \mathrm{M} + 0.093 \\
7.0 \ < \mathrm{M}/M_\odot \leq 100 \quad & \log L = 2.865 \times \log \mathrm{M} + 1.105
\end{aligned}$$

The masses and luminosities of all individual stars are summed up, and result in a total mass and luminosity per cluster. The result for all simulated clusters is shown in the left panel of Fig. 6.3, presenting the relation between the stellar mass of the cluster and the cluster luminosity. In the right panel of Fig. 6.3, I show the relation between $(M/L)_{\mathrm{cluster}}$ and the cluster luminosity. I fit a linear function to the relation and find

$$\log\left(\frac{M/M_\odot}{L/L_\odot}\right) = -0.6 \times \log\left(\frac{L}{L_\odot}\right) + 0.5, \tag{6.8}$$

where M is the mass of the cluster and L the cluster luminosity.

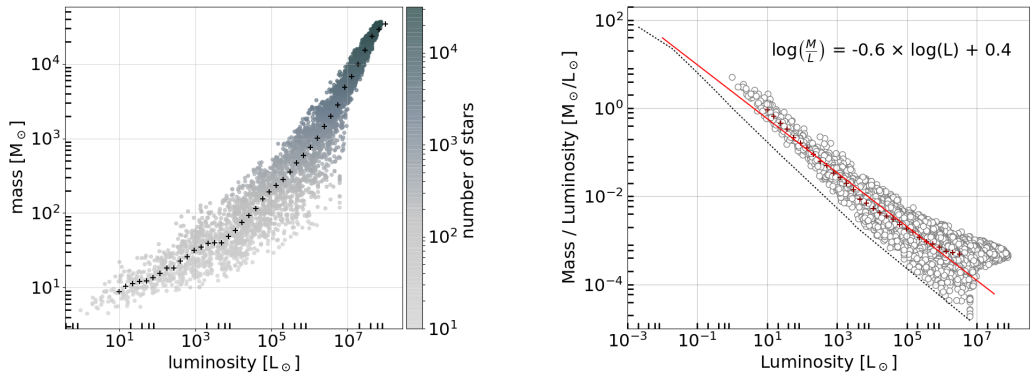

Figure 6.3: *Left panel:* Relation between the stellar mass and stellar luminosity for clusters with different numbers of stars. The black crosses are the mean values of M_{cluster} for different luminosities . *Right panel:* Relation between the ratio $(M/L)_{\mathrm{cluster}}$ with the cluster luminosity. The white circles show all simulated clusters and the red crosses are the mean values of $(M/L)_{\mathrm{cluster}}$ for different luminosities. The red line indicates a linear fit through the mean values. The black dashed line shows the relation between luminosity and mass for a single star (see Eq. 6.7)

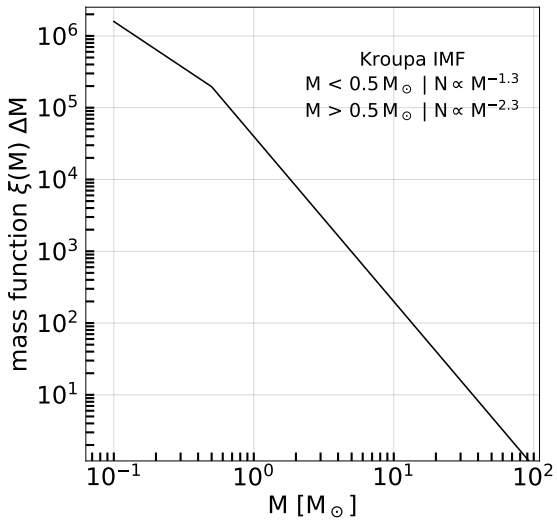

Figure 6.4: Kroupa-Function, which is an empirical relation describing the initial distribution of masses for a population of stars.

Stellar luminosity and mass relation for clusters

▷ The relation between $(M/L)_{\text{cluster}}$ and the cluster luminosity is given by $\log\left(\frac{M/M_\odot}{L/L_\odot}\right) = -0.6 \times \log\left(\frac{L}{L_\odot}\right) + 0.5$.

Part III

Analysis and Results

7 Sagittarius B2 North

One main site of star formation within the Sagittarius B2 molecular cloud complex is Sgr B2 North (N), which has a mass of (1.5-4.1)$\times 10^4$ $M_\odot$ and densities of 10^5–10^7 $M_\odot$ pc^{-3} (Sánchez-Monge et al. 2017; Schmiedeke et al. 2016; Hüttemeister et al. 1995). Our new data sets, described in section 3.2, revealed all sorts of new structures and give new insights in the mechanism of mass accumulation in such an extreme environment. In the following section, I will present these new structures and sketch a picture of the physical properties, in particular related to the events of accretion and feedback. Later, I will interpret the results in the frame of the formation of super-stellar cluster.

7.1 Physical structures in SgrB2(N)

Sgr B2(N) shows the whole beauty of nature and ALMA observations with high-angular resolution of 0.″4 (∼3300 au) and 0.05″ (∼400 au) provide us a stunning images: Slender and arched filaments (section 7.1), an extended bubble of molecular gas (section 7.1), myriad of dust cores (section 7.2.3), glowing H II regions (section 7.3.4) and powerful outflows (section 7.3.1), all these structures form the landscape and interact with each other. In several figures within the following sections all this can be admired, starting this series of pictures with a three-color composite images of our highest angular resolution of 0.″05 (see Fig. 7.1) and 0.″4 (see Fig. 7.2) images. Due to the different uv-coverage (section 3.2), both images show structures on different scales. Since the broad line-survey with thousands of molecular lines (data-set I) enables to study kinematic structures and since data-set II has been taken later, I focus on the data with a resolution of 0.″4. However, the data with 0.″05 have been used to confirm my findings, or even to extend the analysis.

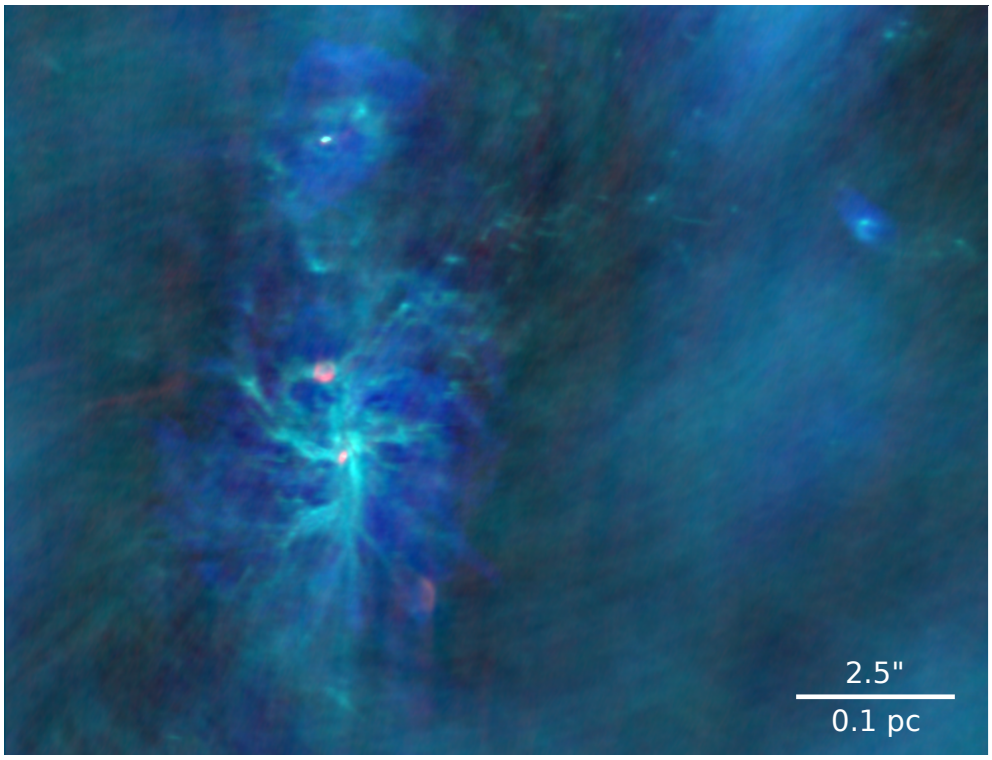

Figure 7.1: Three-color composite image of Sgr B2(N). The green image shows the continuum emission at 220 GHz, the blue image corresponds to the molecular species C_2H_5CN, and the red image to emission at 44 GHz, which traces (hot) ionized gas. The center, which is dominated by the continuum and C_2H_5CN emission, appears petrol. The images of the molecular species C_2H_5CN has been constructed from stacking transitions (see more details in chapter 5) and correspond to peak intensity maps. The continuum emission trace a filamentary structure and many compact sources, while the emission of C_2H_5CN appears more diffuse.

In previous studies (data-set I, Sánchez-Monge et al. 2017) several dust cores have been detected. Many of the compact cores show an extremely rich chemistry, with more than 100 lines per GHz. Among them, S-bearing species like H_2CS and OCS, N-bearing species like CH_3CN and C_2H_5CN, and O-bearing species like CH_3OH, CH_3OCHO and CH_3OCH_3. I used the most isolated lines within the line-survey (data-set I) of these molecular species and produced peak intensity maps. These maps reveal two main types of structures which are illustrated in Fig. 7.2. The dust continuum emission at 242 GHz (see Sánchez-Monge et al. 2017) and species like CH_3OCH_3 (dimethyl ether), CH_3OCHO (methyl formate), CH_3OH, $^{13}CH_3OH$ (methanol) and H_2CS (thioformaldehyde) show extended filamentary structures (green and red colors in Fig. 7.2), whereas other molecules like C_2H_5CN (ethylcyanid) or OCS (carbonylsulfid) trace instead a spherical/bubble-like shape (blue color in Fig. 7.2). The existence of two different morphologies in different molecular species hints at opacity effects, excitation conditions or chemical variations as

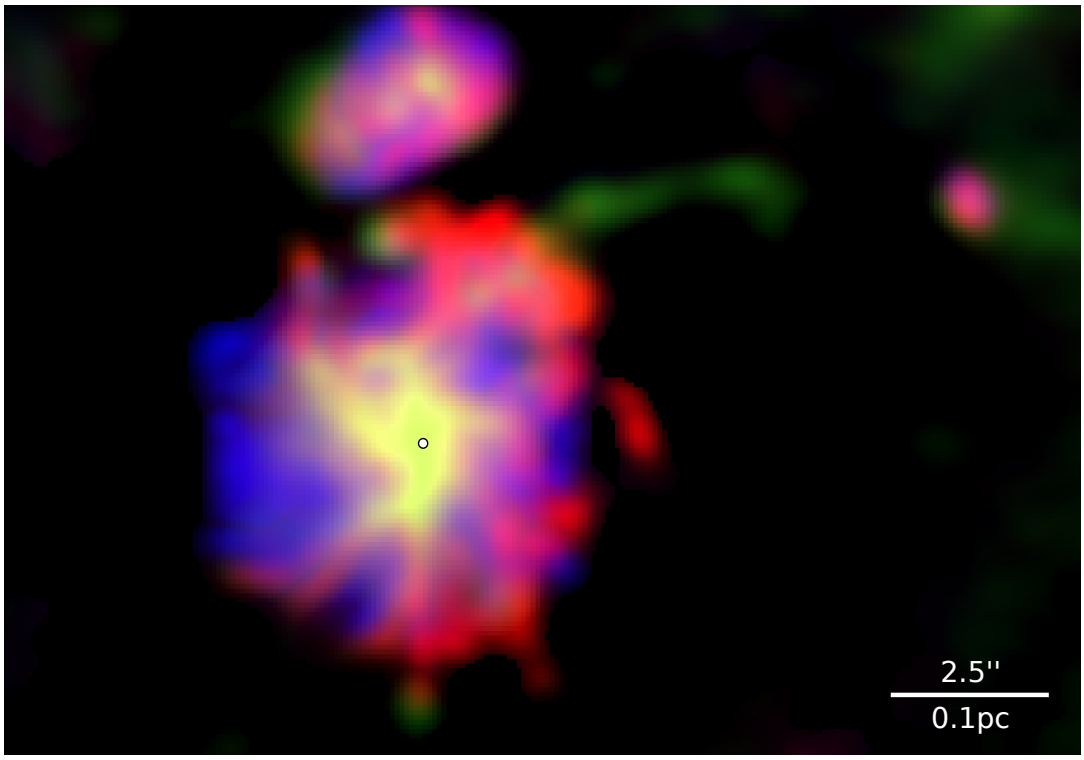

Figure 7.2: Three-color composite image of Sgr B2(N). The green image shows the continuum emission at 242 GHz, the red image corresponds to the molecular species CH_3OCHO, and the blue image to C_2H_5CN. The center, which is dominated by the continuum and CH3OCHO emission, appears yellow. The images of the molecular species have been constructed from stacked cubes (see more details in chapter 5) and correspond to peak intensity maps. The continuum emission and species like CH_3OCHO trace a filamentary structure, while species like C_2H_5CN show a spherical/bubble-like shape. The white circle indicates the position of the central core with coordinates α(J2000)=$17^h47^m19^s.87$, δ(J2000)=$-28°22'18''.43$.

possible origins. Opacity effects are most likely discarded because I detect a large number of species including rare isotopologues (i.e. less affected by opacity effects) tracing both structures. In total I identified eight filaments (see Fig. 7.3, data-set I), which are converging to the central massive hub ($\sim$2000 $M_\odot$, assuming a temperature of 250 K). These filaments are visible in emission of different species. While arms F01, F03, F04, F05, F06, F07, and F08 emit in the molecules CH_3OCH_3, CH_3OCHO, CH_3OH and $^{13}CH_3OH$, arm F02 is only visible in H_2CS. Arm F08 is the most extended and seems to connect the central hub with regions located $\sim$ 0.5 pc to the west. However, the outer (western) part is mainly visible in continuum and not in molecular lines which prevents an analysis of its velocity structure (see Section 7.4). This arm leads to a chalice-shaped area (cf. bright red emission in Fig. 7.2) when approaching the central hub, and contains the dense cores A04, A05, A07 (from Sánchez-Monge et al. 2017), and the H II region H02 (De Pree et al. 2014).

On the contrary, filament F07 appears the shortest, probably due to strong projection effects. Some filaments (F01, F05, F06, F08) harbor embedded cores, while others appear more homogeneous and without clear hints of fragmentation along them, suggesting the existence of different physical conditions (Schwörer et al. in prep). The northern satellite core (containing dense cores A02, A03, A06, and being one of the main targets in the search of complex molecular species, e.g. Belloche et al. 2013) seems to be connected by arms F01 and F02 to the main hub (see more details in Section 7.4). However, arm F01 seems broken, maybe caused by feedback of the neighbor H II region H01. The area to the south-west, in between filaments F05 and F07 looks disordered, and the possibility of another underneath filament can not be excluded (see gray dashed lines in Fig. 7.3, see also Fig. 7.2).

In addition to the detected dust cores, the spherical shape of molecular gas, and the converging filaments, several papers (Schmiedeke et al. 2016, Ginsburg et al. 2018, Gaume et al. 1995) report the presence of H II and ultra-compact H II regions in Sgr B2(N), an evidence for ongoing high-mass star formation. Their spatial extension can be seen in Fig. 7.3. Within the inner 0.2 pc only ultra-compact H II regions has been detected, which hints that relatively little time has passed since high-mass stars started to form. Thus, Sgr B2(N) seems to be in an early stage of high-mass star formation. At least one of these H II regions show emission of the radio recombination line H30α at 231.9 GHz, which will be further investigated in section 7.3.4.

Physical Structures in Sgr B2(N)

- ▷ A filamentary network is visible in Sgr B2(N) in the emission maps of the molecular species CH_3OCHO, CH_3OCH_3 , CH_3OH and H_2CS. In total, eight filaments are found converging to a central hub.
- ▷ Other molecules like C_2H_5CN (ethylcyanid) or OCS (carbonylsulfid) trace instead a spherical/bubble-like shape.
- ▷ Observations in a spatial resolution of $0.05''$ revealed a hierarchical network of filaments (i.e., main filaments, sub-filaments).

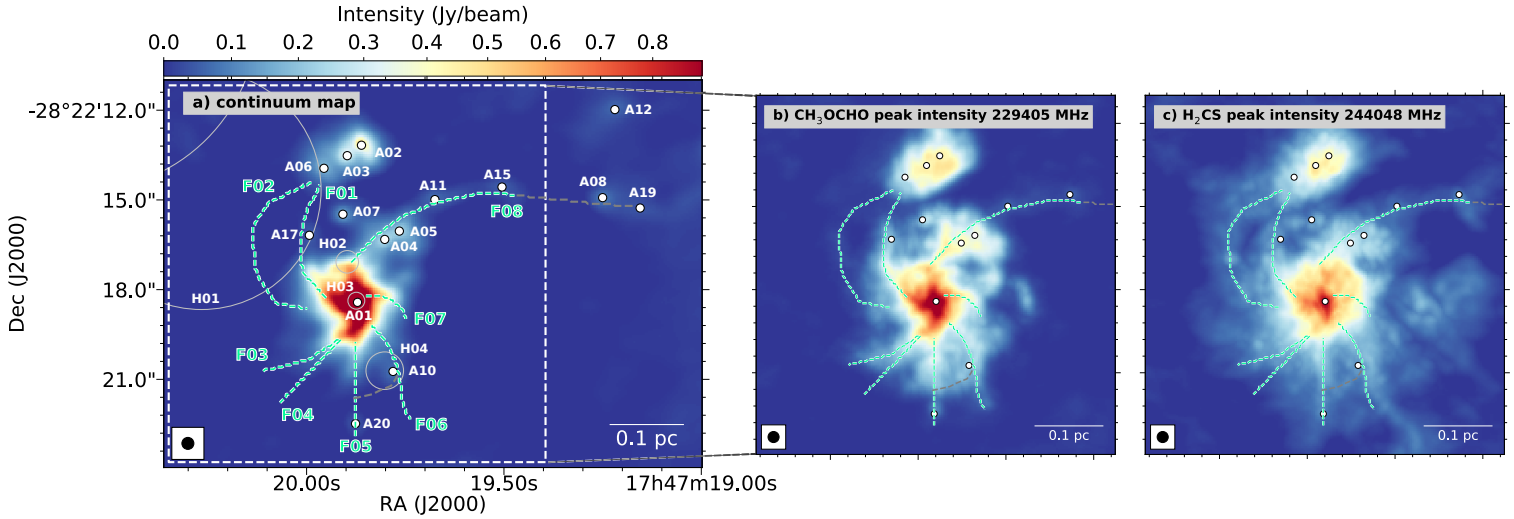

Figure 7.3: *a)* Map of the ALMA 242 GHz continuum emission of Sgr B2(N). The white dots indicate the position of the continuum sources reported in Sánchez-Monge et al. (2017). The green dashed lines trace the path of the filaments identified in the molecular line data (see Section 7.1), while gray dashed lines trace tentative elongated structures not clearly confirmed in the molecular emission maps. The light-gray circles indicate H II regions (see De Pree et al. 2014, Schmiedeke et al. 2016). *b)* Peak intensity map of the bright, isolated transition of CH_3OCHO at 229.404 GHz. *c)* Peak intensity map of the bright H_2CS transition at 244.048 GHz. In all panels, the synthesized beam of $0\farcs4$ is shown in the bottom-left corner, and a spatial scale bar is shown in the bottom-right corner.

7.2 Accretion process

The spatial structure of the converging filaments, together with the presence of the massive central region, suggest that they may be associated with accretion processes, transporting material from the outer regions to the central dense hub. Thus, the velocity structure, as well as the accretion rates along the filaments will be further investigated, presented in the following sections.

7.2.1 Filament Kinematics

The analysis of the velocity structure of each filament has been done using the stacked cubes (see chapter 5), excluding arm F02 which is only visible in H_2CS. This molecule has, in the frequency range of our line ion survey, only four transitions, thus the statistical method of line-stacking offers no significant advantages. The peak velocity map of the stacked transitions of CH_3OCHO (see Fig. 7.4) reveals already a clear velocity gradient from red to blue-shifted velocities between the northern satellite core and the main hub. Overall, I see a smooth velocity structure, except at the interface between the northern and main cores, where several velocity components are present.

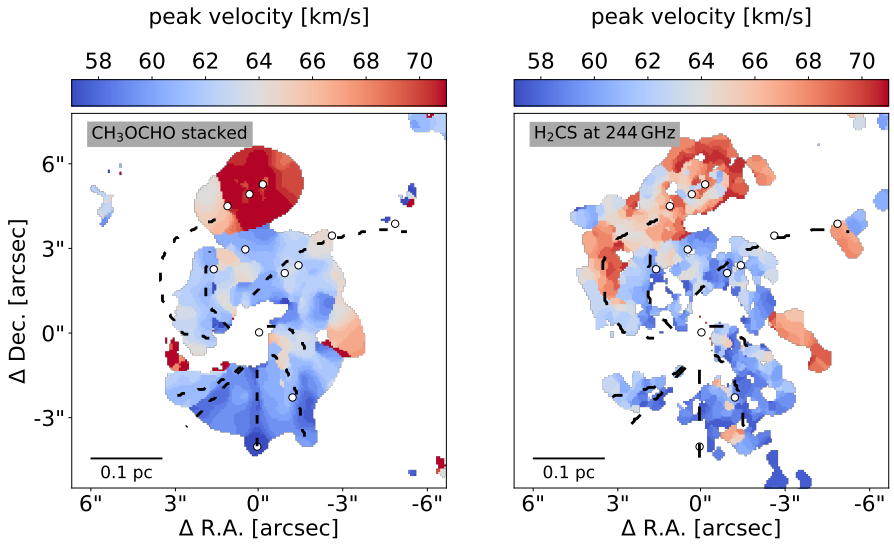

Figure 7.4: Peak velocity map of H_2CS (bottom-panel) and CH_3OCHO (top-panel, using 143 stacked lines, see chapter 5). The emission below 10 σ and the center are masked out.The filaments and position of dense cores are marked with black dashed lines and white dots, respectively.

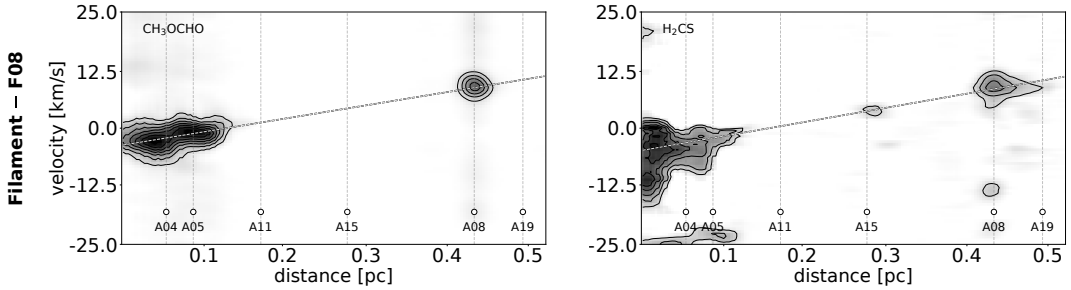

Figure 7.5: Position velocity cut along filament F08 in CH_3OCHO and H_2CS. The emission to the left corresponds to the filament close to the central hub. The emission at about 0.25 pc and 0.4 pc corresponds to the cores A15 and A08, A19. The white dashed line corresponds to a velocity gradient of ∼16 km s^{-1} pc^{-1}, consistent with the mean velocity gradient of F08 (see Table 7.2).

A more detailed study of the velocity structure is obtained by producing position-velocity (pv) cuts along the filaments and by fitting Gaussians to the spectra. In Appendix B, I show the pv-cuts for different molecular species. Most of the filaments are well described by a single velocity component, with the exception of filament F06, for which I consider two velocity components. The Gaussian fits of each spectrum along the filament allow us to derive the velocity and linewidth of each species, and better explore possible variations with distance along the filaments (see Appendix B). For all the filaments, I see velocity gradients in all four species, and I fit them with a linear function. In Table 7.1, I list the velocity gradients of seven filaments for three species. The velocity structure of each filament is consistent between different molecular species, suggesting that these species trace gas with similar kinematic properties. I determine an average velocity gradient of roughly 20 km s^{-1} pc^{-1}. Arm F07 reaches the highest values of 52–70 km s^{-1} pc^{-1}, which together with its short length, suggests that F07 is a filament oriented close to the line of sight. While the gradients in filaments F04, F05, and F06 are negative, i.e. going from red to blue-shifted velocities when moving from the main hub outwards, the gradients in filament F03 and F07 are positive. The pv-cut along the most extended filament F08 shows a connection in its velocity structure between the main hub and the far away western dense cores A15 located at a distance of ∼0.27 pc and A08/A09 located at a distance of ∼0.5 pc (see Fig. 7.5).

The kinematic structure of some filaments shows clear variations in the trend of their velocity structure (see e.g. F03, F08, Fig. 7.6 and Fig. 7.7). This is likely due to the filaments not being perfect straight lines, but having some curvature in the 3D space, which may result in different velocity gradients (along the filaments) when seen in projection. I use these variations to define sub-sections (labeled with roman numbers) along these filaments (see Fig 7.6). I divide filament F03 in two sections from 0.02 to 0.055 pc, and 0.07 to 0.12 pc, and filament F08 in three sections from 0.01 to 0.04 pc, 0.055 to 0.07 pc,

and 0.08 to 0.11 pc. Filament F01 has a weak additional velocity component, best visible in CH_3OH (see Fig. B.2), but also in CH_3OCHO, connecting the northern satellite core with the main hub. I divide F01 in three sections from 0 to 0.03 pc, 0.032 to 0.11 pc and 0.115 to 0.018 pc. Moreover, as discussed above (see also Fig. B.2), F06 has two velocity components in the range 0 to 0.04 pc, that I labeled as F06a and F06b. In addition to the velocity gradient derived for each filament as a single entity, I calculate the velocity gradient for every identified segment (see Table 7.1). In Fig. 7.9 (top panel), I present an overview of the velocity gradients of each filament and sub-filament.

The variation of the velocity linewidth along the filament for each species is shown in Fig. B.4, while the mean linewidths, evaluated as the average Gaussian width along the filament, are shown in Fig. 7.9 (middle panel). Typical linewidths range from 3 to 8 km s^{-1}, with a decreasing trend when moving from the central hub outwards. Along filaments F03, F04, F05 and F08, the linewidth of CH_3OCHO and $^{13}CH_3OH$ behave quite similar, while the linewidth of CH_3OH is in most cases twice the linewidth of the other species. This will be further studied in a forthcoming paper (Schwörer et al. in prep). Filament F05 has a local linewidth minimum at $\sim$0.075 pc, coincident with the position of another filament, which is not unambiguously identified in our current data (see Fig. 7.3 and section 7.1).

I overlay the continuum emission map and the peak intensity map of the molecular species CH_3OH, obtained with data-set II, with the path of the filaments identified in data-set I (consistency check). The image can be found in Appendix B in Fig. B.6. The path of the filaments F01, F05, F07, F08 follows well the peak emission seen in these maps. Filament F03, F04 and F06 are only visible close to the central hub, though the emission gets more diffuse by moving outwards. Filament F05 has some neighboring sub-filaments or fibers. The velocity gradients are consistent between both data-sets. The velocity trends of two exemplary filaments in emission of the molecular species CH_3OH are shown in Fig. 7.8. The linewidths at lower resolution are slightly broader. I also have to note that the absolute velocities are by about $\sim$2 km s^{-1} shifted. However, the gradients, which are used to calculate the accretion rates in the following section, concur. The shift in velocity could by caused either by technical issues or physically, e.g. that both data-sets are tracing material at different scales due to spatial filtering effects (see section 3.2). Another notable difference in the new data set is the appearance of an absorption feature along filament F05 and F07. This may indicate accretion onto the filament. The emission along filament F04 is in data-set II to weak for a good comparison. The kinematic profile of all the other filaments can be found in Appendix B in Fig. B.7–B.9.

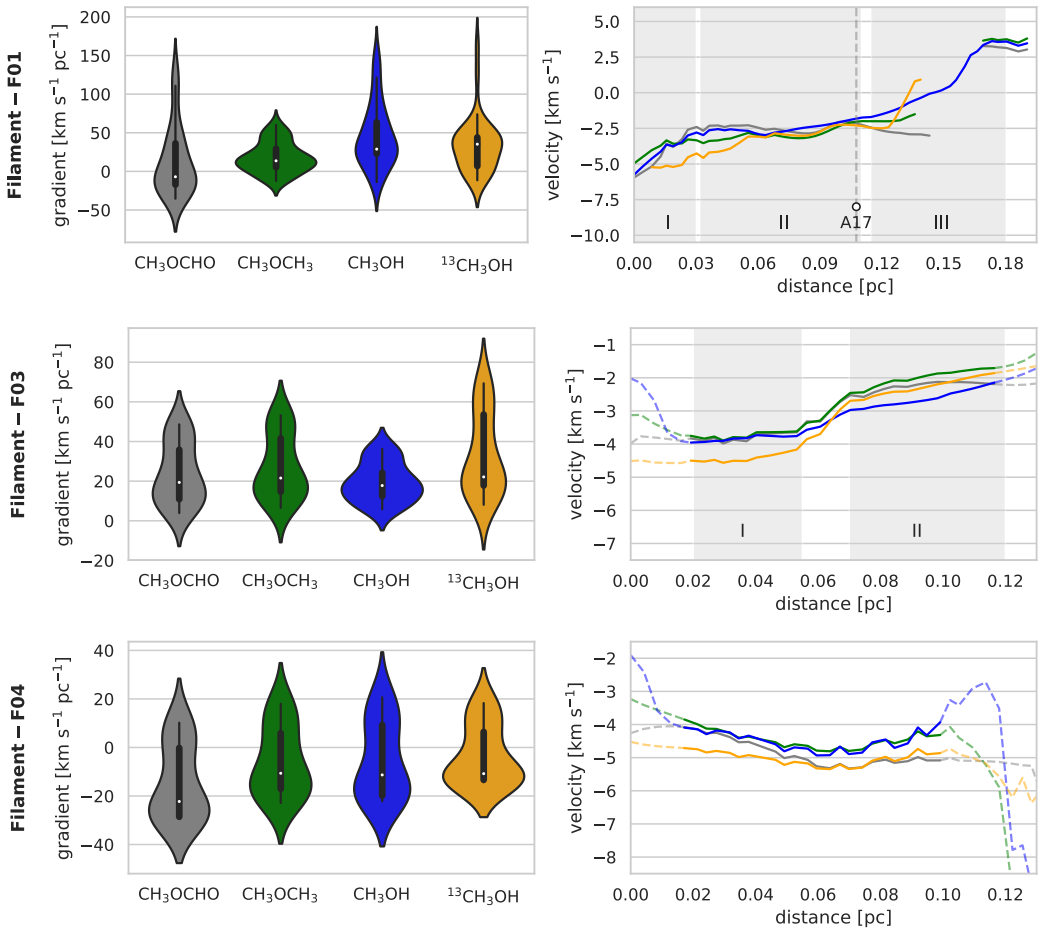

Figure 7.6: *Left panels:* The distribution of velocity gradients along the filaments (determined in sections of 0.014 pc) shown in form of a violin plot. The outer (or violin) shape represents all possible velocity gradients, with broadening indicating how common they are, i.e., the broadest part represents the mode average. The black thin bar indicates all datapoints in the violin interior, while its thicker part corresponds to the quartiles of the distribution, with the white dot indicating the mean value of all velocity gradients along the respective filament. The distribution is shown for the molecules CH_3OCHO, CH_3OCH_3 , CH_3OH and $^{13}CH_3OH$. *Right panel:* Velocity variation along the filaments. The gray areas indicate subsections along the filaments, labeled with roman numbers. The position of the dense cores are indicated by vertical, black dashed lines. Regions where the line emission is below 4σ are plotted with dashed lines.

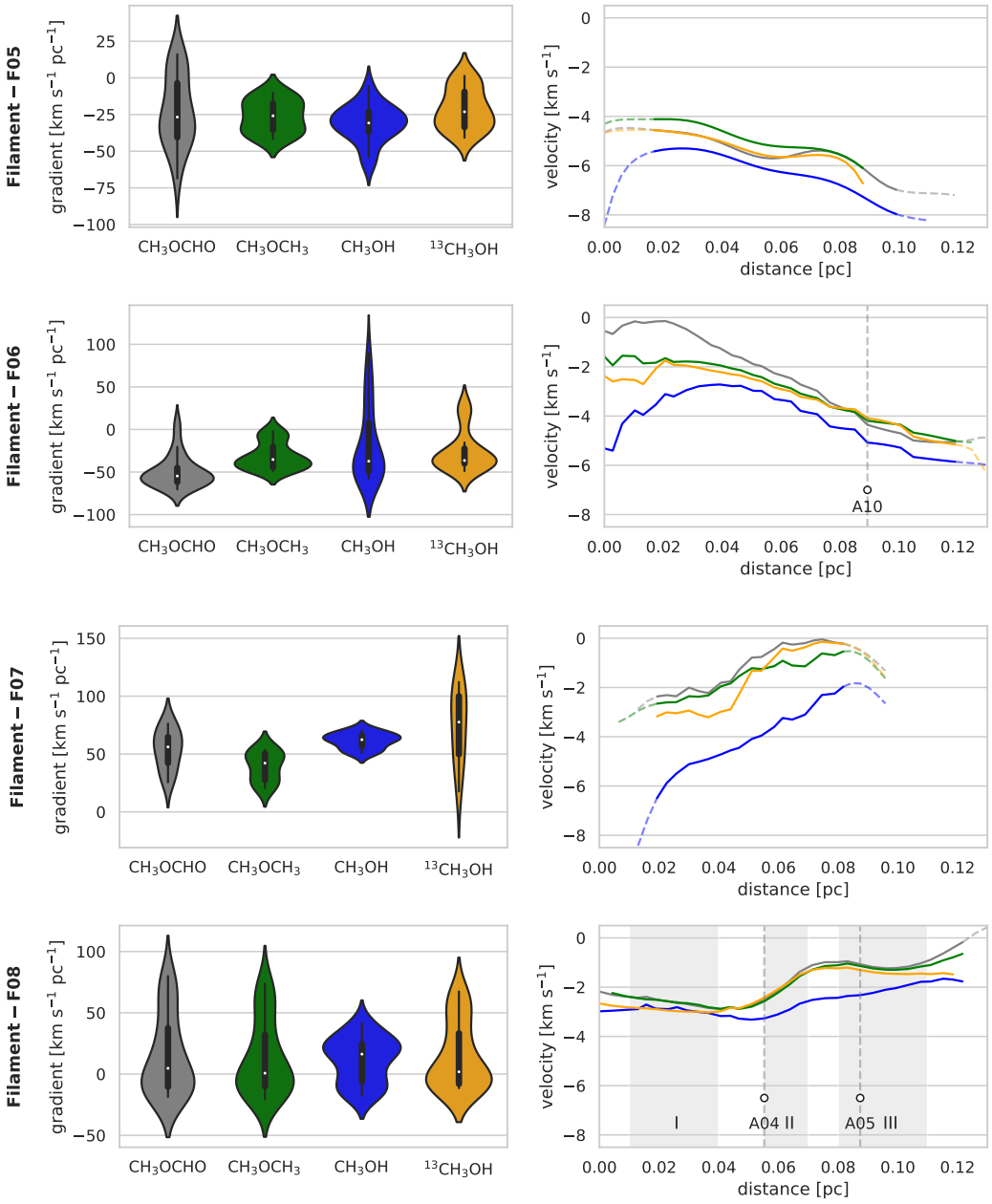

Figure 7.7: Same as Fig. 7.6 for filaments F05, F06, F07 and F08.

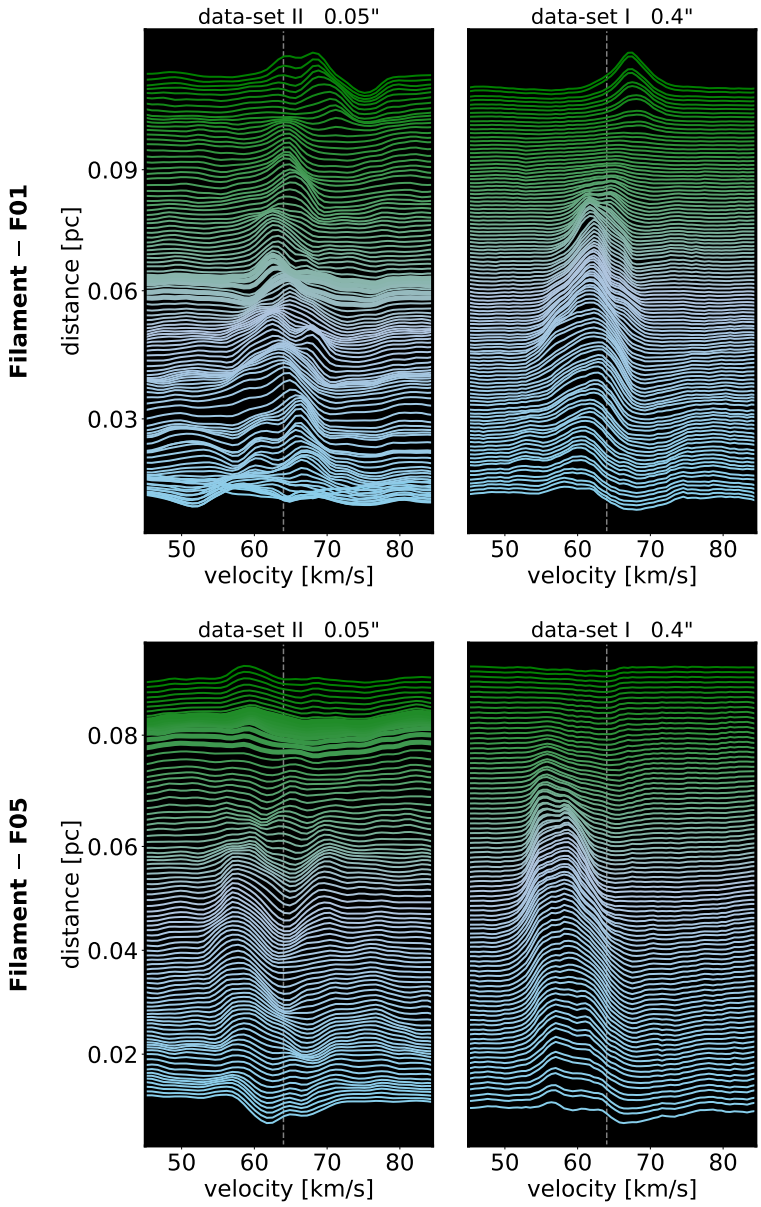

Figure 7.8: Comparison of the velocity trend between both data-sets in the molecular species CH_3OH. The spectra are constructed by stacking lines (see more details in chapter 5). 8 transitions of methanol are included in data-set II and 84 transitions in data-set I, resulting in a better signal-to-noise ratio. The spectra are averaged over a region with the beam size of data-set I. The presented spectra are extracted by moving from the main hub (at 0 pc) outwards along the filaments indicated in Fig. 7.3 and equidistantly plotted on top. The thicker lines at 0.06 pc and 0.08 pc mark the core positions. The dashed vertical line indicates the source velocity at 64 km s^{-1}. The absolute velocities in both resolution differ by 2 km s^{-1}, whereas the velocity trend is consistent.

Table 7.1: Kinematic and physical properties of the filaments in Sgr B2(N)

	velocity gradient (km s^{-1} pc^{-1})				filament parameter[a]			
ID	CH_3OCHO	CH_3OCH_3	CH_3OH	$^{13}CH_3OH$	M ($M_\odot$)	L (pc)	M/L ($M_\odot$ pc^{-1})	$\dot{M}$ ($M_\odot$ yr^{-1})
F01	+31.5±4	+40.0±3	+37.6±2	+34.9±2	1050–490	0.14	7500–3500	0.039 – 0.019
— I	+129.0±10	+60.3±11	+100.3±9	+29.6±11	690–320	0.03	23000–10800	0.057 – 0.027
— II	+1.2±2	+13.5±2	+11.0±2	+26.4±2	380–180	0.08	4800–2300	0.005 – 0.003
— III	+96.4±12	+95.3±7	+88.9±6	+152.2±20	16–7	0.03	540–250	0.002 – 0.001
F03	+20.0±1	+19.9±2	+9.0±3	+28.6±2	620–290	0.13	4800–2200	0.013 – 0.006
— I	+8.4±3	+6.8±2	+6.5±1	+10.4±2	200–95	0.03	6800–3200	0.002 – 0.001
— II	+8.8±2	+16.8±1	+17.7±1	+18.5±1	40–18	0.05	800–380	0.001 – 0.001
F04	−22.1±2	−12.8±2	−12.4±2	−9.7±1	570–270	0.14	4100–1900	0.008 – 0.004
F05	−17.0±2	−20.7±1	−28.0±1	−18.1±1	490–230	0.13	3800–1800	0.010 – 0.005
F06	−54.7±2	−41.0±2	−46.0±2	−39.4±2	410–190	0.16	2500–1200	0.019 – 0.009
— a	−18.1±2	−13.6±1	+67.1±1	−24.3±1	500–240	0.02	25000–12000	0.009 – 0.004
— b	−43.1±2	−103.3±17	−46.4±31	−40.7±7	500–240	0.02	25000–12000	0.023 – 0.011
F07	+52.3±4	+38.9±3	+61.5±2	+70.2±7	970–460	0.10	9700–4600	0.057 – 0.027
F08	+18.0±2	+16.1±2	+11.0±1	+18.2±2	810–380	0.30	2700–1300	0.015 – 0.007
— I	−17.3±2	−14.9±1	−6.1±4	−8.1±1	200–95	0.03	6700–3200	0.003 – 0.002
— II	+94.5±6	+85.2±5	+48.5±7	+77.7±3	210–100	0.01	21000–9900	0.018 – 0.009
— III	+5.8±4	−6.2±3	+23.5±1	−9.9±2	150–70	0.03	5100–2400	0.001 – 0.001

Notes. [(a)] Mass accretion rates have been computed with the median of the velocity gradients of the four species.

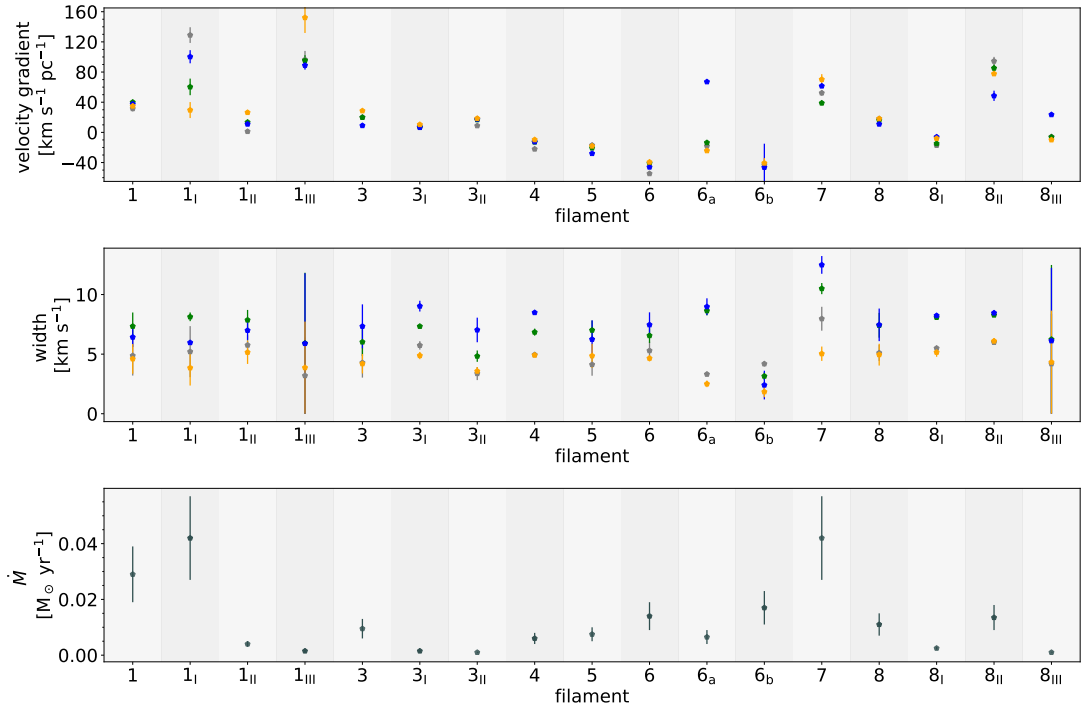

Figure 7.9: Overview picture of the velocity gradients (*top panel*), velocity linewidths (*middle panel*) and mass accretion rates (*bottom panel*) along all filaments and sub-filaments (indicated by roman numbers) in Sgr B2(N), see Sections 7.1 and 7.2.1. Additional velocity components in filament F06 are marked as 6a and 6b. The gray, green, blue and orange symbols correspond to the molecules CH_3OCHO, CH_3OCH_3, CH_3OH and $^{13}CH_3OH$, respectively.

Filament Kinematics

- ▷ The average velocity gradient along the filaments is roughly 20 km s^{-1} pc^{-1}.
- ▷ Typical linewidths range from 3 to 8 km s^{-1}, with a decreasing trend moving outwards.
- ▷ The velocity gradients are consistent in both data-sets.

7.2.2 Mass accretion rates and filament stability

I evaluate the mass accretion rate of each filament using its mass and the derived velocity gradients. The mass of each filament has been estimated from the dust continuum emission at 242 GHz (see Sánchez-Monge et al. (2017)). For optically thin emission, a dust opacity of 0.899 cm^2/g (Ossenkopf & Henning 1994), a dust-to-gas mass ratio of 100, and dust temperatures between 50–100 K, I derive masses of the filaments in the range 200–1000 $M_\odot$ (see Table 7.1). The higher mass values for filaments F01 and F08 are due to the elongation of F01 into the central hub and the presence of the bright chalice-shaped structure surrounding F08. Since filaments F03 and F04 are located close together in the plane of the sky, part of their mass might be double-counted, although the effect should be negligible, since the overlap of the filaments occurs only in about one fourth of their extend.

Following Kirk et al. (2013), I calculate the mass accretion rate implied by our velocity gradients assuming a cylindrical model for our filaments. The mass accretion rate ($\dot{M}$) is derived as

$$\dot{M} = v_{||} \cdot \frac{M_{\rm fil}}{L_{\rm fil}} = \nabla v_{||} \cdot M_{\rm fil}, \tag{7.1}$$

where $M_{\rm fil}$ is the mass of the filament, $L_{\rm fil}$ the length of the filament and $v_{||}$ the velocity parallel to the filament. Considering an inclination α between the filament and the plane of the sky, the parameters that I observe are given by

$$L_{\rm fil,obs} = L_{\rm fil}\cos(\alpha) \quad \text{and} \quad v_{||,\rm obs} = v_{||}\sin(\alpha), \tag{7.2}$$

which modify the mass accretion rate to

$$\dot{M} = \frac{\nabla v_{||,obs} \cdot M_{\rm fil}}{\tan(\alpha)}. \tag{7.3}$$

For the calculation of the mass accretion rates, I assumed a projection angle α of 45°. An angle of 25° roughly doubles our results, while an angle of 65° halves them. For the velocity gradient, I used the median of the values determined for all the species (see Table 7.1). In Fig. 7.9 (bottom panel), I plot the mass accretion rates for all the filaments and sub-filaments. The mass accretion rates along the filaments of Sgr B2(N) are between 0.004–0.04 $M_\odot$ yr^{-1} at the scales of 0.1–0.2 pc (see Table 7.1), thus 10–100 times larger

than rates usually found in star-forming filaments at larger scales of ∼1 pc (e.g.Peretto et al. 2013, Lu et al. 2018, Treviño-Morales et al. in prep). Altogether, considering the average accretion rates listed in Table 7.1, the filaments in Sgr B2(N) accrete at a rate of 0.08–0.16 $M_\odot$ yr^{-1}. This results in a total of 80–160 $M_\odot$ accreted onto the dense hub in about 1000 yr, suggesting a timescale for the formation of the hub of about 60–300 kyr, assuming current accretion rates.

In Section 7.1, I showed that some filaments appear fragmented and harbor embedded cores, which raises the question of how stable the filaments are. The mass-to-length ratio (M/L) is a measure of the stability of the filament (e.g. Ostriker 1964, Fischera & Martin 2012). If this value exceeds a critical limit, the filament will gravitationally collapse under its weight perpendicular to its main axis. Assuming that turbulence can stabilize the filament, the critical value is calculated as

$$\left(\frac{M_{\rm fil}}{L_{\rm fil}}\right)_{\rm crit} \approx \frac{2\sigma^2}{G} \tag{7.4}$$

where σ is the velocity dispersion and G the gravitational constant. Since the measured linewidths are in the range of 3 to 8 km s^{-1} (see Fig. 7.9), I can neglect the thermal contribution, which corresponds to a few 0.1 km s^{-1} for the considered species at 50–100 K. This results in a value of $(M/L)_{\rm crit}$ about (4–30) $\times 10^3$ $M_\odot$ pc^{-1}. According to our measured mass-to-length ratio (see Table 7.1), the filaments in Sgr B2(N) seem to be stable under gravitational collapse. The variation of mass-to-length ratio along the filaments by assuming different temperatures is presented in Fig. B.5 and show a decreasing trend when moving from the central hub outwards.

Mass accretion rates and filament stability

- ▷ Mass accretion rates along the filaments are between 0.004–0.04 M$_\odot$ yr^{-1} and thus 10–100 times larger than rates usually found in star-forming filaments at larger scales.
- ▷ Sgr B2(N) accrete at a rate of 0.08–0.16 $M_\odot$ yr^{-1}.
- ▷ the filaments in Sgr B2(N) seem to be stable under gravitational collapse.

7.2.3 Dense core properties and accretion time scales

The temperatures of the dense cores (from Sánchez-Monge et al. 2017) located within the filaments have been determined by fitting the spectral lines of different molecular species with the software XCLASS (Möller et al. in prep). All values are in the range of 50–200 K and listed in Table 7.2. These high temperatures suggest the presence of already formed stars inside the cores[1]. The stellar content can be derived from the luminosity of the dense cores. Considering them as spherical black bodies, the stellar luminosity is given by the Stefan-Boltzmann equation

$$L = 4\pi r^2 \sigma T^4 \tag{7.5}$$

where r is the radius of the dense cores, σ the Stefan-Boltzmann constant and T the temperature. More details regarding the black body assumption and the validity of the Stefan-Boltzmann are described in Chapter 6.2. The derived luminosities are listed in Table 7.2. The large gas masses of the dense cores (see Sánchez-Monge et al. 2017 and Table 7.2) suggest that not one single star, but a stellar cluster is forming in each core. While the relation between stellar mass and luminosity is known for single stars (e.g., Eker et al. 2018), there is no direct relation for star clusters. Thus, I have simulated 10^5 clusters, and determined the final stellar luminosity and mass (see section 6.2 for details). I find that the cluster luminosity and stellar mass of a cluster follow the relation

$$\log\left(\frac{M/M_\odot}{L/L_\odot}\right) = -0.6 \times \log\left(\frac{L}{L_\odot}\right) + 0.5. \tag{7.6}$$

The stellar mass content, $M_{stellar}$, for each core within the filaments is listed in Table 2. With this, I calculate the ratio between the stellar mass and total mass as

$$M_{\rm stellar,fraction} = \frac{M_{\rm stellar}}{M_{\rm d+g} + M_{\rm stellar}}. \tag{7.7}$$

All values are summarized in Table 7.2 and visualized in Fig. 7.11. For all cores, the stellar mass is within the range 20-90% of the total mass, with a mean (median) value of 50% (44%). I have also investigated the relation of the mass of the different cores with respect to their distance to the central hub. In Fig. 7.12, I plot the core mass (top panel) and the stellar mass ratio (bottom panel) as a function of the distance to the hub. While no striking correlation is found, I see a bi-modal distribution. Cores with masses above 200 $M_\odot$ are located preferentially at distances <0.25 pc, while less massive cores can be found up to distances of about 0.5 pc. Similarly, cores located closer to the central hub

[1]Other mechanisms such as external or shock heating can be excluded. For a typical density of 10^6 cm^{-3} and temperature of 100 K, a heating source would need to see the core as optically thin around the peak (~ 30 μm) of the black body emission. The dust absorption coefficient κ_ν at 30 μm is about 300 cm^{2}g^{-1}, which yields a distance of only 50 au. Therefore, the heating source has to be effectively embedded in order to heat the gas to the measured temperatures. Heating through shocks is also unlikely since for infall rates of ≤ 0.16 $M_\odot$ yr^{-1} and a assumed accretion shock velocity of ~ 8 km s^{-1}, the derived luminosities are only 1700 L$_\odot$, less than the average luminosities derived for our cores

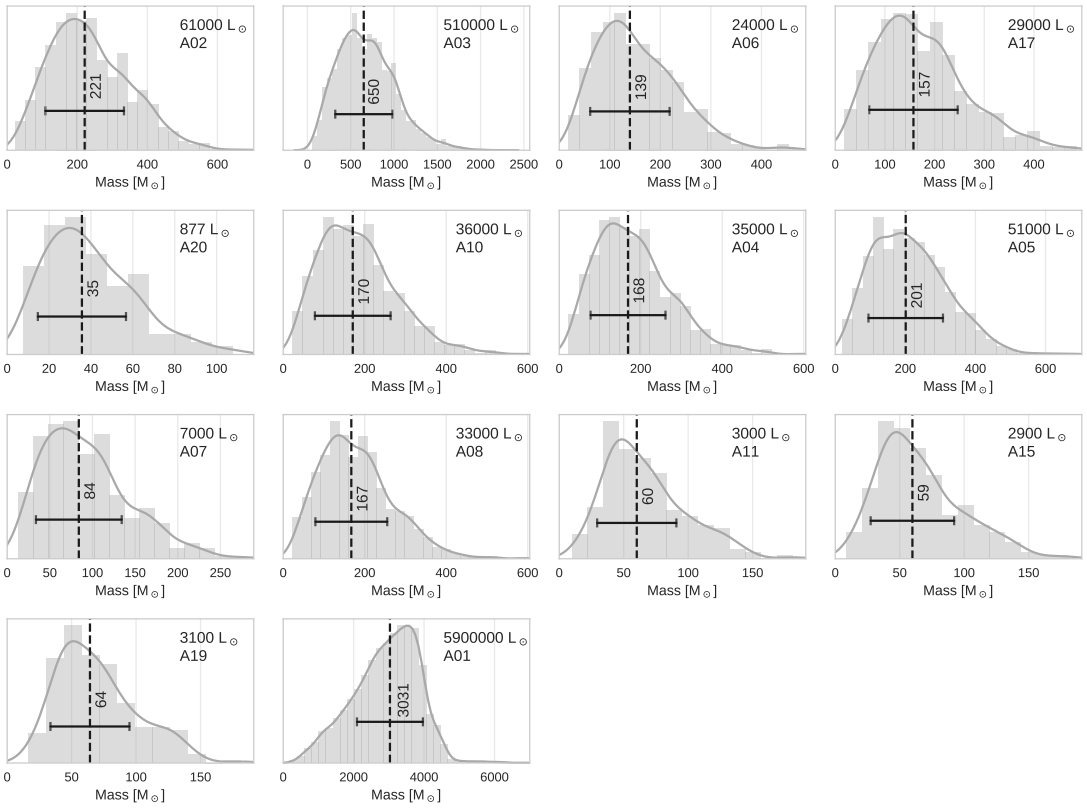

Figure 7.10: Stellar mass distribution of clusters with luminosities according to the observed dense cores in Sgr B2(N). The gray line shows the KDE obtained with the python package `seaborn`. The black dashed vertical lines indicate the mean values of the mass distribution, and the horizontal lines indicate the standard deviation.

can have a higher stellar mass fraction than those located farther away. In section 8 I discuss these results in the context of converging filaments and the formation of a cluster in Sgr B2(N).

One further question of interest is if the dense cores will be accreted onto the central hub before they are disrupted by internal star formation. The time scale for forming stars can be estimated by assuming that the dense cores will collapse on a free-fall time scale

$$t_{\rm ff} = \sqrt{\frac{4\pi^2 r^3}{32 G M_{d+g}}} \tag{7.8}$$

where M is the mass of the dense core and r its radius (values reported in Sánchez-Monge et al. 2017). The $t_{\rm core,ff}$ values are listed in the last column of Table 7.2, and range from 10^3 to 10^4 yr .

I compare the $t_{\rm core,ff}$ with the time required by the dense cores to travel from their position to the central dense hub assuming a free-fall scenario along the filaments, $t_{\rm fil,ff}$

(see Table 7.2). For estimating the gravitational acting central mass (see Equation 7.8), I integrate the flux density over the entire dense hub and assume an averaged temperature of 50–100 K that result, in a mass between (25–10) $\times 10^3$ $M_\odot$. The distance is given by the separation between the core and the central hub. The $t_{\rm fil,ff}$ ranges from 10^3 to 10^4 yr, comparable to the timescale for a core to collapse and form a stellar cluster.

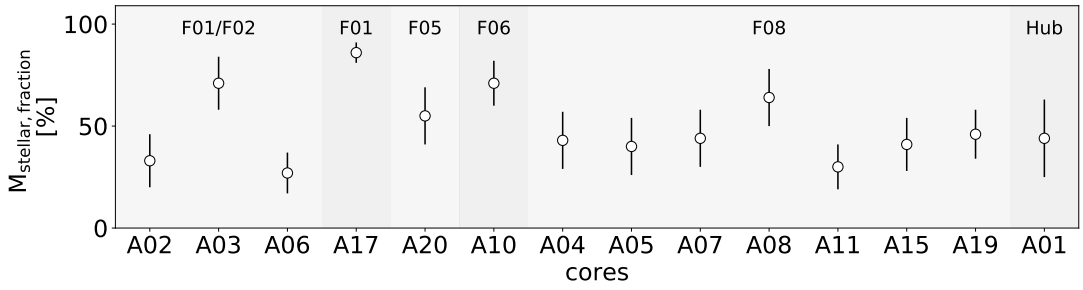

Figure 7.11: Stellar mass fraction (see section 7.2.3) of the dense cores. Cores are grouped by their host filaments.

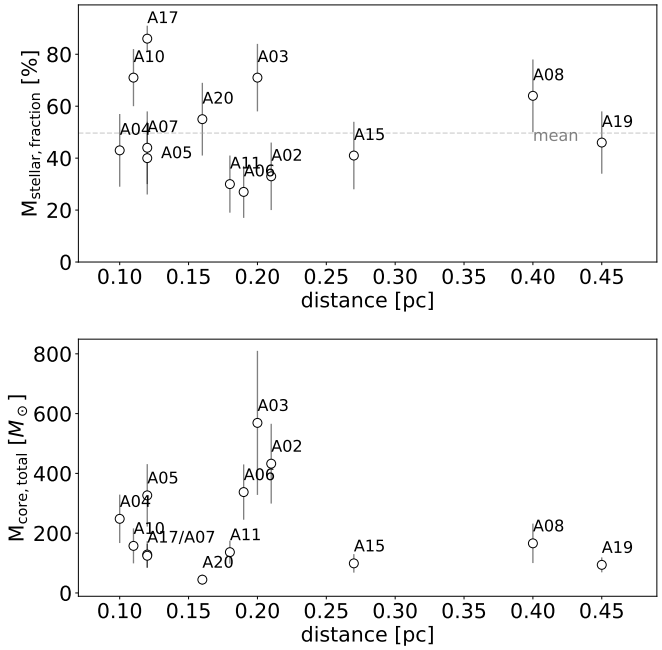

Figure 7.12: *Top panel:* Total mass of the dense cores against their distance to the main hub. *Bottom panel:* Stellar mass fraction of the dense cores against their distance to the main hub. The gray dashed line indicate the mean stellar mass fraction of of 50%.

Table 7.2: Properties and time scales of the dense cores located within filaments in Sgr B2(N)

ID	$\theta_{\rm core}$ [a] ($''$)	$d_{\rm hub}$ [b] (pc)	T [c] (K)	L ($\times 10^3$ $L_\odot$)	$M_{\rm d+g}$ ($M_\odot$)	$M_{\rm stellar}$ [d] ($M_\odot$)	$M_{\rm stellar,ratio}$ (%)	$t_{\rm core,ff}$ (kyr)	$t_{\rm fil,ff}$ (kyr)
F01 A02[e]	0.64	0.21	120	61	300 ± 45	90 – 220	20 – 45	8 ± 0.3	10 – 16
A03[e]	0.70	0.20	195	510	140 ± 20	230 – 650	60 – 85	13 ± 0.6	9 – 15
A06[e]	0.90	0.19	80	24	255 ± 35	60 – 140	20 – 40	14 ± 0.6	9 – 13
A17	0.53	0.12	110	29	15 ± 1	70 – 160	80 – 90	27 ± 1.0	4 – 7
F05 A20	0.44	0.16	50[f]	0.87	20 ± 5	20 – 35	40 – 70	18 ± 0.9	7 – 11
F06 A10	0.64	0.11	105	36	40 ± 5	70 – 170	60 – 80	22 ± 0.9	4 – 6
F08 A04	0.77	0.10	170	360	140 ± 20	70 – 170	30 –60	15 ± 0.6	3 – 5
A05	0.84	0.12	100	51	200 ± 30	80 – 200	25 – 55	15 ± 0.6	4 – 7
A07	0.44	0.12	85	7.3	70 ± 10	35 – 85	30 – 60	9 ± 0.4	4 – 7
A08	0.56	0.40	110	33	55 ± 10	65 – 170	50 – 80	15 ± 0.7	27 – 42
A11	0.84	0.18	50[f]	3.2	100 ± 15	30 – 60	20 – 40	21 ± 0.9	8 – 13
A15	0.80	0.27	50[f]	2.9	60 ± 10	30 – 60	30 – 55	25 ± 1.1	15 – 23
A19	0.83	0.45	50[f]	3.1	50 ± 5	30 – 65	35 – 60	29 ± 1.1	32 – 50
Hub A01	1.45	–	250[f]	5900	1960 ± 280	800 – 3000	25 – 65	11 ± 0.4	–

Notes. [a] Angular radius (θ_{core}) of the cores as listed in Sánchez-Monge et al. (2017) [b] The distance between the core and the hub ($d_{\rm hub}$) is determined from a straight line connecting both, and can, therefore, be a lower limit to the real distance when considering projeciton effects. [c] The temperatures (T) have been determined for different molecular species (Möller et al. in prep) resulting in an error of 10%. After propagation of these errors, we have determined the uncertainties in the gas mass and time scales. [d] The lower value of the stellar mass is obtained from the luminosity listed in the table after decreasing it by a factor of eight. This aims to reproduce: (i) a core radius two times smaller than the measured size, and (ii) a contribution of 50% to the total luminosity coming from accretion and not from stellar radiation. [e] Cores A02, A03, and A06 can also be connected to the central hub via filament F02. [f] Temperatures are not obtained by fitting but assumed.

Dense core properties and accretion time scales

- ▷ The stellar mass of all cores is within the range 20-90% of the total mass, with a mean value of 50%.
- ▷ The free-fall time along the filaments of the cores, is comparable to the timescale for a core to collapse and form a stellar cluster.

7.3 Feedback

Feedback from recently formed stars affects their local environment, determining its structure, composition and chemical evolution (Tielens 2005). There are two main types of feedback: mechanical and radiative. Molecular outflows are an example of the mechanical feedback (two continuous flows of gas), which arise from momentum conservation during the collapse of a rotating core. The outflows observed in Sgr B2(N) are visible in the molecular species SiO, CO, ^{13}CO and C^{18}O (also in SO, SO_2, OCS). The results are presented in section 7.3.1 and 7.3.2.

An example of the radiative feedback, only occurring in the environment of high-mass stars, are H II regions, which are created when the extreme ultraviolet radiation from a high-mass star ionizes and heats the surrounding gas. Recombination of (thermal) electrons with protons leads to neutralization, resulting in observable recombination lines. A recombination line, which is included in both data-sets, is H30α at 231.9 GHz (see section 7.3.4).

7.3.1 Outflow detection and spatial orientation

The molecular species SiO is found to be a good tracer for shocked gas (see e.g., Schilke et al. 1997, Gibb et al. 2004) and is therefore extensively used for tracking outflows. The SiO (5–4) emission towards Sgr B2(N) extends over a velocity range of -60/+60 km s^{-1} around the systemic velocity of 64 km s^{-1}. The integrated emission is shown in Fig. 7.13 and reveals an outflow with an extension of around 0.35 pc. The outflow is oriented in the southeast-northwest direction with its blue shifted emission mainly to the southeast and its red shifted emission to the northwest. The geometrical center of both lobes is close to the position AN01 (indicated with a white circle in Fig. 7.13), likely tracing the location of the powering source(s). The blue-shifted outflow lobe to the east appears more compact and has an elongated, tail like, shape, while the red-shifted, western lobe looks more splashed. The distinct morphology of both outflow wings, raises the question, what may affect the expansion of the outflow in west and east differently. A clear difference is the gigantic H II region in northeast (see Fig. 7.13) and a closer look reveals that this H II region has a common border with the emission of SiO (green contours), which suggest a form of interaction between blue-shifted outflow lobe and H II region.

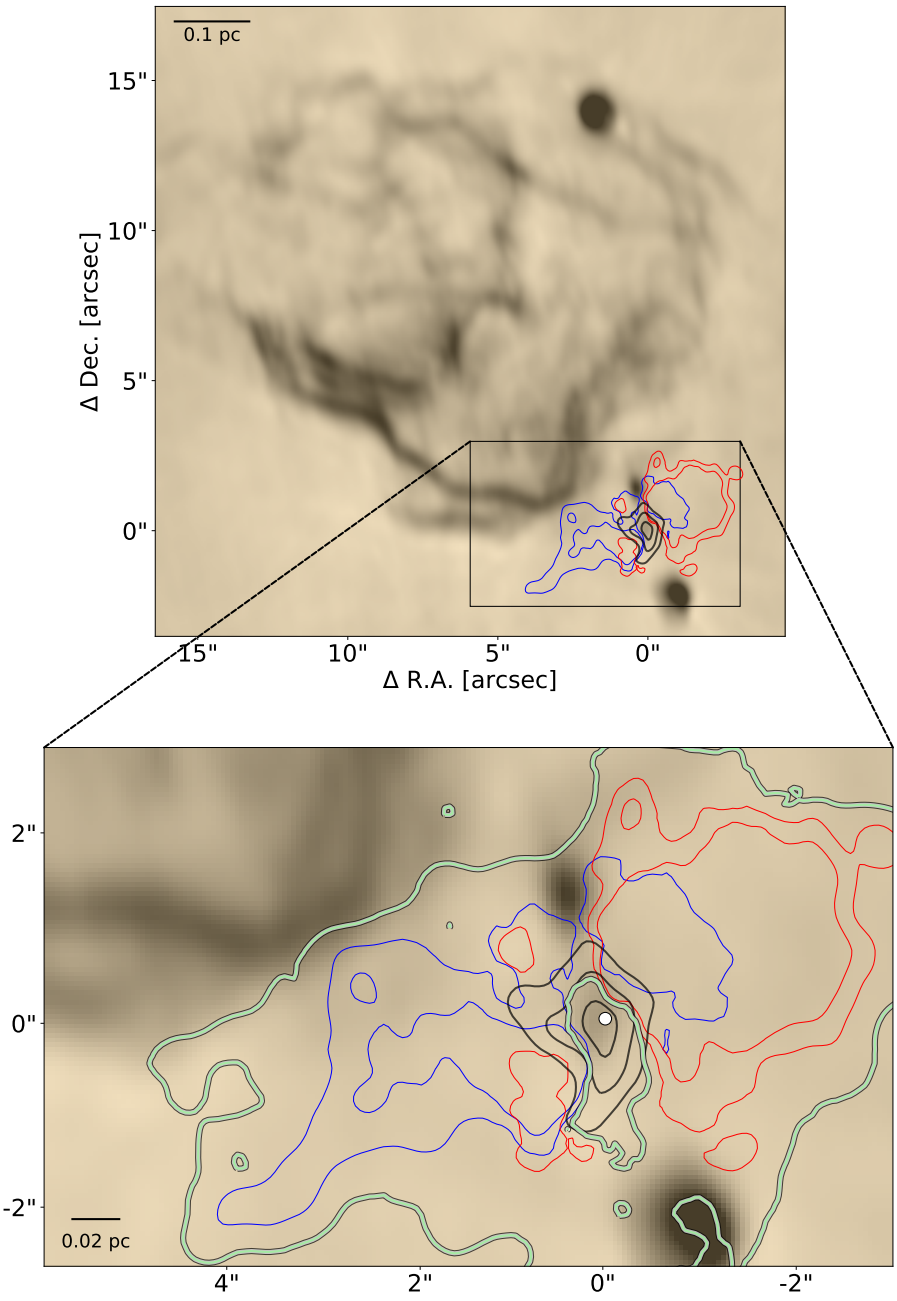

Figure 7.13: *Top panel:* The background image shows the ionized gas (H II regions) observed with VLA in A-Array configuration in its C-band (credit, F. Meng). The blue and red contours are indicating the integrated SiO (5–4) emission between $-16/54$ km s^{-1} and $74/144$ km s^{-1} in levels of 15 and 30% of the peak emission. The black contours show the continuum emission at 242 GHz in levels of 50, 70 and 90%. *Bottom panel:* Same as top panel. The green line shows the total integrated SiO emission (red and blue wing) within 10 σ. The white circle indicates the position of core AN01.

The more compact H II region towards southwest has also a common border with the SiO emission. Moreover, filaments F01 and F02 surround the outflow in east, filament F08 and F06 in west (see Fig. 7.14).

The outflow has also been detected in the molecular species ^{12}CO (2–1) and its isotopologues ^{13}CO and C^{18}O (see Fig. 7.14). The spatial distribution of emission is comparable to that of SiO, but shows some additional features. For instance, parts close to the central hub show deep and wide absorption features (see Fig. B.12, top panel). Moreover following the trail of the blue-shifted wing in the southeast, I found a tiny drop of ^{12}CO emission, not seen in SiO or other molecular species. The emission of ^{13}CO and C^{18}O is more dispersed. The sulfur-bearing species SO, SO_2, CS and OCS are also known to be enhanced in outflows (e.g., Pineau des Forets et al. 1993, Bachiller & Pérez Gutiérrez 1997, Wakelam et al. 2004). Their integrated emission is shown in Fig. 7.15. In particular, the emission of the species CS and SO appear with a shape similar to that of SiO and ^{12}CO. The transition of SiO (6–5) is highly contaminated by the molecular species H_2CO and therefore, it is more difficult to derive the physical properties from the observed line emission.

In the northern (satellite) core, SiO has also been detected, but mainly in absorption at the core position of AN02, AN03 and AN06. Due to the high line density of more than 100 lines per GHz (see Sánchez-Monge et al. 2017), a definitive identification of weak SiO lines is difficult to achieve. Lines with a broad line shape, which are expected to be observed for outflows, have not been detected.

The outflow originating from the dense hub has also been found in SiO (5–4) in our data-set II at higher angular resolution. The spatial structure of the large outflow is also bipolar and has the same southeast-northwest orientation. However, the blue wing of the outflow has now a shape similar to a hammer (see Fig. 7.16, top panel). But the strongest SiO emission in data-set I matches well with this emission. At the eastern edge of the 'hammer' I find a red-shifted velocity component (see bottom-left panel in Fig. 7.16). An additional outflow in the west, not seen in data-set I, has been detected close to core AN08 and AN19 (see Fig. 7.16, bottom panel right), though only the red-shifted lobe is visible. This outflow has also been reported by the authors Bonfand et al. (2017), who find with ALMA observations (band 3, 84–114 GHz, $\sim$1.″6) in emission of SO (2_2–1_1), SO (3_2–2_1) and OCS (8–7) a bipolar morphology with distinct blue and red lobes.

Outflow orientation

- ▷ Two outflows are visible in Sgr B2(N) in the emission maps of the molecular species SiO, CO, SO, SO_2, OCS and CS.
- ▷ The main outflow extends over 0.35 pc, with a clear bi-polar structure.

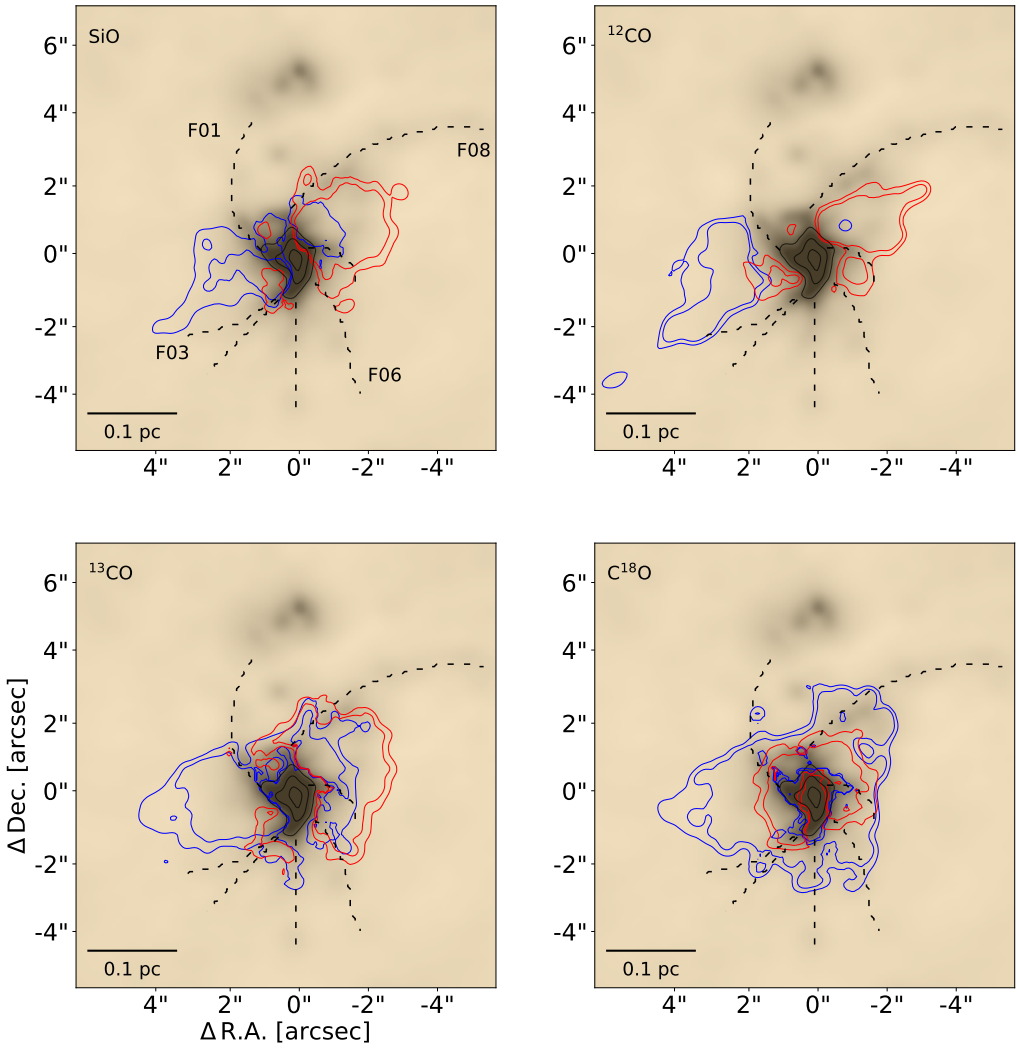

Figure 7.14: The blue and red contours are indicating the integrated emission between $-16/54$ km s^{-1} and $74/144$ km s^{-1} in levels of 15 and 30% of the peak emission for the molecular species SiO, ^{12}CO and its isotopologues ^{13}CO and C^{18}O. The black contours show the continuum emission at 242 GHz in levels of 50, 70 and 90%. The black dashed lines indicate the filaments described in section 7.1. Due to the high line density of more than 100 lines per GHz in the northern satellite core, a definitive identification of weak lines is difficult to achieve. Therefore, the region above a Declination of Δ Dec. $3''$ has been masked out.

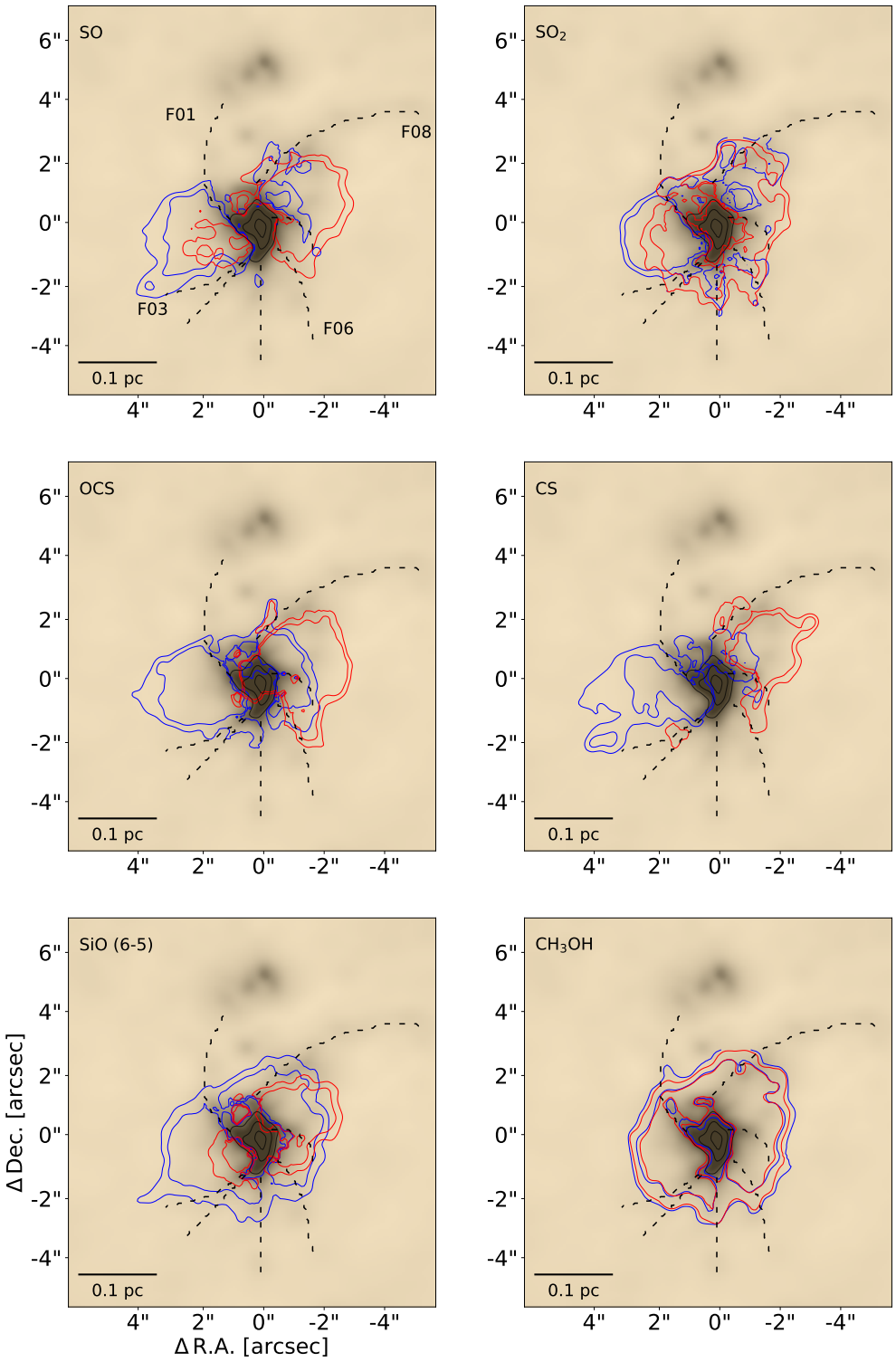

Figure 7.15: Same as Fig. 7.14 for different molecular species.

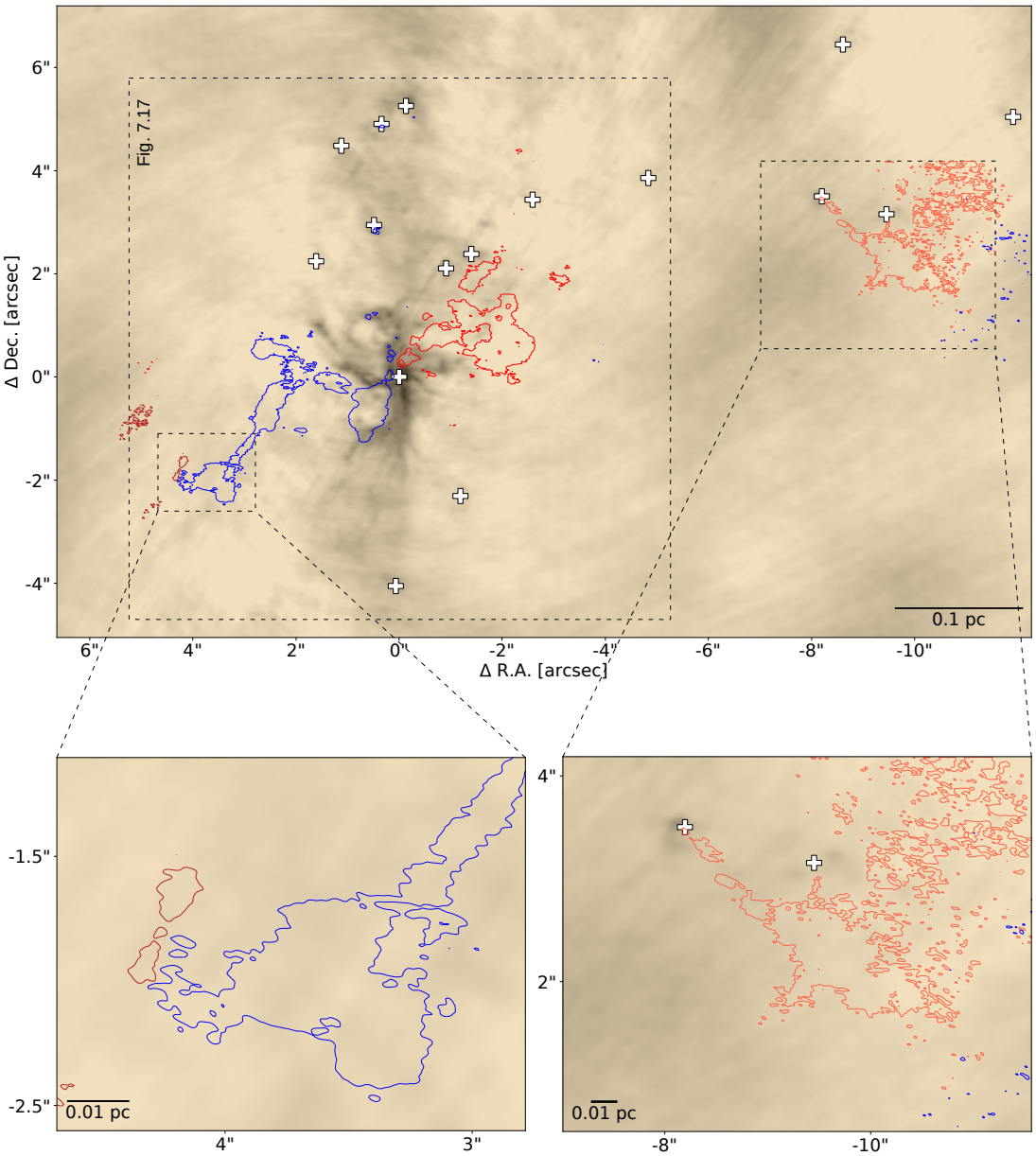

Figure 7.16: Outflows in Sgr B2(N) detected with data-set II in emission of SiO (5–4). The blue and red contours are indicating the integrated SiO (5–4) emission between -16/54 km s^{-1} and 74/144 km s^{-1} within 3 σ. The white crosses mark dense cores reported in Sánchez-Monge et al. 2017. An additional outflow in the west, not seen in data-set I, has been detected close to core AN08 and AN19.

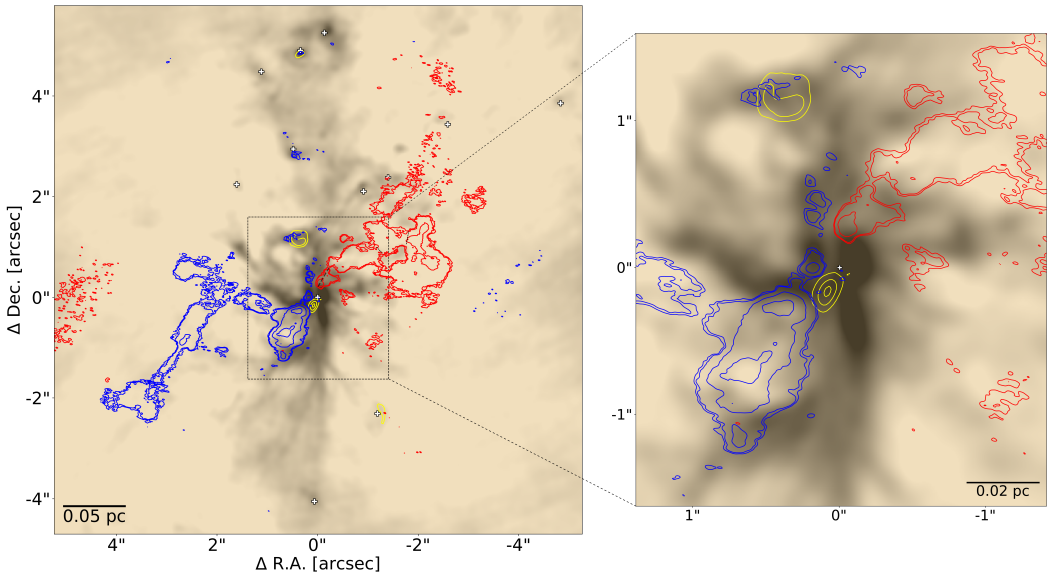

Figure 7.17: Outflow in Sgr B2(N) detected with data-set II in emission of SiO (5–4). Zoom-in of Fig. 7.16. The yellow contours show continuum emission at 44 GHz (credit, A. Ginsburg) indicating ionized gas (H II regions).

7.3.2 Outflow mass and molecular abundance

Most of gas mass, including that of the molecular outflows, is likely to consist of molecular hydrogen, which unfortunately can not be easily observed. Since the column density of H_2 cannot be directly determined and other molecular species (e.g. SiO, CO) have to be used to determine the properties of the outflow, the relative abundance of H_2 to these other molecular species is required. The abundance ratio of SiO to H_2 is not well known and can vary for different physical conditions by several orders of magnitude from 10^{-12} up to 10^{-7} (e.g., Gerner et al. 2014, Codella et al. 2005, Nisini et al. 2007). Fortunately, the abundance of ^{12}CO to H_2 in interstellar clouds is better constrained and is about 10^{-4} (Frerking et al. 1982). Therefore, I can use the emission of ^{12}CO and its well constrain abundance to calculate the column density of H_2 and to derive the outflow mass. However, ^{12}CO is often found to be optically thick within the outflows (Kong et al. 2018, e.g., Goldsmith et al. 1984; Arce & Goodman 2001). If I do not correct for opacity, I would miss a substantial amount of the total mass. Moreover, a huge fraction of the ^{12}CO outflow is only seen in absorption. Having all this in mind, I will use the less abundant ^{13}CO, I will correct its emission for opacity with the isotopologue C^{18}O, derive the column density of H_2 and finally determine the outflow mass.

Another aspect to take into account is the fact that the outflow is further extended than seen in emission of ^{13}CO. Therefore, I compare the column density of SiO with the column

density of H_2 and constrain the SiO abundance in the area, where H2 column density is determined as indicated in the previous steps. With the newly determined abundance of SiO to H_2, I can derive the outflow mass considering the emission throughout the whole extent of the outflow.

Determination of the optical depth of ^{13}CO and conversion to H_2 mass:
By assuming that the frequency of ^{13}CO and C^{18}O are similar and taking into account that $\tau_{\mathrm{C}^{13}\mathrm{O}}$=R $\tau_{\mathrm{C}^{18}\mathrm{O}}$ (where R is the abundance ratio), the optical depth τ can be derived by dividing their modified Planck functions, which results in

$$\frac{T_{\mathrm{C}^{18}\mathrm{O}}}{T_{^{13}\mathrm{CO}}} = \frac{1 - e^{-\frac{\tau_{^{13}\mathrm{CO}}}{R}}}{1 - e^{-\tau_{^{13}\mathrm{CO}}}}, \tag{7.9}$$

where $T_{\mathrm{C}^{18}\mathrm{O}}$ and $T_{^{13}\mathrm{CO}}$ are the brightness temperatures of both isotopologues. The equation is visualized in Fig. 7.18. The isotopologue ratios of ^{12}CO to ^{13}CO and ^{12}CO to C^{18}O are found to be 20 and 250 for Sgr B2(N) (Belloche et al. 2013). Hence, the abundance ratio R of ^{13}CO to C^{18}O is 12. I calculate the optical depth of ^{13}CO per voxel and present the results in Fig. 7.19. For velocities close to the systemic velocity, ^{13}CO has the tendency to get optically thick, while for higher velocities the medium appears optically thin.

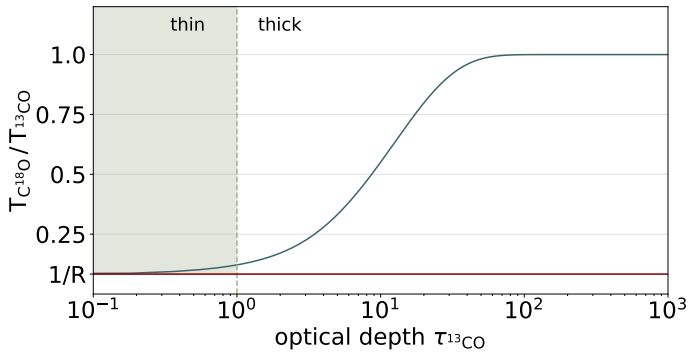

Figure 7.18: Relation between optical depth and intensity ratio of both isotopologues. This ratio can not be below 1/R (see Eq. 7.9), indicated by the red line. For any optical depth below 1 the medium is optically thin, above optically thick.

Knowing the optical depth, it is also possible to derive the excitation temperature T_{ex} numerically, since the brightness temperature T_{mb} is given by the modified Planck function (see section 6.1)

$$T_{\mathrm{mb},^{13}\mathrm{CO}} = B(T_{\mathrm{ex}})\,(1 - e^{-\tau_{^{13}\mathrm{CO}}}), \tag{7.10}$$

where $B(T_{\rm ex})$ is the Planck function. The excitation temperature for different velocities is shown in Fig. 7.20 and ranges from 10 to 50 K. For regions, where the optical depth τ can not be determined (e.g. lines are in absorption or the emission is below the 3 K threshold, 15 σ) the temperature stays unconstrained.

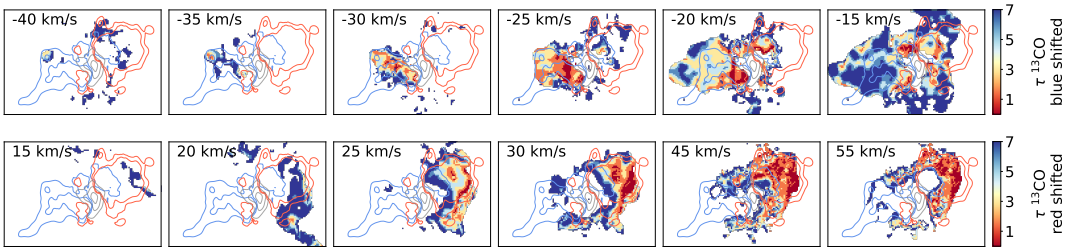

Figure 7.19: Top: Optical depth of ^{13}CO derived by assuming an abundance ratio of 25 for ^{13}CO to C^{18}O. The velocity are given with respect to the systemic velocity of 64 km s^{-1} for Sgr B2(N). The emission below 5 K has been masked out. The red and blue contours indicate the outflow seen in emission of SiO (5–4). The grey contours show the continuum emission.

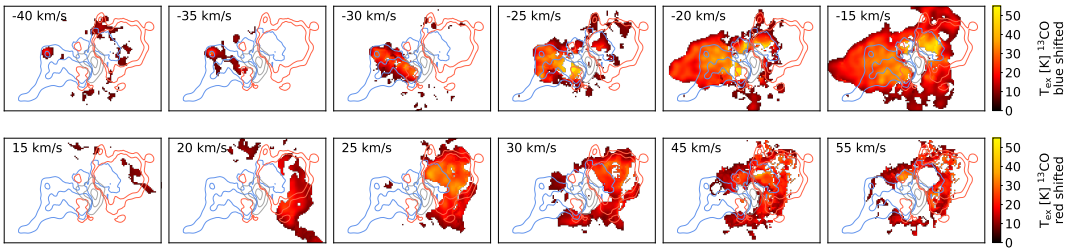

Figure 7.20: Top: Excitation temperature $T_{\rm ex}$ of ^{13}CO derived by assuming an abundance ratio of 25 for ^{13}CO to C^{18}O. The velocity are given with respect to the systemic velocity of 64 km s^{-1} for Sgr B2(N). The emission below 5 K has been masked out. The red and blue contours indicate the outflow seen in emission of SiO (5–4). The grey contours show the continuum emission.

The H_2 column density per velocity channel can be calculated (see Zhang et al. 2016, Feddersen et al. 2020) as

$$\frac{dN_{H_2}}{d\nu} = \frac{dN_{\rm mol}}{d\nu}\frac{1}{f} \tag{7.11}$$

$$= \left(\frac{8\pi\, k\, \nu_{\rm ul}^2}{h\, c^3\, A_{\rm ul}\, g_{\rm u}}\right) Q_{\rm rot}(T_{\rm ex})\, e^{E_{\rm u}/kT_{\rm ex}} \frac{T_{\rm R}(\nu)}{f}, \tag{7.12}$$

where $N_{\rm mol}$ is the column density of ^{13}CO, $\nu_{\rm ul}$=220.398 GHz the frequency of the ^{13}CO transition, $A_{\rm ul}$=6.07514×10^{-7} s^{-1} the Einstein A coefficient, $E_{\rm u}$/k=15.87 K the energy of the upper level, $Q_{\rm rot}$ the partition function, $g_{\rm u}$=10 the degeneracy of the upper level and f=5×10^{-6} the abundance ratio between ^{13}CO and H_2. All given parameters, also for other molecular species, are listed in Table B.1. $T_{\rm R}(\nu)$ is the opacity corrected brightness temperature. The correction term (Goldsmith & Langer 1999) is given by

$$T_R = T_{\rm mb}\, \frac{\tau}{1 - e^{-\tau}}. \tag{7.13}$$

Finally, the mass per velocity channel is calculated with

$$\frac{dM}{d\nu} = \mu_{\rm H_2}\, m_H A_{\rm px}\, \frac{dN_{H_2}}{d\nu}, \tag{7.14}$$

where $\mu_{\rm H_2}$=2.8 is the mean molecular weight of H_2 (Kauffmann et al. 2008), $m_{\rm H}$=1.674 × 10^{-24} g is the mass of the hydrogen atom, and $A_{\rm px}$=8×10^6 pc^2 the spatial area of a pixel.

Since the emission of ^{13}CO is more extended than that of C^{18}O, i.e. the optical depth τ is not constrained all over the place (see Fig. 7.21), I calculate the mass in three different ways: (1, optically thin) I assume ^{13}CO is optically thin everywhere, (2, opacity corrected) I only consider regions where the optical depth τ is determined, and (3, opacity model) I use a combination of both, assuming an optical depth for the unconstrained regions that is equal to the minimum optical depth of the constrained area. In the regions where the optical depth is unknown, the temperature is also unknown. To solve this uncertainty, I introduced a temperature model that follows the trend of the area with temperature measurements (see Fig. 7.21). The derived excitation temperature vary for different velocities, this effect has not been included in the temperature model though. The results of all scenarios are presented in Fig. 7.22. The H_2 mass per velocity channel is in the order of $10^{-3.5}\ M_\odot\,{\rm km}^{-1}\,{\rm s}$ by assuming ^{13}CO as optically thin. After opacity correction, the mass per velocity channel increases to roughly $10^{-2.5}\ M_\odot\,{\rm km}^{-1}\,{\rm s}$.

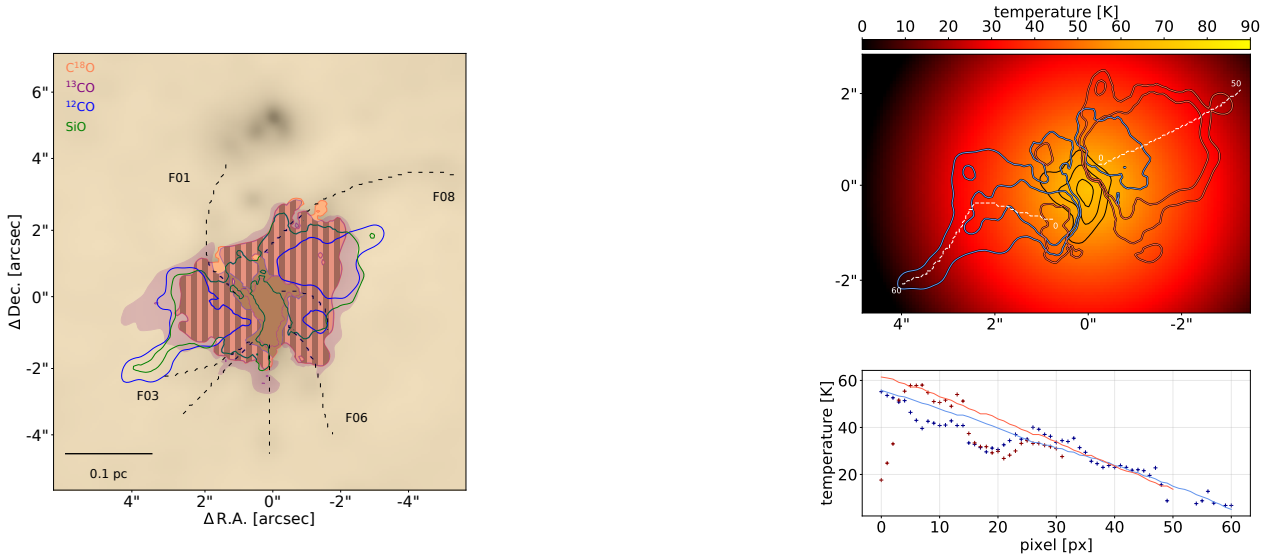

(a) optical depth

(b) temperature profile

Figure 7.21: *a)* Integrated emission of SiO (green), CO (blue) and its isotopologues ^{13}CO (purple) and C^{18}O (orange).The hatched area shows the region where emission of ^{13}CO and C^{18}O overlaps and therefore the optical depth could be determined. In the violet region the temperature and optical depth have been modeled. It is important to note that the extensions of the hatched area changes per velocity channel. The dashed lines are indicating the filaments presented in section 7.1. *b) Top panel*: Temperature profile used to calculate the column densities in regions, where T_{ex} is unconstrained. *Bottom panel:* Temperature trend following the white dashed path in the top panel. The blue and red crosses show the excitation temperatures derived from the optical depth of ^{13}CO. The red and blue line show the modeled temperature values extracted from the same positions.

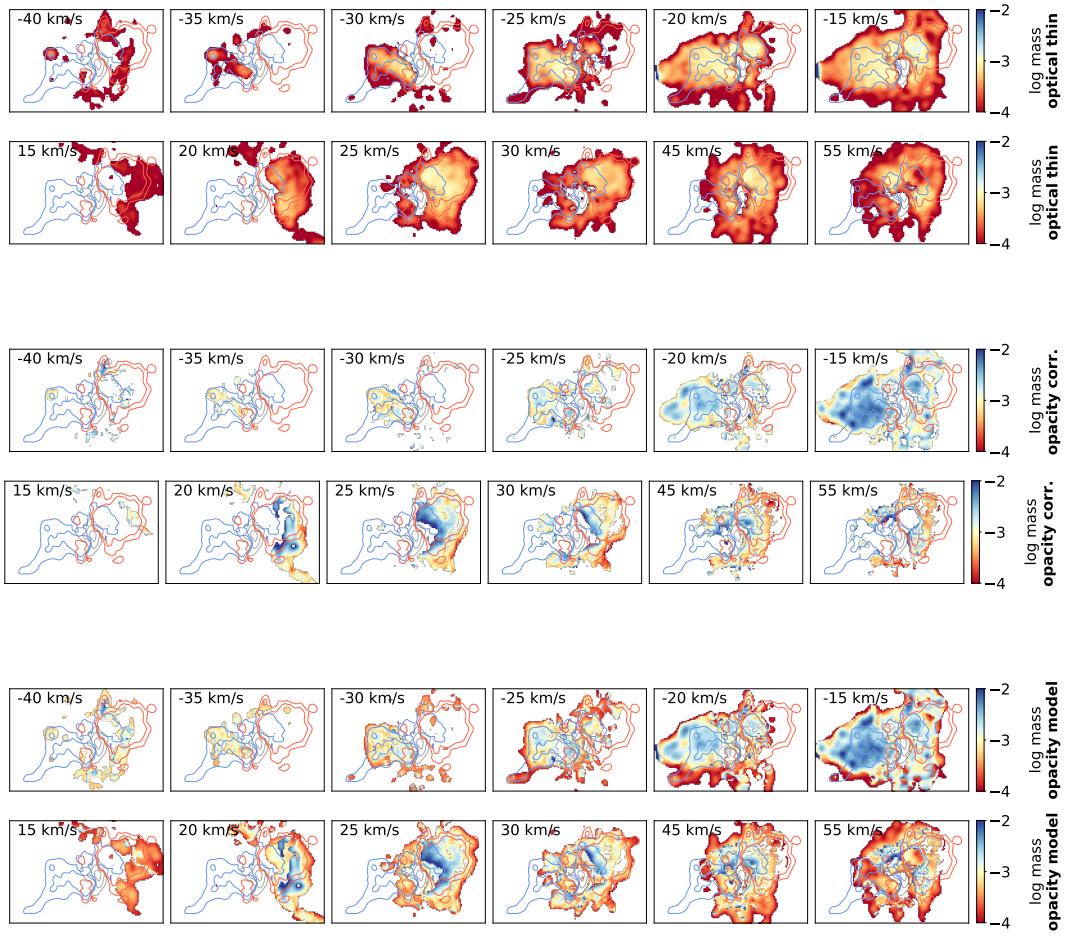

Figure 7.22: Calculated H_2 mass derived from emission of ^{13}CO by assuming an abundance ratio of 5×10^{-6}. *Top panel:* The mass has been calculated by assuming the medium as optically thin. *Middle panel:* The emission of ^{13}CO has been opacity corrected by the isotopologue $C^{18}O$. *Bottom panel:* In regions where the optical depth could not be derived, the opacity and temperature have been modeled.

Determination of the SiO to H_2 abundance and outflow mass:
In the next step, I calculate the column density of SiO per voxel. Together with the H_2 column density of the same voxel (determined above by using the emission of ^{13}CO), Eq. 7.11 provides the SiO to H_2 abundance. The abundance per voxel for the same three different scenarios (assuming ^{13}CO as optically thin, opacity corrected and opacity modeled) is presented in Fig. 7.23. By assuming ^{13}CO as optically thin, the median abundance of SiO to H_2 is $10^{-8.0\pm0.3}$ within the red-shifted lobe of the outflow (north-west), and $10^{-8.1\pm0.4}$ for the blue-shifted one (south-east). After correcting for opacity, the abundance slightly decreases to $10^{-8.5\pm0.4}$ and $10^{-8.8\pm0.4}$. In the mixed scenario the abundance is $10^{-8.4\pm0.4}$ and $10^{-8.7\pm0.5}$. I note that after the opacity correction the abundance stays no longer constant with velocity, but shows an increasing trend for higher outflow velocities. The difference is roughly one order of magnitude. Within the blue lobe of the outflow, the slope flattens beyond a velocity of -22 km s^{-1}. Similar effect happens for the red lobe after 31 km s^{-1}. In order to take into account this effect, I modeled this trend with linear functions using the python package `pwlf`, which performs piecewise linear least squares fits. The slopes, as well as the median abundance for different velocity sections are listed in Table. 7.3. The abundance is not affected in view of the spatial distance to the center of the outflow (see Fig. B.16). Finally, I use the velocity depending abundance of SiO to H_2 to derive the outflow mass. The optically thin scenario gives a outflow mass of 31±6 $M_\odot$ (blue lobe) and 22±4 $M_\odot$ (red lobe). The opacity correction leads to higher masses of 150±30 $M_\odot$ and 81 ±16$M_\odot$. For the mixed scenario I derive masses of 130±26 $M_\odot$ and 60±12 $M_\odot$. It is important to note that the term 'opacity corrected' is related to the ^{13}CO emission, which has been used to derive the abundance of SiO to H_2. The emission of SiO is for all scenarios assumed to be optically thin. The outflow mass derived from our data-set II is in a comparable order of magnitude. In the optically thin scenario I obtain an outflow mass of 22±4 $M_\odot$ (blue lobe) and 19±4 $M_\odot$ (red lobe). After opacity correction theses masses increase to 61±12 $M_\odot$ and 54±11 $M_\odot$. In the third scenario the masses are 49±10 $M_\odot$ and 46±9 $M_\odot$. Since this data-set is filtering out extended emission, the masses are lower than measured with data-set I. All values are listed in Table. 7.3.

As discussed in section 7.3.1, another outflow is detected in the SiO images of data-set II (see Fig. 7.16). Assuming the same SiO to H_2 abundance of the main outflow, I determined an outflow mass for this second outflow of 8±2 $M_\odot$ (for the optically thin scenario) and 25±5 $M_\odot$ (for the opacity corrected).

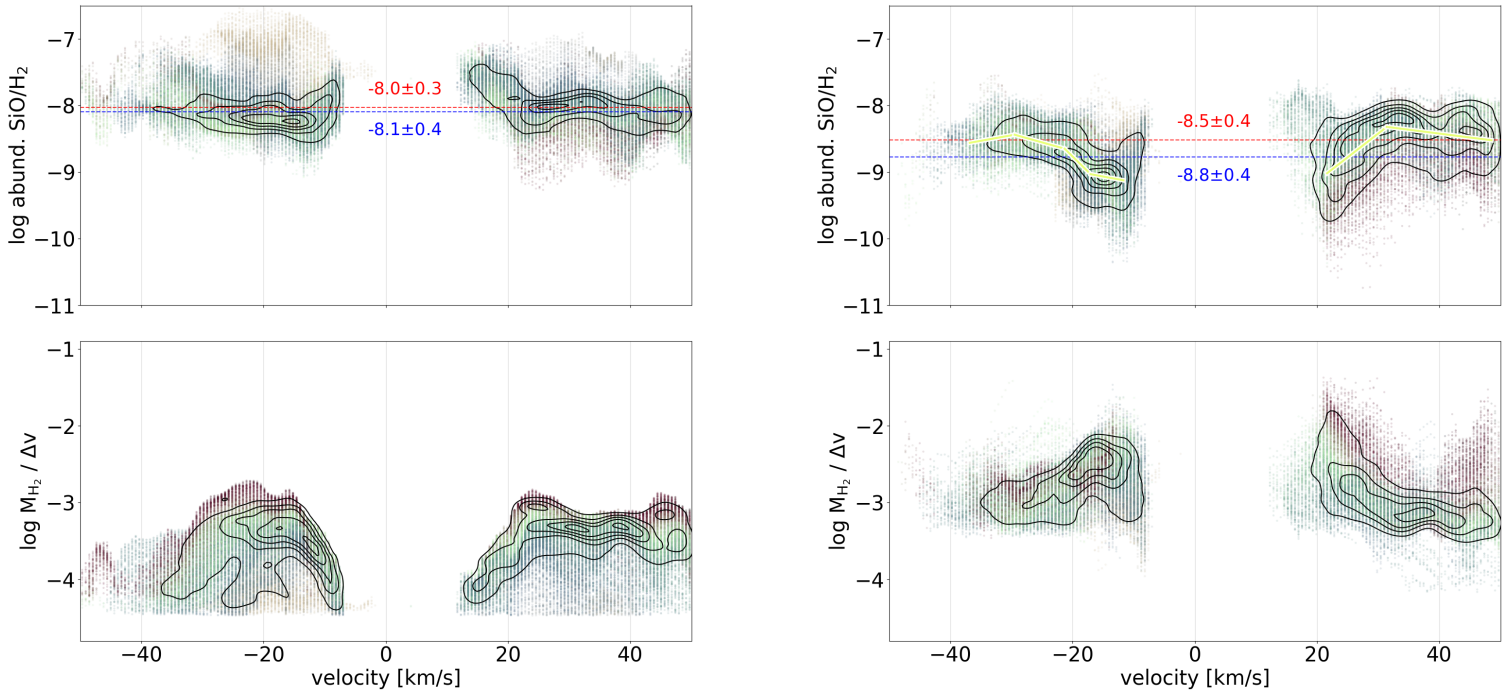

(a) optically thin

(b) opacity corrected

Figure 7.23: *Top panels*: SiO to H_2 abundance per voxel for three different scenarios (a) optically thin, (b) opacity corrected and (c) opacity modeled. The red and blue lines indicate the median abundance of SiO within the red/blue wing of the outflow. After opacity correction (b,c) the abundance is increasing for higher velocity relative to the systemic velocity (here indicated as 0 km s^{-1}, e.i., by 64 km s^{-1} corrected). I performed linear fits for different velocity sections shown with white-green lines. The black contours show the KDE of all values for each outflow lobe. The scatter color represent the distance to the central source AN01, visualized in panel (d). *Bottom panels*: H_2 mass per voxel derived from emission of ^{13}CO. This mass has been used to derive the SiO abundance.

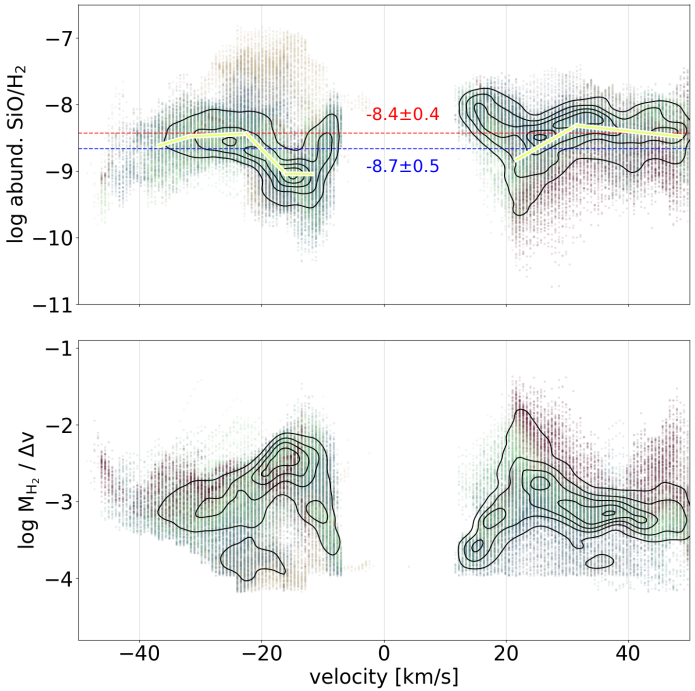

(c) opacity modeled

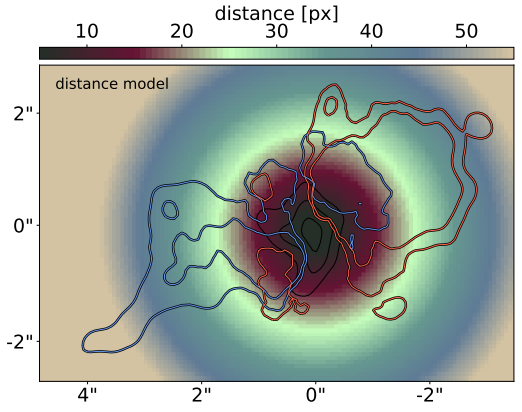

(d) color-code distance

Figure 7.24: Fig. 7.23 continued.

Table 7.3: Outflow properties

SiO abund.	optically thin		opacity corrected		opacity model	
	red wing	blue wing	red wing	blue wing	red wing	blue wing
median[a]	$10^{-8.0\pm0.3}$	$10^{-8.1\pm0.4}$	$10^{-8.5\pm0.4}$	$10^{-8.8\pm0.4}$	$10^{-8.4\pm0.4}$	$10^{-8.7\pm0.5}$
mean $-36/-30$ km s^{-1}	–	–	–	$10^{-8.5}$ $0.016_{\rm m}$,$-7.95_{\rm b}$	–	$10^{-8.6}$ $0.03_{\rm m}$,$-7.63_{\rm b}$
mean $-30/-22$ km s^{-1}	–	–	–	$10^{-8.6}$ $-0.03_{\rm m}$,$-9.20_{\rm b}$	–	$10^{-8.5}$ $-0.01_{\rm n}$,$-8.34_{\rm b}$
mean $-22/-17$ km s^{-1}	–	–	–	$10^{-8.8}$ $-0.09_{\rm m}$,$-10.57_{\rm b}$	–	$10^{-8.7}$ $-0.09_{\rm m}$,$-10.54_{\rm b}$
mean $-17/-11$ km s^{-1}	–	–	–	$10^{-9.1}$ $-0.02_{\rm m}$,$-9.32_{\rm b}$	–	$10^{-9.0}$ -0.0 ,$-9.05_{\rm b}$
mean 21.5/31.5 km s^{-1}	–	–	$10^{-8.7}$ $0.07_{\rm m}$,$-10.6_{\rm b}$	–	$10^{-8.6}$ $0.05_{\rm m}$,$-10.0_{\rm b}$	–
mean 34.5/48.5 km s^{-1}	–	–	$10^{-8.4}$ $-0.01_{\rm m}$,$-8.0_{\rm b}$	–	$10^{-8.3}$ $-0.01_{\rm m}$,$-8.1_{\rm b}$	–

continued

	optically thin		opacity corrected		opacity model	
	red wing	blue wing	red wing	blue wing	red wing	blue wing
outflow mass[b] data-set I	22 $M_\odot$	31 $M_\odot$	81 $M_\odot$	149 $M_\odot$	60 $M_\odot$	129 $M_\odot$
data-set II	19 $M_\odot$	22 $M_\odot$	61 $M_\odot$	54 $M_\odot$	49 $M_\odot$	46 $M_\odot$
outflow energy[b] data-set I	1.95×10^{47} erg	1.85×10^{47} erg	6.61×10^{47} erg	7.32×10^{47} erg	5.31×10^{47} erg	6.39×10^{47} erg
data-set II	1.8×10^{48} erg	3.4×10^{47} erg	5.6×10^{48} erg	8.1×10^{47} erg	4.4×10^{48} erg	7.1×10^{47} erg

Note. m and b indicate the slope and intercept of the linear fit to the abundance for different velocity sections shown in Fig. 7.23. The fit has been performed in logarithmic scales. 'Opacity corrected' and 'opacity model' are related to the ^{13}CO emission that has been used to derive the abundance. The emission of SiO is assumed as optically thin for all scenarios.
(a) The error in the median abundance is given by the standard deviation
(b) The error of the outflow mass is dominated by the error in the flux measurement and the error in the excitation temperature. The average determined excitation temperature is ∼40 K. By assuming an error of 10 K and an error of 10% in the flux measurement, the average error of the outflow mass results in $M_{err} = \sqrt{[(-E_{up}/kT_{ex})\Delta T_{ex}]^2 + [0.1]^2} \times 100\% \approx 15\%$. By assuming an error of 20 K in the excitation temperature, the error increases to ∼ 20%. The error of the outflow energy is similar, since its error is dominated by the error in the mass.

Column densities and abundance of different molecular species:
The technique that I used to estimate the abundance of SiO, can also be applied to other molecular species, which are found to be associated with outflows. I developed an automatized python tool, which is using the infrastructure of XCLASS. Similar to the described procedure in the line stacking chapter (see chapter 5), I select the bright lines of certain molecular species above a 10σ threshold in the frequency range 211 to 275 GHz. For example, for the case of CH_3OH, 85 lines. For all these transitions I acquire with XCLASS the in the CDMS or JPL listed parameters, $A_{\rm ul}$ the Einstein A coefficient, $Q_{\rm rot}$ the partition function, $g_{\rm u}$ the degeneracy of the upper level and $E_{\rm l}/{\rm k}$ the energy of the lower level, which I convert to the upper level in units of Kelvin. All parameters are listed in Table. B.1. The ratio of the above derived column density of H_2 per voxel to the column density of a certain molecular species (calculated with Eq. 7.12) for the same voxel, determines their relative abundance. With this method I estimated the abundance of several molecular species like SO_2, SO, OCS, CS, H_2CS, H_2CO, HNCO, CH_3OH and the isotopologues of SiO. I have to note that this method is sensible to the assumed excitation temperature. In particular, the results of transitions with high energy levels ($E_{\rm l}/{\rm k} \gtrsim 100$ K) are highly uncertain. This aspect will be further discussed in Appendix B.3. Moreover, the obtained abundance can differ substantially for different transitions of the same molecular species due to line blendings. Also opacity effects are not considered in my calculations. However, this method give a rough idea of the order of magnitude. A few examples of different molecular species are presented in Fig. 7.25. The derived column densities and abundance to H_2 are listed in Table. B.2, their medians of all observed transitions are presented in Table. 7.4 and visualized in Fig. 7.28. The (median) abundance of the selected molecular species ranges from 10^{-8} to 10^{-4}. The 10^{-4} abundance of CH_3OH seems quite high at first sight, but Bonfand et al. (2017) report a $2{\times}10^{-5}$ abundance of methanol towards the northern satellite core of Sgr B2(N). This value is within the given error of roughly one order of magnitude (see Table. 7.4).

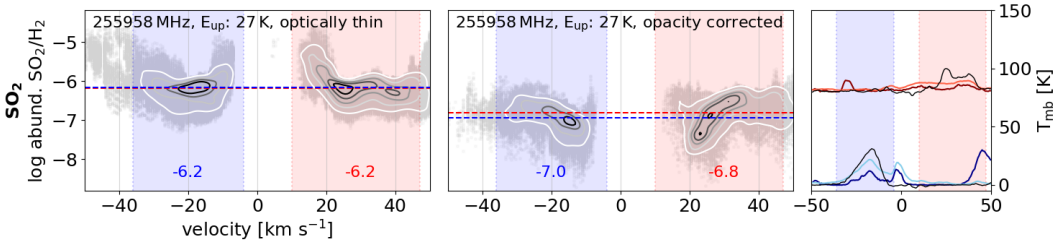

Figure 7.25: Figure continues.

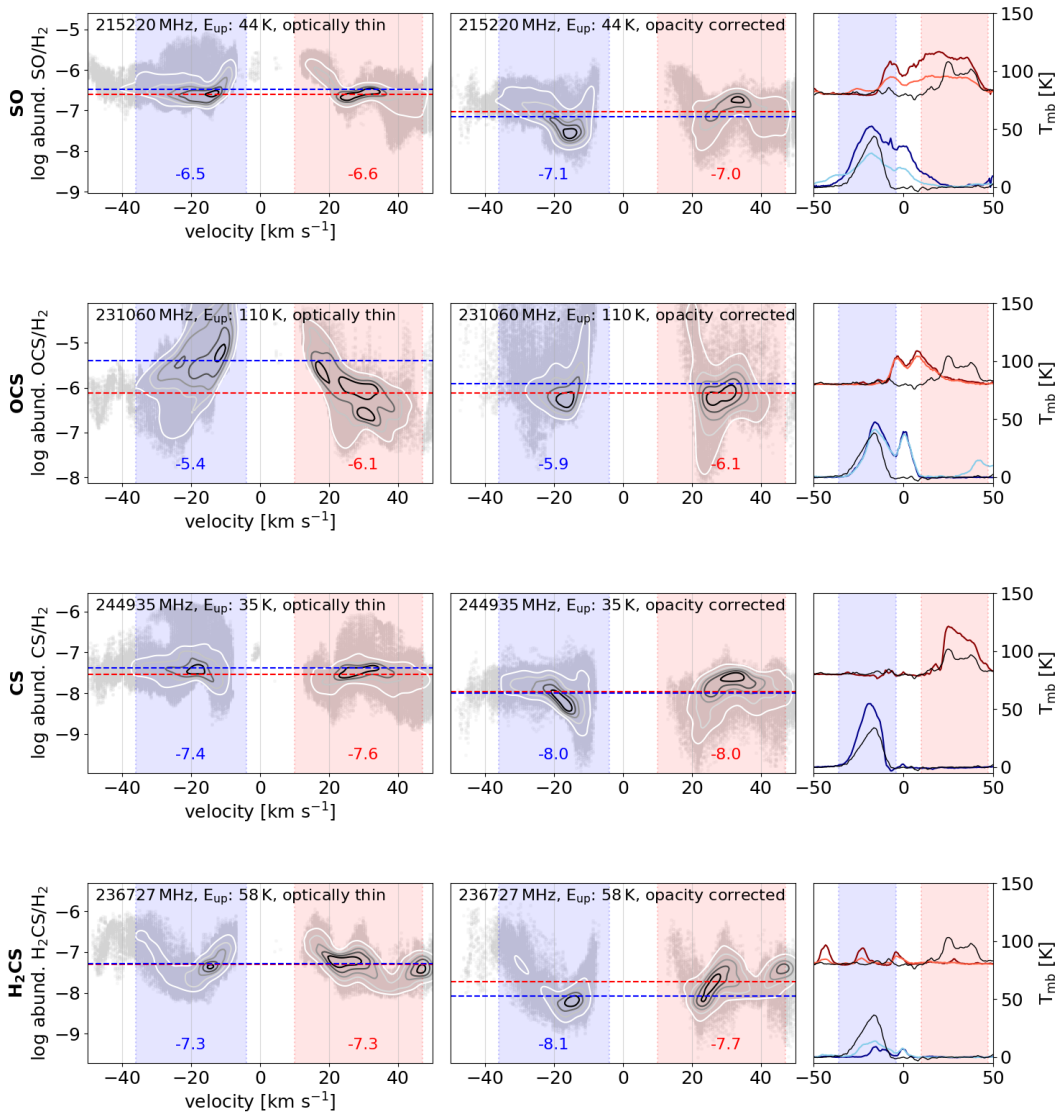

Figure 7.26: Figure continues.

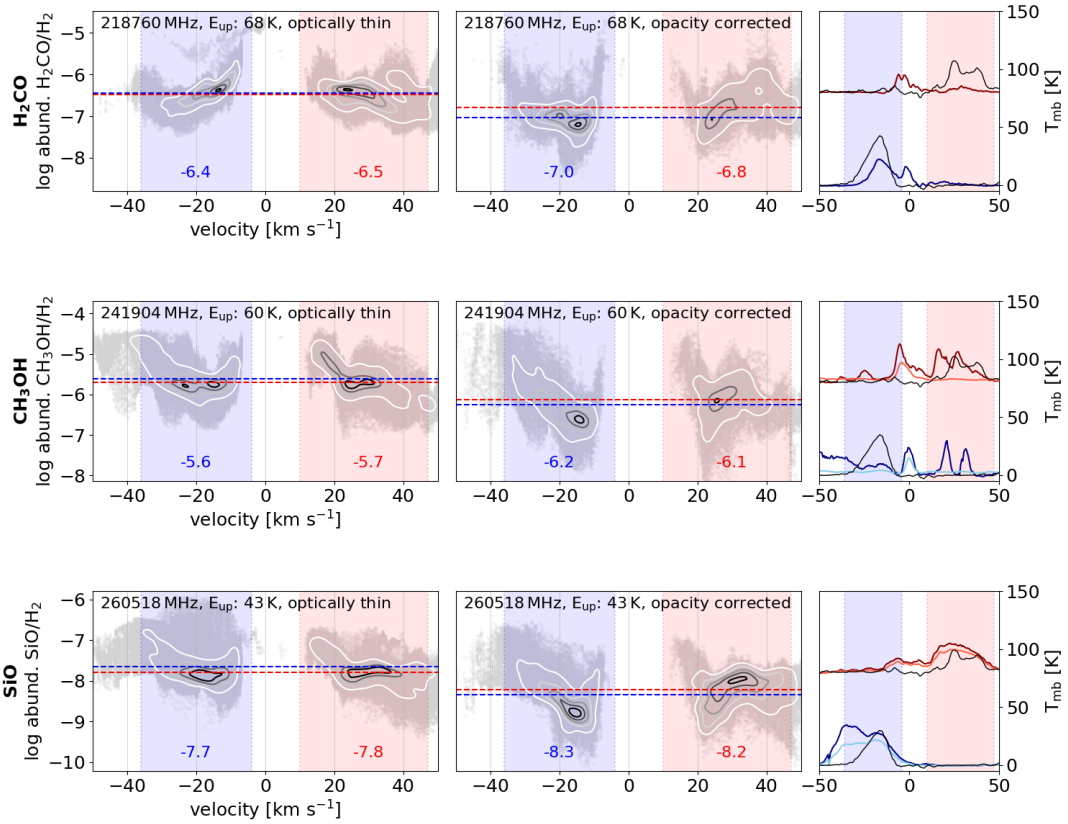

Figure 7.27: *Left and middle panel*: Abundance to H_2 of different molecular species. The blue and red area indicate the range in which the column density and abundance have been determined. The red and blue dashed line show the median abundance on the respective side of the outflow. *Right panel*: The spectra in blue and red are averaged spectra of the selected molecular specie within both outflow wings. The black spectrum shows as reference emission of ^{13}CO. Stacked spectra of all transitions of the selected molecular species are colored in light blue and light red. These spectra can help to identify eventual line blendings, i.e. if the spectra differ substantially. The peaks close to the systemic velocity are not considered within the calculations, since at these velocities no emission of SiO or CO has been detected. Therefore, this emission is most likely not associated to the outflow.

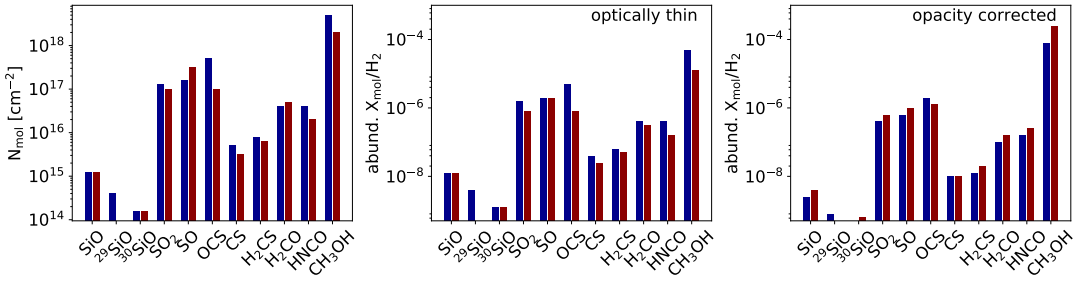

Figure 7.28: Mean column densities and abundance to H_2 for different molecular species. The red bars corresponds to the red lobe of the outflow, the blue bars to the blue lobe. The term 'opacity corrected' is related to emission ^{13}CO, which has been used to derive the abundance. The emission of all presented molecular species is assumed as optically thin.

Table 7.4: Median abundances with respect to H_2 and median column densities.

mol.	N_{mol} $[10^x$ cm$^{-2}]$		abund.$[10^x]/H_2$ optically thin		abund.$[10^x]/H_2$ opacity corrected	
	blue wing	red wing	blue wing	red wing	blue wing	red wing
^{29}SiO	14.6±0.4	15.3±0.3	-8.4±0.5	-7.9±0.3	-9.1±0.6	-8.2±0.4
^{30}SiO	14.2±0.4	14.2±0.2	-8.9±0.5	-8.9±0.4	-9.6±0.6	-9.2±0.5
SO_2	17.1±0.4	17.0±0.3	-5.8±0.4	-6.1±0.4	-6.4±0.7	-6.2±0.6
SO	17.2±0.3	17.5±0.3	-5.7±0.4	-5.7±0.4	-6.2±0.5	-6.0±0.4
OCS	17.7±0.8	17.0±0.4	-5.3±0.9	-6.1±0.6	-5.7±1.1	-5.9±1.0
CS	15.7±0.4	15.5±0.4	-7.4±0.4	-7.6±0.4	-8.0±0.4	-8.0±0.5
H_2CS	15.9±0.3	15.8±0.3	-7.2±0.4	-7.3±0.4	-7.9±0.5	-7.7±0.6
H_2CO	16.6±0.4	16.7±0.4	-6.4±0.3	-6.5±0.4	-7.0±0.4	-6.8±0.4
HNCO	16.6±0.3	16.3±0.3	-6.4±0.4	-6.8±0.4	-6.8±1.0	-6.6±0.8
CH_3OH	18.7±0.4	18.3±0.4	-4.3±0.6	-4.9±0.5	-4.1±1.4	-3.6±0.9

Note. The values of individual transitions can be found in Table. B.2. The term 'opacity corrected' is related to the ^{13}CO emission that has been used to derive the abundance. The emission of these molecules is assumed to be optically thin.

Comparison of column densities with previous findings:
I compare my measured column densities with the column densities reported by Belloche et al. (2013) in Fig. 7.29. The authors performed an unbiased, spectral line survey towards Sgr B2(N) with the IRAM 30 m telescope in the 3 mm window. However, they did not resolve the outflow or the two main cores spatially. Hence, their obtained spectra are the product of mixed emission originated from different structures (e.g., main hub, northern satellite core or outflow). Their measured column densities are obtained with XCLASS by fitting multiple (velocity) components to the spectra, from which I present the component close to the source velocity (i.e., the obtained column densities correspond most likely to central region). In comparison to their obtained column densities, I see an enhancement of SiO within the outflow area (Fig. 7.29, left panel). The column densities of the other molecular species are 10–100 times lower within the outflow lobes, including the sulfur-bearing molecules, which should be enhanced in outflows though. An explanation might be that the authors take optical depth effects into account, which I neglect in my calculations. Correcting my values for opacity would result in higher column densities.

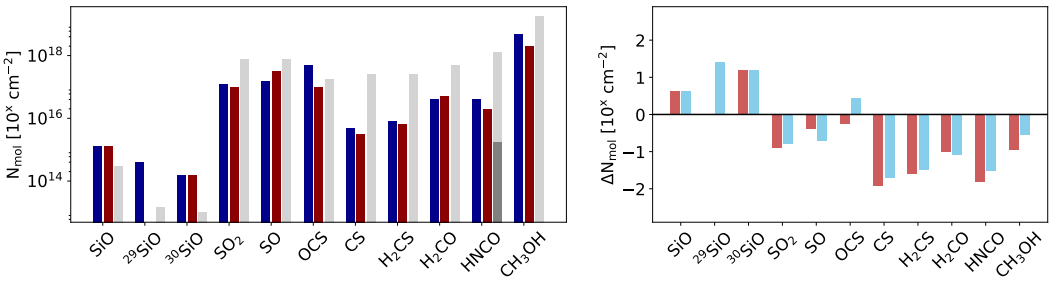

Figure 7.29: Column densities of different molecular species as listed in Table 7.4 compared to column densities as reported by Belloche et al. (2013). The authors performed an unbiased, spectral line survey towards Sgr B2(N) with the IRAM 30 m telescope. However, the outflow is not resolved spatially. Their measured column densities are obtained by XCLASS fits using multiple (velocity) components, from which I selected the component at ∼0 km s^{-1} with respect to the source velocity of 64 km s^{-1}. *Left panel:* The red bars correspond to my measured column densities within the red lobe of the outflow and the blue bars correspond the blue lobe. The grey bars indicate the column densities as reported by the cited authors. *Right panel:* Difference between my measured column densities and the values reported by the cited authors.

Outflow mass and molecular abundance

- ▷ The SiO to H_2 abundance is approximately $10^{-8.7}$.
- ▷ The SiO abundance increases with velocity.
- ▷ The total mass of the main outflow is roughly 230 $M_\odot$.
- ▷ The outflow mass in the west is about 25 $M_\odot$ (only one lobe observed).
- ▷ The abundance to H_2 of other molecular species that are known to be outflow tracer are in range of 10^{-8} to 10^{-4}.

7.3.3 Outflow Energetics

The kinetic energy per velocity channel can be calculated as

$$\frac{dE}{dv} = \frac{1}{2}\frac{dM}{dv} \times v_{\rm out}^2, \tag{7.15}$$

where dM is the above calculated mass per velocity and v_{out} the outflow velocity relative to the source velocity (v_{sys}=∼64 km s^{-1}). This results for the optically thin scenario in a kinetic energy of 1.85×10^{47} erg (blue-shifted lobe) and 1.95×10^{47} erg (red-shifted lobe), in total ∼3.8×10^{47} erg. After opacity correction these values increase to 7.32×10^{47} erg and 6.61×10^{47} erg, in total ∼1.4×10^{48} erg. All values are listed in Table. 7.3.

Assuming that the outflow has been expanding with a constant and uniform velocity since it has ignited, the dynamical time can be calculated by dividing the length (extension of the outflow) by the maximum outflow velocity

$$t_{\rm dyn} = L/v_{\rm max}. \tag{7.16}$$

The maximum velocity is roughly 40/60 km s^{-1} (blue/red shifted lobe), and the projected length L_{obs}=∼ 5/3.5 arcsec. Assuming a projection angle of 45°, we can determine a de-projected length as L=L_{obs}/cos(α). This results in a dynamical time t_{dyn}=7000/3200 yr. Together with the above calculated masses (optically thin scenario), the outflow is ejecting 0.0044/0.0068 $M_\odot$ yr^{-1}, or in total roughly 0.011 $M_\odot$ per year. After opacity correction this value increases to 0.047 $M_\odot$ per year. Compared with our measured accretion rates of 0.16 $M_\odot$ yr^{-1} (see section 7.2.2), approximately ∼30% of the gathered material gets ejected. All results are discussed in section 7.4.2.

Outflow energetics

- ▷ The energy output of the main outflow amount to ∼1.4×10^{48} erg.
- ▷ The main outflow ejects in total roughly 0.047 $M_\odot$ per year.
- ▷ Its age is estimated to be 3200–7000 yr.

7.3.4 Ionized Gas

The presence of an H II region is an evidence of ongoing high-mass star formation, since only massive stars can produce enough UV photons to ionize the surrounding gas. However, our observed continuum emission at 1 mm is mainly dominated by the emitting dust. In order to introduce the H II regions I use VLA data, at the C-band (4–8 GHz, spatial resolution of ∼0.45″, in A-Array configuration, credit Meng et al. 2019[2], project 16B-031) and Q-band (33–50 GHz, spatial resolution of ∼0.07″, credit A. Ginsburg[3], project 18A-229). Besides of continuum emission at lower frequencies, ionized gas can also be studied with radio recombination lines (RRLs). These lines are the result of the recombination of (thermal) electrons with protons. After that, these electrons cascade into lower energy levels by emitting photons. The following section will focus on the recombination line H30α at 231 GHz, which is included in data-set I and II. In addition I had access to ALMA 3 mm data with similar high angular resolution of ∼0.07 ″ as data-set II (credit A. Ginsburg). In the covered frequency range are included the RRLs H40α at 99 GHz and H42α at 86 GHz.

In Figure 7.30 I show the ionized gas as detected via VLA emission in the C and Q bands, and compare it to the ALMA emission. I find two spots, which are possibly associated with emission of the RRL H30α and strong continuum emission in C and in Q band; in the northern satellite core a very compact and bright object (above T_B=4800 K) with the coordinates α(J2000)=$17^h47^m19^s.89$, δ(J2000)=$-28°22'13\overset{''}{.}54$ and close to filament F06 with coordinates α(J2000)=$17^h47^m19^s.79$, δ(J2000)=$-28°22'20\overset{''}{.}73$. The latter detection is uncertain, since the intensities of the two observed lines at 231.9 GHz are in the same order of the neighboring molecular lines. In this frequency range the only candidates of confusion (checked in CDMS and JPL) are the molecular species $^{33}SO_2$ and CH_3OCH_3. For both species I create a synthetic spectrum with XCLASS. By assuming for $^{33}SO_2$ a column density of 10^{16} (motivated by the column density of 10^{17} derived for SO_2 in section 7.3.2) and a temperature of 100 K (close to the average core temperatures), I obtain a (synthetic) line intensity of ∼10 K (observed line intensities ∼25 K). By assuming for CH_3OCH_3 a column density of 10^{18} (similar as reported in Belloche et al. 2013) and a temperature of 100 K , I can reconstruct the two neighboring observed transitions with similar line intensities of ∼20 K and ∼25 K. In order to fit the observed spectrum, the transitions need to be shifted by -5 km s^{-1} (with respect to the source velocity). This velocity fits also well the velocity at the same position (within filament F06) obtained with the species CH_3OH in section 7.2.1, see Fig. 7.7). The similarity between synthetic and observed spectrum suggest that the observed transitions may not be RRLs.

[2]I. Physikalisches Institut, Universität zu Köln, Zülpicher Strasse 77, 50937, Köln, Germany.
[3]Department of Astronomy, University of Florida, P.O. Box 112055, Gainesville, FL, USA.

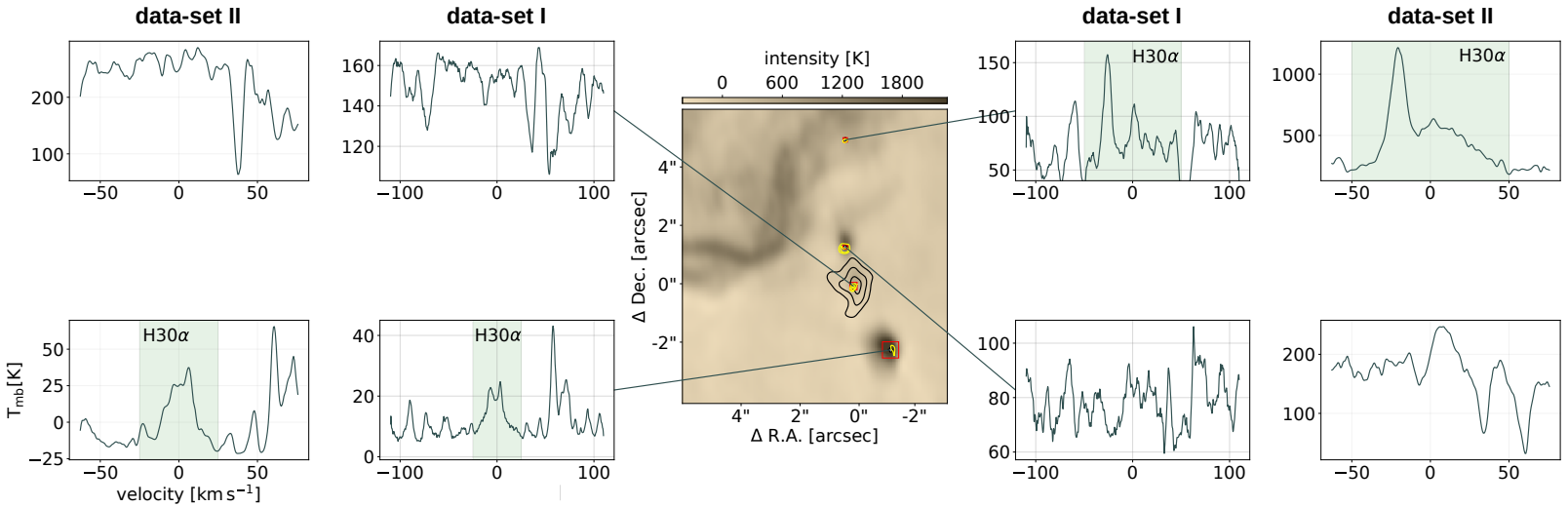

Figure 7.30: The background image shows the ionized gas (H II regions) observed with VLA in A-Array configuration in its C-band (credit, F. Meng). The yellow contours show continuum emission of VLA Q-band data (credit, A. Ginsburg) in levels of 20, 50 and 90% of its peak emission. The black contours indicate the continuum emission (data-set I) at 242 GHz in levels of 50, 70 and 90%. The spectra are averaged along the red marked boxes in order to get a better signal-to-noise ratio. Two spots are possibly associated with the RRL H30α (top right, with the coordinates α(J2000)=$17^h47^m19^s.89$, δ(J2000)=$-28°22'13''.54$ and bottom left with the coordinates α(J2000)=$17^h47^m19^s.79$, δ(J2000)=$-28°22'20''.73$).

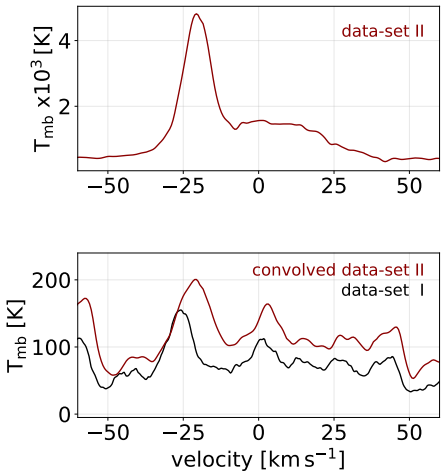

Figure 7.31: *Top panel:* spectrum extracted from data-set II at the position with the coordinates α(J2000)=$17^h47^m19^s.89$, δ(J2000)=$-28°22'13''.54$. *Bottom panel:* Comparison between both data-sets after convolving data-set II to the same beam size of 0.4 ″. Both spectra show a very similar line pattern. However, there is a velocity shift of the main peak of ∼5 km s^{-1}. Also the continuum level differs about roughly 50 K.

The spectrum towards the bright compact source shows a discrepancy between data-set I and II (see Fig. 7.30, top panel, right). In order to make a better comparison of the flux, I convolve the high angular resolution data with the same beam of the lower-resolution data (0.″4), resulting in a spectrum (Fig. 7.31) with similar line pattern and line intensities. However, I have to note a velocity shift of the main peak of ∼5 km s^{-1}and a continuum difference of 50 K. The following analysis has been performed with data-set II.

Figure 7.32 shows the bright compact source in more detail. The 3D visualization makes visible that all the spectra across this compact source has two distinct velocity components; a bright but narrow component I and a wide but less intense one (component II). The peak intensity map of the bright component I (red contours in Fig. 7.32) shows a more circular and symmetric pattern as expected for a point-like source, while the peak intensity of the other component has an extended shape. The velocity of both components stays constant and their emission peaks at the same position (see Fig. 7.32, middle panel). I fitted Gaussians to both components and obtained brightness temperatures of 3722/1136 K, velocities of -20.6/-0.2 km s^{-1}(with respect to the source velocity of 64 km s^{-1}) and linewidths of 9.8/45.8 km s^{-1}. I present the spectra of all covered recombination lines in Fig. 7.33. All line properties (velocity, linewidth, intensity) are listed in Table 7.5. The RRLs H40α and the H42α have only a single, broad component.

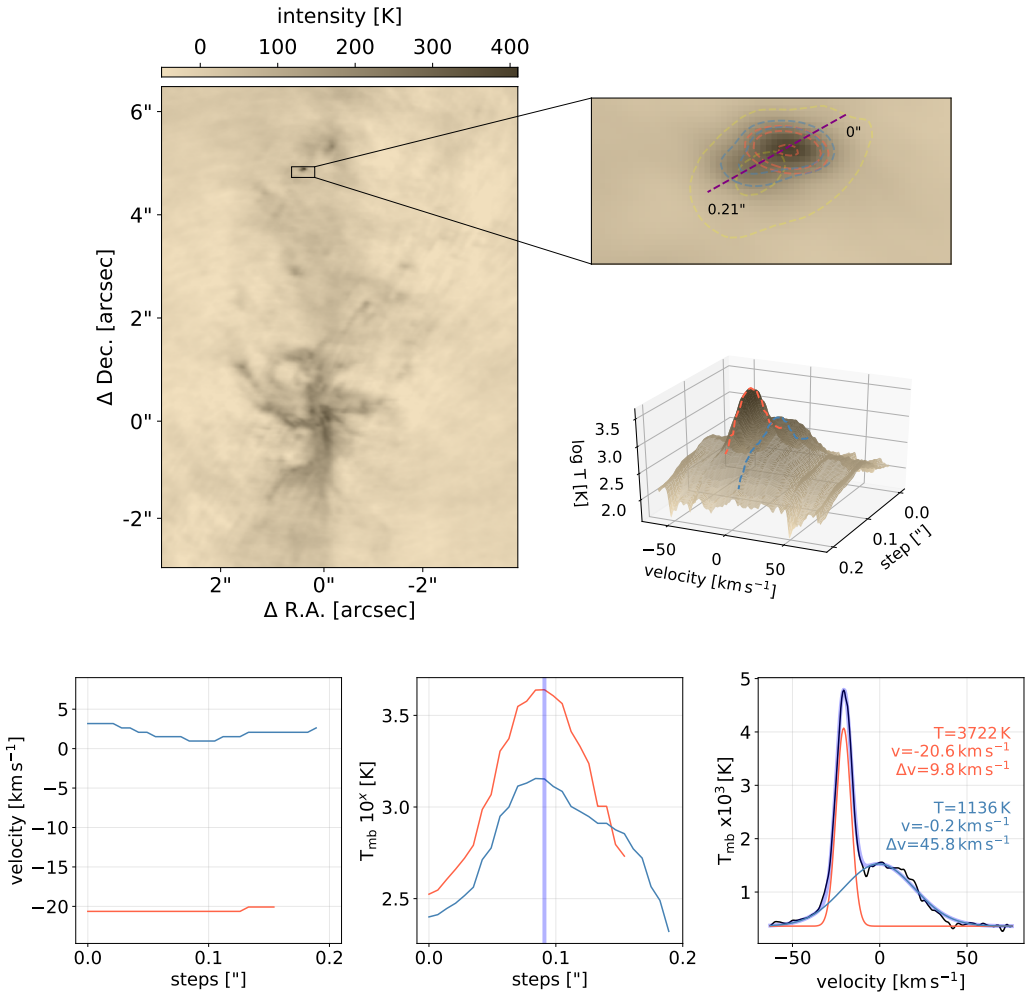

Figure 7.32: The large map shows the continuum emission of data-set II averaged over all spectral windows. The zoom-in presents the identified bright object with the coordinates α(J2000)=$17^h47^m19^s.89$, δ(J2000)=$-28°22'13''.54$ in more detail. The yellow contours indicate the Q band emission, the red contours the peak intensity of the bright component and the blue contours the peak intensity of the second, weaker component. The red and blue dashed lines in the 3D figure trace the peak positions of both components. The velocity and peak intensity cut presented in the middle of the figure is taken along the purple line shown in the zoom-in panel. The spectrum in the bottom is taken at the peak position of the bright source (blue line at 0.09″). I fitted two Gaussians to the spectra in order to obtain the brightness temperature, velocity and velocity width. The blue transparent line shows the overall fit.

Component I of the H30α line shows a surprisingly high brightness temperature compared to the recombination lines at lower frequencies. Calculations of the level populations of atomic hydrogen in H II-regions have shown that global population inversions can exist

Table 7.5: Properties of RRLs.

line	freq [GHz]	T_L [K][a]	T_{cont} [K][a]	v_{off} [km s^{-1}][a]	v_{width} [km s^{-1}][a]	line [mJy][b]	continuum [mJy][b]
H30α	231.901	3722	359	-20.6	9.8	591.84	53.44
		1136		-0.2	45.8	155.94	
H40α	99.022	374	530	2.5	70.6	17.85	27.96
H42α	85.688	247	523	3.2	58.2	13.07	27.82

Note. [(a)] Parameter determined from Gaussian fit. Their errors will be dominated by the uncertainty in the flux measurement (typically roughly 10%) rather than by the fitting process. The velocity v_{off} is given with respect to the source velocity of Sgr B2(N) of 64 km s^{-1}. The continuum brightness temperature is a mixture of ionized gas and dust emission. [(b)] Extracted from one individual pixel at the peak position of the emission. The line intensity is continuum subtracted.

(Cillié 1936,Baker & Menzel 1938), which leads to the formation of recombination lines under non-LTE conditions. Hence, stimulated emission can occur. RRLmaser amplification is expected to be a common phenomenon in UC H II-regions with evidence of stellar winds (Jiménez-Serra et al. 2013, in MonR2 H II region, Martin-Pintado et al. 1989, in MWC 349 A). The suspicion is that component I could also be a RRL-maser.

Component II of the H30α line has a broad linewidth, which is consistent with what is expected to be found towards ultra or hypercopmact H II regions (Kurtz et al. 2000; Kurtz 2005). In order to explore the nature of the H II region, I study the spectral index (α, defined as $T_\nu \propto \nu^\alpha$). A spectral index with values of -1.4 are typically associated with jets and winds, while values of -2.1 are usually found towards optically thin H II regions (see Sánchez-Monge et al. 2013b). I determine the spectral index from the flux measured at the C and Q band images. Since the spatial resolution of $\sim$0.45″ in the C band is a factor 6.4 lower than our ALMA observations, the detected source (d$\approx$0.16″) stays unresolved, while in the Q-band the source is resolved. Therefore, I use the source size (0.16″) to convert the measured flux in the C band into brightness temperature. The spectral index I obtained is in the range -1.5 to -2.7 (see Fig. 7.34). Hence, we can not use this data to favor or discard one of the above scenarios (optically thin or partially optically thick).

As an exercise to derive the physical parameters of the HII region, I assume the optically thin scenario and extrapolate the flux of the Q-band image to the wavelength/frequency of our ALMA observations (i.e., 1 and 3 mm), where the RRLs are detected. This extrapolation from the Q-band to the ALMA bands is necessary, since the emission at 1 and 3 mm may be dominated by dust rather than by the free-free radiation of the ionized gas. Finally, the line to continuum ratio gives the electron temperature T_e determined from the expression

$$\left[\frac{T_e}{K}\right] = 2200 \left[\frac{\nu}{GHz}\right]^{0.96} \left[\frac{T_L}{T_C}\right]^{-0.87} \left[\frac{\Delta v}{km\,s^{-1}}\right]^{-0.87}, \quad (7.17)$$

where T_C is the continuum brightness temperature (ionized gas), T_L the line emission, ν the frequency and Δv the linewidth. This results in electron temperatures of 1900 K

derived from H42α emission, 1000 K (H40α) and 600 K (H30α). All values are much lower than the normally expected 10^4 K (see Sánchez-Monge et al. 2013b, Meng et al. 2019). But also by assuming an error of 20% in the continuum and line emission and velocity width, I obtain maximum electron temperatures of 3300 K (H42α), 1700 K (H40α) and 1100 K (H30α), which are still roughly one order of magnitude too low, suggesting that the assumption of an optically thin scenario (and thus also the equation) is not valid. Towards some ultracompact H II-regions, the presence of ionized stellar winds modifies the internal electron density structure of these sources (with $n_e > 10^7$ cm^{-3}) and will form optically thick cores. The assumption of optically thin and LTE thus becomes obsolete. This could be one possible explanation for my results and will be further discussed in section 7.4.3.

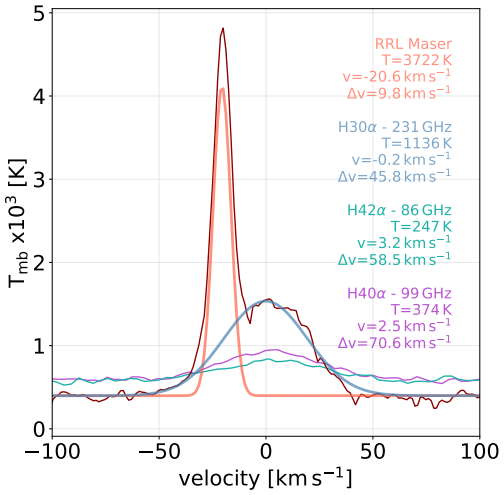

Figure 7.33: Spectrum of the recombination lines H30α, H40α and H42α. The brightness temperature, velocity and velocity width are obtained by fitting Gaussians to the spectra. The measured values are presented within the figure. The bright component in the H30α is thought to be a RRL maser, while the others are thermal RRLs.

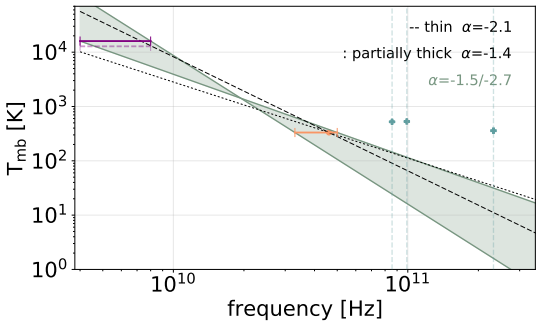

Figure 7.34: Determination of the spectral index α towards the bright source detected in the northern satellite core of Sgr B2(N). The purple bar shows the C-band continuum emission assuming that the entire flux is emitted from the unresolved source. The transparent bar below indicates that only 80% of the measured emission has its origin from the source. The orange bar shows the Q-band continuum emission. The dotted line represents the partially optically thick scenario by only considering the Q-band data and the dashed line the optically thin scenario. The blue crosses mark the continuum emission at 1 and 3 mm.

Ionized gas in Sgr B2(N)

- ▷ A bright compact object has been detected in the northern satellite core with two components in the H30alpha line: RRL-maser and thermal-RRL.
- ▷ The spectral index of this UC H II region is in the range -1.5 to -2.7 and the thermal emission may therefore be partially optically thick.

7.4 Discussion

7.4.1 Converging filaments

The analysis of transitions of different molecular species revealed a network of filaments in Sgr B2(N), converging toward a central massive core. I derived velocity gradients along the filaments, which are 10–100 times larger than is usually found in other star-forming regions at larger scales (e.g. Peretto et al. 2013, Lu et al. 2018). I have considered here if these large velocity gradients can be caused by other mechanisms rather than accretion to the center, for example expanding motions associated with outflows or explosive events like the one seen in Orion KL (e.g. Bally et al. 2017). For outflows, typical linewidths are 30–100 km s^{-1} (e.g. Wu et al. 2004, López-Sepulcre et al. 2010, Sánchez-Monge et al. 2013a), roughly ten times larger than what I measure. Furthermore, common outflow tracers are CO, HCO^+ and SiO (e.g. Wu et al. 2004, Sánchez-Monge et al. 2013a, but see also Palau et al. 2011, 2017) and not complex molecules like CH_3OCHO or CH_3OCH_3 which I find tracing the filamentary structure of Sgr B2(N). Explosion events such as that in Orion KL are also a doubtful explanation since they produce clear and straightforward radial structures. Contrary to this, the structures that I identified in Sgr B2(N) appear curved and bent, which leaves us with accreting filaments as the most plausible explanation. For cylindrical, spatially tilted filaments, the transport of material along them toward the dense hub (i.e. velocities close to the center are higher than outwards) would result in different signs of the velocity gradient, as I find in Sgr B2(N) (see Fig. 7.9 and Table 7.1). In this scenario, positive velocity gradients correspond to filaments extending backwards, and vice-versa, allowing me to have an idea of the possible 3D structure of the region. In Fig. 7.35 I show the distribution of filaments in Sgr B2(N) colored by velocity gradient, in which red corresponds to positive velocity gradients (filaments located in the back) and blue to negative velocity gradients (filaments located in front). A remarkable case in Sgr B2(N) are the neighboring filaments F03 and F04. Filament F03 would be located in the back while F04 in front of the hub. Overall, filaments F03, F07, and F08 would be located in the back, and F04, F05, and F06 would be in front (see Fig. 7.35). In addition to the velocity field, I find that the linewidths for many filaments (e.g. F01, F03, F05, F06, and F08, see Fig. B.4) increase when approaching the center[4]. This effect, combined with the increasing mass-to-length ratio (derived independently from the continuum emission) when moving inwards, suggests that the accretion or infall rates onto the filaments may be increasing in the vicinity of the main hub.

Finally, the high mass accretion rates (0.08–0.16 $M_\odot$ yr^{-1}) point to a short time necessary to accumulate a large mass reservoir. Also some filaments appear extended, connecting

[4]I note that the increase of linewidth toward the center may be partially caused by the line stacking method. The positions along the filament close to the center show a richer chemistry (i.e., more line features). This excess of lines, compared to the outer positions, may result in a artificial increase of the linewidth (see section 5.2 for further detail).

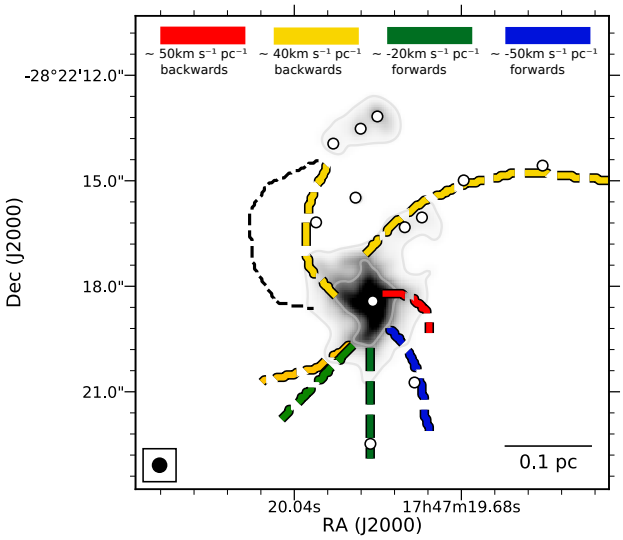

Figure 7.35: Filaments in Sgr B2(N) colored by their mean velocity gradient as derived for the molecular species CH_3OCHO, CH_3OCH_3, CH_3OH and $^{13}CH_3OH$. The velocity gradient ranges from -50 km s^{-1} pc^{-1} (blue), corresponding to filaments located in front, to $+50$ km s^{-1} pc^{-1} (red), corresponding to filaments located in the back. The gray contours indicating 242 GHz continuum emission at a level of 1.2 Jy beam^{-1}. The white circles represent the dense cores, and the black dashed line shows the filament F02, only visible in H_2CS.

multiple dense cores with the main hub. In particular, filament F08 extends up to the distant western cores A08 and A19, located at distances ∼0.5 pc. Although the molecular line emission is not bright in the filament between core A05 and cores A08 and A19, the velocity in A19 fits the velocity gradient obtained in the region of the filament closer to the hub (see Fig. 7.5). This suggests that these cores, even if being far away, are connected to the central hub. Similarly, the northern core seems to be connected to the main hub trough filaments F01 and F02. Despite filament F01 being affected by the H II region H01, the emission of CH_3OH reveals, through a second velocity component, a link between the northern core and the hub (see Fig. B.2). Filament F02, which is only visible in the emission of H_2CS, shows a smooth velocity gradient from highly red to blue-shifted velocities when moving from the northern core to the central hub (see Fig. B.3). This suggests that the distant cores as well as the northern core may fall onto the hub, increasing the gas and stellar density, and favoring Sgr B2(N) to become a super stellar cluster.

7.4.2 Outflow properties

Emission of molecular species like CO (2–1) and SiO (5–6) revealed two outflows in Sgr B2(N). The main outflow has an extension of roughly 0.35 pc, which is within the typical range of 0.01 to 3.98 pc (Wu et al. 2004). Its orientation points in southeast-northwest direction with its blue shifted emission in southeast and most of its red shifted emission in northwest. The geometrical center of both lobes is close to the position of the core AN01, likely tracing the location of the powering source. Due to the high central dust and gas mass of $> 2000\ M_{\odot}$, the high luminosity of $5.9{\times}10^{6}\ L_{\odot}$ and the derived stellar mass content of $\sim$3000 $M_{\odot}$, it is to be expected that the outflow is not driven by a single source but by multiple young stellar objects. Therefore, the observed outflow would not be a single entity but a collection of outflows. The clear separation of the blue and red-shifted emission hints that most outflows of the powering sources are well aligned. It is also noticeable that the large H II region to the northeast has a common border with the SiO emission. Moreover, filaments F01 and F02 surround the outflow to the east, filament F08 and F06 to the west (see Fig. 7.14). One could gain the impression that the outflow is trapped inside filaments and H II regions; suggesting, that the the H II region and the outflow are located in the same plane.

I also found that the SiO to H_2 abundance ($\sim 10^{-8\pm0.5}$, opacity corrected $10^{-8.7\pm0.4}$) increases with velocity. Since most of the SiO is released to the gas phase through the sputtering of Si-bearing material in grains (e.g., Schilke et al. 1997, Gusdorf et al. 2008), the correlation could be explained by stronger mechanical forces for higher velocities, which would make the releasing process more yielding. A similar correlation has been found by Sánchez-Monge et al. (2013a), who report that the excitation conditions change (densities and/or temperatures increase) with velocity of the outflow. This may be complementary to the increase of abundance, and consistent in the physical picture of higher velocities, stronger shocks.

I compare all derived parameter like outflow mass M ($53\pm7\ M_{\odot}$, opacity corrected $230\pm34\ M_{\odot}$), kinetic energy E ($3.8{\times}10^{47}$, $1.4{\times}10^{48}$ erg), dynamical time t_{dyn} (3000–7000 yr) and mass loss rate dM/dt ($1.1{\times}10^{-2}$, $4.7{\times}10^{-2}\ M_{\odot}\,yr^{-1}$) with other sources in Fig. 7.36. The presented sources are taken from the catalog of Wu et al. (2004)[5]. All sources with a luminosity of above 10^3 $L_{\odot}$ are grouped as high-mass objects. Sgr B2(N) is one of the most luminous and massive sources. The determined outflow mass ranges in the upper segment and follows, as pointed out by the cited authors, the linear relation between source luminosity and outflow mass. The kinetic energy is also increasing with luminosity and the obtained value for Sgr B2(N) fits well. The fact that these correlations hold for such a broad range of luminosities suggests that the luminosity of the powering source determines the outflow energetics, and that the driving mechanisms are similar for all luminosities. However, this linear behavior could be interpreted (as suggested for the mechanical force by López-Sepulcre et al. 2009) both as a single outflow powered by a

[5]catalog downloaded from VizieR, J/A+A/426/503/table1a & table1b

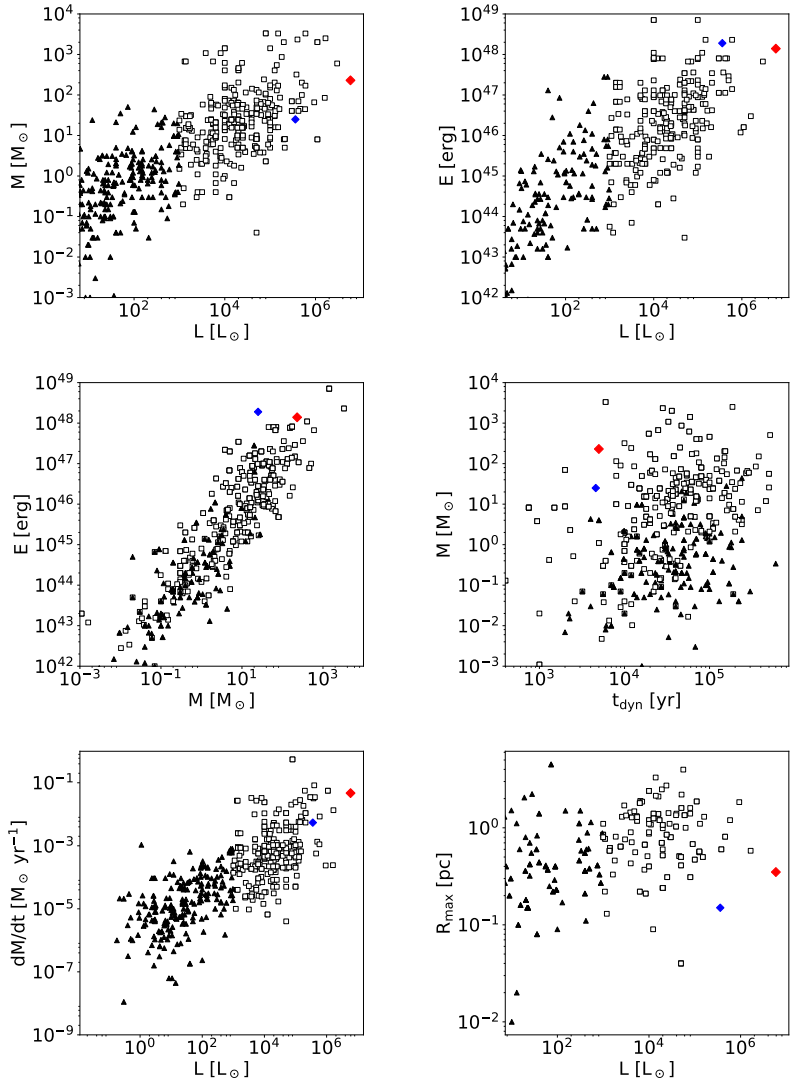

Figure 7.36: Properties of molecular outflows as reported in Wu et al. 2004. The filled triangles represent the low mass objects, while the open boxes indicate the sources with high mass. The red marker show the outflow properties of the main outflow in Sgr B2(N), the blue marker represents the outflow found in the west close to core AN08. For the latter, only the red-shifted lobe has been observed. Presented are the relations between the parameters bolometric luminosity L, outflow mass M, kinetic energy E, dynamical time t_{dyn}, mass loss rate dM/dt and outflow diameter along the major axis R_{max}.

more luminous source, or by more than one outflow coming from less luminous sources, each of them contributing to the overall outflow energetics. Beuther et al. (2002) claims a weakening of the correlation between mass loss rate dM/dt and luminosity L towards the highest luminosities. I can not find any evidence for saturation in my analysis, which is in agreement with the work of López-Sepulcre et al. (2009), who neither find this behavior.

A previous study of Sgr B2(N) derived a larger outflow mass of ∼2000 $M_\odot$ (Higuchi et al. 2015), however the authors used a value of 1.2×10^{-9} as SiO to H_2 abundance. This abundance has been derived from $C^{18}O$ (1–0), which is blended by the molecular species HNCO (ν_5=1), CH_3CN (ν_4=1), and C_2H_5OCHO (e.g., Belloche et al. 2013) and hence, the determination might be imprecise. Taking my estimated abundance as a basis, the masses would be comparable. Their estimated dynamical time scale of 5×10^3 coincides with my findings (3000–7000 yr). The mass loss rate of 4.7×10^{-2} $M_\odot\,\mathrm{yr}^{-1}$ found for Sgr B2(N) is about on third of the accretion rate. This ratio is consistent with the values reported for other sources (e.g., Tomisaka 1998).

7.4.3 New radio recombination line maser object

I found in the northern satellite core of Sgr B2(N) a very compact and bright object (above T_B=4800 K) with coordinates α(J2000)=$17^h47^m19^s.89$, δ(J2000)=$-28°22'13\farcs54$, which shows radio recombination line maser emission. It is known that towards some ultracompact H II-regions, the presence of ionized stellar winds modifies the internal electron density structure of these sources (with $n_e>10^7$ cm^{-3}), leading to the formation of optically thick cores, where RRLmaser can form (Jiménez-Serra et al. 2013, in MonR2 H II region, Martin-Pintado et al. 1989, in MWC 349 A). These ionized winds can be generated from evaporating disks that are left after star formation (Hollenbach et al. 1994, Jaffe & Martín-Pintado 1999).

In order to explore the nature of the UC H II region, I determined its the spectral index (α, defined as $T_\nu \propto \nu^\alpha$) with the VLA emission in the C and Q band. The spectral index I obtained is in the range of −1.5 to −2.7. Thus, I can rule out an optically thick H II region (spectral index of 0 expected). But also the scenario of an optically thin H II regions seems not to be realistic, since I derive under this assumption from the observed thermal RRLs (H30α, H40α, H42α) electron temperatures of 600–2000 K (expected 10^4, see Sánchez-Monge et al. 2013b or Meng et al. 2019). The remaining scenario is the presence of a partially optically thick H II region. However, for further investigation a better sampling of the frequency range is required, as well as a better spatial resolution. The C-band data used for my analysis do not resolve the source and thus, the uncertainty is large. In summary, I found a RRL-maser and showed that the thermal emission may be partially optically thick. This is in agreement with the properties found for MWC349, which may suggest that both RRLs (maser and thermal) are produced by the same object: A photo-evaporating disk with a RRL-maser.

Part IV

Conclusion

8

High-mass cluster formation

The high densities found in Sgr B2(N) (10^9 cm^{-3}, or 10^7 $M_\odot$ pc^{-1}, see Sánchez-Monge et al. 2017), the large mass reservoir of the envelope, and high star formation activity in a number of dense cores suggest that Sgr B2(N) may gather enough mass to form a super-stellar cluster or young massive cluster (YMC), therefore constituting a good candidate YMC progenitor. The formation of YMCs is still poorly understood, and different scenarios have been proposed (e.g. Portegies Zwart et al. 2010; Longmore et al. 2014 for a review, and Bressert et al. 2012; Fujii 2015; Fujii & Portegies Zwart 2016; Howard et al. 2018). The "in-situ formation" scenario proposes that the required amount of gas mass is gathered into the same volume of the final stellar cluster before star formation sets in. The extreme densities required to form a YMC, entail that the accumulated gas has a short free-fall time, which in turn implies that the time for gathering the final mass has to be short or, alternatively, the star formation activity is delayed until the accumulation of the total mass. In a second scenario, the "conveyor belt formation" theory proposes that the mass reservoir extends farther away than the final stellar cluster size. Thus, stars can form in regions with much lower densities and be transported toward the center of the cluster, increasing the final density of the YMC (for more details see chapter 2.2). My analysis of the properties of Sgr B2(N) suggests a mix of the two scenarios. On one side, the dense cores located within the filaments already harbor stars, according to our simulations in the ballpark of 2000 (see chapter 6.2), before merging into the main hub. This supports the idea of the conveyor belt models ("dry" merger), in which star forming clusters are transported throughout the filaments toward the center of the region. On the other hand, the stellar mass ratio is 50%, that is, the dense cores are still surrounded by dense gas while reaching the central region. Although the statistics are small, I see the trend that

dense cores located closer to the central hub can be more massive than in the outer regions, (see Fig. 7.12) suggesting that they have acquired more mass on their way to the main hub. In addition, the comparison of timescales listed in Table 7.2 suggests that the dense cores can reach the center before they have exhausted all the gas to form stars. Finally, the measured high mass accretion rates (0.08–0.16 $M_{\odot}$ yr^{-1}) point to a short time necessary to accumulate a large mass reservoir, as proposed by the in-situ ("wet" merger) formation scenarios. Assuming constant accretion rates, the central dense hub, with (25–10) $\times$ 10^3 $M_{\odot}$, has been assembled in only 60–300 kyr. However, the fraction of stars is large ($\sim$ 50%) compared to the amount of gas mass in the cores. As a result I cannot consider this process as a clear wet merger, but as a "damp" merger. The mass expulsion by the outflow compared to the accretion rate is roughly in the order of one third. However, due to the the high accretion rates and the already large mass concentrated in the central hub, Sgr B2(N) has the potential to become a YMC or super stellar cluster similar to the Arches or Quintuplet, which are also located in the CMZ near the Galactic center.

9 Summary

I have studied the spatial distribution and kinematic properties of a number of molecular species detected in the high-mass star-forming region Sgr B2(N). I made mainly use of ALMA observations with an angular resolution of 0.″4 (corresponding to 3300 au) and covering the frequency range from 211 to 275 GHz (data-set I). In addition I had access to ALMA observations with an angular resolution of 0.″05 (corresponding to 400 au) and covering the frequency range from 216.9–220.8/230.8–234.7 GHz.

The rich chemistry of Sgr B2(N) results in the detection of thousands of lines, often overlapping and therefore difficult to analyze. In order to overcome this problem, I have developed a python-based tool that stacks lines of any given molecular species resulting in an increase of the final signal-to-noise ratio and averaging out line blending effects. This has permitted to study the distribution of the molecular emission and its kinematic properties. My main results are summarized in the following:

- ▷ I have identified two different spatial structures related to the molecular emission in Sgr B2(N). Molecular species like CH_3OCH_3, CH_3OCHO, CH_3OH, or H_2CS show a filamentary network similar to the distribution of the dust continuum emission at 242 GHz. Contrary to that, species like OCS or C_2H_5CN show a spherical or bubble-like distribution.

- ▷ I have identified eight filaments, which converge toward the central massive core or hub. All but one filament are traced in multiple molecules, including rare isotopologues. Filament F02 is detected in our dataset in only one molecule, H_2CS. The filaments extent for about 0.1 pc (some up to 0.5 pc) and have masses of a few hundred $M_\odot$. The structure and distribution of the filaments, together with the

presence of a massive central region (∼2000 $M_\odot$), suggest that these filaments play an important role in the accretion process and transport mass from the outer regions to the central hub.

- ▷ From the line emission, I measure velocity gradients along the filaments on the order of 20–100 km s^{-1} pc^{-1} at scales of ∼0.1 pc. This is 10–100 times larger than typical velocity gradients found in other star forming regions at larger scales (∼1 pc). I derive mass accretion rates in individual filaments of up to 0.05 $M_\odot$ yr^{-1}, which add to a total of 0.16 $M_\odot$ yr^{-1} when considering the accretion of all the filaments into the central hub.

- ▷ The dense cores identified in the 242 GHz continuum emission map are found distributed along these filaments. I have determined the stellar mass content of these cores, and compare the timescale for the dense cores to collapse and form stars or clusters, with the timescale required for them to be accreted onto the central hub. Considering simple approximations, the free-fall timescale for the core collapse is longer than the time of accretion onto the hub. This suggests that although stars and clusters can form within the cores while being accreted, they will not exhaust all the gas. This is consistent with the stellar mass fractions of 50% (with respect to the total mass) that I derive. This suggests a scenario of a damp merger Sgr B2(N).

- ▷ Two outflows have been detected in emission of the molecular species SiO, CO and its isotopologues. The abundance ratio of SiO to H_2 has been determined of about $10^{-8.7\pm0.4}$, as derived from emission of $C^{18}O$, and it shows an increase with velocity. The total mass of the main outflow contains roughly 230 $M_\odot$ and thus ranks high compared to other sources in other star forming regions. Similar high is the energy output with 10^{48} erg and the mass loss rate of 0.047 $M_\odot$yr^{-1}. This mass loss rate corresponds to one third of the mass accretion rate. The dynamical time of the outflow is estimated to be 3200–7000 years.

- ▷ I found in the northern satellite core two components in the H30alpha line: A RRL-maser, with a brightness temperature of ∼3700 K and a linewidth of ∼10km s^{-1}, and a thermal RRL, with a brightness temperature of ∼1100 K and a linewidth of ∼46km s^{-1}. With the VLA C and Q band emission I obtained for the ultra-compact H II region a spectral index in the range of −1.5 to −2.7, suggesting the thermal emission may be partially optically thick. The presence of the RRL-maser along with the partially thick thermal emission, is in agreement with the properties found for MWC349, which may suggest that both RRLs (maser and thermal) are produced by the same object: A photo-evaporating disk with a RRL-maser.

In summary, Sgr B2(N) contains a central hub with large densities ($\sim 10^9$ cm^{-3}, or 10^7 $M_\odot$ pc^{-3}), a series of massive dense cores ($\sim$200 $M_\odot$) with the potential to form stellar clusters, an massive and high-energetic outflow, and a network of filaments converging toward a central hub, with large velocity gradients and high mass accretion rates (up to 0.16 $M_\odot$ yr^{-1}). The large mass already contained in the central hub ($\sim$2000 $M_\odot$ in about 0.05 pc size) together with the merging process of dense cores already harboring stellar clusters, suggest that Sgr B2(N) has the potential to become a super stellar cluster like the Arches or Quintuplet clusters.

10 Outlook

In the following outlook I show how to expand the knowledge of SgrB2(N), which is a really good candidate of a YMC progenitor. Also the nearby star forming region SgrB2(M) may be also another relevant target as presented in the following sections. However, in order to gain more insight in the formation process of YMCs, it is also required to study other sources. Several candidates within our Galaxy are thought to be likely YMC progenitors at different evolutionary stages: G0.253+0.016 (e.g., Longmore et al. 2012, Rathborne et al. 2014) and the clouds 'd', 'e' and 'f' (e.g., Immer et al. 2012, Walker et al. 2015, Walker et al. 2016) within the CMZ. These clouds could slightly increase the statistics necessary to establish common properties and phenomena of YMCs.

10.1 Sagittarius B2 North

Although many physical processes have been evaluated in this work, some points are worth to study in more detail. The following list do not claim to be complete, but I singled out a few interesting aspects:

Dense core properties:
In Sánchez-Monge et al. (2017) 20 continuum sources/dense cores have been detected towards Sgr B2(N). However, our new data-set II resolved many more, including tail like structures (compare Fig. 7.1 and Fig. 7.3). The 1 and 3 mm data could be used to determine the dust mass of all detected sources with the aim to study the spatial distribution of massive objects (mass segregation). The temperature, required in order to derive masses, could be determined by fitting molecular lines with XCLASS. Their SEDs, constraint with

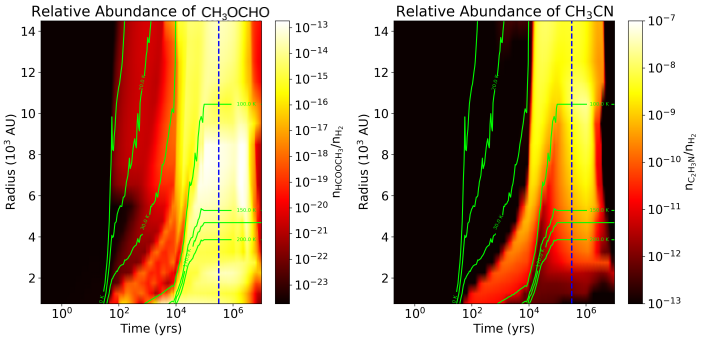

Figure 10.1: Molecular abundance predicted from Saptarsy for a collapsing core (credit Liem Ngo & Dirk Schäfer). The blue dashed line indicates the estimated age of SgrB2(N).

archival data at 22 and 45 GHz and new VLA data at 22, 15, and 5 GHz (credit A. Ginsburg), could help to estimate the free-free contribution and therefore to study the physical nature of these objects. Moreover, the same analysis as performed in section 7.2.3 (stellar mass fraction, free-fall time, spatial distribution of massive cores) could be repeated including the new sources, which would provide a better statistic.

Bubble of molecular gas:
I discovered in SgrB2(N) that the emission of many different molecular lines reveal a filamentary structure, which one could describe as converging arms towards the central massive core. This structure is visible in continuum and transitions of different molecules like CH_3OCHO and CH_3OCH_3, whereas other molecules like C_2H_5CN and CH_3CN trace rather a bubble shape (see section 7.1). The origin of these two different structures for different molecular species is still not understood, however, some preliminary results obtained with the astrochemical code Saptarsy [1] may give some first hints. All Bubble tracer molecules seem to have a drop in the abundance at the center of the dense core. Whereas the abundance of the other molecules is more uniformly distributed (e.g., Fig. 10.1). Hence it might be that the bubble molecules are better tracer of the surrounding diffuse gas while the filament molecules are good tracer of denser regions like in the filaments. However, more effort has to be invested to understand the chemical reactions in more detail, a work which will be continued by my colleague Liem Ngo.

A horizontal cut trough the bubble in emission of molecular species like C_2H_5CN and CH_3CN ('bubble tracer') reveals a pronounced velocity component from -16 km s^{-1} to $+16$ km s^{-1} with respect to the source velocity (see Fig. 10.2), which is not seen in emission

[1] Saptarsy is a rate-equation-based 1D astrochemical code. The code calculates abundances of different molecular species around a dense core, which are collapsing in a free-fall scenario, for a given temperature evolution. For more details see Choudhury et al. (2015).

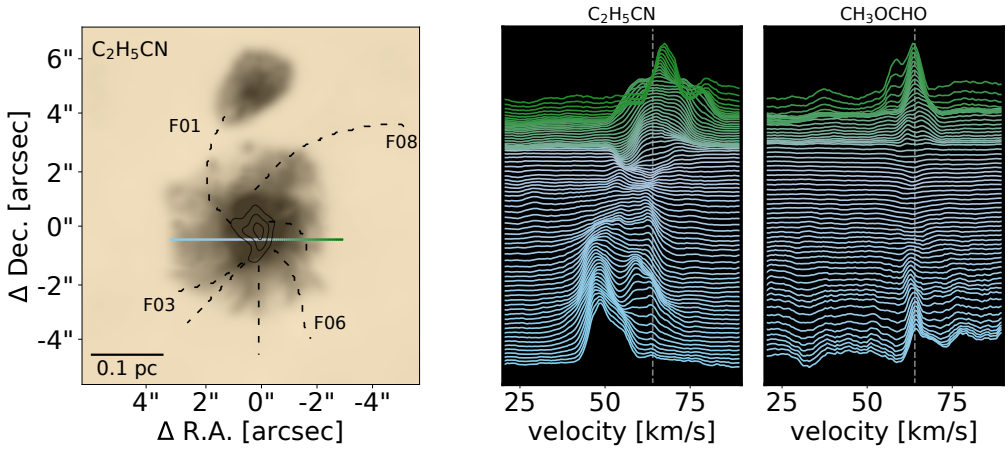

Figure 10.2: *Right panel:* Bubble of molecular gas in emission of C_2H_5CN. The dashed lines show the filaments identified in section 7.1. The blue-green line indicate the cut along the the neighboring spectra have been extracted. *Middle and left panel*: The spectra have been constructed from stacking transitions (see more details in chapter 5), are normalized to their peak emission and equidistantly plotted on top. The grey dashed line shows the systemic velocity of Sgr B2. The molecular specie C_2H_5CN shows velocity features not seen in CH_3OCHO.

of molecules like CH_3OCHO and CH_3OCH_3 ('filament tracer'). This velocity difference could be originated by a (Keplerian-)rotating structure. For Keplerian rotation, one can write

$$\frac{v^2}{R} = \frac{GM}{R^2}, \tag{10.1}$$

where R is the radius, v the rotation velocity, G the Gravitational constant and M the mass of the object. Assuming a rotation velocity of 16 km $s^{-1}$and a radius of 0.1 pc gives a mass of about 6000 $M_\odot$. The central hub alone, contains already $\sim$2000 $M_\odot$, and the bubble may be even more massive. Consequently, the derived mass is in a similar order of magnitude as the measured mass based on dust emission. Thus, the scenario of rotation is conceivable. However, that is a very vague presumption. A three-dimensional model (e.g. with RADMC-3D[2] or XCLASS cubefit function) of the region would be required to take for instance also projection effects and an appropriate density profile into account.

Filaments and magnetic fields:
The presence of filaments in molecular clouds at many different scales suggest that these entities play an important role during the early phases of the star formation (see section 1.3), i.e., during the mass accumulation process. Numerical simulations (Seifried & Walch 2015) show that the properties of these filaments can in turn be strongly influenced

[2]RADMC-3D is a code package for diagnostic radiative transfer calculations.

by magnetic fields. While a magnetic field aligned to the major axis of a filament can stabilize it against radial collapse and reduce fragmentation, magnetic fields perpendicular to the filaments will result in the formation of narrower filaments . On the other hand, observations of star forming regions provide us with information on the interplay between the three main forces: gravity, magnetic fields and turbulence. Tang et al. (2019) observed the G34 region and found a correlation between local velocity gradients and the orientation of the magnetic field, almost as if the gas flow was guided by it. On 0.5-pc scales, several studies (e.g., W51, Koch et al. 2018, W43, Cortes et al. 2016, NGC6334V, Juárez et al. 2017) also confirm that the magnetic field orientation is imprinted in the dynamics of the flowing material. But what is the role of the magnetic field in this extremely dense and compact filaments as found towards Sgr B2(N)? In order to study the impact of magnetic fields in this kind of extreme environments, polarization measurements in a similar spatial resolution as data-set II are required. ALMA proposals for this purpose have already been submitted over the last years.

10.2 Sagittarius B2 Main

Sgr B2 contains two main sites of star formation (see section 3.1): Sgr B2(N), scope of this work, and Sgr B2(M). Previous studies have revealed a very different chemical composition of the two objects, with Sgr B2(M) being very rich in sulphur-bearing species and Sgr B2(N) in complex organic molecules (e.g. Belloche et al. 2013, Neill et al. 2014, Corby et al. 2015). Besides, the authors find different morphologies in the two objects, with Sgr B2(M) being highly fragmented into many cores and Sgr B2(N) remaining monolithic consisting in only a main core and a northern (satellite) core. Also our ALMA observations (data-set I) revealed that in general, Sgr B2(N) is chemically richer than Sgr B2(M). It has also been found that the total mass in Sgr B2(M) is distributed in different fragments, while most of the mass in Sgr B2(N) is concentrated in a dense hub (Sánchez-Monge et al. 2017). In contrary to Sgr B2(N), we could not identify a filamentary network in Sgr B2(M). Moreover, Schmiedeke et al. (2016) and Ginsburg et al. (2018) reported a stellar mass of $\sim 1.5 \times 10^4$ $M_\odot$, one order of magnitude larger than found for Sgr B2(N).

Over all, Sgr B2(M) seems to be more evolved and therefore in a later state of cluster formation. Thus, it would be from great interest to get deeper insight in Sgr B2(M) in order to study the time-evolution of YMCs. Due to the immediate vicinity ($\sim$1.9 pc) of both objects it is conceivable that Sgr B2(M) and Sgr B2(N) will merge and form a giant cluster, similar to cluster R136 located in 30 Doradus Nebula in the Large Magellanic Cloud.

As preliminary result, I present in Fig. 10.3 the outflow detected towards Sgr B2(M). Due to the different morphology seen in emission of SiO and CO, I focus on the common feature, a red shifted lobe of the outflow, between $4''$ to $0''$ (Δ R.A.) and $-1''$ to $2''$

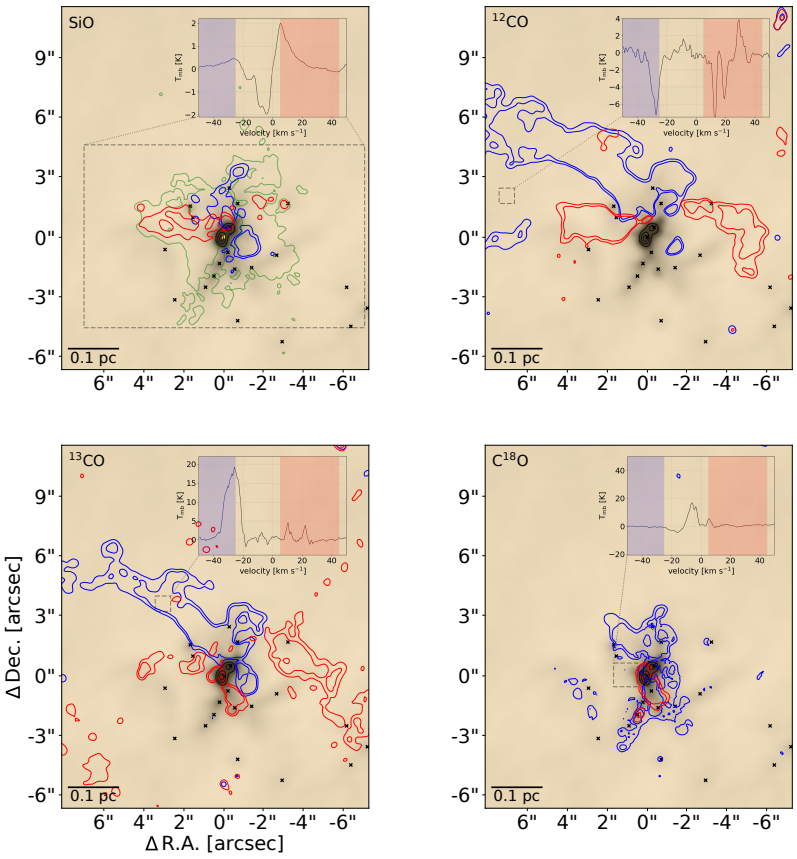

Figure 10.3: Outflow in Sgr B2(M). The background image shows continuum emission at 220 GHz (data-set II). The crosses indicate the dense cores identified in Sánchez-Monge et al. (2017). The spectra in each panel are averaged over an area indicated by the grey boxes. The blue and red contours show the integrated emission along -50 to -25 km s^{-1}, 5 to 45 km s^{-1} respectively. The green contours are indicating the SiO emission down to a level of 15 σ. The yellow cross mark the position of core A01 with coordinates α(J2000)=17^{h}47^{m}20^s.16, δ(J2000)=−28°23′04.″67. The spectrum in the top right panel shows that also below the extended arched shaped emission ^{12}CO has been detected, though only in absorption. Suggesting that the entire area is filled with ^{12}CO with the center being optically thick.

(Δ Dec.). Following the instruction of section 7.3.2, I derive an outflow mass of the sub-region of ∼1.4 $M_\odot$. As basic parameters a ^{12}CO to H_2 abundance ratio of 10^{-4} and a excitation temperature of 100 K has been used. I assumed this part of the outflow as optically thin, since almost no emission in ^{13}CO and C^{18}O has been detected. This results in a SiO to H_2 abundance ratio of $10^{-7.2}$ (see Fig. 10.4), which is roughly one order of magnitude larger than found for Sgr B2(N). It is also striking that most SiO

emission (tracing shocks) is distributed around the central core. The other identified cores show no strong evidences of active outflows and seem to be more quiescence. In further investigations, more derived molecular abundances of different molecular species in and around the other cores, together with chemical codes like Saptarsy, could help to evaluate the chemical evolution of Sgr B2(N) and (M).

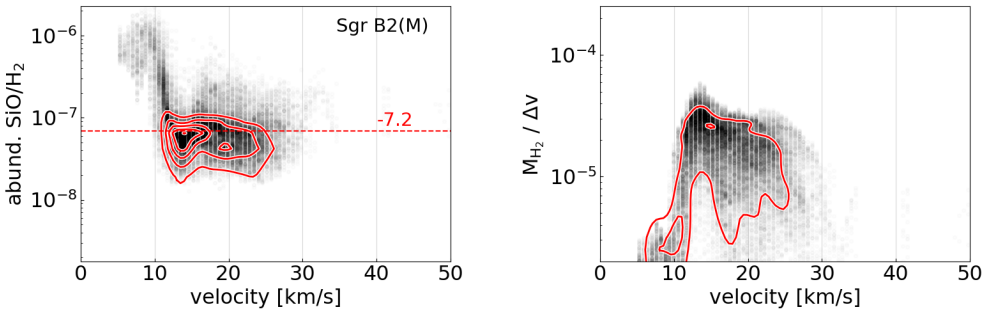

Figure 10.4: *Left panel:* SiO abundance per voxel in Sgr B2(M) based on the the red shifted lobe of the outflow shown in Fig. 10.3 (top panel, left) between $4''$ to $0''$ (Δ R.A.). The red contours show a KDE of the abundance per voxel. *Right panel:* Outflow mass per voxel and its KDE (red contours).

Bibliography

André, P., Men'shchikov, A., Bontemps, S., et al. 2010, Astronomy and Astrophysics, 518, L102

Arce, H., & Goodman, A. 2001, Science with the Atacama Large Millimeter Array, 99

Arzoumanian, D., André, P., Didelon, P., et al. 2011, Astronomy and Astrophysics, 529, L6

Bachiller, R., & Pérez Gutiérrez, M. 1997, Astrophysical Journal, Letters, 487, L93

Baker, J. G., & Menzel, D. H. 1938, Astrophysical Journal, 88, 52

Belloche, A., Müller, H. S. P., Menten, K. M., Schilke, P., & Comito, C. 2013, Astronomy and Astrophysics, 559, A47

Beuther, H., Schilke, P., Sridharan, T. K., et al. 2002, Astronomy and Astrophysics, 383, 892

Beuther, H., Bihr, S., Rugel, M., et al. 2016, Astronomy and Astrophysics, 595, A32

Blitz, L. 1993, Protostars and Planets III, 125

Bonfand, M., Belloche, A., Menten, K. M., et al. 2017, Astronomy and Astrophysics, 604, A60

Bonnell, I. A., Bate, M. R., & Zinnecker, H. 1998, Monthly Notices of the RAS, 298, 93

Bressert, E., Ginsburg, A., Bally, J., et al. 2012, Astrophysical Journal, Letters, 758, L28

Carroll, B., & Ostlie, D. 2014, An Introduction to Modern Astrophysics, Pearson New International Edition, ISBN 10: 1-292-02293-0, , (cit on pp. 452, 1391)

Clark, J. S., Negueruela, I., Crowther, P. A., et al. 2005, Astronomy and Astrophysics, 434, 949

Choudhury, R., Schilke, P., Stéphan, G., et al. 2015, Astronomy and Astrophysics, 575, A68

Cillié, G. G. 1936, Monthly Notices of the RAS, 96, 771

Codella, C., Bachiller, R., Benedettini, M., et al. 2005, Monthly Notices of the RAS, 361, 244

Corby, J. F., Jones, P. A., Cunningham, M. R., et al. 2015, Monthly Notices of the RAS, 452, 3969

Cortes, P. C., Girart, J. M., Hull, C. L. H., et al. 2016, Astrophysical Journal, Letters, 825, L15

De Pree, C. G., Peters, T., Mac Low, M.-M., et al. 2014, Astrophysical Journal, Letters, 781, L36

de Wit, W. J., Testi, L., Palla, F., et al. 2005, Astronomy and Astrophysics, 437, 247

Draine, B. T., & Lee, H. M. 1984, Astrophysical Journal, 285, 89

Eker, Z., Bakış, V., Bilir, S., et al. 2018, Monthly Notices of the RAS, 479, 5491

Endres, C. P., Schlemmer, S., Schilke, P., et al. 2016, Journal of Molecular Spectroscopy, 327, 95

Feddersen, J. R., Arce, H. G., Kong, S., et al. 2020, arXiv e-prints, arXiv:2004.03504

Field, G. B. 1969, Astrophysics and General Relativity, Volume 1, 59

Fischera, J., & Martin, P. G. 2012, Astronomy and Astrophysics, 542, A77

Frerking, M. A., Langer, W. D., & Wilson, R. W. 1982, Astrophysical Journal, 262, 590

Fujii, M. S. 2015, Publications of the ASJ, 67, 59

Fujii, M. S., & Portegies Zwart, S. 2016, Astrophysical Journal, 817, 4

Gaume, R. A., Claussen, M. J., de Pree, C. G., et al. 1995, Astrophysical Journal, 449, 663

Gerner, T., Beuther, H., Semenov, D., et al. 2014, Astronomy and Astrophysics, 563, A97

Gibb, A. G., Wyrowski, F., & Mundy, L. G. 2004, Astrophysical Journal, 616, 301

Ginsburg, A., Henkel, C., Ao, Y., et al. 2016, Astronomy and Astrophysics, 586, A50

Ginsburg, A., Bally, J., Barnes, A., et al. 2018, Astrophysical Journal, 853, 171

Goicoechea, J. R., Rodríguez-Fernández, N. J., & Cernicharo, J. 2004, Astrophysical Journal, 600, 214

Goldsmith, P. F., Snell, R. L., Hemeon-Heyer, M., et al. 1984, Astrophysical Journal, 286, 599

Goldsmith, P. F., Lis, D. C., Hills, R., & Lasenby, J. 1990, Astrophysical Journal, 350, 186

Goldsmith, P. F., & Langer, W. D. 1999, Astrophysical Journal, 517, 209

Gravity Collaboration, Abuter, R., Amorim, A., et al. 2018, Astronomy and Astrophysics, 615, L15

Gusdorf, A., Cabrit, S., Flower, D. R., et al. 2008, Astronomy and Astrophysics, 482, 809

Hacar, A., Tafalla, M., Forbrich, J., et al. 2018, Astronomy and Astrophysics, 610, A77

Higuchi, A. E., Hasegawa, T., Saigo, K., et al. 2015, Astrophysical Journal, 815, 106

Hollenbach, D., Johnstone, D., Lizano, S., et al. 1994, Astrophysical Journal, 428, 654

Houghton, H. E. 1942, Monthly Notes of the Astronomical Society of South Africa, 1, 107

Howard, C. S., Pudritz, R. E., Harris, W. E., & Sills, A. 2018, arXiv:1808.07081

Hüttemeister, S., Wilson, T. L., Mauersberger, R., et al. 1995, Astronomy and Astrophysics, 294, 667

Iben, I. 1965, Astrophysical Journal, 142, 421

Immer, K., Menten, K. M., Schuller, F., et al. 2012, Astronomy and Astrophysics, 548, A120

Izquierdo, A. F., Galván-Madrid, R., Maud, L. T., et al. 2018, Monthly Notices of the RAS, 478, 2505

Jaffe, D. T., & Martín-Pintado, J. 1999, Astrophysical Journal, 520, 162

Jiménez-Serra, I., Báez-Rubio, A., Rivilla, V. M., et al. 2013, Astrophysical Journal, Letters, 764, L4

Juárez, C., Girart, J. M., Zamora-Avilés, M., et al. 2017, Astrophysical Journal, 844, 44

Kauffmann, J., Bertoldi, F., Bourke, T. L., et al. 2008, Astronomy and Astrophysics, 487, 993

Kirk, H., Myers, P. C., Bourke, T. L., et al. 2013, Astrophysical Journal, 766, 115

Klessen, R. S., Ballesteros-Paredes, J., Li, Y., et al. 2004, The Formation and Evolution of Massive Young Star Clusters, 299

Klessen, R. S., & Glover, S. C. O. 2016, Saas-Fee Advanced Course, 43, 85

Koch, P. M., Tang, Y.-W., Ho, P. T. P., et al. 2018, Astrophysical Journal, 855, 39

Kong, S., Arce, H. G., Feddersen, J. R., et al. 2018, Astrophysical Journal, Supplement, 236, 25

Kroupa, P. 2001, Monthly Notices of the RAS, 322, 231

Kurtz, S. 2005, Massive Star Birth: A Crossroads of Astrophysics, 111

Kurtz, S., Cesaroni, R., Churchwell, E., et al. 2000, Protostars and Planets IV, 299

Lada, C. J., & Lada, E. A. 2003, Annual Review of Astron and Astrophys, 41, 57

Leroy, A. K., Bolatto, A. D., Ostriker, E. C., et al. 2018, Astrophysical Journal, 869, 126

Lindroos, L., Knudsen, K. K., Vlemmings, W., Conway, J., & Martí-Vidal, I. 2015, Monthly Notices of the RAS, 446, 3502

Longmore, S. N., Rathborne, J., Bastian, N., et al. 2012, Astrophysical Journal, 746, 117

Longmore, S. N., Kruijssen, J. M. D., Bastian, N., et al. 2014, Protostars and Planets VI, 291

Loomis, R. A., Öberg, K. I., Andrews, S. M., et al. 2018, Astronomical Journal, 155, 182

López-Sepulcre, A., Codella, C., Cesaroni, R., et al. 2009, Astronomy and Astrophysics, 499, 811

López-Sepulcre, A., Cesaroni, R., & Walmsley, C. M. 2010, Astronomy and Astrophysics, 517, A66

Lu, X., Zhang, Q., Liu, H. B., et al. 2018, Astrophysical Journal, 855, 9

Marsh, K. A., Kirk, J. M., André, P., et al. 2016, Monthly Notices of the RAS, 459, 342

Martin-Pintado, J., Bachiller, R., Thum, C., et al. 1989, Astronomy and Astrophysics, 215, L13

Mathis, J. S., Rumpl, W., & Nordsieck, K. H. 1977, Astrophysical Journal, 217, 425

Maud, L. T., Hoare, M. G., Galván-Madrid, R., et al. 2017, Monthly Notices of the RAS, 467, L120

McKee, C. F., & Ostriker, J. P. 1977, Astrophysical Journal, 218, 148

McMullin, J. P., Waters, B., Schiebel, D., et al. 2007, Astronomical Data Analysis Software and Systems XVI, 127

Mehringer, D. M., Palmer, P., Goss, W. M., et al. 1993, Astrophysical Journal, 412, 684

Meng, F., Sánchez-Monge, Á., Schilke, P., et al. 2019, Astronomy and Astrophysics, 630, A73

Mills, E. A. C., Ginsburg, A., Clements, A. R., et al. 2018, Astrophysical Journal, Letters, 869, L14

Molinari, S., Abergel, A., Rivera-Ingraham, A., et al. 2010, 38th COSPAR Scientific Assembly, 2

Möller, T., Endres, C., & Schilke, P. 2017, Astronomy and Astrophysics, 598, A7

Morris, M., & Serabyn, E. 1996, Annual Review of Astron and Astrophys, 34, 645

Müller, H. S. P., Schlöder, F., Stutzki, J., et al. 2005, Journal of Molecular Structure, 742, 215

Nakamura, F., & Li, Z.-Y. 2008, Astrophysical Journal, 687, 354

Neill, J. L., Bergin, E. A., Lis, D. C., et al. 2014, Astrophysical Journal, 789, 8

Nisini, B., Codella, C., Giannini, T., et al. 2007, Astronomy and Astrophysics, 462, 163

Ossenkopf, V., & Henning, T. 1994, Astronomy and Astrophysics, 291, 943

Ostriker, J. 1964, Astrophysical Journal, 140, 1529

Palau, A., Fuente, A., Girart, J. M., et al. 2011, Astrophysical Journal, Letters, 743, L32

Palau, A., Walsh, C., Sánchez-Monge, Á., et al. 2017, Monthly Notices of the RAS, 467, 2723

Palmeirim, P., André, P., Kirk, J., et al. 2013, Astronomy and Astrophysics, 550, A38

Peretto, N., Fuller, G. A., Duarte-Cabral, A., et al. 2013, Astronomy and Astrophysics, 555, A112

Pfalzner, S., & Kaczmarek, T. 2013, Astronomy and Astrophysics, 559, A38

Pickett, H. M., Poynter, R. L., Cohen, E. A., et al. 1998, Journal of Quantitative Spectroscopy and Radiative Transfer, 60, 883

Pineau des Forets, G., Roueff, E., Schilke, P., et al. 1993, Monthly Notices of the RAS, 262, 915

Pols, S., Schwörer, A., Schilke, P., et al. 2018, Astronomy and Astrophysics, 614, A123 (Paper III)

Portegies Zwart, S. F., McMillan, S. L. W., & Gieles, M. 2010, Annual Review of Astron and Astrophys, 48, 431

Pudritz, R. E., & Kevlahan, N. K.-R. 2013, Philosophical Transactions of the Royal Society of London Series A, 371, 20120248

Qin, S.-L., Schilke, P., Rolffs, R., et al. 2011, Astronomy and Astrophysics, 530, L9

Rathborne, J. M., Longmore, S. N., Jackson, J. M., et al. 2014, Astrophysical Journal, 786, 140

Reid, M. J., Menten, K. M., Brunthaler, A., et al. 2014, Astrophysical Journal, 783, 130

Sánchez-Monge, Á. (2011), "Massive star formation - ionized and molecular gas in the first evolutionary stages", PhD thesis, department d'astronomia i meteorologia, universitat de barcelona, sanchez@ph1.uni-koeln.de (cit. on pp. 3 , 234)

Sánchez-Monge, Á., López-Sepulcre, A., Cesaroni, R., et al. 2013a, Astronomy and Astrophysics, 557, A94

Sánchez-Monge, Á., Kurtz, S., Palau, A., et al. 2013b, Astrophysical Journal, 766, 114

Sánchez-Monge, Á., Beltrán, M. T., Cesaroni, R., et al. 2014, Astronomy and Astrophysics, 569, A11

Sánchez-Monge, Á., Schilke, P., Schmiedeke, A., et al. 2017, Astronomy and Astrophysics, 604, A6

Seifried, D., & Walch, S. 2015, Monthly Notices of the RAS, 452, 2410

Schilke, P., Walmsley, C. M., Pineau des Forets, G., et al. 1997, Astronomy and Astrophysics, 321, 293

Schilke, P. 2015, EAS Publications Series, 227

Schmiedeke, A., Schilke, P., Möller, T., et al. 2016, Astronomy and Astrophysics, 588, A143

Schmiedeke, A. (2017), "Radiative transfer modeling of Sagittarius B2", PhD thesis, I. Physikalisches Institut der Universität zu Köln, Zülpicher Straße 77, 50937, Köln, Germany, schmiedeke@ph1.uni-koeln.de (cit. on pp. 24 , 123)

Suri, S., Sánchez-Monge, Á., Schilke, P., et al. 2019, Astronomy and Astrophysics, 623, A142

Takagi, S., Murakami, H., & Koyama, K. 2002, 8th Asian-pacific Regional Meeting, Volume II, 215

Tan, J. C., & McKee, C. F. 2002, Hot Star Workshop III: The Earliest Phases of Massive Star Birth, 267

Tan, J. C., Beltrán, M. T., Caselli, P., et al. 2014, Protostars and Planets VI, 149

Tang, Y.-W., Koch, P. M., Peretto, N., et al. 2019, Astrophysical Journal, 878, 10

Thompson, A. R., Moran, J. M., & Swenson, G. W. 2017, Interferometry and Synthesis in Radio Astronomy

Thorwirth, S., Müller, H. S. P., Roth, D. A., et al. 2000, Young European Radio Astronomers' Conference (YERAC), 56

Tielens, A. , G., G., M. 2005, The physics and chemistry of the interstellar medium, Cambridge University Press , ISBN: 0-521-82634-9, (cit on pp. 22, 495)

Tomisaka, K. 1998, Astrophysical Journal, Letters, 502, L163

Treviño-Morales, S. P., Fuente, A., Sánchez-Monge, Á., et al. 2019, Astronomy and Astrophysics, 629, A81

Wakelam, V., Castets, A., Ceccarelli, C., et al. 2004, Astronomy and Astrophysics, 413, 609

Walker, D. L., Longmore, S. N., Bastian, N., et al. 2015, Monthly Notices of the RAS, 449, 715

Walker, D. L., Longmore, S. N., Bastian, N., et al. 2016, Monthly Notices of the RAS, 457, 4536

Ward-Thompson, D., & Whitworth, A.P. 2011, An Introduction to Star Formation, Cambridge University Press , ISBN: 9780511974021

Williams, D., & Viti, S. 2014, Observational Molecular Astronomy, Cambridge University Pres, ISBN: 978-1-107-01816-7

Wilson, T. L., Rohlfs, K., & Hüttemeister, S. 2009, Tools of Radio Astronomy, by Thomas L. Wilson; Kristen Rohlfs and Susanne Hüttemeister. ISBN 978-3-540-85121-9. Published by Springer-Verlag, Berlin, Germany, 2009.,

Wu, Y., Wei, Y., Zhao, M., et al. 2004, Astronomy and Astrophysics, 426, 503

Zhang, A. C., Li, Y., Chen, J. N., et al. 2016, 79th Annual Meeting of the Meteoritical Society, 6002

Erklärung

Hiermit versichere ich an Eides statt, dass ich die vorliegende Dissertation selbstständig und ohne die Benutzung anderer als der angegebenen Hilfsmittel und Literatur angefertigt habe. Alle Stellen, die wörtlich oder sinngemäß aus veröffentlichten und nicht veröffentlichten Werken dem Wortlaut oder dem Sinn nach entnommen wurden, sind als solche kenntlich gemacht. Ich versichere an Eides statt, dass diese Dissertation noch keiner anderen Fakultät oder Universität zur Prüfung vorgelegen hat; dass sie - abgesehen von unten angegebenen Teilpublikationen und eingebundenen Artikeln und Manuskripten - noch nicht veröffentlicht worden ist sowie, dass ich eine Veröffentlichung der Dissertation vor Abschluss der Promotion nicht ohne Genehmigung des Promotionsausschusses vornehmen werde. Die Bestimmungen dieser Ordnung sind mir bekannt. Darüber hinaus erkläre ich hiermit, dass ich die Ordnung zur Sicherung guter wissenschaftlicher Praxis und zum Umgang mit wissenschaftlichem Fehlverhalten der Universität zu Köln gelesen und sie bei der Durchführung der Dissertation zugrundeliegenden Arbeiten und der schriftlich verfassten Dissertation beachtet habe und verpflichte mich hiermit, die dort genannten Vorgaben bei allen wissenschaftlichen Tätigkeiten zu beachten und umzusetzen. Ich versichere, dass die eingereichte elektronische Fassung der eingereichten Druckfassung vollständig entspricht.

Teilpublikation:

The physical and chemical structure of Sagittarius B2. IV. Converging filaments in the high-mass cluster forming region Sgr B2(N)

***Schwörer, A.**; Sánchez-Monge, Á.; Schilke, P.; Möller, T.; Ginsburg, A.; Meng, F.; Schmiedeke, A.; Müller, H. S. P.; Lis, D.; Qin, S. -L.; 2019, Astronomy and Astrophysics, 628, A6*

Köln, 12.07.2020: 

Andreas Stefan Schwörer

Acknowledgement

This work was supported by the Deutsche Forschungsgemeinschaft (DFG) through grant Collaborative Research Centre 956 (subproject A6 and C3, project ID 184018867) and from BMBF/Verbundforschung through the projects ALMA-ARC 05A11PK3 and 05A14PK1. This thesis makes use of the following ALMA data: ADS/JAO.ALMA#2013.1.00332.S and ALMA#2016.1.00550.S. ALMA is a partnership of ESO (representing its member states), NSF (USA) and NINS (Japan), together with NRC (Canada) and NSC and ASIAA (Taiwan) and KASI (Republic of Korea), in cooperation with the Republic of Chile. The Joint ALMA Observatory is operated by ESO, AUI/NRAO and NAOJ. In order to do the analysis and plots, I used the python packages `scipy`, `numpy`, `pandas`, `matplotlib`, `astropy`, `aplpy`, `seaborn` and `pwlf`.

After the formal acknowledgment, a few more personal words: Dear Peter and dear Álvaro, thank you both so much for supervising me in the past years. If someone had told me before we met that I will have once a Ph.D. in astrophysics, I would have shacked my head in disbelieve. Dear Peter, you asked me 4 years ago if I want to join your group. I changed all the plans I had and today I am sure it was the right, yes, the best decision! You gave me the opportunity to learn so many new things and to gain experiences that have broaden my horizon a lot. I also appreciated your constant support to participate on workshops and conferences, even if far distant. I am very grateful! Dear Álvaro, a simple 'muchas gracias' or 'moltes grácies' is not fair in light of your support. You fulfilled so many roles in all this years: supervisor, colleague, gildas expert, good friend, yes, you even became my (academic) big brother. I admire how you answered all my questions, even the stupid or repetitive ones, patiently and always comprehensibly. I may forget at some point the astrophysical knowledge that you taught, but I will never forget your selfless dedication and (science) idealism. Thank you so much! From my big brother, to my little bro: Fanyi, I thank you for all the coffee breaks, your interesting stories (not the ones about Feynman), the equations which you derived for my practical courses, and of course, thank you for our unforgettable journey through Japan. I will also always remember your hospitality in Peking, an amazing city by the way, and your passion for food (e.g., Lammhaxe). I wish you and your young family all the best! This list is not complete without mentioning my other office mates, our charming ladies Mahya and Sü. Thanks you so much for all the funny moments, serious mouse calls and gymnastic exercises. The past years

with you were thoroughly wonderful! Also thank you for the nice atmosphere to all the other group members: Thomas, Anika, Stefan, Dirk, Liem, Nassim, Mitra, Flavia, Roja, Niraj, Tiwanwei, Veena, Claudia, Wiebke and Kai. The internationality of our group was really outstanding and I enjoyed all the inspiring discussions. A big thank you goes out to Adam for sharing generously the beautiful high-angular resolution data of Sgr B2 and all the helpful comments.

Ganz besonders möchte ich mich bei meinen Eltern bedanken, ohne die diese Dissertation aus so vielen verschiedenen Gründen nie möglich gewesen wäre. Liebe Mama, lieber Papa, euch ist diese Arbeit gewidmet als Dank für meine wundervolle und sorgenfreie Kindheit. Von Anfang an habt ihr stets geschaut, mich und auch meine Geschwister zu fördern und uns so vieles zu ermöglichen. Und all das ohne Druck und immer mit dem nötigen Verständnis, wenn eingeschlagene Wege doch noch einmal geändert wurden. Vielen Dank, dass ihr mich - obwohl ich gesehen habe wie schwer es euch gefallen ist - vor nun über 10 Jahren nach Köln habt ziehen lassen; der Start in eine wunderbare Studentenzeit. Es lebt sich so viel einfacher, wenn man weiß, man hat einen Ort, an dem man immer zurückkehren kann und bedingungslos geschätzt wird. Tausend Dank! Wenn ich von einer schönen Kindheit rede, seid natürlich auch ihr, liebe Elena und lieber Manuel, gemeint. Auch von euch habe ich so vieles gelernt und freue mich immer auf unser Wiedersehen in Freiburg. Ich wünsche euch und euren Lieben, Mona und Erdem, alles Gute; vor allem auch unserem jüngsten Familienmitglied, meinem Patenkind Prinzessin Zoè, die mich in den letzten 8 Monaten beim Schreiben meiner Arbeit stets bildlich angestrahlt hat. Lieber Jan, lieber Simon, auch euch möchte danken für die vergangenen Jahre, unsere zahlreichen Reisen (manchmal unter fragwürdigen hygienischen Umständen) und Feierabendbiere am Rhein. Danke für eure Ausdauer beim Anhören meiner Beschwerden und vor allem für die Bestätigung, zurecht empört zu sein. Liebe Anna, vor allem dir gilt es zu danken! Nicht nur für die zurückliegenden Corona-Monate, die ohne dich nur schwer erträglich gewesen wären, nein, für all die Jahre, in denen wir uns jetzt kennen. Danke für all deine aufbauende Worte, deinen Zuspruch, die Einladungen zu Abendessen und WG-Parties, dein Gespür in den Momenten ungefragt da zu sein, in denen man dich dringend braucht, die unbeschwerten Stunden, die Urlaube in Holland oder Belgien und noch so vieles mehr.

Euch allen,

Vielen Dank • moltes gràcies • 谢谢 • ممنون خیلی • çok teşekkürler • cảm ơn nhiều • muito obrigado • மிக்க நன்றி

Astrophysical units and physical constants

symbol	value	unit	description
c	2.99792458×10^{10}	cm s^{-1}	speed of light in vacuum
h	6.62607015e-27	erg s	Planck constant
k_B	1.380649×10^{-16}	erg K^{-1}	Boltzmann constant
σ	5.67×10^{-5}	erg cm^{-2} s^{-1} K^{-4}	Stefan-Boltzmann constant
G	6.67430×10^{-8}	dyn cm^2 g^{-2}	gravitational constant
m_H	1.6733×10^{-24}	g	mass of hydrogen
$M_\odot$	1.98847×10^{33}	g	solar mass
$L_\odot$	3.839×10^{33}	erg s^{-1}	solar luminosity
Jy	10^{-23}	erg s^{-1} cm^{-2} Hz^{-1}	Jansky
$''$	1/60	$'$ arcmin	arcsecond
	1/3600	$^\circ$ (degree)	
au	1.49598073×10^{13}	cm	astronomical unit
pc	1 au/tan(1$''$)≈206265	au	parsec

Note. The values are taken from CASA/NRAO and listed in the cgs-system.

A

The line stacking method - Add on

For a description of the line stacking method see chapter 5. While this chapter focuses on the accuracy of the obtained parameter velocity, the appendix includes the same analysis for the parameter linewidth v_{width}. The number of required transitions in order to get a reliable result rely on the present conditions, for instance how strong the transitions are blended. In my setup, I use a synthetic spectrum of C_2H_3CN with two components and stack different numbers of transitions, between 2 and 101. To each sub-spectrum I add noise of 4 K as well as Gaussians (simulating blending lines) with random amplitudes between 4 K and 97 K, which corresponds to an intensity 1.2 times higher than the maximum amplitude in the synthetic spectrum ('relative line intensity'). As already mentioned in section 5.2, the amplitudes of the added Gaussians are randomly but also uniformly distributed. However, in observations, the intensity distribution of blending lines seems to follow a power law function with an exponent of -1, as shown within this appendix (see Fig. A.3). Therefore, the result of my simulations must be understood as an extreme case and an upper limit. The total number of added Gaussians has been fixed to 20, which corresponds to 50 lines per GHz, a line density also found in previous studies for Sgr B2(N) (Sánchez-Monge et al. 2017). The resulting linewidths are determined by fitting Gaussians and presented in Fig. A.1 and A.2 and listed in Table. A.1. For comp II , the fidelity of the linewidth drops below 1 σ for 13 transitions (3 σ for 18 transitions) and converges to the input value. For comp I, the weaker transition with lower intensity, 26 transitions are required to stack until the standard deviation drops below 3 σ.

Table A.1: Obtained linewidths for different number of stacked transitions.

no. trans[a]	lines per GHz[(d)]	component I			component II		
		v_{width}[b] [km s^{-1}] 5 km s^{-1}	$\mid \Delta v_{width} \mid$[c] [km s^{-1}] mean	$\mid \Delta v_{width} \mid$[c] [km s^{-1}] median	v_{width}[b] [km s^{-1}] 2 km s^{-1}	$\mid \Delta v_{width} \mid$[c] [km s^{-1}] mean	$\mid \Delta v_{width} \mid$[c] [km s^{-1}] median
2	50	3.82±1.29	2.25±0.86	2.11±0.86	4.05±1.79	2.25±1.73	1.47±1.73
3	50	4.64±2.37	2.72±1.95	2.36±1.95	3.23±5.98	2.57±5.87	1.22±5.87
4	50	4.62±3.15	2.55±2.88	2.15±2.88	4.14±2.13	2.35±2.07	1.08±2.07
5	50	4.49±2.11	2.54±1.7	2.13±1.7	4.03±1.72	2.33±1.62	1.19±1.62
6	50	4.87±2.1	2.52±1.68	1.82±1.68	3.73±1.42	1.89±1.37	0.71±1.37
7	50	5.02±2.23	2.57±1.82	1.89±1.82	3.76±1.4	1.84±1.38	0.65±1.38
8	50	5.61±3.3	2.81±3.0	1.85±3.0	3.54±1.48	1.71±1.44	0.47±1.44
9	50	5.08±2.24	2.37±1.9	1.66±1.9	3.42±2.45	1.9±2.37	0.47±2.37
10	50	5.48±2.46	2.72±2.07	1.66±2.07	2.9±0.95	1.08±0.9	0.35±0.9
11	50	5.66±3.91	2.95±3.64	1.66±3.64	3.24±1.32	1.41±1.28	0.38±1.28
12	50	5.5±2.1	2.41±1.74	1.59±1.74	3.06±1.07	1.18±1.04	0.32±1.04
13	50	5.31±1.85	2.31±1.46	1.48±1.46	3.04±1.34	1.17±1.32	0.34±1.32
14	50	5.36±1.87	2.29±1.49	1.51±1.49	3.02±2.37	1.14±2.36	0.31±2.36
15	50	6.17±2.67	2.73±2.37	1.5±2.37	2.58±0.8	0.73±0.77	0.24±0.77
16	50	5.73±2.82	2.31±2.6	1.28±2.6	2.59±0.74	0.75±0.71	0.28±0.71
17	50	5.68±1.98	2.27±1.65	1.29±1.65	2.6±0.81	0.74±0.78	0.24±0.78
18	50	5.98±2.56	2.36±2.33	1.31±2.33	2.38±0.54	0.52±0.51	0.22±0.51
19	50	5.66±1.77	2.08±1.47	1.26±1.47	2.55±0.83	0.65±0.81	0.24±0.81
20	50	5.29±1.46	1.83±1.15	1.15±1.15	2.45±0.93	0.59±0.91	0.21±0.91
23	50	5.3±1.65	1.77±1.39	1.04±1.39	2.41±0.6	0.51±0.58	0.19±0.58
26	50	5.14±1.35	1.54±1.11	1.04±1.11	2.26±0.33	0.35±0.31	0.19±0.31
29	50	5.52±1.57	1.73±1.34	1.06±1.34	2.19±0.36	0.29±0.34	0.16±0.34
32	50	5.63±1.66	1.84±1.42	0.97±1.42	2.17±0.24	0.26±0.22	0.17±0.22
35	50	5.5±1.37	1.47±1.18	0.81±1.18	2.15±0.26	0.24±0.24	0.15±0.24
38	50	5.4±1.26	1.38±1.07	0.75±1.07	2.18±0.26	0.26±0.24	0.16±0.24
41	50	5.44±1.29	1.4±1.11	0.81±1.11	2.13±0.13	0.2±0.11	0.13±0.11
44	50	5.24±1.11	1.15±0.96	0.77±0.96	2.15±0.19	0.21±0.18	0.14±0.18
47	50	5.29±1.2	1.22±1.05	0.72±1.05	2.12±0.12	0.19±0.09	0.14±0.09
50	50	5.1±0.94	1.0±0.8	0.62±0.8	2.11±0.11	0.17±0.08	0.13±0.08
53	50	5.11±0.98	1.05±0.83	0.68±0.83	2.11±0.11	0.17±0.09	0.12±0.09
56	50	5.19±1.06	1.07±0.93	0.66±0.93	2.11±0.09	0.17±0.07	0.13±0.07
59	50	5.01±0.79	0.97±0.63	0.71±0.63	2.11±0.09	0.15±0.07	0.11±0.07
62	50	5.06±0.8	0.89±0.67	0.63±0.67	2.12±0.09	0.15±0.07	0.11±0.07
65	50	5.0±0.69	0.86±0.54	0.61±0.54	2.13±0.09	0.17±0.07	0.13±0.07
68	50	4.97±0.58	0.75±0.44	0.58±0.44	2.13±0.09	0.16±0.07	0.12±0.07
71	50	5.07±0.88	0.91±0.75	0.59±0.75	2.13±0.09	0.16±0.07	0.12±0.07
74	50	4.97±0.76	0.85±0.63	0.57±0.63	2.12±0.08	0.16±0.07	0.13±0.07
77	50	4.92±0.52	0.69±0.39	0.54±0.39	2.12±0.08	0.15±0.06	0.12±0.06
80	50	4.88±0.58	0.7±0.46	0.54±0.46	2.11±0.07	0.14±0.06	0.1±0.06
83	50	4.91±0.53	0.67±0.41	0.52±0.41	2.13±0.08	0.15±0.06	0.13±0.06
86	50	4.99±0.6	0.72±0.47	0.5±0.47	2.12±0.08	0.15±0.06	0.13±0.06
89	50	4.98±0.5	0.69±0.36	0.54±0.36	2.12±0.07	0.15±0.06	0.13±0.06
92	50	4.88±0.46	0.67±0.33	0.52±0.33	2.12±0.07	0.14±0.06	0.11±0.06
95	50	4.96±0.51	0.67±0.38	0.52±0.38	2.13±0.07	0.15±0.06	0.12±0.06
98	50	4.94±0.56	0.65±0.45	0.55±0.45	2.11±0.06	0.13±0.05	0.1±0.05
101	50	4.84±0.41	0.62±0.29	0.53±0.29	2.12±0.07	0.14±0.06	0.12±0.06

Notes. [(a)] Number of stacked transitions. [(b)] v_{width} indicates the by the line stacking method obtained linewidth. The listed values are the mean of all 150 iterations per bunch of stacked transitions. The error is the related standard deviation of all iterations per bunch of stacked transitions. [(c)] $\mid \Delta v_{width} \mid$ indicates the absolute difference between the expected value (5 km s^{-1}/−2 km s^{-1}) and by the line stacking method obtained value. The listed values are the mean/median of all 150 iterations per bunch of stacked transitions. [(d)] To the synthetic spectrum of each transitions Gaussians with random amplitudes and linewidths at random velocities have been added (see sec. xx). 50 lines per GHz, corresponds to 20 Gaussians in the selected velocity range.

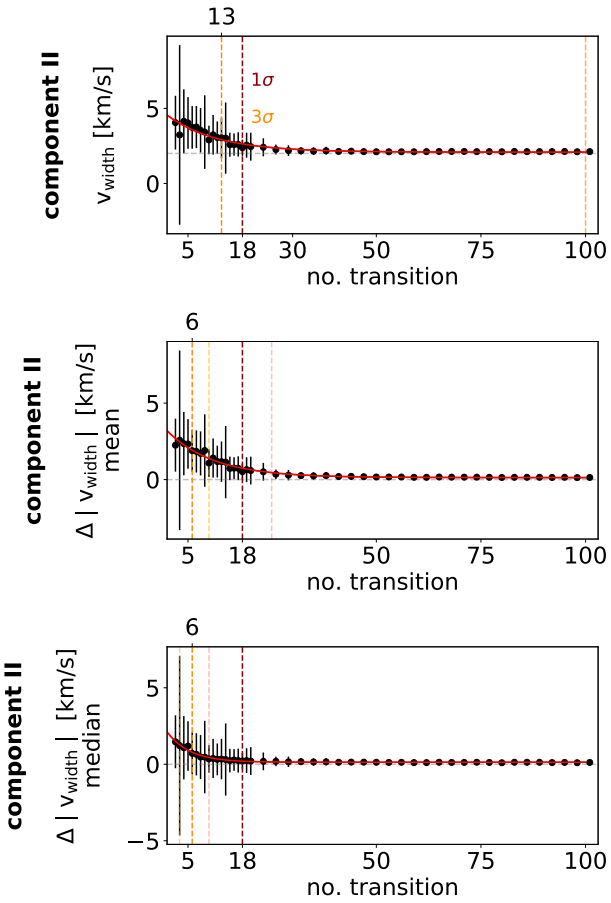

Figure A.1: Visualization of Table A.1. The by the line stacking method obtained linewidth converges to the input width of 2 km s^{-1}. The red and orange dashed lines indicate, where the standard deviation (error) of the measured linewidth drops below 1 or 3 σ. The transparent lines show where the obtained linewidth deviates less than 1 and 3 σ.

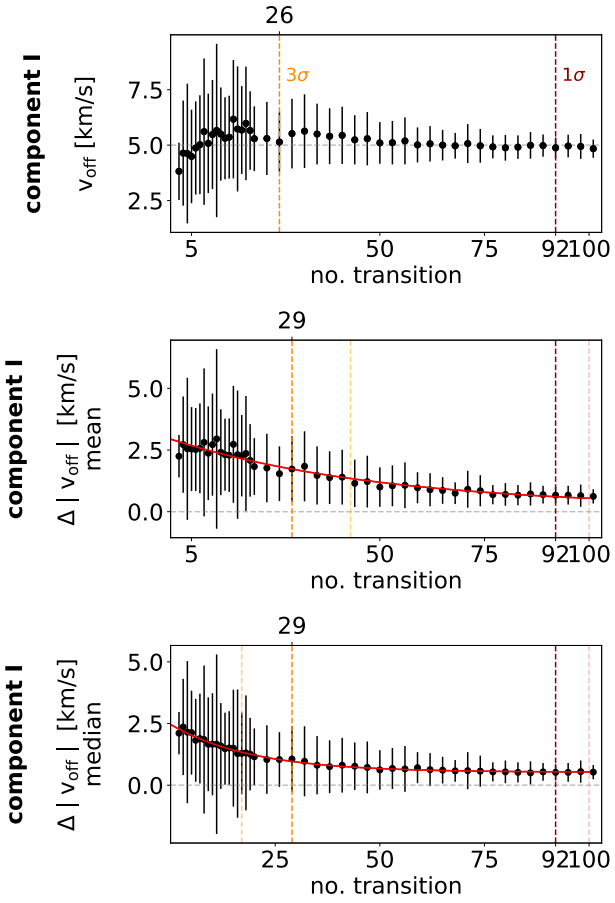

Figure A.2: Same like Fig. A.1 for component I.

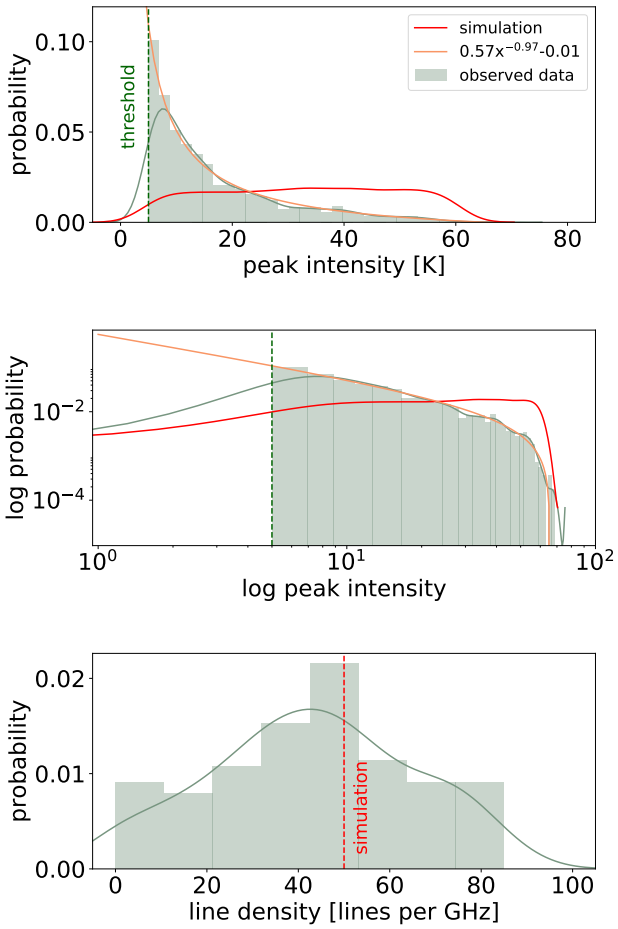

Figure A.3: *Top panel:* Distribution of the peak intensities of the neighboring lines surrounding 165 transitions of C_2H_3CN within a velocity range of -50 to 50 km s^{-1}. The spectrum has been extracted in Sgr B2(N) at a position with coordinates α(J2000)=$17^h47^m19^s.89$, δ(J2000)=$-28°22'20''.38$. The red line indicates the random and uniform distribution of blending lines used for my simulations in section 5.2. The orange line show a power law fit of the observed distribution. *Middle panel:* Same like top panel in logarithmic scale. *Bottom panel:* The histogram and KDE show the distribution of the number of blending lines surrounding 165 transitions of C_2H_3CN. To assume a line density of 50 lines per GHz in my simulation seems to be reasonable.

B

Sagittarius B2 North - Add on

Additional material concerning filament properties are presented in section B.1. I also overlay the emission maps of data-set II with the path of the filaments identified in data-set I. In section B.2 I show spectra of the molecular species SiO (5–4), CO (2–1) and its isotopologues ^{13}CO and C^{18}O observed towards the outflow in Sgr B2(N). Tables of the abundance and column densities of different molecular species, as well as the spectral line parameters I made use of, are documented in section B.3. There you also find a figure concerning the SiO abundance depending on the distance to the center in Sgr B2(N).

B.1 Filament properties

In Fig. B.1 I present peak intensity maps of selected transitions of different molecular species. The path of the filaments is overlaid on all of them. The filamentary structures are clearly visible in molecular species CH_3OCHO, CH_3OCH_3, CH_3OH and $^{13}CH_3OH$. For other species such as C_2H_5CN and OCS, the bubble-shape structure dominates the emission.

Figure B.2 shows the position-velocity plots produced along the main spines of the filaments as depicted in Fig. 7.3. We have used the stacked cubes of the molecular species CH_3OCHO, CH_3OCH_3, CH_3OH and $^{13}CH_3OH$, shown in gray, green, blue and orange, respectively. The position-velocity plots are obtained following a similar approach to what is implemented in the python tool `pvextractor`, and considering an averaging width across the filament of $0\farcs4$, corresponding to the synthesized beam. Similarly, Fig. B.3 shows the position-velocity plot along filament F02, which is only visible in H_2CS.

In order to constrain the velocity properties, I fit Gaussians to the spectra along the filaments to study the variation of velocity and linewidth. In Fig. B.4, I plot the variation of the linewidth. In section 7.2.1, the variation of velocity with distance has already been presented.

In Fig. B.5 I plot the variation of mass-to-length ration along the filament. The mass has been computed for segments of 0.011 pc in length and for three different dust temperatures: 50 K, 100 K, and 300 K. Taking the 50 K case as an example, for all filaments has been found an increase of mass when approaching the center of the region. This may be due to a higher mass content in the inner regions of the filaments, or alternatively this can be an artifact produced by a wrong temperature assumption. If the filament is hotter in the inner regions (e.g., 6 times hotter, from 50 K to 300 K) the increase in mass towards the center is less significant, although still existing in many filaments.

In Fig. B.6 I overlay the continuum emission map and the peak intensity map of the molecular species CH_3OH of data-set II with the path of the filaments identified in data-set I. In the following figures B.7–B.9 I present the velocity trend along the filaments and check for consistency with the gradients obtained in section 7.2.1.

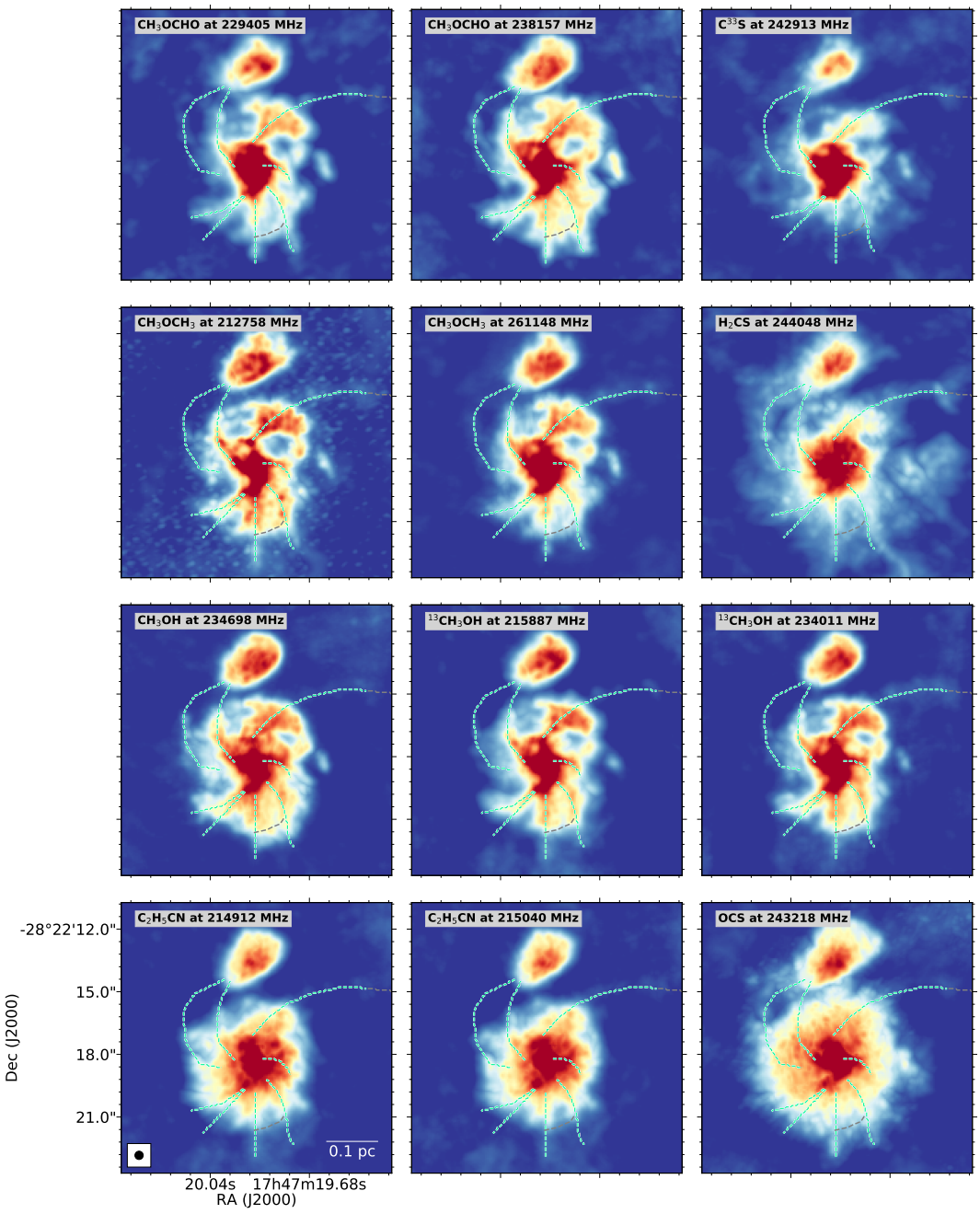

Figure B.1: Peak intensity maps of transitions of various molecular species showing either the filamenary structure or bubble shape. The green dashed lines trace the path of the filaments identified in the stacked data (see section 7.1).

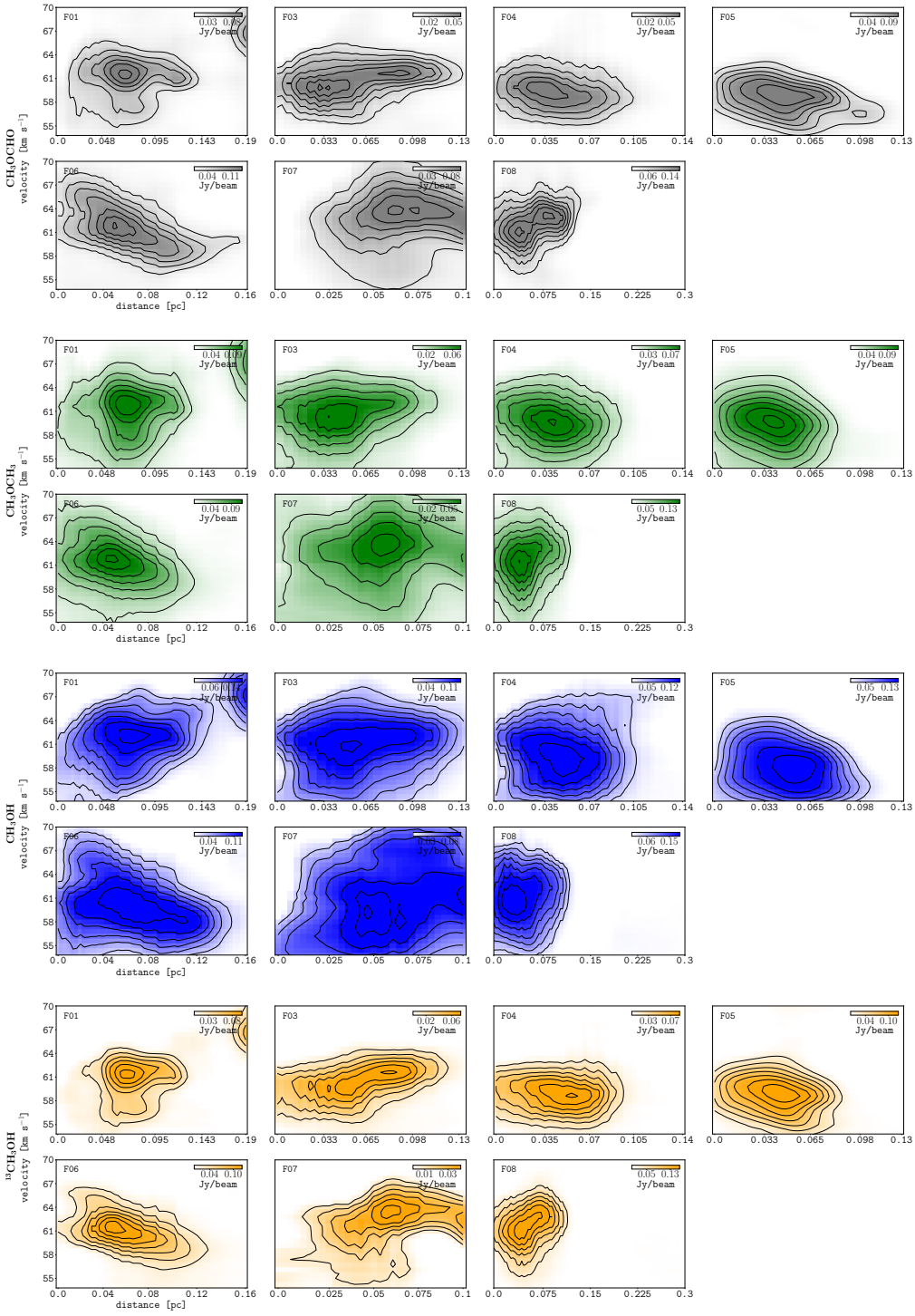

Figure B.2: Position-velocity plots along each filament, for the molecules CH_3OCHO (gray), CH_3OCH_3(green), CH_3OH (blue), and $^{13}CH_3OH$ (orange), from top to bottom.

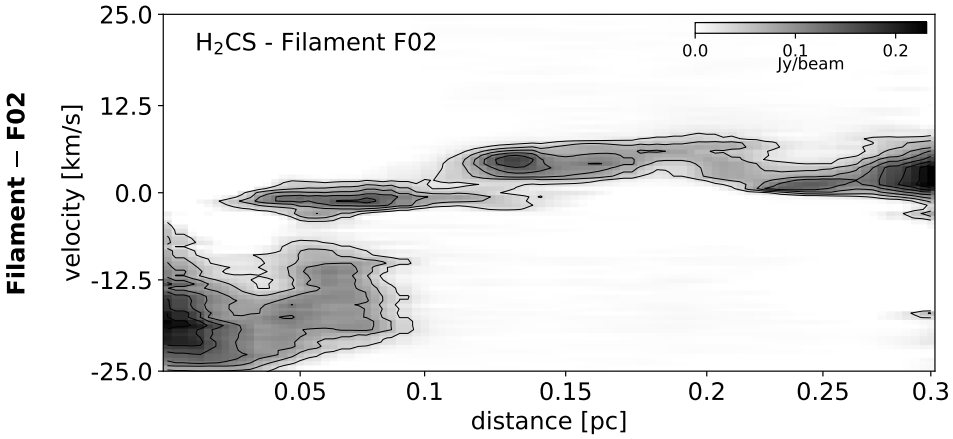

Figure B.3: Position velocity cut along filament F02 in H_2CS. The emission to the left corresponds to the filament close to the central hub. The emission at about 0.27 pc corresponds to the northern satellite core.

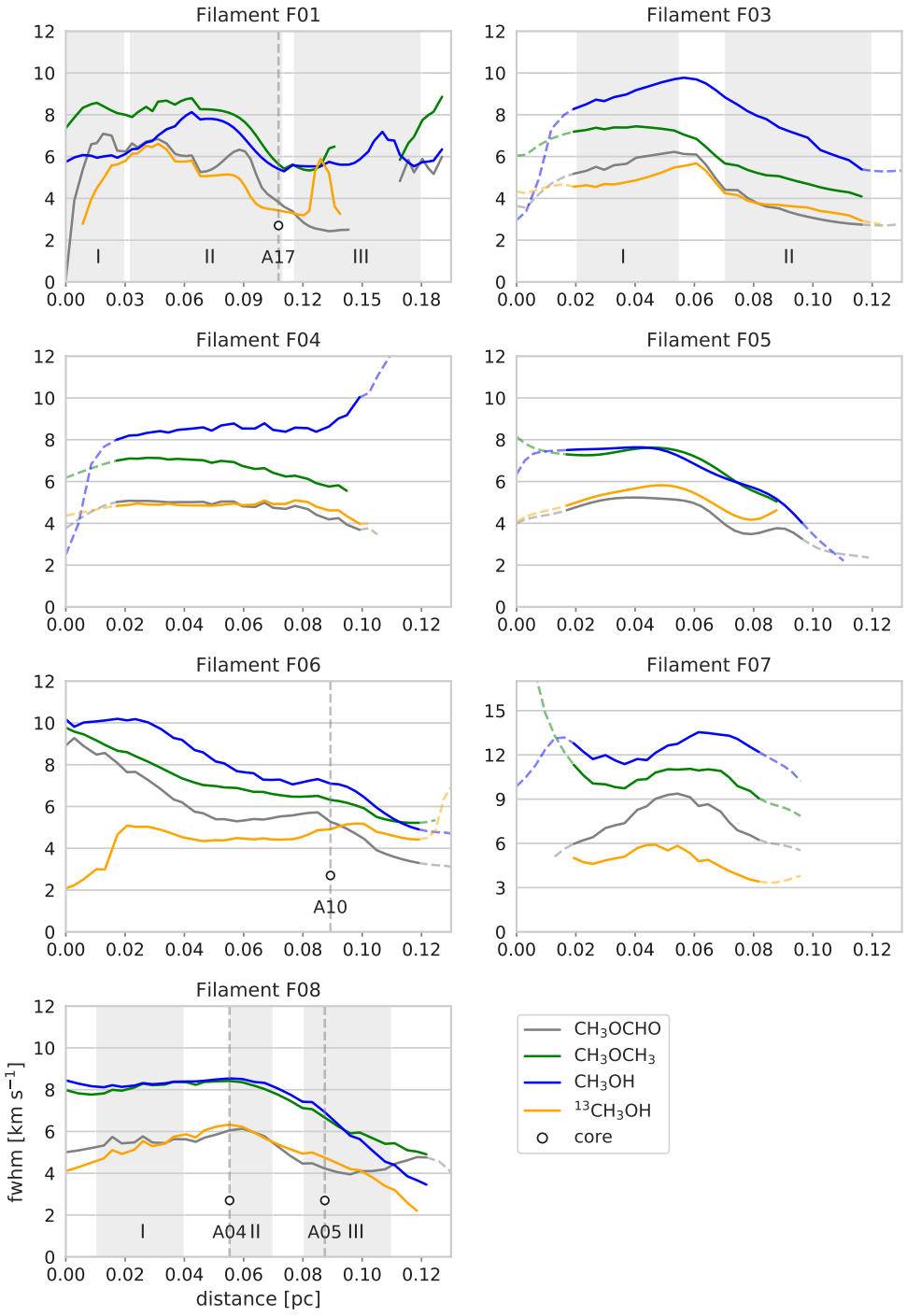

Figure B.4: Variation of the line width along the filaments. The position of the dense cores are indicated by vertical, black dashed lines. Sections where the line emission is below 4σ are plotted with dashed lines.

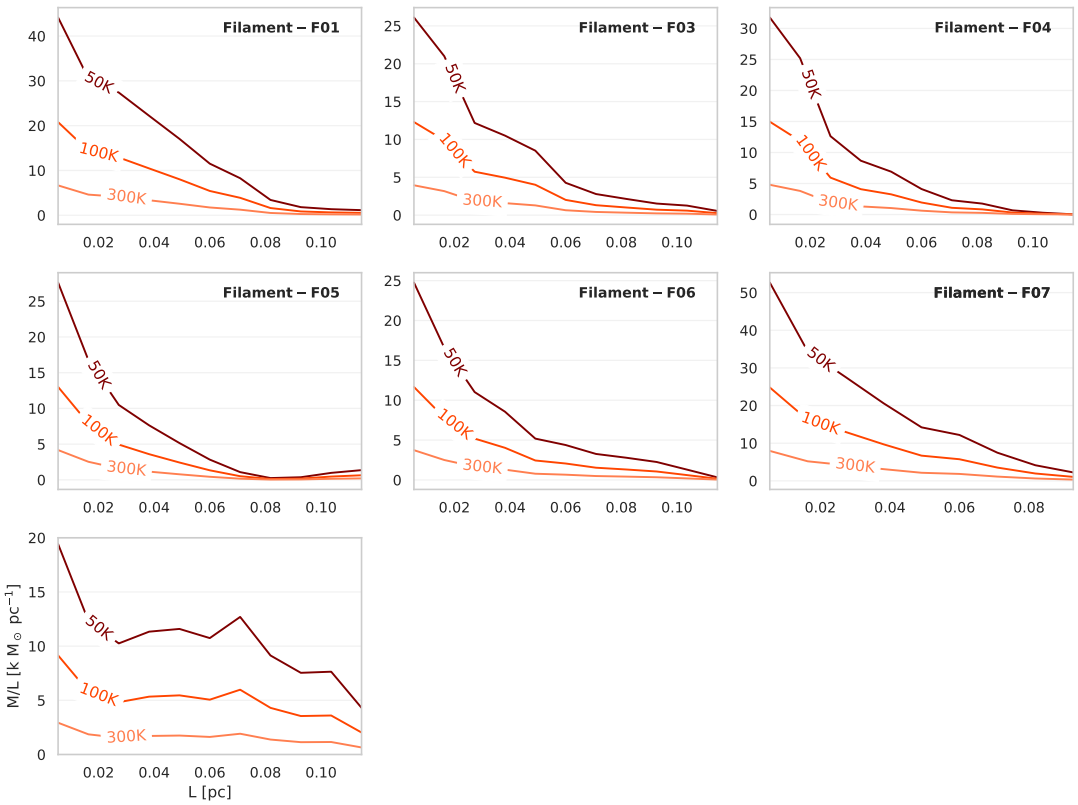

Figure B.5: Variation of mass-to-length ratio (M/L) along the filaments, computed along sections of 0.011 pc in length. The different lines correspond to different assumed temperatures: 50 K (dark), 100 K (orange) and 300 K (light orange).

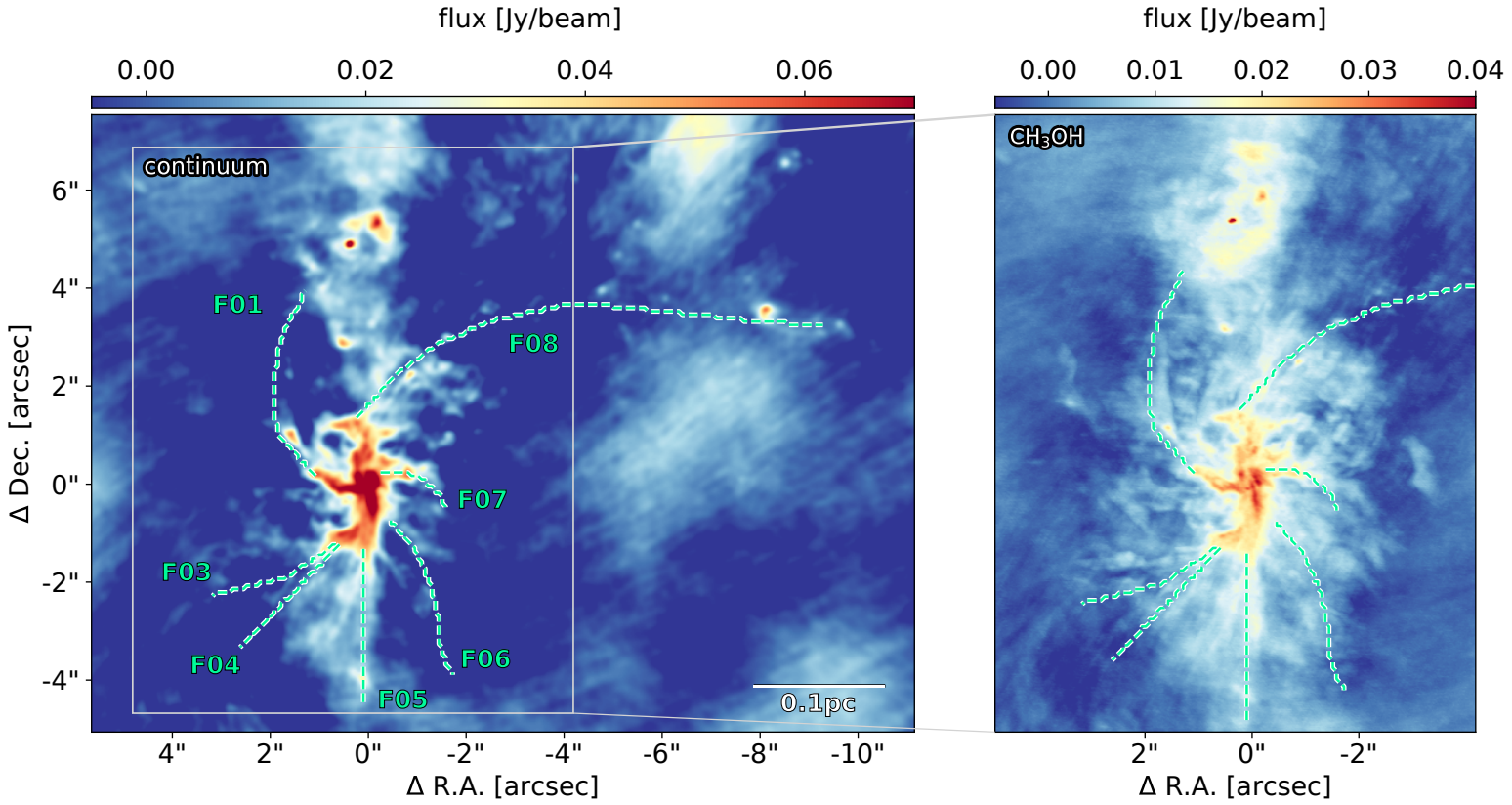

Figure B.6: *Left panel:* Map of the ALMA 220 GHz continuum emission of Sgr B2(N) in data-set II. The green dashed lines trace the path of the filaments identified in data-set I. Calibration artifacts disturbing the image (e.g., between the right ascension of $-4''$ and $-8''$). To overcome this issue it may help to clean deeper. *Right panel:* Peak intensity map of 8 stacked transitions of the molecular species CH_3OH. The velocity trend along each filament is shown in Fig. 7.8 and Fig. B.7–B.9.

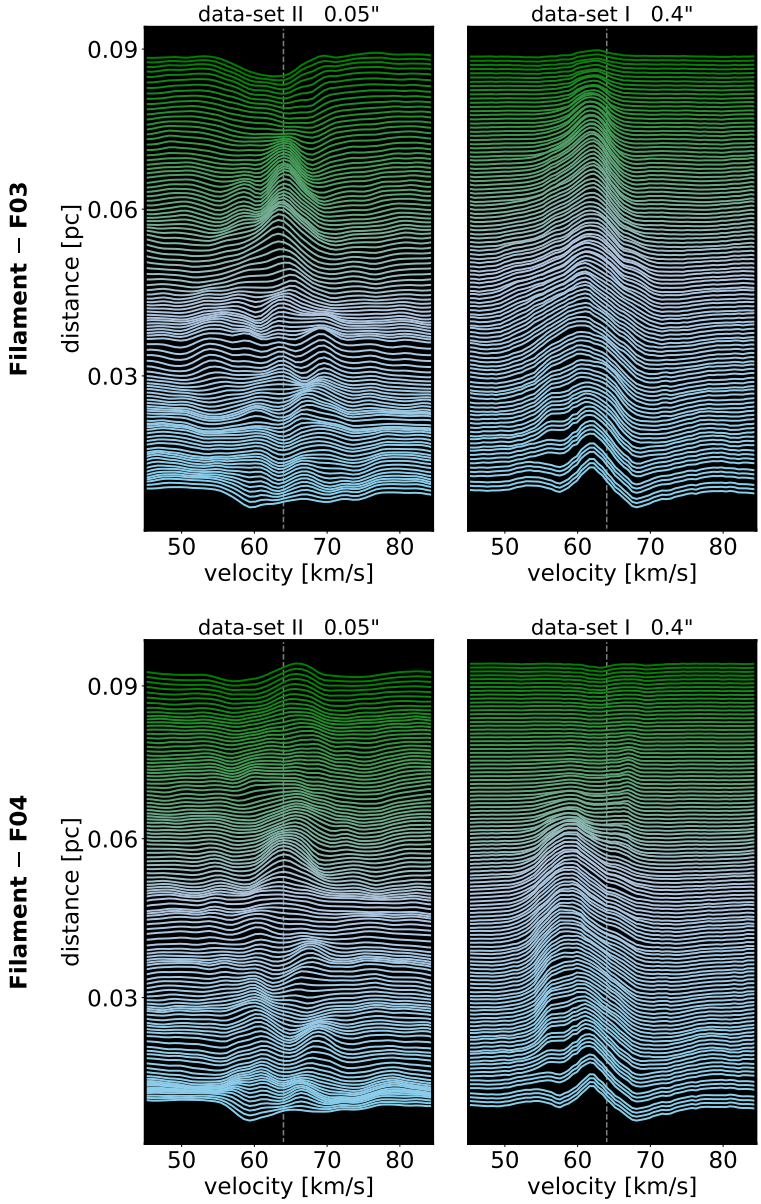

Figure B.7: Comparison of the velocity trend between both data-sets in the molecular species CH_3OH. The spectra are constructed by stacking lines (see more details in chapter 5). 8 transitions of methanol are included in data-set II and 84 transitions in data-set I, resulting in a better signal-to-noise ratio. The spectra are averaged over a region with the beam size of data-set I. The presented spectra are extracted by moving from the main hub (at 0 pc) outwards along the filaments indicated in Fig. 7.3 and equidistantly plotted on top. The thicker lines mark the core positions. The dashed vertical line indicates the source velocity at 64 km s^{-1}.

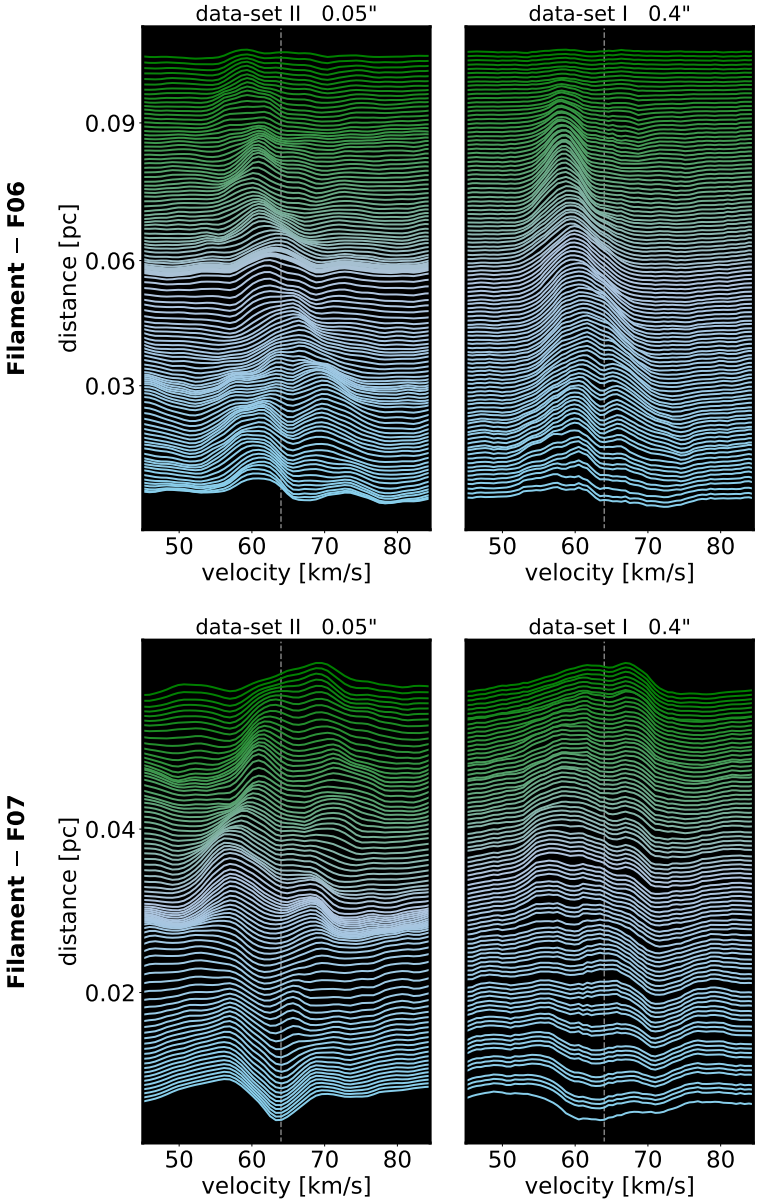

Figure B.8: Figure B.7 continued

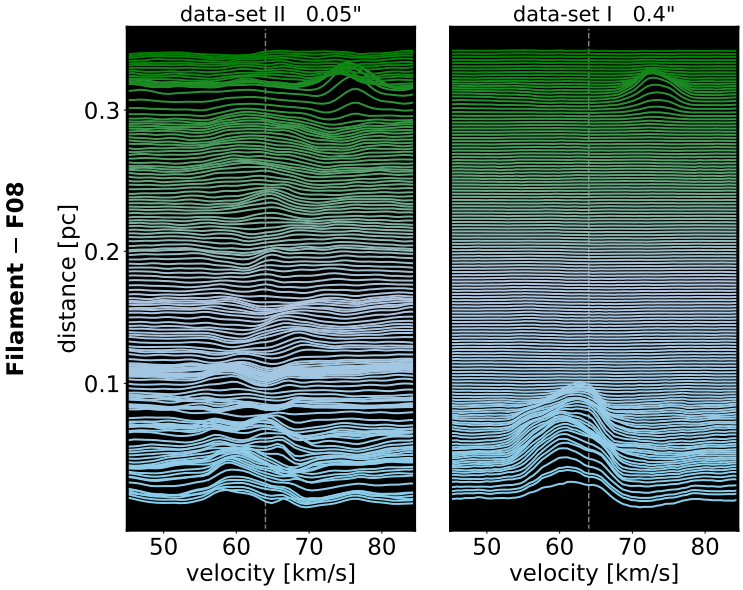

Figure B.9: Figure B.8 continued

B.2 Spectra of outflow tracers

The outflow towards Sgr B2(N) as detected in the molecular species SiO (5–4), CO (2–1) and its isotopologues ^{13}CO and C^{18}O is presented in Fig. B.10. Seven positions across the map have been selected and the extracted spectra are shown in Fig. B.11–B.14. The velocity range of the outflow is marked in blue (lower velocities with respect to the source velocity) and red (shifted to higher velocities).

In the spectra, extracted at the position D, located in the dense hub, the molecular lines of the selected species are, due to the high density, all observed in absorption, but clearly detected. The spectra, extracted at the position G towards the satellite core, are very line-rich with having also many lines in absorption. Thus, a definitive identification of weak SiO lines is difficult to achieve. The absorption feature of ^{12}CO is saturated and has a broad line shape.

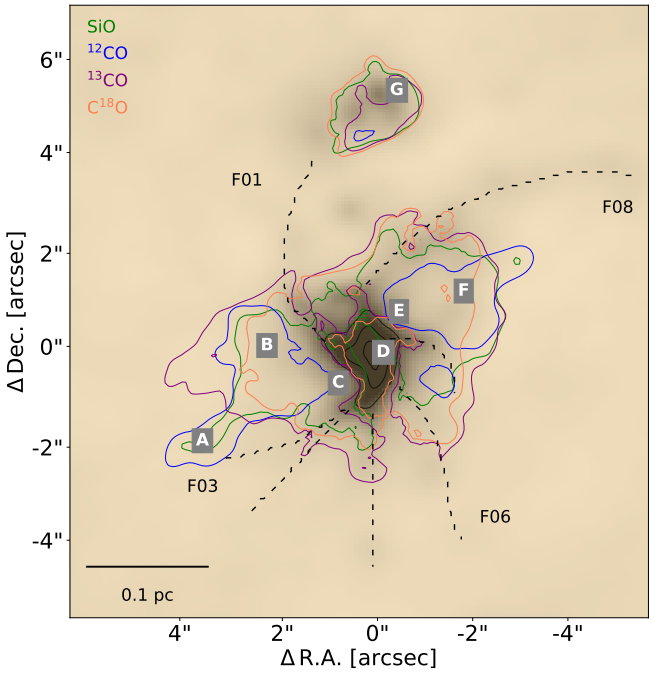

Figure B.10: The outflow towards Sgr B2(N) as detected in the molecular species SiO, CO and its isotopologues ^{13}CO and C^{18}O. The spectra extracted from positions marked with the letters A–G are shown in Fig. B.11–B.14

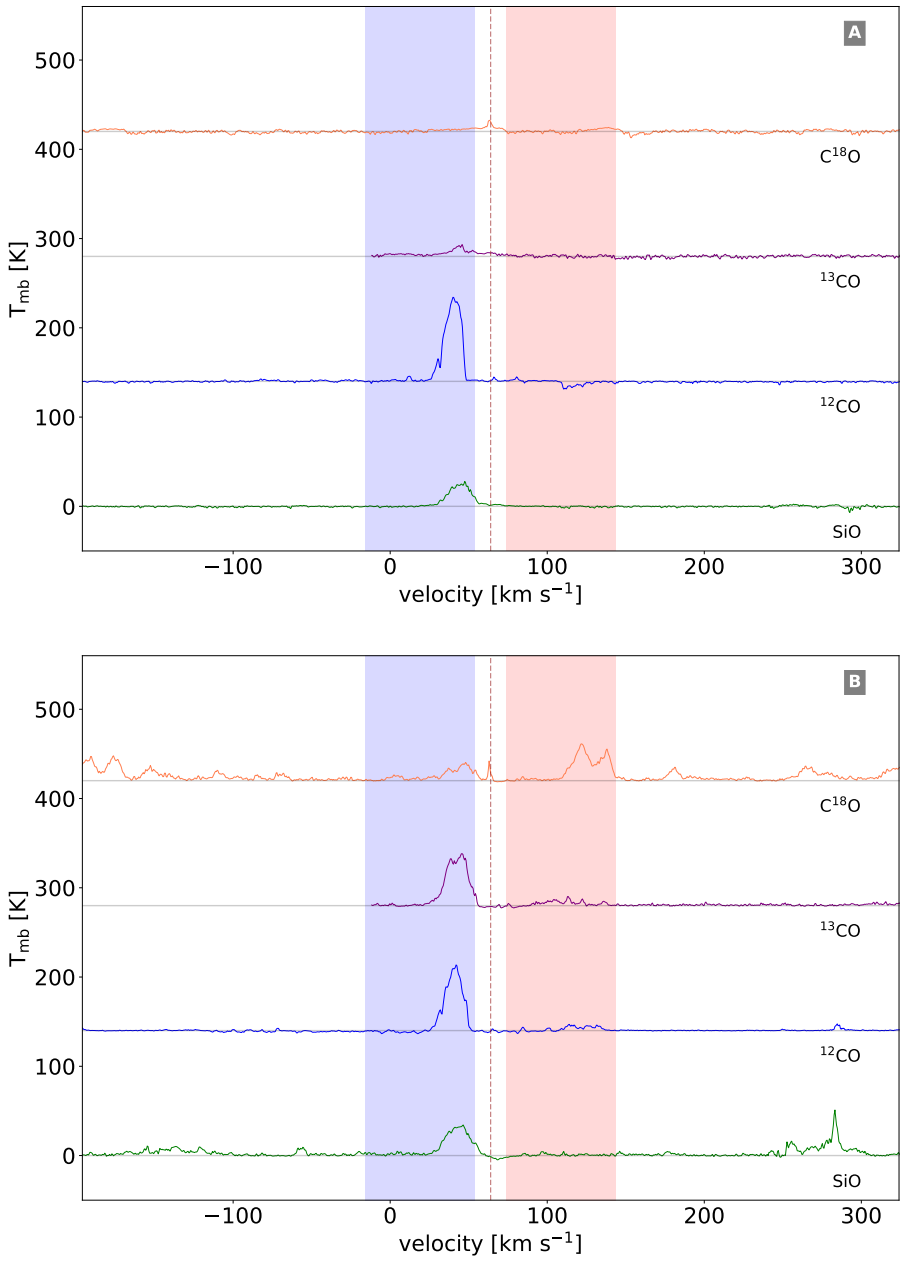

Figure B.11: Spectra extracted from positions marked in Fig. B.10 for the molecular species SiO (green) and ^{12}CO (blue) and its isotopologues ^{13}CO (purple) and C^{18}O (orange). The dark red vertical line indicates the systemic velocity of Sgr B2(N). The blue and red marked areas show the range, within the SiO (5-4) emission has been detected and is associated to the outflow emission. The grey horizontal lines indicate the continuum levels.

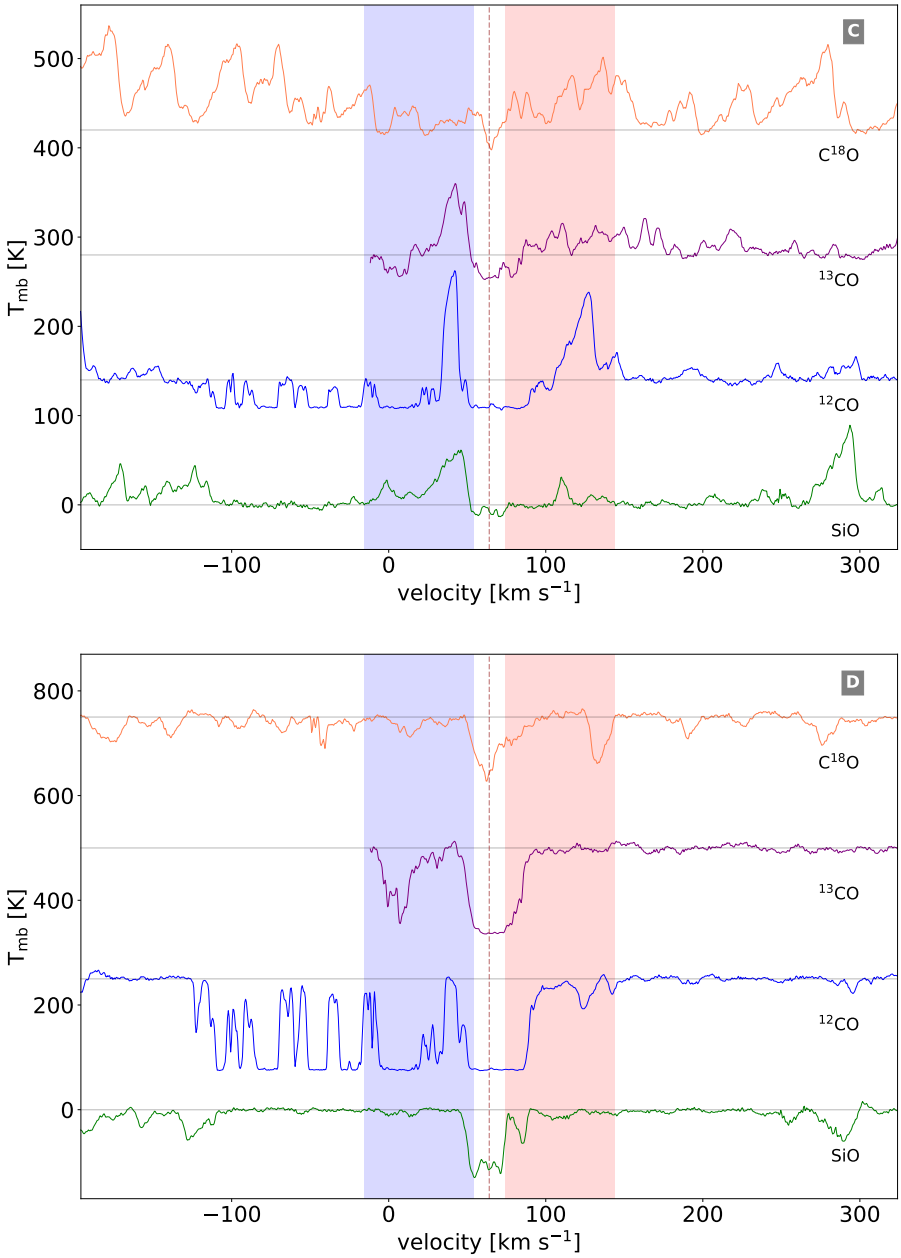

Figure B.12: Same as Fig. B.11

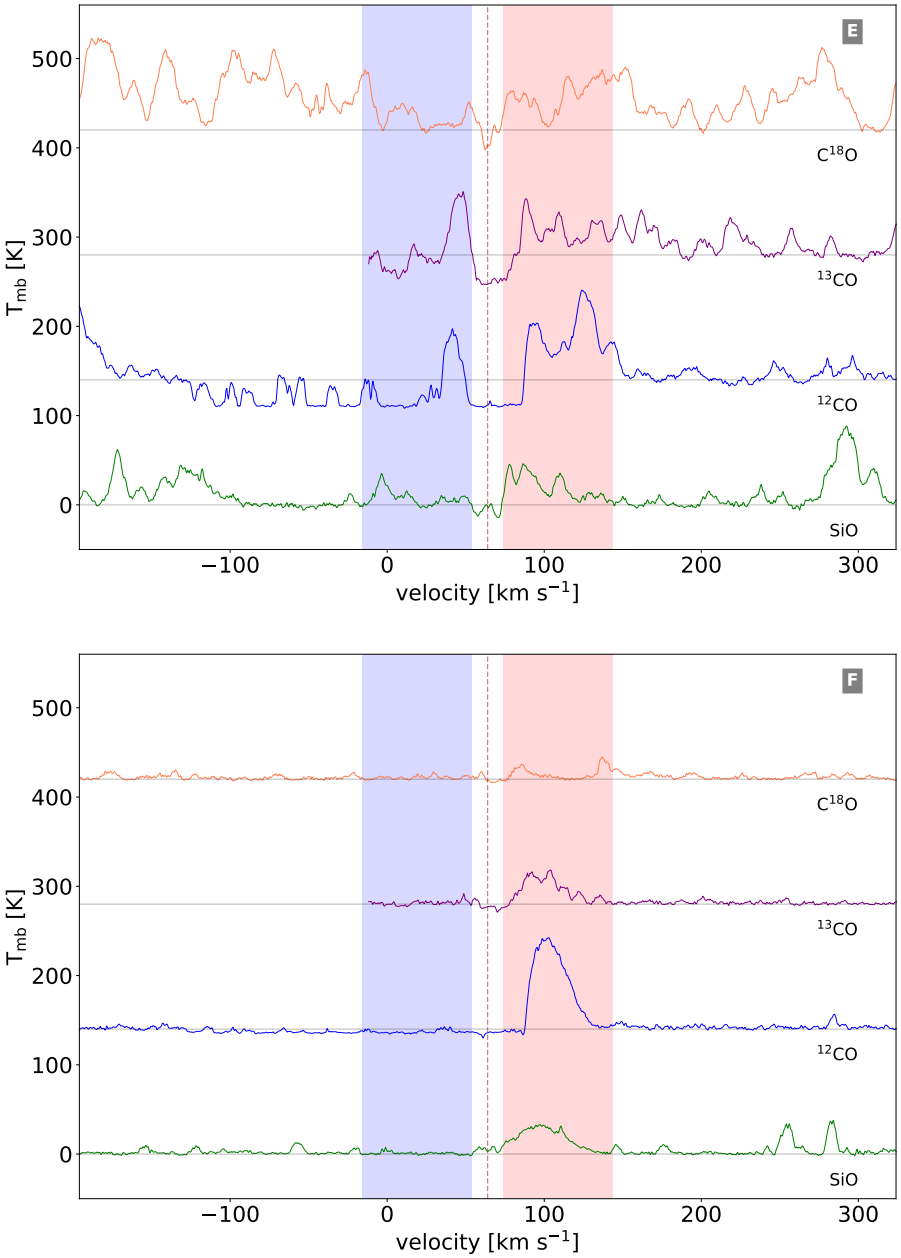

Figure B.13: Same as Fig. B.11

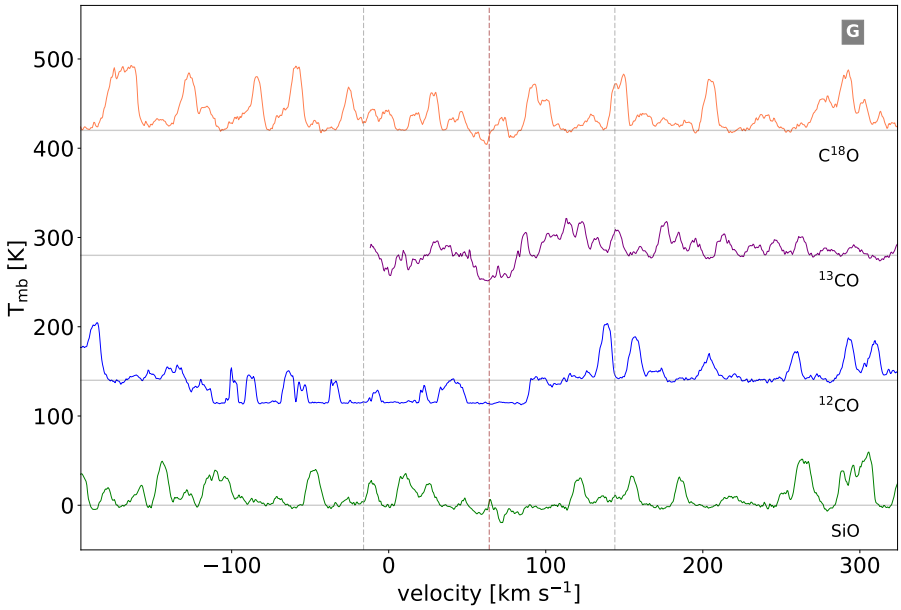

Figure B.14: Same as Fig. B.11

B.3 Molecular abundances and column densities

In Fig. B.15 I demonstrate that the calculation of the column density rely more on the assumed excitation temperature for transitions with higher excitation energy levels than for transitions with lower excitation energy levels. For this purpose, I used a modified version of the population diagram method (also known as rotational diagram) as presented in Goldsmith & Langer (1999). I calculate the column densities of different molecular species, listed in Table B.2, based on the equation

$$\frac{dN_{\rm mol}}{d\nu} = \left(\frac{8\pi\, k\, \nu_{\rm ul}^2}{h\, c^3\, A_{\rm ul}\, g_{\rm u}} \right) Q_{\rm rot}(T_{\rm ex})\, e^{E_{\rm u}/kT_{\rm ex}}\, T_{\rm B}(\nu), \tag{B.1}$$

where $\nu_{\rm ul}$ is the frequency of the selected transition, $A_{\rm ul}$ the Einstein A coefficient, $E_{\rm u}$/k the energy of the upper level, $\rm Q_{rot}$ the partition function, $g_{\rm u}$ the degeneracy of the upper level and $\rm T_B(\nu)$ the brightness temperature. The spectral line parameters can be found in Table B.1. As brightness temperature I used an averaged brightness temperature over a representative section within the red, respectively blue, shifted lobe of the outflow towards Sgr B2(N). The excitation temperature has been assumed to be 40 K (according to the temperatures obtained in section 7.3.2). However, the column densities derived for different transitions of the same molecular species (e.g., CH_3OH) show an increase with higher energy levels (see Fig. B.15, top left). Physically, the column density should stay constant over all transitions for the same molecular species. The top right panel in Fig. B.15 demonstrate the alteration of the colum densities by modifying the assumed excitation temperature for all selected transitions. Modifying the excitation temperature to 100 K results in a more constant column density of $\sim 8\times10^{17}$ cm^{-2} over all transitions (see Fig. B.15, bottom right). Thus, the assumed excitation temperature was most likely not well constraint. Though, the new column density value is still similar to previously derived value for transitions with lower energy levels. The bottom left panel shows the standard deviation of all calculated column densities for different excitation temperatures, having the minimum at roughly 60 K. However, the key message of this exercise is not that the excitation temperature was incorrectly assumed, but rather that the column density for transitions with lower energy levels (as the case for the transitions of SiO (5–6) and CO (2–1) in the analysis part) does not rely so much on the assumed excitation temperature. Therefore, the derived column density and also the SiO abundance seem to be reasonable. However, for a correct determination of the column density, also the opacity of the medium is relevant. I assumed the outflow in the selected molecular species (Table B.2) as optically thin, which may be not correct all over the place.

Besides of the demonstration above, this Appendix includes the Fig. B.16, which shows the SiO abundance and outflow mass depending on the distance to the center towards Sgr B2(N). I found no significant in- or decrease of the abundance with distance. The outflow mass seems to increase slightly by moving to the center.

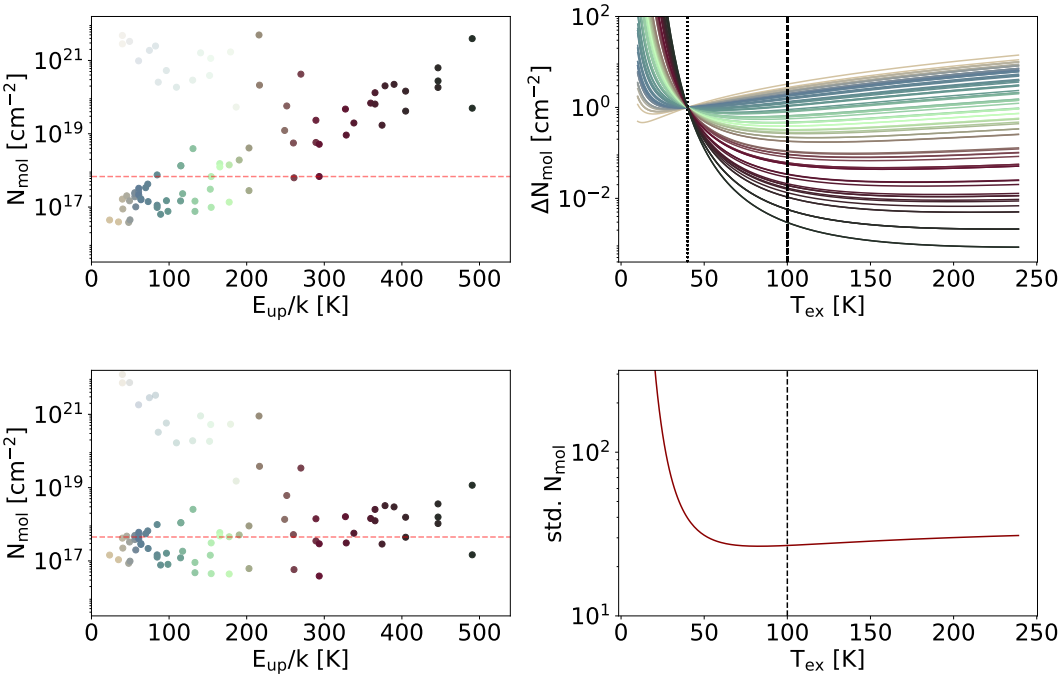

Figure B.15: *Top left:* Column densities of different transitions of the molecular species CH_3OH within the red shifted lobe of the outflow towards Sgr B2(N). The excitation energy levels are color coded for the following panels. The values of low energy levels (< 200 K), but with high column densities ($\sim 10^{21}$ cm^{-2}) are most like due to line blending effects not correctly determined. The red horizontal dashed line indicates the median column density excluding the blended transitions. *Top right:* Change in the column density by alternating the excitation temperature. The transitions are color coded by their excitation energy levels (see previous panel). The dotted black line at 40 K corresponds to the excitation temperature used to determine the column density in the previous panel, the black dashed line at 100 K indicates the excitation temperature used in the following panel. *Bottom left:* Column density determined for different transitions of CH_3OH assuming an excitation temperature of 100 K. The red dashed line indicate the median column density excluding the blended transitions. *Bottom right:* Standard deviation of all column density values of different transitions of the molecular species CH_3OH by alternating the assumed excitation temperature. The minimum is at roughly 60 K.

Table B.1: Catalog entries of the CDMS database used to derive column densities.

molecule	frequency [MHz]	transition	$A_{\rm ul}$ [$\rm s^{-1}$]	$E_{\rm u}/{\rm k}$ [K]	$g_{\rm u}$
CO	230538	2–1	6.9106e-07	16.596	5
^{13}CO	220398	2–1	6.0751e-07	15.866	10
C^{18}O	219560	2–1	6.0116e-07	15.806	5
SiO	217104	5–4	5.2135e-04	31.259	11
	260518	6–5	9.1459e-04	43.762	13
^{29}SiO	214385	5–4	5.0036e-04	30.867	11
	257254	6–5	8.7796e-04	43.213	13
^{30}SiO	211852	5–4	4.8293e-04	30.503	11
	254215	6–5	8.4719e-04	42.703	13
SO_2	214689	$16_{3,13}$–$16_{2,14}$	9.9021e-05	147.833	33
	216643	$22_{2,20}$–$22_{1,21}$	9.2712e-05	248.441	45
	221965	$11_{1,11}$–$10_{0,10}$	1.1382e-04	60.361	23
	225153	$13_{2,12}$–$13_{1,13}$	6.5235e-05	92.984	27
	226300	$14_{3,11}$–$14_{2,12}$	1.0677e-04	118.984	29
	234421	$16_{6,10}$–$17_{5,13}$	2.3492e-05	213.316	33
	236216	$16_{1,15}$–$15_{2,14}$	7.5045e-05	130.664	33
	237068	$12_{3,9}$–$12_{2,10}$	1.1413e-04	93.96	25
	240942	$18_{1,17}$–$18_{0,18}$	7.0239e-05	163.065	37
	241615	$5_{2,4}$–$4_{1,3}$	8.4560e-05	23.589	11
	244254	$14_{0,14}$–$13_{1,13}$	1.6386e-04	93.9	29
	245561	$62_{15,47}$–$63_{14,50}$	3.3422e-05	2343.685	125
	248057	$15_{2,14}$–$15_{1,15}$	8.0555e-05	119.328	31
	251199	$13_{1,13}$–$12_{0,12}$	1.7554e-04	82.178	27
	251210	$8_{3,5}$–$8_{2,6}$	1.1977e-04	55.202	17
	254280	$6_{3,3}$–$6_{2,4}$	1.1365e-04	41.402	13
	255553	$4_{3,1}$–$4_{2,2}$	9.2841e-05	31.293	9
	255958	$3_{3,1}$–$3_{2,2}$	6.6258e-05	27.62	7
	256246	$5_{3,3}$–$5_{2,4}$	1.0737e-04	35.887	11
	257099	$7_{3,5}$–$7_{2,6}$	1.2229e-04	47.835	15
	258942	$9_{3,7}$–$9_{2,8}$	1.3183e-04	63.471	19
	262256	$11_{3,9}$–$11_{2,10}$	1.4081e-04	82.8	23
	267537	$13_{3,11}$–$13_{2,12}$	1.5125e-04	105.823	27
	271529	$7_{2,6}$–$6_{1,5}$	1.1073e-04	35.496	15
	273752	$17_{2,16}$–$17_{1,17}$	9.9670e-05	149.218	35
SO	214357	7_8–7_7	3.4171e-06	81.245	15
	215220	5_5–4_4	1.2165e-04	44.104	11

	219949	6_5–5_4	1.3615e-04	34.985	13
	236452	1_2–2_1	1.4455e-06	15.808	3
	246404	2_3–3_2	1.0274e-06	21.051	5
	251825	5_6–4_5	1.9635e-04	50.661	11
	254573	8_9–8_8	4.3239e-06	99.699	17
	258255	6_6–5_5	2.1615e-04	56.498	13
	267197	3_4–4_3	7.2578e-07	28.681	7
OCS	218903	18–17	3.0384e-05	99.81	37
	231060	19–18	3.5783e-05	110.899	39
	243218	20–19	4.1783e-05	122.572	41
	255374	21–20	4.8430e-05	134.828	43
	267530	22–21	5.5735e-05	147.667	45
CS	244935	5–4	2.9806e-04	35.266	11
H_2CS	236727	$7_{1,7}$–$6_{1,6}$	1.9199e-04	58.619	45
	244048	$7_{1,6}$–$6_{1,5}$	2.1032e-04	60.025	45
	270521	$8_{1,8}$–$7_{1,7}$	2.9032e-04	71.602	51
	274521	$8_{0,8}$–$7_{0,7}$	3.0814e-04	59.315	17
H_2CO	218222	$3_{0,3}$–$2_{0,2}$	2.8180e-04	20.956	7
	218475	$3_{2,2}$–$2_{2,1}$	1.5714e-04	68.094	7
	218760	$3_{2,1}$–$2_{2,0}$	1.5774e-04	68.111	7
	225697	$3_{1,2}$–$2_{1,1}$	2.7719e-04	33.449	21
	227583	$17_{2,15}$–$17_{2,16}$	8.4113e-06	590.43	35
HNCO	218981	$10_{1,10}$–$9_{1,9}$	1.4222e-04	101.079	21
	219798	$10_{0,10}$–$9_{0,9}$	1.4693e-04	58.019	21
	220584	$10_{1,9}$–$9_{1,8}$	1.4537e-04	101.502	21
	240875	$11_{1,11}$–$10_{1,10}$	1.9042e-04	112.639	23
	241774	$11_{0,11}$–$10_{0,10}$	1.9639e-04	69.623	23
	242639	$11_{1,10}$–$10_{1,9}$	1.9465e-04	113.147	23
	262769	$12_{1,12}$–$11_{1,11}$	2.4846e-04	125.25	25
	263748	$12_{0,12}$–$11_{0,11}$	2.5588e-04	82.28	25
	264693	$12_{1,11}$–$11_{1,10}$	2.5394e-04	125.85	25
CH_3OH	212613	$10_{0,10}$–$9_{2,7}$	5.1360e-09	140.603	84
	213379	$13_{6,8}$–$14_{5,9}$	1.0660e-05	389.916	108
	213428	$1_{1,0}$–$0_{0,0}$	3.3706e-05	23.367	12
	216857	$6_{3,4}$–$7_{1,6}$	1.7999e-08	96.459	52
	216945	$5_{1,4}$–$4_{2,3}$	1.2135e-05	55.871	44
	218440	$4_{2,3}$–$3_{1,2}$	4.6863e-05	45.459	36
	220078	$8_{0,8}$–$7_{1,6}$	2.5157e-05	96.614	68
	220401	$10_{5,6}$–$11_{4,8}$	1.1184e-05	251.643	84

226939	$14_{2,12}$–$13_{3,11}$	1.7030e-07	269.846	116
227229	$12_{1,12}$–$11_{2,10}$	2.6123e-07	186.431	100
227814	$16_{1,16}$–$15_{2,13}$	2.1838e-05	327.238	132
229589	$15_{4,11}$–$16_{3,14}$	2.0839e-05	374.438	124
229758	$8_{1,8}$–$7_{0,7}$	4.1912e-05	89.103	68
230027	$3_{2,1}$–$4_{1,4}$	1.4860e-05	39.828	28
231281	$10_{2,9}$–$9_{3,6}$	1.8314e-05	165.348	84
232418	$10_{2,8}$–$9_{3,7}$	1.8675e-05	165.401	84
232783	$18_{3,16}$–$17_{4,13}$	2.1649e-05	446.532	148
232945	$10_{3,7}$–$11_{2,9}$	2.1267e-05	190.369	84
233795	$18_{3,15}$–$17_{4,14}$	2.1978e-05	446.58	148
234683	$4_{2,3}$–$5_{1,4}$	1.8740e-05	60.923	36
236936	$14_{1,13}$–$13_{2,12}$	3.1115e-05	260.203	116
237429	$7_{1,6}$–$6_{2,4}$	1.0822e-07	86.052	60
239746	$5_{1,5}$–$4_{1,4}$	5.6642e-05	49.06	44
241057	$9_{3,7}$–$10_{0,10}$	8.5601e-08	152.171	76
241700	$5_{0,5}$–$4_{0,4}$	6.0355e-05	47.935	44
241767	$5_{1,5}$–$4_{1,4}$	5.8060e-05	40.391	44
241791	$5_{0,5}$–$4_{0,4}$	6.0465e-05	34.817	44
241806	$5_{4,1}$–$4_{4,0}$	2.1802e-05	115.16	44
241806	$5_{4,1}$–$4_{4,0}$	2.1802e-05	115.16	44
241829	$5_{4,1}$–$4_{4,0}$	2.1898e-05	130.817	44
241832	$5_{3,3}$–$4_{3,2}$	3.8657e-05	84.618	44
241842	$5_{2,4}$–$4_{2,3}$	5.1154e-05	72.53	44
241879	$5_{1,4}$–$4_{1,3}$	5.9604e-05	55.871	44
241879	$5_{1,4}$–$4_{1,3}$	5.9604e-05	55.871	44
241904	$5_{2,3}$–$4_{2,2}$	5.0934e-05	60.724	44
242446	$14_{1,14}$–$13_{2,11}$	2.2899e-05	248.931	116
243915	$5_{1,4}$–$4_{1,3}$	5.9649e-05	49.66	44
246228	$3_{2,1}$–$2_{1,1}$	4.8730e-09	39.828	28
246873	$19_{3,16}$–$19_{2,17}$	8.2705e-05	490.648	156
247161	$16_{2,15}$–$15_{3,13}$	2.5722e-05	338.138	132
247228	$4_{2,2}$–$5_{1,5}$	2.1229e-05	60.925	36
248282	$17_{3,14}$–$17_{2,15}$	8.3051e-05	404.828	140
248885	$16_{3,13}$–$16_{2,14}$	8.3168e-05	365.393	132
249192	$16_{3,13}$–$15_{4,12}$	2.5373e-05	378.275	132
249419	$15_{3,12}$–$15_{2,13}$	8.3197e-05	328.275	124
249887	$14_{3,11}$–$14_{2,12}$	8.3178e-05	293.474	116
250506	$11_{0,11}$–$10_{1,10}$	8.4568e-05	153.097	92
250924	$11_{3,8}$–$11_{2,9}$	8.2409e-05	202.982	92

251164	$10_{3,7}$–$10_{2,8}$	8.1795e-05	177.455	84
251359	$9_{3,6}$–$9_{2,7}$	8.0893e-05	154.248	76
251517	$8_{3,5}$–$8_{2,6}$	7.9566e-05	133.36	68
251641	$7_{3,4}$–$7_{2,5}$	7.7594e-05	114.793	60
251738	$6_{3,3}$–$6_{2,4}$	7.4573e-05	98.545	52
251811	$5_{3,2}$–$5_{2,3}$	6.9664e-05	84.618	44
251866	$4_{3,1}$–$4_{2,2}$	6.1002e-05	73.012	36
251890	$5_{3,3}$–$5_{2,4}$	6.9714e-05	84.618	44
251917	$3_{3,1}$–$3_{2,2}$	4.3596e-05	63.727	28
251917	$3_{3,1}$–$3_{2,2}$	4.3596e-05	63.727	28
251984	$8_{3,6}$–$8_{2,7}$	7.9845e-05	133.36	68
252090	$9_{3,7}$–$9_{2,8}$	8.1337e-05	154.247	76
252252	$10_{3,8}$–$10_{2,9}$	8.2445e-05	177.454	84
252485	$11_{3,9}$–$11_{2,10}$	8.3360e-05	202.979	92
253221	$13_{3,11}$–$13_{2,12}$	8.4862e-05	260.985	108
253755	$14_{3,12}$–$14_{2,13}$	8.5571e-05	293.464	116
254423	$11_{5,6}$–$12_{4,8}$	1.7894e-05	289.223	92
254423	$11_{5,6}$–$12_{4,8}$	1.7894e-05	289.223	92
255241	$16_{3,14}$–$16_{2,15}$	8.7100e-05	365.369	132
256228	$17_{3,15}$–$17_{2,16}$	8.7981e-05	404.794	140
257402	$18_{3,16}$–$18_{2,17}$	8.8963e-05	446.532	148
258780	$19_{3,17}$–$19_{2,18}$	9.0096e-05	490.583	156
260254	$11_{3,8}$–$12_{2,11}$	9.3678e-08	215.894	92
261704	$12_{6,7}$–$13_{5,8}$	1.7777e-05	359.769	100
265259	$5_{3,3}$–$6_{1,5}$	2.0380e-08	82.531	44
265289	$6_{1,5}$–$5_{2,4}$	2.5840e-05	69.801	52
266196	$3_{2,1}$–$3_{0,3}$	2.9887e-09	39.828	28
266292	$4_{2,2}$–$4_{0,4}$	5.3605e-09	49.115	36
266496	$5_{2,3}$–$5_{0,5}$	8.2976e-09	60.724	44
266838	$5_{2,4}$–$4_{1,3}$	7.7344e-05	57.069	44
266864	$6_{2,4}$–$6_{0,6}$	1.1779e-08	74.657	52
267403	$9_{0,9}$–$8_{1,7}$	4.6700e-05	117.457	76
268368	$8_{2,6}$–$8_{0,8}$	2.0236e-08	109.493	68
269668	$9_{2,7}$–$9_{0,9}$	2.5114e-08	130.399	76
271457	$10_{2,8}$–$10_{0,10}$	3.0343e-08	153.63	84
273497	$13_{1,13}$–$12_{2,11}$	7.1182e-07	216.53	108
273840	$11_{2,9}$–$11_{0,11}$	3.5838e-08	179.189	92

Note. $A_{\rm ul}$ is the Einstein A coefficient, $E_{\rm u}$/k the energy of the upper level and $g_{\rm u}$ the degeneracy of the upper level.

Table B.2: Abundances with respect to H_2 and column densities of different molecular species derived from individual transitions.

mol.	freq.	E_{up}/k	N_{mol} [10^x cm^{-2}]		optical thin abund.[10^x]/H_2		opacity corrected abund. [10^x] /H_2	
	[MHz]	[K]	blue wing	red wing	blue wing	red wing	blue wing	red wing
SiO	217104	31.26	14.89±0.29	15.02±0.26	-8.1±0.36	-8.03±0.31	-8.78±0.39	-8.52±0.42
	260518	43.76	15.35±0.28	15.27±0.3	-7.66±0.47	-7.79±0.39	-8.35±0.59	-8.22±0.45
^{29}SiO	214385	30.87	14.57±0.32	15.21±0.31	-8.49±0.43	-7.89±0.32	-9.11±0.46	-8.34±0.36
	257254	43.21	14.62±0.43	15.31±0.37	-8.37±0.62	-7.82±0.36	-9.0±0.75	-8.1±0.47
^{30}SiO	211852	30.5	14.28±0.48	14.45±0.26	-8.84±0.64	-8.69±0.39	-9.56±0.64	-9.14±0.45
	254215	42.7	14.21±0.31	14.04±0.17	-8.87±0.44	-9.02±0.36	-9.54±0.48	-9.34±0.48
SO_2	241615	23.59	16.79±0.41	16.82±0.37	-6.24±0.37	-6.31±0.33	-7.03±0.43	-7.02±0.43
	255958	27.62	16.84±0.38	16.92±0.35	-6.16±0.4	-6.18±0.39	-6.95±0.37	-6.81±0.43
	255553	31.29	16.73±0.37	16.8±0.37	-6.22±0.35	-6.29±0.38	-6.97±0.36	-6.91±0.45
	271529	35.5	16.66±0.39	16.99±0.38	-6.26±0.36	-6.11±0.34	-7.02±0.37	-6.67±0.39
	256246	35.89	16.83±0.41	16.98±0.36	-6.13±0.34	-6.18±0.42	-6.84±0.44	-6.68±0.41
	254280	41.4	16.09±0.3	16.14±0.26	-6.97±0.33	-7.09±0.34	-7.67±0.36	-7.7±0.39
	257099	47.84	16.94±0.3	16.85±0.35	-6.05±0.34	-6.23±0.36	-6.71±0.47	-6.69±0.42
	251210	55.2	17.07±0.31	17.22±0.26	-5.94±0.32	-5.92±0.31	-6.56±0.49	-6.29±0.45
	221965	60.36	16.76±0.34	16.74±0.32	-6.25±0.36	-6.38±0.35	-6.86±0.44	-6.73±0.46
	258942	63.47	16.93±0.34	16.97±0.35	-6.09±0.36	-6.17±0.37	-6.68±0.44	-6.49±0.47
	251199	82.18	17.19±0.25	17.16±0.25	-5.7±0.5	-5.96±0.41	-6.4±0.85	-6.06±0.65
	262256	82.8	17.11±0.3	17.09±0.3	-5.84±0.39	-5.98±0.35	-6.41±0.7	-6.1±0.65
	225153	92.98	17.2±0.34	17.1±0.33	-5.82±0.39	-5.98±0.44	-6.33±0.72	-6.1±0.61
	244254	93.9	17.18±0.48	16.95±0.33	-5.78±0.58	-6.15±0.45	-6.37±0.77	-6.24±0.65
	237068	93.96	17.25±0.24	17.03±0.33	-5.78±0.39	-6.08±0.46	-6.33±0.97	-6.2±0.68
	267537	105.82	16.99±0.39	16.44±0.26	-5.64±0.46	-6.71±0.41	-6.25±1.29	-6.67±0.75

	226300	118.98	17.05±0.36	17.05±0.28	-5.89±0.5	-6.04±0.38	-6.55±1.08	-5.91±0.77
	248057	119.33	17.56±0.5	17.58±0.31	-5.42±0.58	-5.6±0.44	-5.85±1.04	-5.46±0.8
	236216	130.66	17.82±0.42	17.48±0.29	-5.06±0.51	-5.62±0.42	-5.52±1.27	-5.37±0.87
	214689	147.83	17.6±0.5	17.38±0.34	-5.39±0.6	-5.74±0.51	-5.71±1.33	-5.36±0.99
	273752	149.22	17.98±0.55	17.71±0.4	-4.95±0.66	-5.35±0.56	-5.32±1.38	-5.14±1.12
	240942	163.06	17.92±0.43	17.79±0.4	-5.05±0.54	-5.33±0.56	-5.31±1.59	-4.9±1.18
	234421	213.32	19.33±0.85	18.48±0.51	-3.72±0.98	-4.67±0.74	-3.86±1.54	-4.04±1.68
	216643	248.44	18.95±1.03	18.21±0.68	-4.0±1.19	-4.87±0.86	-4.2±2.08	-3.79±1.83
SO	236452	15.81	nan±nan	18.35±0.46	nan±nan	-4.83±0.45	nan±nan	-5.58±0.45
	246404	21.05	18.45±0.41	18.15±0.38	-4.56±0.51	-5.01±0.5	-5.26±0.55	-6.01±0.49
	267198	28.68	18.81±0.48	18.58±0.41	-4.27±0.43	-4.61±0.47	-5.03±0.41	-5.26±0.42
	219949	34.98	16.21±0.28	16.23±0.29	-6.76±0.33	-6.82±0.36	-7.46±0.34	-7.38±0.43
	215220	44.1	16.48±0.24	16.53±0.3	-6.47±0.33	-6.59±0.36	-7.15±0.42	-7.03±0.41
	251826	50.66	15.9±0.27	15.92±0.3	-7.14±0.39	-7.25±0.43	-7.84±0.43	-7.66±0.54
	258256	56.5	16.7±0.24	16.69±0.26	-6.19±0.44	-6.42±0.36	-6.91±0.57	-6.72±0.45
	214357	81.24	18.2±0.21	17.9±0.27	-4.83±0.43	-5.21±0.34	-5.38±0.91	-5.26±0.51
	254573	99.7	17.71±0.24	17.46±0.25	-5.3±0.56	-5.74±0.36	-5.39±1.32	-5.94±0.74
OCS	218903	99.81	17.5±0.68	16.93±0.28	-5.47±0.83	-6.28±0.47	-6.06±0.81	-6.15±0.77
	231060	110.9	17.62±0.75	17.0±0.38	-5.4±0.86	-6.12±0.61	-5.92±0.88	-6.12±0.98
	243218	122.57	17.75±0.82	17.19±0.36	-5.27±0.92	-5.97±0.55	-5.63±1.07	-5.65±1.01
	255374	134.83	17.97±0.9	17.39±0.48	-4.98±1.0	-5.72±0.73	-5.36±1.23	-5.48±1.24
	267530	147.67	18.33±0.64	16.69±0.4	-4.42±0.69	-6.42±0.62	-5.72±1.32	-5.94±1.35
CS	244935	35.27	15.66±0.39	15.53±0.35	-7.38±0.42	-7.55±0.37	-7.99±0.4	-7.96±0.47
H_2CS	236727	58.62	15.76±0.26	15.77±0.29	-7.28±0.4	-7.31±0.34	-8.08±0.55	-7.72±0.43
	274521	59.31	16.78±0.35	16.3±0.37	-6.28±0.43	-6.83±0.47	-6.9±0.65	-7.28±0.58
	244048	60.03	16.0±0.31	15.76±0.27	-7.07±0.35	-7.31±0.41	-7.77±0.44	-7.77±0.59
	270521	71.6	15.55±0.22	15.46±0.25	-7.64±0.35	-7.39±0.4	-8.21±0.46	-7.77±0.7

H_2CO	218222	20.96	15.65±0.44	15.91±0.4	-7.37±0.32	-7.32±0.38	-8.13±0.44	-7.94±0.39
	225697	33.45	15.47±0.37	15.5±0.29	-7.52±0.32	-7.67±0.27	-8.16±0.42	-8.15±0.43
	218475	68.09	16.64±0.29	16.93±0.35	-6.42±0.33	-6.26±0.4	-6.99±0.46	-6.59±0.54
	218760	68.11	16.65±0.29	16.65±0.35	-6.45±0.35	-6.48±0.34	-7.03±0.43	-6.79±0.43
	227583	590.43	23.82±2.18	22.41±2.4	0.92±2.36	-0.68±2.56	3.58±8.11	4.06±4.14
HNCO	219798	58.02	15.98±0.33	15.79±0.28	-7.07±0.35	-7.32±0.35	-7.66±0.39	-7.69±0.46
	241774	69.62	16.04±0.29	16.01±0.42	-6.82±0.55	-7.01±0.45	-7.35±0.89	-7.19±0.66
	263748	82.28	16.49±0.34	16.05±0.29	-6.53±0.37	-7.09±0.39	-7.06±0.68	-7.23±0.64
	218981	101.08	16.52±0.37	16.31±0.27	-6.49±0.44	-6.85±0.4	-6.93±0.87	-6.79±0.76
	220584	101.5	17.04±0.33	16.6±0.31	-5.9±0.52	-6.57±0.4	-6.51±1.03	-6.54±0.69
	240875	112.64	16.59±0.34	16.54±0.32	-6.41±0.4	-6.58±0.47	-6.8±1.05	-6.44±0.85
	242639	113.15	16.9±0.24	16.73±0.29	-6.16±0.48	-6.51±0.4	-6.61±1.3	-6.37±0.76
	262769	125.25	17.01±0.39	16.32±0.31	-6.08±0.43	-6.84±0.51	-6.46±1.07	-6.57±0.95
	264693	125.85	16.93±0.4	16.62±0.29	-6.13±0.43	-6.57±0.44	-6.51±1.05	-6.29±0.89
CH_3OH	213427	23.37	16.82±0.26	16.65±0.16	-6.24±0.37	-6.2±0.26	-7.19±0.31	-6.75±0.35
	241791	34.82	16.81±0.33	16.59±0.32	-6.2±0.43	-6.45±0.39	-7.02±0.41	-7.1±0.44
	246228	39.83	20.67±0.41	21.45±0.49	-2.06±0.62	-1.69±0.44	-3.06±0.46	-2.3±0.42
	266196	39.83	20.91±0.28	21.68±0.51	-1.98±0.43	-1.54±0.48	-2.73±0.43	-2.13±0.51
	230027	39.83	17.21±0.26	17.22±0.27	-5.98±0.35	-5.89±0.29	-6.79±0.3	-6.34±0.35
	241767	40.39	16.73±0.34	16.95±0.48	-6.14±0.49	-6.2±0.43	-7.09±0.47	-6.78±0.56
	218440	45.46	17.13±0.38	17.31±0.46	-5.87±0.4	-5.91±0.43	-6.57±0.54	-6.57±0.44
	241700	47.93	17.11±0.41	16.58±0.23	-5.94±0.42	-6.54±0.32	-6.64±0.46	-7.21±0.39
	239746	49.06	16.86±0.36	17.17±0.46	-6.18±0.53	-5.84±0.52	-7.03±0.38	-6.61±0.69
	266292	49.11	20.93±0.47	21.52±0.48	-2.05±0.58	-1.62±0.45	-2.69±0.67	-2.26±0.45
	243915	49.66	16.74±0.33	16.65±0.35	-6.25±0.45	-6.4±0.38	-7.06±0.35	-6.89±0.5
	241887	55.87	17.12±0.34	17.28±0.4	-5.85±0.55	-5.77±0.5	-6.47±0.68	-6.14±0.63

241879	55.87	17.16±0.33	17.39±0.33	-5.76±0.56	-5.74±0.37	-6.6±0.64	-6.05±0.58
216945	55.87	17.3±0.24	17.36±0.34	-5.69±0.43	-5.74±0.42	-6.54±0.54	-6.31±0.42
266838	57.07	17.07±0.39	17.01±0.4	-5.87±0.39	-6.12±0.5	-6.52±0.46	-6.71±0.54
241904	60.72	17.48±0.32	17.42±0.34	-5.62±0.46	-5.69±0.46	-6.25±0.67	-6.14±0.55
266496	60.72	20.73±0.36	20.99±0.43	-2.31±0.46	-2.17±0.45	-2.66±0.6	-2.56±0.57
234683	60.92	17.46±0.26	17.33±0.25	-5.58±0.38	-5.8±0.4	-6.17±0.56	-6.18±0.51
247228	60.92	17.5±0.38	17.51±0.41	-5.44±0.45	-5.61±0.46	-6.08±0.64	-6.07±0.39
251917	63.73	17.07±0.24	17.2±0.26	-5.78±0.4	-5.9±0.44	-6.06±0.56	-6.45±0.56
251923	63.73	17.03±0.24	17.22±0.27	-6.06±0.31	-5.88±0.36	-6.6±0.52	-6.34±0.47
265289	69.8	17.27±0.32	17.53±0.44	-5.69±0.51	-5.7±0.5	-6.51±0.61	-6.02±0.59
241852	72.53	17.29±0.31	17.63±0.32	-5.54±0.57	-5.48±0.47	-6.56±0.95	-5.81±0.61
251866	73.01	16.82±0.35	17.15±0.28	-6.37±0.69	-5.98±0.4	-7.2±0.37	-6.14±0.53
266864	74.66	20.65±0.3	21.27±0.38	-2.22±0.51	-1.84±0.42	-2.73±0.82	-2.12±0.52
265259	82.53	20.92±0.41	21.39±0.36	-1.82±0.73	-1.82±0.31	-2.59±1.25	-2.01±0.52
251890	84.62	17.31±0.48	17.05±0.31	-5.35±0.68	-6.13±0.41	-6.46±0.7	-6.49±0.57
241842	84.62	17.69±0.32	17.88±0.34	-5.36±0.48	-5.23±0.51	-5.95±0.72	-5.36±0.78
251811	84.62	17.19±0.34	16.99±0.3	-5.42±0.58	-6.12±0.54	-5.91±1.06	-6.72±0.73
237429	86.05	20.3±0.35	20.41±0.32	-2.82±0.34	-2.74±0.32	-3.3±0.67	-2.87±0.56
229758	89.1	17.23±0.3	16.8±0.17	-5.75±0.43	-6.27±0.4	-6.35±0.8	-6.58±0.78
216857	96.46	20.19±0.14	20.73±0.38	-2.43±0.42	-2.38±0.59	-1.65±1.14	-2.51±0.77
220078	96.61	17.47±0.31	17.17±0.29	-5.57±0.51	-5.92±0.46	-6.37±0.6	-6.42±0.81
251738	98.55	16.88±0.29	16.88±0.32	-6.31±0.46	-6.4±0.41	-6.98±0.52	-6.83±0.61
268368	109.49	20.52±0.26	20.27±0.1	-2.5±0.57	-2.98±0.25	-2.66±1.3	-3.35±0.53
251641	114.79	17.07±0.28	17.17±0.31	-6.02±0.55	-6.07±0.39	-6.44±1.21	-5.71±0.75
241813	115.16	18.31±0.46	18.12±0.33	-4.57±0.69	-4.95±0.5	-4.97±1.33	-4.86±0.79
241806	115.16	18.26±0.4	18.13±0.31	-4.62±0.69	-4.93±0.54	-5.02±1.4	-4.79±0.87
267403	117.46	17.87±0.43	17.36±0.28	-4.67±0.58	-5.8±0.41	-4.3±1.2	-5.49±0.76
269668	130.4	20.56±0.22	20.46±0.21	-2.56±0.48	-2.68±0.37	-2.58±1.3	-2.28±0.87

241829	130.82	18.65±0.48	18.59±0.42	-4.25±0.66	-4.5±0.62	-4.79±1.38	-4.45±1.02
251984	133.36	17.12±0.4	16.88±0.19	-6.07±0.53	-6.27±0.35	-6.52±0.79	-5.58±0.89
251517	133.36	17.41±0.41	17.16±0.3	-5.76±0.56	-5.99±0.53	-6.28±0.75	-6.02±1.1
212613	140.6	20.89±0.2	21.21±0.27	-1.97±0.58	-1.98±0.39	-1.52±1.71	-1.29±0.78
241057	152.17	20.23±0.27	20.59±0.34	-2.74±0.62	-2.57±0.54	-1.38±1.98	-2.15±1.02
250506	153.1	17.71±0.5	17.49±0.36	-5.31±0.62	-5.69±0.57	-5.62±1.29	-5.17±1.1
271458	153.63	21.03±0.28	21.06±0.32	-2.04±0.5	-2.15±0.49	-1.93±1.8	-1.62±0.99
252090	154.25	17.34±0.47	16.99±0.21	-5.69±0.72	-6.17±0.38	-5.97±1.95	-5.08±1.23
251359	154.25	17.96±0.36	17.83±0.33	-4.97±0.5	-5.31±0.42	-5.2±1.61	-4.86±0.91
231281	165.35	18.18±0.44	18.18±0.41	-4.8±0.78	-4.94±0.63	-4.97±2.16	-4.08±1.29
232418	165.4	18.19±0.29	18.09±0.44	-4.88±0.54	-4.89±0.69	-4.92±1.92	-4.47±1.5
252252	177.45	17.36±0.51	17.13±0.24	-5.7±0.64	-5.52±0.53	-5.99±1.61	-3.7±1.75
251164	177.46	18.25±0.46	18.15±0.4	-4.63±0.69	-5.03±0.53	-4.85±2.01	-4.19±1.2
273840	179.19	21.36±0.41	21.23±0.41	-1.55±0.76	-1.95±0.56	-1.27±2.48	-1.38±1.18
227229	186.43	19.76±0.27	19.73±0.43	-3.15±0.68	-3.42±0.64	-2.75±2.58	-2.5±1.2
232945	190.37	19.15±0.5	18.28±0.37	-3.74±0.77	-4.95±0.56	-3.95±2.26	-4.07±1.31
252485	202.98	17.58±0.64	17.45±0.25	-5.35±0.73	-5.73±0.34	-5.46±1.93	-4.73±1.32
250924	202.98	18.88±0.57	18.61±0.38	-3.96±0.79	-4.5±0.55	-4.11±2.31	-3.61±1.35
260254	215.89	21.63±0.58	21.7±0.41	-1.35±0.73	-1.43±0.54	-1.45±2.45	-0.4±1.33
273497	216.53	19.81±0.32	20.33±0.49	-3.0±0.61	-2.88±0.64	-0.96±2.93	-1.75±1.36
242446	248.93	19.44±0.63	19.09±0.37	-3.4±0.91	-4.15±0.54	-3.02±3.17	-2.59±1.56
220401	251.64	20.69±1.89	19.76±0.84	-2.28±2.06	-3.35±1.06	-2.35±2.38	-2.08±1.71
236936	260.2	18.68±0.55	18.75±0.55	-4.25±0.71	-4.48±0.68	-3.98±2.57	-2.45±1.8
253221	260.98	18.32±1.06	17.8±0.44	-4.79±1.19	-5.22±0.66	-4.72±1.43	-3.29±2.12
226939	269.85	20.67±0.33	20.63±0.83	-2.09±0.62	-2.43±1.0	1.53±3.62	-0.23±2.28
254419	289.22	19.07±0.69	19.37±0.98	-4.13±0.82	-3.69±1.08	-3.56±2.41	-0.35±2.24
254423	289.22	19.05±0.55	18.76±0.68	-3.93±0.59	-4.07±0.69	-3.53±2.75	-1.08±2.51
253755	293.46	18.21±0.39	17.83±0.28	-4.85±0.69	-5.35±0.35	-3.08±3.63	-2.75±1.83

249887	293.47	19.27±1.03	18.71±0.8	-3.74±1.18	-4.48±0.95	-3.7±2.42	-2.81±1.98
227814	327.24	19.52±0.71	19.67±0.67	-3.52±0.86	-3.46±0.81	-2.65±3.23	-1.13±1.97
249419	328.27	19.77±1.04	18.96±0.91	-3.1±1.18	-4.11±1.11	-2.29±3.94	-2.49±2.41
247161	338.14	20.67±0.97	19.29±0.98	-2.26±1.11	-3.76±1.22	-1.6±3.96	-1.22±2.96
261704	359.77	20.32±1.22	19.84±1.03	-2.79±1.41	-3.13±1.23	-1.74±3.01	-0.49±2.92
255241	365.37	19.99±1.11	20.12±1.26	-2.89±1.3	-2.9±1.45	-1.7±4.47	-0.86±2.92
248885	365.39	19.82±1.08	19.81±0.97	-3.28±1.24	-3.33±1.13	-2.8±3.14	-1.05±2.76
229589	374.44	20.14±0.72	19.23±0.74	-3.07±0.87	-4.07±0.87	-2.45±2.2	-1.56±2.25
249192	378.27	20.29±0.91	20.31±0.79	-2.64±1.2	-2.87±0.91	-0.57±5.34	-0.37±2.36
213377	389.92	19.7±0.51	20.35±1.46	-3.39±0.6	-2.73±1.62	-1.24±1.72	0.22±2.76
256228	404.79	21.37±1.85	20.16±1.36	-1.46±2.04	-2.94±1.56	-0.73±4.9	-0.32±3.57
248282	404.83	19.99±0.87	19.62±1.02	-3.09±0.97	-3.59±1.18	-2.2±3.44	-0.57±2.8
232783	446.53	22.45±1.92	20.26±1.33	-0.46±2.06	-2.83±1.51	0.62±5.06	1.54±3.78
257402	446.53	22.21±2.35	20.8±1.31	-0.71±2.47	-2.29±1.5	0.22±4.63	0.91±3.58
233795	446.58	20.84±1.33	20.44±1.63	-2.13±1.53	-2.72±1.81	0.59±5.64	1.22±3.3
258780	490.58	21.42±1.42	21.6±2.2	-1.47±1.59	-1.5±2.41	0.24±6.2	0.79±4.23
246873	490.65	21.38±1.54	19.7±1.05	-1.52±1.73	-3.56±1.22	0.32±6.29	1.0±3.62

Note. The abundance ratios are derived from the total outflow mass, which has been calculated based on emission of ^{13}CO. As abundance ratio of $^{13}CO/H_2$ I assumed 5×10^{-6}. The exact procedure is described in section 7.3.2. The physical coefficients used to calculate the molecular column densities are listed in Table B.1. 'Opacity corrected' is related to emission ^{13}CO, which has been used to derive the abundance. The emission of all listed molecules is assumed as optically thin.

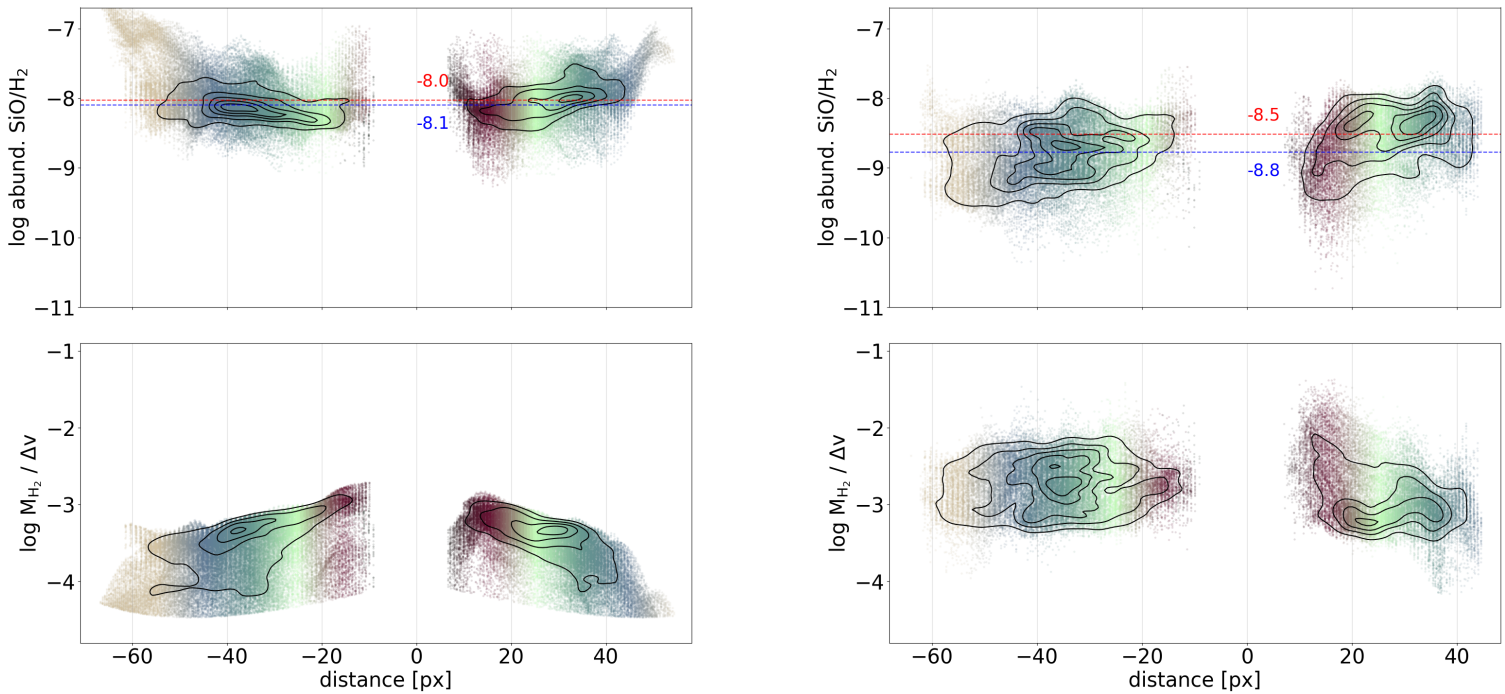

(a) optical thin

(b) opacity corrected

Figure B.16: *Top panels*: SiO to H_2 abundance per voxel vs. distance for three different scenarios (a) optically thin, (b) opacity corrected and (c) opacity modeled. The red and blue lines indicate the median abundance of SiO within the red/blue wing of the outflow. After opacity correction (b,c) the abundance is increasing for higher velocity with respect to the systemic velocity. The scatter color represent the distance to the central source AN01, visualized in panel (d). *Bottom panels*: H_2 mass per voxel vs. distance derived from emission of ^{13}CO, which has taken to determine the SiO abundance.

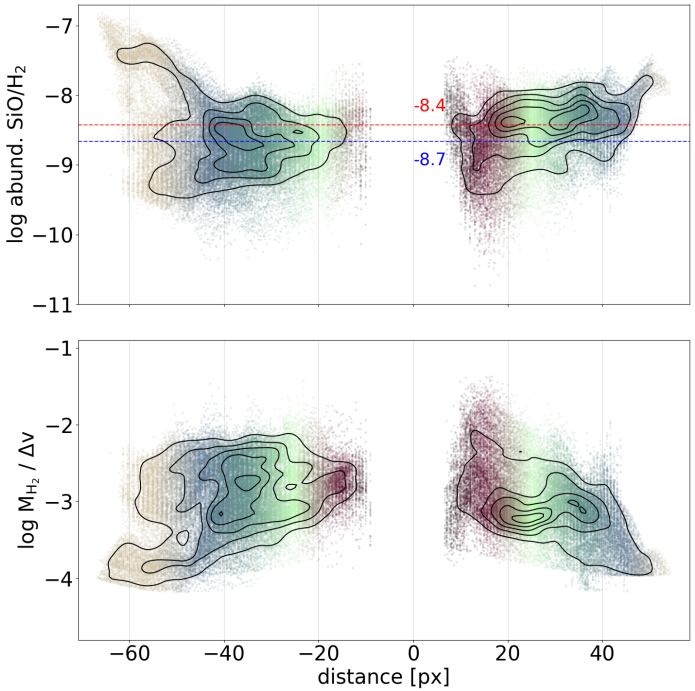

(c) opacity modeled

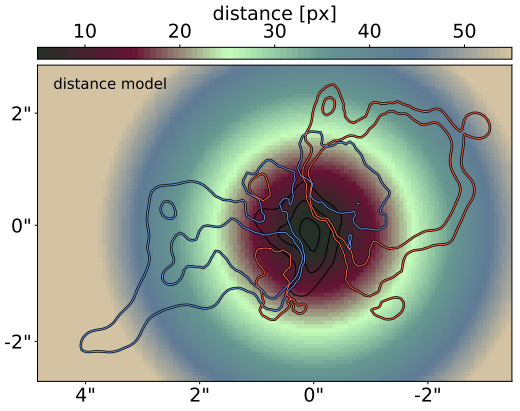

(d) color-code distance

Figure B.17: Fig. B.16 continued.

C

Synthetic Spectra of (complex) Molecules

This appendix includes synthetic spectra created with XCLASS of the molecular species, which I used in the analysis part of my thesis. The selected frequency range corresponds to the ALMA band 6, which has been covered in our observations of data-set I. The assumed column densities and temperatures are indicated within the figures. The velocity is set to 0 km s^{-1} and the velocity width to 3 km s^{-1}.

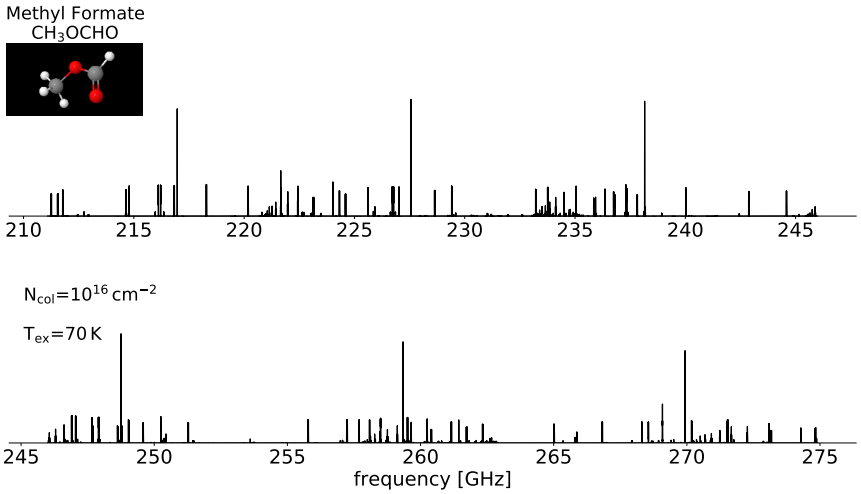

Figure C.1: Figure continues.

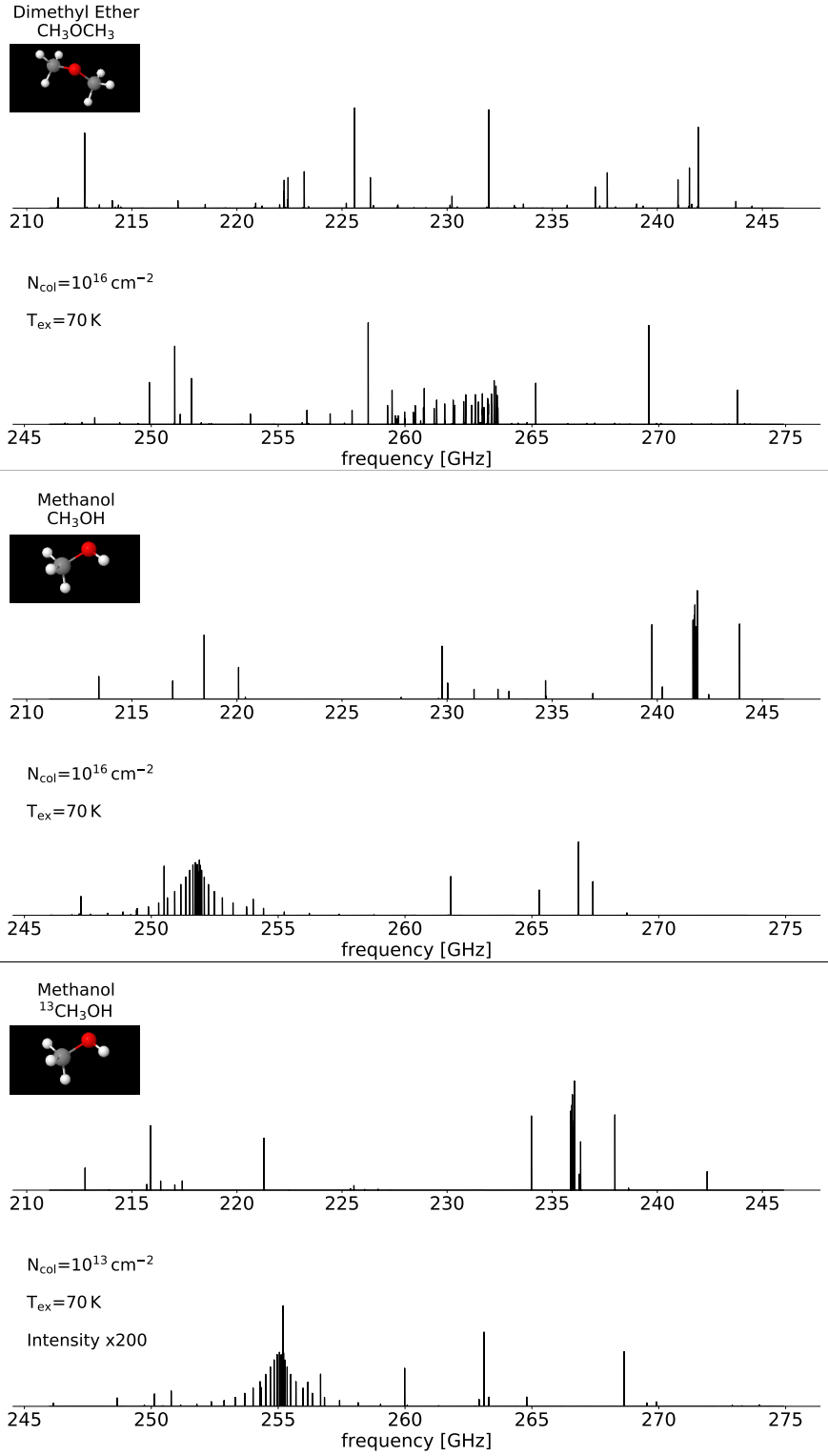

Figure C.2: Figure continues.

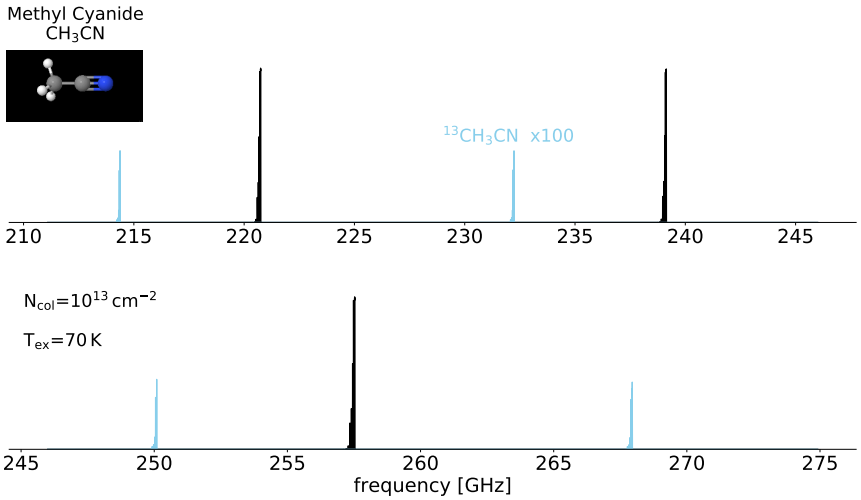

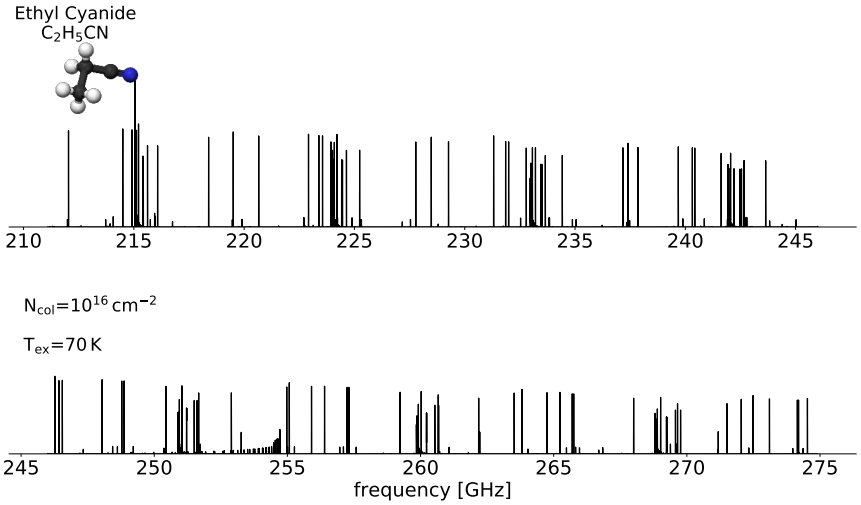

Figure C.3: Figure continues.

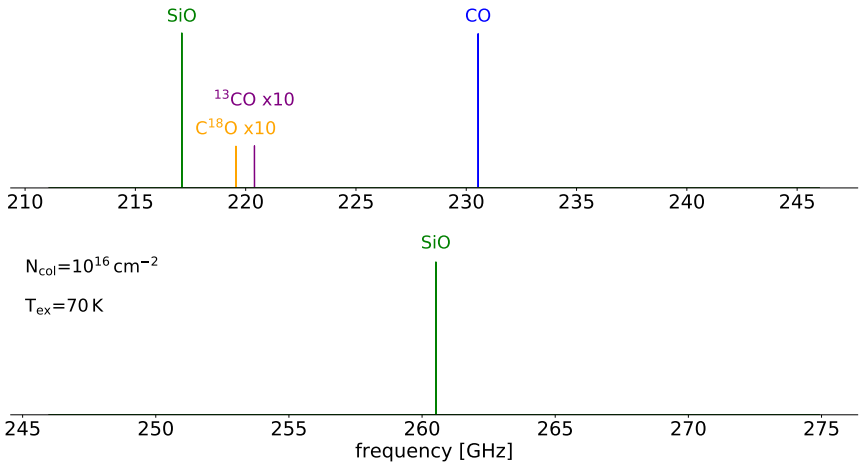

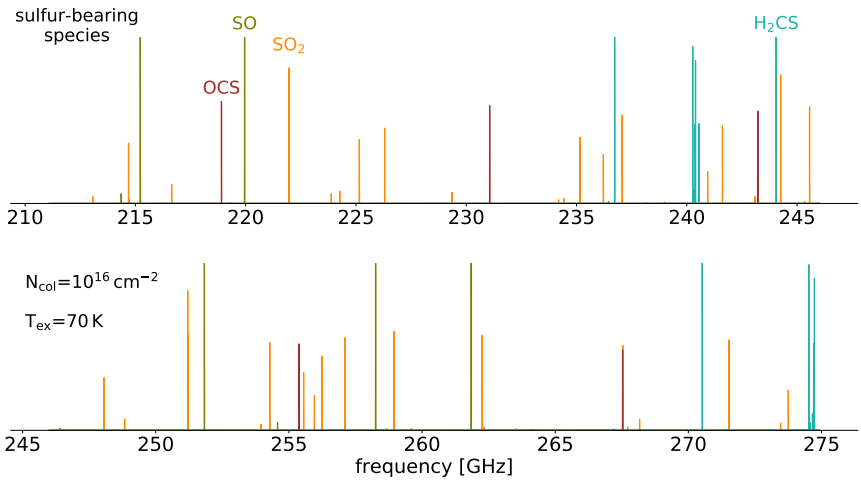

Figure C.4: Synthetic spectra of (complex) molecular species created with XCLASS. The 3D molecule images are taken from the kinetic database for astrochemistry (KIDA, except C_2H_5CN). The column densities and temperatures are not derived by fitting data, but assumed. The purpose of this figure is to indicate the frequencies of bright transitions of the selected molecular species. Low intensities of isotopologues are scaled up.

Notes: